Analytical Motion Planning on 3D-Lie Groups

by

Craig David Maclean

A Thesis Submitted in Partial Fulfilment of the Requirements for the Degree of Doctor of Philosophy

to the

Department of Mechanical and Aerospace Engineering

University of Strathclyde

Scotland

2014

Declaration

This thesis is the result of the author's original research. It has been composed by the author and has not been previously submitted for examination which has led to the award of a degree.

Signed:

Date:

Acknowledgements

Carrying out the work for this thesis has been a long, hard process and I must thank those who helped me through it.

Firstly my supervisor Dr. James Biggs has been invaluable in giving me advice, putting up with my panicky stream-of-consciousness e-mails and bearing with me during the first few months when any mention of a Lie group, elliptic function or differentiable manifold would be met with a slight cocking of the head and a low whine. Also, I'd like to thank the other staff and students within the Mechanical and Aerospace Engineering department who have provided me with advice, support and levity when needed.

Secondly, I'd like to thank my family for their quiet support throughout my PhD. You might not know it, but you helped a lot. Particularly my wee mammy for never making any fuss even when she has every right to, my wee dog Tippi for all the stress-relieving walks and my dad, who's hopefully watching over me from somewhere.

Lastly, I'd like to thank my girlfriend Erin for her unwavering support. Thanks for having faith in me when I didn't have faith in myself, for putting up with the times when I was fed up or stressed out and for knowing when I needed a cuddle and when I needed a kick. I couldn't have done it without you sweetie.

Abstract

In this thesis optimal analytical controls derived using the framework of geometric control theory are used to plan motions for real engineering systems, and their performance assessed.

Beginning with the nonholonomic wheeled robot on the 3-D Special Euclidean group, the co-ordinate free Maximum Principle of optimal control is used to create a kinematic motion planner via parametric optimisation. The reachable sets of the planner are investigated, and an obstacle avoidance framework is created and demonstrated. The practical applicability of this motion planner is assessed in both the unit speed and arbitrary speed cases.

Subsequently, the natural motions of an axisymmetric and asymmetric rigid body are derived in convenient quaternion form, which is particularly suitable for practical implementation. The initial angular velocities of the rigid body are parametrically optimised to produce attitude reference tracks for a small spacecraft. It is shown through comparison with a standard proportional-derivative controller that the natural motions require lower accumulated torque to track. Additional testing of the axisymmetric references, which are comprised of simple trigonometric functions, found that the references can be utilised in a "bang-off-bang" manner in low disturbance environments to save on computation and control effort.

Next, the general solution to the optimal control problem of a rigid body constrained to spin at a constant rate is derived. This takes the form of a Weierstrass elliptic function which is impractical for motion planning. However, a particular case is identified that is comprised of trigonometric functions and utilised to plan efficient motions for a spin-

ning solar sail and compared in simulation to a pure spin benchmark. The geometric references are found to limit the spacecraft body rates, while tracking requires lower accumulated torque in most cases. Finally, an actuator study is carried out to identify the technology requirements for reference tracking for a spinning solar sail.

Contents

List of Figures

List of Tables

Nomenclature

A_r	Reflective area of solar sail (m^2)
A_s	Area of nano-spacecraft face (m^2)
A_v	Area of control vane (m^2)
A_1, A_2, A_3	Basis of the Lie algebra
a_c	Characteristic acceleration of solar sail (m/s^2)
$\bar{a}_{ext}$	Acceleration due to external forces vector (m/s^2)
$\bar{a}_{SRP}$	Acceleration due to solar radiation pressure vector (m/s^2)
$\bar{B}$	Magnetic field vector in body reference frame (Teslas)
$\bar{B}_{grf}$	Magnetic field vector in geomagnetic reference frame (Teslas)
c_l	Speed of light (m/s)
C_d	Drag coefficient of spacecraft
F	Isomorphism from Special Unitary group $SU(2)$ to the unit quaternions $\mathbb{H}$
$\bar{F}_{SRP}$	Solar radiation pressure force vector (N)
H	Hamiltonian
$\bar{h}_w$	Reaction wheel angular momentum vector (Nms)
$\hat{I}, \hat{J}, \hat{K}$	Basis of the Geocentric Equatorial and Heliocentric Ecliptic reference frames
I_N	Accumulated torque of reaction wheels (Nms)
$\hat{i}, \hat{j}, \hat{k}$	Basis of the body reference frame
J	Inertia matrix of spacecraft (kgm^2)
J_s	Symmetric moment of inertia of spacecraft (kgm^2)
J_w	Moment of inertia of reaction wheels (kgm^2)

K_ω, K_q	Gain matrices
$\bar{l}_v$	Vector from centre of pressure of control vane to centre of mass of spacecraft (m)
M	Casimir function
$\bar{M}_{res}$	Residual dipole of spacecraft vector (Am^2)
$\bar{M}_{mtq}$	Dipole of magnetorquer (Am^2)
M_{max}	Maximum requested dipole (Am^2)
m_a	Attached mass (excluding sail) (kg)
m_s	Sail mass (kg)
m_{sm}	Sliding mass (kg)
$m_{s/c}$	Total mass of spacecraft (kg)
$\bar{N}_{ad}$	Air drag torque vector (Nm)
$\bar{N}_c$	Control torque vector (Nm)
$\bar{N}_{des}$	Desaturation torque vector (Nm)
$N_{des(max)}$	Maximum desaturation torque (Nm)
$\bar{N}_e$	External torque vector (Nm)
$\bar{N}_{gg}$	Gravity gradient torque vector (Nm)
$\bar{N}_{md}$	Residual dipole torque vector (Nm)
$\bar{N}_{mtq}$	Magnetic torque vector (Nm)
$\bar{N}_{SRP}$	SRP torque vector (Nm)
$\bar{N}_{sm}$	Sliding mass torque vector (Nm)
$\bar{N}_v$	Control vane torque vector (Nm)
$\bar{N}_w$	Reaction wheel torque vector (Nm)
$N_{w(max)}$	Maximum reaction wheel torque (Nm)
$\hat{n}_c$	Unit vector of cone centreline
$\hat{n}_p$	Unit vector of spacecraft body x-axis
$\hat{n}_{sail}$	Sail normal unit vector
$\hat{n}_v$	Control vane normal unit vector
P	Mean solar radiation pressure at 1 au ($\mathrm{N/m}^2$)
p_1, p_2, p_3	Increments to free parameters

$Q(t)$	Rotation matrix on $SO(2)$
$\bar{q}$	Quaternions of the body frame with respect to inertial frame
$\bar{q}_{bo}$	Quaternions of the body frame with respect to orbital frame
$\bar{q}_e$	Quaternion error vector
$\bar{q}_d$	Desired quaternion vector
$\hat{R}, \hat{T}, \hat{N}$	Basis of the RTN reference frame
$R(t)$	Rotation matrix on $SU(2)$
R_{ob}	Quaternion rotation matrix from RTN to body frame
$\bar{r}$	Radial vector from Earth to spacecraft (m)
$\bar{r}_{m/p}$	Centre of mass to centre of pressure vector (m)
$\bar{r}_{sun}$	Radial vector from Sun to spacecraft (m)
$S(t)$	Rotation matrix on $SO(3)$
S_0	Solar constant ($\mathrm{W/m^2}$)
T	Manoeuvre time (s)
t	Time (s)
$\bar{u}$	Control signal vector
$\bar{u}_{des}$	Desaturation control signal vector
v	Spin rate of spacecraft (rad/s)
v_r	Surge speed of wheeled robot (m/s)

α	Cone angle (rad)
$\bar{\gamma}$	Position vector of wheeled robot (m)
δ	Clock angle (rad)
δ_c	Half angle of obstacle cone (rad)
δ_p	Angle between spacecraft body x-axis and cone centreline unit vectors (rad)
η_m	Geomagnetic longitude (rad)
θ	Orientation of wheeled robot (rad)
κ	Reflectance factor
λ_m	Geomagnetic latitude (rad)
$\lambda_1, \lambda_2, \lambda_3$	Extremal curves
μ	Gravitational parameter (m^3/s^2)
μ_m	Earth's magnetic dipole strength (Wbm)
ρ	Density of air (kg/m^3)
σ_a	Attached mass assembly loading (kg/m^2)
σ_s	Sail assembly loading (kg/m^2)
τ	Stabilisation time (s)
$\varphi_1, \varphi_2, \varphi_3$	Euler angles (rad)
Ω	Skew symmetric angular velocity matrix
ω_r	Angular velocity of wheeled robot (rad/s)
$\bar{\omega}$	Angular velocity vector of body frame with respect to inertial frame (rad/s)
$\bar{\omega}_{bo}$	Angular velocity vector of body frame with respect to orbital frame (rad/s)
$\bar{\omega}_e$	Angular velocity error vector (rad/s)
$\bar{\omega}_{oi(b)}$	Orbital rate vector with respect to inertial frame, expressed in body frame (rad/s)
$\bar{\omega}_w$	Reaction wheel angular velocity vector (rad/s)

Chapter 1

Introduction

The Motion Planning Problem (M.P.P) for an autonomous system can be generalised as the task of finding a feasible motion that carries the body under consideration from configuration to configuration. Motion planning is a crucial part of many robotics tasks, such as computing collision free paths for robot arms in assembly lines [1, 2] and planning trajectories for simple car-like robots [3, 4]. Additionally, motion planning is also becoming increasingly important in a number of other diverse areas including guiding needles in neurosurgery [5], the design of artificial intelligence in computer games [6] and for autonomous systems such as planning trajectories for Unmanned Air Vehicles [7] and generating attitude control manoeuvres for spacecraft [8].

As a result of the breadth of applications, each with inherent system specific restrictions, many differing approaches have been taken to solve the motion planning problem. For example some systems may have poor sensing capabilities and so will have to operate under large uncertainties [9, 10], while other systems may have limited actuation and so are constrained to move along certain paths [11, 12].

However, there are three major challenges in motion planning for most autonomous rigid body systems: planning with respect to nonholonomic (velocity) constraints; creating optimal or near optimal paths and; computing paths which avoid forbidden zones in the configuration space. While many motion planning methods focus on only one of these topics, the complexity of planning for constrained, multiple degree of freedom

rigid body systems means that few methods exist which can satisfy all of these criteria without excessive computation.

These challenges are discussed in turn in Sections 1.1-1.3 below, together with a review of the work undertaken on each topic.

1.1 Nonholonomic Constraints

As discussed previously, a system may be subject to constraints which arise due to limitations or inaccuracies in the system hardware. However, there are two broad classes of constraints which occur in motion planning problems at a fundamental level: holonomic and nonholonomic constraints. A holonomic system has constraints only on the configuration variables: that is, it's position and orientation [13]. Consider the simple rigid 2D pendulum, shown below in Figure 1.1.

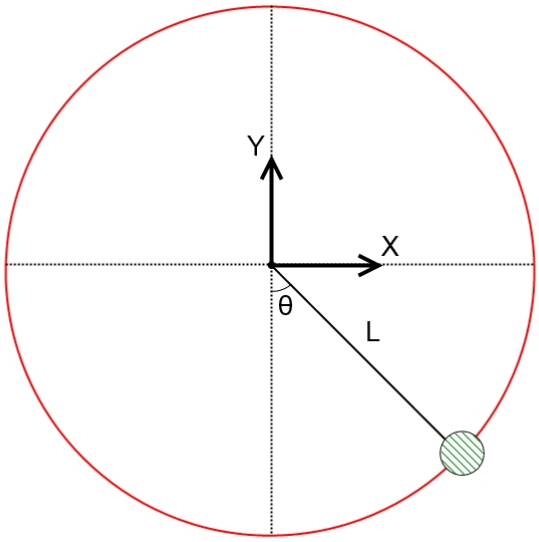

Figure 1.1: Simple 2D pendulum.

The positions and orientations through which the pendulum can move are limited by the length of the pendulum. Therefore this is an example of a holonomic system [13]. A nonholonomic system, however, also has constraints on the velocities of the system. A wheeled robot with wheels constrained to roll in the direction they are pointing (i.e.

without slipping), such as that shown in Figure 1.2, is an example of a nonholonomic system [14]. Additionally, this no-slip condition is imposed by the kinematics of the system and so is referred to as a kinematic nonholonomic constraint. A constraint imposed by system dynamics, such as the conservation of angular momentum of a rotating rigid spacecraft with no disturbances, shown in Figure 1.3, is referred to as a dynamic nonholonomic constraint [13]. Both types of nonholonomic constraint will be considered in this thesis.

Figure 1.2: A simple wheeled robot model. Robot is constrained to move in the direction of the front wheels (Image Credit: yourduino.com).

While planning for holonomic systems is relatively straightforward, nonholonomic path planning is more complicated as the velocity constraints render certain paths infeasible. In addition, the nonholonomic constraint cannot simply be integrated to obtain a holonomic constraint. In this sense nonholonomic constraints are non-integrable [13] and nonlinear control theory does not provide an explicit procedure for constructing controls for nonholonomic systems.

Due to this complexity, linearisation has been employed to simplify the nonholonomic path planning problem. However, Laumond [15] in the case of the simple wheeled robot, and Leonard, for drift-free, left-invariant systems [16], show that linearisation can render the system uncontrollable. Moreover, these methods are generally not optimal or adaptable to obstacle avoidance.

While the use of linearisation to reduce the complexity of nonholonomic motion plan-

ning has limitations, when the configuration space of the nonholonomic system can be represented by a matrix Lie group the integrals of motion of the system can be exploited to simplify the path planning problem [17]. A considerable body of work exists on planning for nonholonomic systems using the Lie group approach. Bloch [13] describes the formulation of controls for a variety of nonholonomic mechanical systems while Selig [18], and Murray and Sastry [19] focus on nonholonomic problems in the context of robotics. The general idea is to use control functions to generate motions in the directions of iterated Lie brackets: that is, the system directions that are not directly controlled. Murray and Sastry [20] extended the work of Brockett [21] on steering drift free nonholonomic systems, and showed that for certain classes of system the controls for generating Lie bracket motions take the form of sinusoids. A particular benefit of this method is the ability to satisfy orientation constraints by exploiting the periodicity of the controls. However, to date the method has not been adapted to include obstacle avoidance and is not optimal. Leonard [16, 22] also utilises periodic controls in an averaging method for the unicycle robot and spacecraft attitude control problem. Nonetheless, the method is not optimal and relies on local coordinate representations, meaning that only small reorientations can be performed without excessive computation.

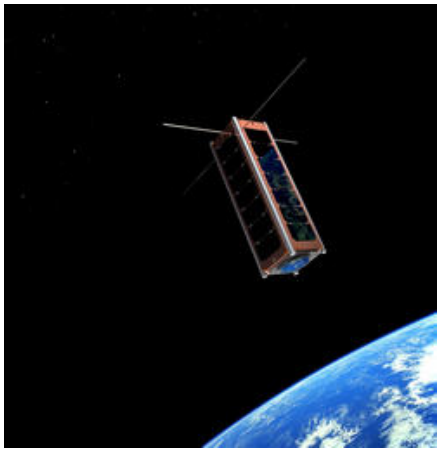

Figure 1.3: A small Cubesat spacecraft in orbit (Image Credit: Clyde Space Ltd).

Meanwhile, numerical path planning techniques such as pseudospectral optimal control

[23] and shooting methods [24] can also be adapted to include nonholonomic constraints. The constraints are specified as differential equations and numerical iteration techniques employed until a solution is found which satisfies the boundary conditions while respecting the nonholonomic constraints. However, the iterative nature of these methods means that they can require significantly more computation than the simple analytical methods produced by the Lie group approach.

Sampling based motion planning methods, such as the rapidly exploring dense trees (RDTs) commonly used in robot motion planning, can be adapted to include nonholonomic constraints through the use of motion primitives constructed using nonholonomic path planning [14]. Meanwhile, approximation methods, such as those proposed by Laumond [15, 25], first generate a holonomic path to the goal, ignoring the nonholonomic constraints. A complete feasible path is then generated by discretising the holonomic path into sub-goals, and joining these sub-goals via nonholonomic paths. However, these methods can again be computationally intensive.

As a result of the need for a tradeoff between the simplicity of the Lie group approaches and the optimality of numerical techniques, geometric control theory [17, 26] was introduced as a new approach to the problem of planning for nonholonomic systems. Geometric control theory was developed to address both the problems of controllability, through the use of Lie groups, and optimality, through the incorporation of the Maximum Principle of optimal control. This approach has been used to generate optimal controls for an aeroplane constrained to move forward at constant velocity [27] and an autonomous underwater vehicle which cannot move laterally [28], where helical trajectories were obtained for ascent/descent manoeuvres. However, the kinematic solutions were derived with respect to an ideal environment and the suitability of the motions for practical implementation was not tested in practice in the face of the limitations imposed by actuators, on-board computational capacity and a realistic environment. In the case of the repointing of a nonholonomic spinning spacecraft [29], where the references generated using geometric control theory were tested in simulation, the analysis was limited to showing simple motion tracking and the method was not rigorously compared to other attitude control methods. Thus the practical appli-

cability of references generated using geometric control theory has not been thoroughly investigated to date.

1.2 Optimal Control

While the nonholonomic motion planning methods discussed in Section 1.1 are effective in finding a path between the start and end configurations, there are often multiple solutions to these problems. Therefore it is often desirable when planning motions to not merely satisfy conditions on state variables, but also to find the path which minimises or maximises a certain performance metric. For example for a robotic arm operating under time constraints, an effective motion planning algorithm would compute the shortest time path for the robot arm to reach it's goal [30]. In contrast for a flexible structure such as the spin stabilised solar sail IKAROS [31], shown in Figure 1.4, slow and smooth manoeuvres are necessary to limit oscillation of the sail membrane [31, 32, 33].

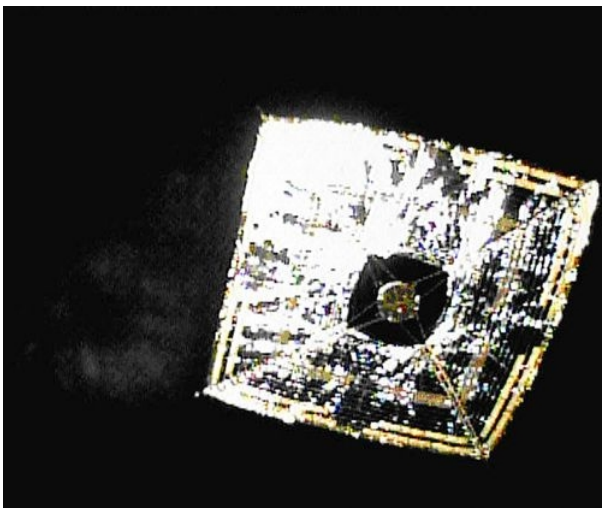

Figure 1.4: IKAROS spin stabilised solar sail (Image Credit: JAXA).

The difficulty of constructing optimal paths for a system scales with the number of constraints placed on the system, and on it's degrees of freedom. For example for a freely manoeuvrable point mass in an obstacle free planar environment, a simple straight line

path is optimal in terms of control effort and time. However, if the configuration space contains obstacles or there are constraints on the orientation of the system then this algorithm may no longer be optimal.

Consequently, this difficulty in constructing exact, optimal paths, has led to a large number of non-linear numerical optimisation techniques being employed to generate optimal trajectories. These methods generally reformulate the motion planning problem as a nonlinear programming problem, via discretisation of the optimal control problem and approximation of the equations of the system. A numerical optimisation method is then applied to minimise or maximise a specified cost function. These numerical optimisation methods broadly fall into two categories: direct search methods, such as the simplex based Nelder-Mead algorithm [34, 35], when derivative information is not available and ; gradient based methods, such as Newton's method, when derivative information is known [35]. However, these methods do not always find the absolute maxima or minima of the cost function and so more complex global methods have been developed.

Figure 1.5: The International Space Station in orbit (Image Credit: NASA).

In recent years, considerable attention has focussed on globally optimal pseudospectral optimal control methods [36]. In these methods the state of the system is approximated at carefully selected discrete points, known as quadrature nodes, using time-dependent global interpolating polynomials. These polynomials are then differentiated to give

the approximate time derivative of the state, and used in conjunction with nonlinear programming methods to find optimal solutions. The advantage of these methods is that the careful choice of node points offers a faster rate of convergence than other methods [37]. Pseudospectral methods have been used to plan motions for a range of systems, from the attitude control of the International Space Station shown in Figure 1.5, to planning collisions free paths for nonholonomic wheeled robots [37]. However, while these numerical methods are optimal with respect to the specified cost, they can be computationally intensive in comparison to simple analytical Lie group methods. Additionally, convergence can be difficult to achieve unless an accurate initial guess is supplied.

As a result of numerical methods requiring an initial guess, they are often viewed as being complimentary to other motion planning methods, such as Rapidly Exploring Random Trees (RRTs). The RRT method, which incrementally builds a "tree" of paths in the search space, is used to generate an initial guess [14]. The optimisation method is then applied to improve the solution generated by the motion planner. For example Kuwata [38] utilises a Rapidly Exploring Random Tree (RRT) method to generate the initial trajectory for a car-like vehicle in a real world environment, before an optimisation algorithm is applied to smooth the trajectory. Additionally, optimisation methods can be used in conjunction with RRT methods to bias the growth region towards an area which minimises a specified cost function [39]. Other examples of this include trajectory shortcutting [40], in which the initial trajectory is assigned a number of nodes along it's length, and algorithms check to see if these nodes can be connected at any point in order to decrease the total distance travelled. However, these methods are heavily reliant on heuristics - the application of human experience - to the problem, which means that finding a suitable solution is not guaranteed.

While optimisation is often viewed as being supplementary to local path planners, geometric control theory has shown potential in combining optimal control with nonholonomic motion planning methods via incorporation of the Maximum Principle of optimal control [41]. This enables controls to be derived which inherently respect the necessary conditions for optimality. These controls can then be used to plan motions, or

as an initial guess in a global numerical optimiser. However, in order to derive analytical controls using the geometric control theory framework a quadratic cost function is employed. This cost function, although meaningful, may not always be the most practical, appropriate choice for the system under consideration. Nevertheless, the method enables the reduction of a functional optimisation problem to a much simpler parametric optimisation problem. In this simpler context additional practical cost functions can be assigned to the resulting subset of motions.

1.3 Obstacle Avoidance

The task of planning motions for nonholonomic systems, while difficult due to the inherent velocity constraints, is further complicated in real-world environments by the presence of regions which the system cannot pass through. For example a feasible path for a wheeled robot must not cause a collision with an obstacle [14, 42], while a spacecraft with delicate optical equipment, such as the Hubble Space telescope shown in Figure 1.6, must manoeuvre while avoiding the Sun [43].

Figure 1.6: The Hubble Space Telescope (Image Credit: NASA).

The problem of motion planning in the presence of obstacles was considered by Nilsson

[44] in 1969, when he introduced the concept of a visibility graph to find collision-free paths for a robot amongst polygonal obstacles. The robot and goal configurations are represented by points, and together with the polygonal obstacles they are assigned vertices. An algorithm is then run to determine which vertices can be connected in order to create a collision free path between the robot and the goal. A further planning algorithm, such as the A^* method proposed by Nilsson [44], is then utilised to find the shortest collision-free path from the robot to the goal. Lozano-Perez and Wesley [45] extended this work to create a complete path planner for polyhedral robots moving amongst polygonal/polyhedral obstacles, while Laumond generalised the method for nonpolygonal obstacles consisting of line sections and circular arcs [46].

Building on his visibility graph based complete path planner for polygonal/polyhedral robots moving amongst polygonal/polyhedral obstacles, Lozano-Perez introduced the concept of the configuration space [9] to robot motion planning. Defining the configuration space of a system such as a wheeled robot or spacecraft as the set of possible transformations (rotations or translations) that could be applied to the system [9], obstacles or other undesirable states in the workspace map as forbidden regions in the configuration space [14, 42]. Motion planning while avoiding these forbidden regions then reduces to finding feasible paths through the "free space": that is, the region of the configuration space free of forbidden regions. While many different methods of obstacle avoidance exist, most follow this simple notation as it enables problems involving different systems to be solved using the same motion planning methodologies [14].

Complete path planners, such as that proposed by Lozano-Perez, have the advantage that the system is described without compromise. This means that if a solution exists, the planner will find it, otherwise it will report that no feasible solutions exist [14]. Examples of complete motion planners include the work of Schwartz and Sharir on the classical 'Piano mover's problem', who consider a number of cases including a polygonal body [47] and circular bodies [48] moving between polygonal walls. However, complete path planners are complex and difficult to implement in practice [2, 14]. This led to the development of simpler, heuristic planners such as the potential field method.

Potential field methods assign an attractive potential to the goal configuration and a repulsive potential to the undesirable areas of the configuration space [49]. They have been used in applications such as path planning for robot arms, where a repulsive potential is assigned to any obstacles in the configuration space [50], and the attitude control of spacecraft, where the target attitude is assigned an attractive potential and undesirable attitudes a repulsive potential [51]. The potential field methods can suffer from problems of local minima, which can cause the planner to become "stuck" at an undesirable point [49]. However, this can be overcome by adding a random-walk element to the motion planning to escape the local minima [14, 49]. Additionally, the potential field methods can demand excessive control effort [52, 53] making them far from optimal if care is not taken to constrain the rate of the control. Furthermore, while the potential field methods have proven effective, the reliance on heuristics means that parameters have to be manually tuned for each application, leading to the development of other sampling based methods for obstacle avoidance.

Sampling based methods, such as Probabilistic Roadmap Methods (PRMs), repeatedly sample configurations in the configuration space and exclude those which intersect an obstacle [2, 42]. This results in a topological graph in the free space which maps to the workspace, enabling collision-free paths to be planned. The construction of the roadmap is performed during a pre-processing phase, before a local planner is employed to generate feasible paths. These methods have the advantage of being able to plan trajectories between multiple initial and final configurations using the same roadmap. However, the lengthy pre-processing stage means these methods may be unsuitable for fast implementation. As a result, less comprehensive but faster methods such as rapidly exploring dense trees (RDTs) have been utilised. These methods attempt to connect the initial configuration to any final configuration by incrementally constructing a "tree" of paths, rather than mapping the free space in a pre-processing stage. When the presence of an obstacle is detected, the edge stops at the boundary of the obstacle and path generation is continued in a different direction. A further algorithm is then run to choose the most suitable obstacle free path by joining the edges [14].

Additionally, the pseudospectral methods described previously can be adapted to in-

clude simple obstacle avoidance by including the forbidden region as an additional path constraint [37]. However, obstacle avoidance algorithms typically require feasible solutions to be swiftly evaluated on-board, which may mean that these intensive numerical methods are difficult to implement in practice. Moreover, in robot motion planning these numerical algorithms must have their feasibility evaluated at each time-step, further increasing the computational load [14].
Finally, despite showing promise in generating optimal analytical controls for nonholonomic systems, the references derived using geometric control theory have to date not been implemented in an obstacle avoidance algorithm.

1.4 Objectives of the Research

As a result of the need to find a compromise between the effectiveness of numerical optimisation techniques and the simplicity of Lie group based motion planning for nonholonomic systems, this work aims to extend the research carried out to date on geometric control theory to assess if it can be applicable to practical problems and improve, in some way, current motion planning problems. The aims of this work can then be summarised as follows:

- To derive optimal, global motion planners for systems with dynamic and kinematic nonholonomic constraints using the mechanisms of geometric control theory.
- To link the fields of geometric control, which to this point has been primarily theoretical, and real engineering applications.
- To assess the practicality of geometric motion planning on Lie groups for spacecraft motion planning through numerical simulation and rigorous comparison with other methods.
- To create a simple framework for obstacle avoidance within the geometric motion planners.

1.5 Contributions of the Thesis and Relevant Publications

The following contributions have been made.

- The work first carried out by Biggs [54] on the use of geometric control theory for nonholonomic robot path planning for a robot which moves at arbitrary speed is extended. The properties of elliptic functions are explored to derive particular cases of the general solution, and the geometric meaning of the solutions is investigated. The reachable sets of the method are defined and a simple obstacle avoidance framework is detailed. Additionally, a motion planning algorithm for the nonholonomic unit speed wheeled robot with drift is derived, and the time-limited reachable sets investigated. Relevant publications:
  - Maclean, C. and Biggs, J. D., "Path Planning for Simple Wheeled Robots: sub-Riemannian and Elastic Curves on SE(2)," Robotica, Vol. 31, No. 8, pp. 1285-1297, 2013.
- Novel analytical expressions for the time evolution of the quaternions of an axisymmetric and asymmetric rigid body are derived via application of the mechanisms of geometric control theory. The expressions are included in global motions planners. These planners are assessed through rigorous numerical simulation in a realistic environment and considering actuator constraints. The references are compared to a conventional quaternion feedback controller in terms of accumulated torque and computational efficiency, and an obstacle avoidance framework is detailed. Relevant publications:
  - Maclean, C., Pagnozzi, D. and Biggs, J. D., "Computationally Light Attitude Controls for Resource Limited Nano-spacecraft", In: Proceedings of the 2011 International Astronautical Congress, Cape Town, South Africa, 2011.
  - Pagnozzi, D., Maclean, C. and Biggs, J. D., "A New Approach to the Solution of Free Rigid Body Motion for Attitude Maneuvers", In: European Control Conference, Zurich, Switzerland, 2013.

  - Maclean, C., Pagnozzi, D. and Biggs, J. D., "Planning Natural Repointing Manoeuvres for Nano-Spacecraft," IEEE Transactions on Aerospace and Electronic Systems, Accepted January 2014, In Press.

- The geometric motion planning method for a spin stabilised spacecraft proposed by Biggs [29] is extended. The general form of the solution is derived, and the case of Biggs shown to be a particular case of this. The references generated by Biggs are rigorously tested in simulation for the first time via application to a spinning solar sail. A comparison with pure spin benchmark references is made to assess the performance of the geometric method in terms of accumulated torque, and constrained repointing is investigated. The references are further applied in simulation to the repointing of a nano-spacecraft, and compared to the novel natural motion method derived in this thesis and a standard proportional derivative controller. The axisymmetric natural motions are found to be a subset of the geometric spin repointing method. An actuator study is carried out to determine the technology requirements for tracking references for a spinning solar sail. Relevant publications:

  - Maclean, C. and Biggs, J. D., "Attitude Motion Planning for a Spin Stabilised Disk Sail," In: Proceedings of the 2012 International Astronautical Congress, Naples, Italy, 2012.

1.6 Outline of the Thesis

This thesis is organised as follows. In Chapter 2 the theory behind motion planning on matrix Lie groups is introduced, together with the framework of geometric control theory which will be used in subsequent sections to derive optimal controls. Following this, in Chapter 3, this framework is applied to the nonholonomic wheeled robot and used to derive a simple kinematic motion planner. An obstacle avoidance framework which exploits the reachable sets of the planner is described and an example given for a circular obstacle in a known environment. The complexity of the motion planning

is then increased in Chapter 4 by considering the repointing of a spacecraft subject to a dynamic nonholonomic constraint due to the conservation of angular momentum. The derived references exploit the natural motion of the spacecraft and are applied in simulation, taking into account actuator constraints and environmental disturbances, and are compared to a proportional-derivative controller benchmark. In Chapter 5 the previously derived references for the repointing of a spacecraft subject to a kinematic nonholonomic constraint on the spin rate are applied in simulation to a solar sail spacecraft, and are compared to benchmark pure spin references. The method is additionally applied to the nano-spacecraft of Chapter 4 to provide a comparison with the natural motion method. An actuator study is carried out to determine the feasibility of tracking the reference motions using currently available solar sail actuators. Finally, the outcomes of the thesis and areas of future research are detailed in Chapter 6.

Chapter 2

Motion Planning on 3D-Lie groups

In Chapter 1 it was stated that the configuration space of rigid body systems can be represented by a Lie group. In this chapter the background theory on optimal kinematic motion planning for systems defined on matrix Lie groups is described. This will be applied in the following chapters to develop motion planning algorithms which will then have their practical applicability assessed. Kinematic systems defined on matrix Lie groups, when lifted to their Hamiltonian form through the Maximum Principle of optimal control, exhibit integrals of motion. These integrals enable the complexity of the problem to be reduced, thus simplifying the process of deriving analytical optimal controls.

Some preliminary definitions regarding group theory are stated before the concepts of matrix Lie groups and their accompanying Lie algebra are introduced. Following this, the matrix Lie groups which are of particular relevance to this thesis are presented: the Special Euclidean group of the plane, $SE(2)$; the Special Unitary group of complex orthogonal 2×2 matrices, $SU(2)$ and ; the Special Orthogonal group of 3×3 rotational matrices, $SO(3)$. Subsequently, it is shown how matrix Lie groups and their Lie algebras can be used to represent the kinematics of many practical engineering systems. The planar wheeled robot and the rotating rigid body are given as examples.

A quadratic cost function which minimises the control effort of the manoeuvres is defined next, together with a description of how the Lie bracket can be used to determine controllability. The Maximum Principle of optimal control is then stated and applied to generate an optimal Hamiltonian based on the kinematics and cost function of the system. Finally, the problem is lifted to the dual of the Lie algebra via the Poisson bracket, yielding the Hamiltonian vector fields which in certain cases can be solved to give the analytical optimal controls.

2.1 3D-Matrix Lie Groups

As stated in Chapter 1, the matrix Lie group setting lends itself naturally to non-holonomic optimal control problems as the conserved quantities of the system can be exploited to simplify the derivation of the controls. In order to understand the mathematical theories utilised in the derivation of the kinematic optimal controls, some fundamental definitions from group theory and manifold theory are stated, before moving on to discuss the particular cases of matrix Lie groups and Lie algebras.
Firstly, it is necessary to state the general definition of a group [13]:

Definition 1. *A group is a set G, together with a map $G \times G$ into G (denoted $g \circ h$) which has the following properties:*

1. *Associativity:*

$$g \circ (h \circ k) = (g \circ h) \circ k \quad \forall \quad g, h, k \in G \tag{2.1}$$

2. *An identity element:*

$$g \circ e = e \circ g \quad \forall \quad g \in G \tag{2.2}$$

   where e is the identity element.

3. *An inverse element:*

$$g \circ h = h \circ g \quad \forall \quad g \in G, h \in G \tag{2.3}$$

The mapping $G \times G$ into G is referred to as the product operation of the group.

Essentially this means that the product of two elements of the group is itself an element of the group, and the group is said to be closed under this product operation. Thus in order to identify a group it is necessary for elements of the group to have closure, associativity, an identity element and a unique inverse.

A simple example of a group is the group of integers $\mathbb{Z}$ which for $a, b, c \in \mathbb{Z}$ are closed under addition ($a + b \in \mathbb{Z}$), satisfy associativity ($a + (b + c) = (a + b) + c$), has the identity zero ($a + 0 = 0 + a = a$) and has a unique inverse ($a + b = b + a = 0$, where $b = -a$).

It follows that a subgroup can be defined as:

Definition 2. *A subgroup of a group G is a subset H of G for which:*

1. *The identity is an element of H*
2. *If $h \in H$, then $h^{-1} \in H$.*
3. *If $h_1, h_2 \in H$, then $h_1 \circ h_2 \in H$.*

Therefore H is itself a group. Subsequently, the semi-direct product which enables new groups to be formed via the product of existing groups can be defined as:

Definition 3. *Let G and H be groups. The semi-direct product of G and H, denoted $G \circledS H$, is the set of ordered pairs (g, h) with $g \in G, h \in H$, where the product of two elements is given by*

$$(g_1, h_1)(g_2, h_2) = (g_1 \circ g_2, h_1 + g_1 h_2) \tag{2.4}$$

An example of this is the Special Euclidean group of rotations and translations on a plane, $SE(2)$, which is the semi-direct product of the Euclidean plane, $\mathbb{R}^2$, and the Special Orthogonal group of 2×2 rotation matrices, $SO(2)$. Additionally, mappings exist between certain groups which enable elements of one group to be mapped to another. This is useful as computations may be more easily performed on a particular group. For example Klein [55] found that for a symmetric rigid body in a constant gravitational field utilising the Special Unitary group $SU(2)$, the set of 2×2 complex unitary matrices with determinant one, rather than the Special Orthogonal group $SO(3)$, the set of

3×3 orthogonal matrices with determinant one, as the configuration space simplified the derivation process. These mappings are defined as:

Definition 4. *Let G and H be groups. A map $\Phi : G \to H$ is called a homomorphism if $\Phi(gh) = \Phi(g)\Phi(h) \quad \forall g, h \in G$. If the mapping is bijective (one-to-one and onto), then Φ is called an isomorphism.*

G and H are said to be isomorphic, denoted $G \cong H$, if an isomorphism exists between them. An example of this is $SU(2)$ and the unit quaternions $\mathbb{H}$. If the mapping $\Phi(gh)$ is two-to-one, such that each element of G corresponds to two elements of H, then the mapping is known as a double cover. This definition will be key to the discussion of the relationship between the Special Unitary group $SU(2)$, the unit quaternions $\mathbb{H}$ and the Special Orthogonal group $SO(3)$ in Section 2.2.4.
These definitions detail the basic theory behind groups as applicable to the work in this thesis. Before proceeding to discuss matrix Lie groups, it is necessary to additionally define a smooth manifold.

Definition 5. *An n-dimensional smooth manifold M is a set of points together with a finite or countably infinite set of subsets $U_\alpha \subset M$ and one-to-one smooth mappings $\phi_\alpha : U_\alpha \to \mathbb{R}^n$ such that:*

1. *$\cup_\alpha U_\alpha = M$. Therefore the entire manifold can be covered by the co-ordinate charts U_α.*
2. *For each nonempty intersection $U_\alpha \cap U_\beta, \phi_i(U_\alpha \cap U_\beta)$ is an open subset of $\mathbb{R}^n$, and the bijective mapping $\phi_\alpha \circ \phi_\beta^{-1} : \phi_3(U_\alpha \cap U_\beta) \to \phi_\alpha(U_\alpha \cap U_\beta)$ is a smooth function.*
3. *The family $\{U_\alpha, \phi_\alpha\}$ is maximal with respect to conditions 1 and 2. Therefore the definition of a manifold is independent of a choice of atlas.*

The Lie groups which are the subject of this thesis are both groups and smooth manifolds, meaning that group operations are performed on a smooth structure. With these preliminary definitions stated, some general definitions of matrix Lie groups, the Lie algebra and it's dual from Bloch [13] can now be introduced:

Definition 6. *A matrix Lie group, G, is a set of invertible $n \times n$ matrices that are closed under matrix multiplication and that are a submanifold of $\mathbb{R}^{n\times n}$.*

Following this, the Lie algebra, which are associated with the tangent space at the identity of the Lie groups, can be defined:

Definition 7. *A Lie algebra $\mathfrak{g}$, of a matrix Lie group G, is a set of $n\times n$ matrices that is a vector space with respect to the usual operations of matrix addition and multiplication by real numbers (scalars) and that is closed under the matrix Lie bracket operation $[\cdot,\cdot]$ such that if $X, Y \in \mathfrak{g}$ then*

$$[X, Y] = XY - YX \tag{2.5}$$

As Lie algebras are linear spaces they are often easier to perform computations on, while they also contain information about their corresponding matrix Lie group. Thus it is possible to ask questions of the Lie algebra, rather than the matrix Lie groups, and the solution process is much simplified. The Lie group and the Lie algebra can be related using the matrix exponential. One such method is the Wei-Norman approach [56]:

Definition 8. *Consider the Lie algebra $\mathfrak{g}$ of a Lie group G with a basis $A_1..., A_3$. For left invariant systems on 3D-Lie groups of the form*

$$\frac{dg}{dt} = g(t)\sum_{i=1}^{n} A_i \tag{2.6}$$

where $n \leq 3$ and g is an element of G, the Wei-Norman representation states that there exists a neighbourhood of $t = 0$ in which the solution to (2.6) can be represented in the form

$$g(t) = e^{s_1(t)A_1}e^{s_2(t)A_2}e^{s_3(t)A_3} \tag{2.7}$$

where $s_1(t), s_2(t)$ and $s_3(t)$ are scalar functions of t.

The matrix exponential serves as the mechanism by which information is passed from the Lie algebra, which is simpler to perform calculations on, and the matrix Lie group.

Furthermore, as Poisson calculus will be utilised to derive the optimal kinematic controls, it is necessary to introduce Poisson structures and the dual space of the Lie algebra:

Definition 9. *Let P be a manifold and $\Gamma(P)$ the set of smooth, real-valued functions on P. The pair $(P, \{,\})$ is called a Poisson manifold if $\{,\}$ satisfies:*

1. *Bilinearity. $\{f, g\}$ is bilinear in f and g.*

2. *Anticommutavity:*

$$\{f, g\} = -\{g, f\} \tag{2.8}$$

3. *Jacobi's identity:*

$$\{\{f, g\}, h\} + \{\{h, g\}, g\} + \{\{g, h\}, f\} = 0 \tag{2.9}$$

4. *Leibniz's rule:*

$$\{fg, h\} = f\{g, h\} + g\{f, h\} \tag{2.10}$$

These conditions make $(\Gamma(P), \{,\})$ a Lie algebra. For left-invariant systems on 3D-Lie groups, $\hat{p}$ defines the mapping from the Lie algebra $\mathfrak{g}$ to the dual of the Lie algebra $\mathfrak{g}^*$. The dual space $\mathfrak{g}^*$ is a Poisson manifold and the Poisson bracket can be expressed in terms of the Lie bracket as

$$\{\hat{p}(\cdot), \hat{p}(\cdot)\} = -\hat{p}([\cdot, \cdot]) \tag{2.11}$$

where $(\cdot) \in \mathfrak{g}$. This relation will be utilised in order to derive the Hamiltonian vector fields which define the optimal extremal solutions. Moreover, it is appropriate to also state a particular class of Lie groups which will be utilised in this thesis, in semisimple Lie groups:

Definition 10. *A Lie group G is said to be semisimple if it's Lie algebra $\mathfrak{g}$ is semisimple. That is, if the Lie algebra is a direct sum of simple Lie algebras.*

The integration procedure on semisimple Lie groups is reduced to solving a Lax pair [17, 57] and hence is much simplified. This will be discussed in Section 2.5.3. The

Special Unitary $SU(2)$ and Special Orthogonal $SO(3)$ Lie groups are semisimple, while the Special Euclidean group of the plane $SE(2)$ is not.

With the mathematical preliminaries defined, the structure of the matrix Lie groups $SE(2), SU(2)$ and $SO(3)$ and their accompanying algebra are first discussed. These 3D-Lie groups will be utilised in the proceeding chapters in the derivation of motion planning algorithms. In particular the mappings between $SU(2)$ and $SO(3)$ and the unit quaternions, which are commonly used to represent the kinematics of spacecraft in practical engineering problems, are discussed. Thereafter, the general kinematic representation using the matrix Lie group approach is introduced. Finally, these concepts are related to the specific matrix Lie groups $SE(2), SU(2)$ and $SO(3)$, and linked to the real world engineering applications considered in this thesis in the form of the planar wheeled robot and the free rigid body.

2.2 Examples of 3D-Matrix Lie Groups

In this section the matrix Lie groups which will be studied in this thesis are detailed, and identified with the configuration space of real world engineering problems.

2.2.1 The Special Euclidean Group SE(2)

The Special Euclidean group $SE(2)$, whose elements represent the configuration described by an orthonormal frame attached to a Euclidean plane, can be used to represent the rigid body motion of planar systems such as the wheeled robot shown in Figure 1.2.

Formally, $SE(2)$ is the semi-direct product of Euclidean plane $\mathbb{R}^2$ and the Special Orthogonal group $SO(2)$ of 2×2 orthonormal rotation matrices. Thus, it is the set of all 3×3 matrices of the form

$$\begin{pmatrix} Q(t) & \bar{\gamma} \\ 0 & 1 \end{pmatrix} \tag{2.12}$$

where $Q(t) \in SO(2)$ represents the rotational component of the motion, and $\bar{\gamma} \in \mathbb{R}^2$ the translational component. The basis elements of the Lie algebra, $\mathfrak{se}(2)$, of the matrix Lie group $SE(2)$ are given by

$$A_1 = \begin{pmatrix} 0 & 0 & 1 \\ 0 & 0 & 0 \\ 0 & 0 & 0 \end{pmatrix}, A_2 = \begin{pmatrix} 0 & 0 & 0 \\ 0 & 0 & 1 \\ 0 & 0 & 0 \end{pmatrix}, A_3 = \begin{pmatrix} 0 & -1 & 0 \\ 1 & 0 & 0 \\ 0 & 0 & 0 \end{pmatrix} \tag{2.13}$$

Under the action of the Lie bracket, defined by $[X, Y] = YX - XY$ with $X, Y \in \mathfrak{se}(2)$, the basis satisfy the commutative table shown in Table 2.1.

Table 2.1: Commutative table for basis on $\mathfrak{se}(2)$

	A_1	A_2	A_3
A_1	0	0	$-A_2$
A_2	0	0	A_1
A_3	A_2	$-A_1$	0

Applying the Wie-Norman representation (2.7), it is found that

$$g(t) = e^{X(t)A_1} e^{Y(t)A_2} e^{\theta(t)A_3} \tag{2.14}$$

where $g(t)$ is an element of $SE(2)$. Therefore physically the basis represent the infinitesimal motion of the planar rigid body in the translational ($X, Y \in \mathbb{R}^2$) and rotational ($\theta \in SO(2)$) directions.

2.2.2 The Special Unitary Group SU(2)

The special unitary group $SU(2)$ is the set of all 2×2 complex unitary matrices which have determinant one. A complex matrix, R, is unitary if it satisfies the relation $R^*R = I$ where R^* is the conjugate transpose of R and I is the identity matrix. The

elements of $SU(2)$ are of the form

$$\begin{pmatrix} z_1 & z_2 \\ -\bar{z}_2 & \bar{z}_1 \end{pmatrix} \tag{2.15}$$

with $z_1, z_2 \in \mathbb{C}$ and $\bar{z}_1, \bar{z}_2$ their complex conjugates such that $|z_1|^2 + |z_2|^2 = 1$.
The basis of the Lie algebra $\mathfrak{su}(2)$ of the Lie group $SU(2)$ are given by

$$A_1 = \tfrac{1}{2}\begin{pmatrix} i & 0 \\ 0 & -i \end{pmatrix}, A_2 = \tfrac{1}{2}\begin{pmatrix} 0 & 1 \\ -1 & 0 \end{pmatrix}, A_3 = \tfrac{1}{2}\begin{pmatrix} 0 & i \\ i & 0 \end{pmatrix} \tag{2.16}$$

where i is the imaginary unit. Once again, under the action of the Lie bracket (2.5) with $X, Y \in \mathfrak{su}(2)$, the basis commute as shown in Table 2.2.

Table 2.2: Commutative table for basis on $\mathfrak{su}(2)$

	A_1	A_2	A_3
A_1	0	A_3	$-A_2$
A_2	$-A_3$	0	A_1
A_3	A_2	$-A_1$	0

Physically the basis A_1, A_2, A_3 describe the infinitesimal motion of the rigid body in the roll, pitch and yaw directions respectively.
Note that the Special Unitary group $SU(2)$ is isomorphic to the unit quaternions $\mathbb{H}$. The quaternions are the most commonly used kinematic representation of the attitude of a spacecraft, as they are singularity free and only four differential equations must be integrated, making them computationally light [32]. It follows that $SU(2)$ can be used to represent the attitude kinematics of a rigid body such as the nanospacecraft shown in Figure 1.3, and mapped exactly to the quaternions as shown in Section 2.2.4. The kinematics will be treated in Section 2.3.3.

2.2.3 The Special Orthogonal Group SO(3)

The Special Orthogonal group $SO(3)$ is made up of the set of 3×3 orthogonal matrices with determinant one. Therefore the elements $R \in SO(3)$ can be formalised as

$$SO(3) \triangleq \{R \in \mathbb{R}^{3\times 3} : R^T R = I \quad and \quad det(R) = 1\} \tag{2.17}$$

where I is the 3×3 identity matrix. The Special Orthogonal group $SO(3)$ is a subgroup of the Orthogonal group $O(3)$, which contains all 3×3 orthogonal matrices with determinant equal to plus or minus one. While the elements of $O(3)$ correspond to combinations of rotations and reflections, elements of $SO(3)$ correspond solely to rotations. Consequently $SO(3)$ can be thought of as the set of all 3×3 rotation matrices. The basis of the Lie algebra $\mathfrak{so}(3)$ of the matrix Lie group $SO(3)$ are given by

$$A_1 = \begin{pmatrix} 0 & 0 & -1 \\ 0 & 0 & 0 \\ 1 & 0 & 0 \end{pmatrix}, A_2 = \begin{pmatrix} 0 & 0 & 0 \\ 0 & 0 & 1 \\ 0 & -1 & 0 \end{pmatrix}, A_3 = \begin{pmatrix} 0 & 1 & 0 \\ -1 & 0 & 0 \\ 0 & 0 & 0 \end{pmatrix} \tag{2.18}$$

The Lie algebra's commutator is defined by (2.5) with $X, Y \in \mathfrak{so}(3)$, satisfying the relations in Table 2.3.

Table 2.3: Commutative table for basis on $\mathfrak{so}(3)$

	A_1	A_2	A_3
A_1	0	A_3	$-A_2$
A_2	$-A_3$	0	A_1
A_3	A_2	$-A_1$	0

Using the Wei-Norman representation, (2.7), it follows that

$$g(t) = e^{\varphi_1(t)A_1} e^{\varphi_2(t)A_2} e^{\varphi_3(t)A_3} \tag{2.19}$$

where $g(t)$ is an element of $SO(3)$. Physically the basis represent the infinitesimal

motion of the freely rotating rigid body around the $\hat{j}$ body-axis by an angle φ_1, the $\hat{\imath}$ body-axis by an angle φ_2 and the $\hat{k}$ body-axis by an angle φ_3. These angles are conventionally referred to as pitch, roll and yaw respectively.

The pitch, roll and yaw rotation angles are part of a rotational set commonly known as the euler angles. These consist of multiple different sets of three rotations which rotate a body from an initial attitude to a desired attitude. The euler angles can also be utilised to describe the configuration space of a rigid body. However, this kinematic representation is inherently local and suffers from problems with singularities [32, 58]. The rotation matrix formed from (2.19) is equivalent to the $\varphi_3 \leftarrow \varphi_1 \leftarrow \varphi_2$ euler angle rotation sequence [58].

Rotation matrices on $SO(3)$ can also be used to directly represent the kinematics of practical engineering problems, such as the rigid body nanospacecraft shown in Figure 1.3, overcoming the singularities inherent in the euler angle representation. This will be discussed in detail in Section 2.3.3. However $SO(3)$ does not map exactly to the most widely used attitude parameterisation, the unit quaternions $\mathbb{H}$, as will now be discussed in Section 2.2.4.

2.2.4 Mapping from $SU(2)$ to $SO(3)$

It has been stated that the kinematics of a rigid body can be represented as quaternions on $\mathbb{H}$ or equivalently using the Lie algebra of the matrix Lie group $SU(2)$. This one-to-one and onto mapping is known as an isomorphism. The matrix Lie group $SU(2)$ is isomorphic to the unit quaternions with $F : SU(2) \leftrightarrow \mathbb{H}$

$$F : \begin{pmatrix} z_1 & z_2 \\ -\bar{z}_2 & \bar{z}_1 \end{pmatrix} \leftrightarrow \mathbf{z}_1 + \mathbf{z}_2 \cdot \mathbf{j} = q_0\mathbf{e} + q_1\hat{i} + q_2\hat{j} + q_3\hat{k} \tag{2.20}$$

defining the co-ordinate change. The complex numbers $z_1 = q_0 + iq_1, z_2 = q_2 + iq_3$ are regarded in their quaternion form $\mathbf{z}_1 = q_0\mathbf{e} + q_1\mathbf{i}, \mathbf{z}_2 = q_2\mathbf{e} + q_3\mathbf{i}$. For more details of this isomorphism see [17] pp. 169-171.

In most practical applications, the attitude kinematics of the spacecraft are parame-

terised using the unit quaternions $\mathbb{H}$ as they are global, computationally efficient, and singularity-free [32]. However as shown in Section 2.2.3 the rotational kinematics of a rigid body can also be represented using $SO(3)$, the set of rigid body rotation matrices. On the Special Orthogonal group rotations are defined uniquely and globally [59], whereas $SU(2)$ is double cover of $SO(3)$ [17, 60]. This means that there is a homomorphism F which maps $SU(2)$ and $SO(3)$ and which is two-to-one, rather than the one-to-one and onto mapping between $SU(2)$ and the unit quaternions $\mathbb{H}$ (2.20). This also means that the Lie algebras of $SU(2)$ and $SO(3)$ are isomorphic via the relation:

$$\begin{pmatrix} 0 & -x_3 & x_2 \\ x_3 & 0 & -x_1 \\ x_2 & x_1 & 0 \end{pmatrix} \leftrightarrow 2 \begin{pmatrix} \frac{i}{2}x_1 & \frac{1}{2}(x_2 + ix_3) \\ -\frac{1}{2}(x_2 - ix_3) & -\frac{i}{2}x_1 \end{pmatrix} \tag{2.21}$$

Therefore since there is a double cover of $SU(2)$ on $SO(3)$, and as $SU(2)$ is isomorphic to the unit quaternions, it follows that each unique rotation on $SO(3)$ corresponds to two sets of quaternions $\pm\bar{q}$. This ambiguity can present problems for some attitude controllers when the attitude is parameterised in terms of quaternions, with a small attitude error on $SO(3)$ interpreted as a large error in $\mathbb{H}$ and resulting in excessive control effort [61, 62].

In contrast, the use of rotation matrices on $SO(3)$ enables the attitude kinematics to be specified uniquely and globally. However, when $SO(3)$ is used as the configuration space a set of nine differential equations must be propagated [58]. For small spacecraft with limited computational capacity, such as those considered in Chapter 4, this can be prohibitively computationally intensive for on-board implementation. Consequently, the four quaternion differential equations are generally preferred in practice [32, 58].

In addition to the computational simplicity of the quaternion representation, as stated previously, Klein [55] discovered that for some systems simpler solutions can be obtained when $SU(2)$ rather than $SO(3)$ is used as the configuration space. Therefore as a result of the potential simplicity of utilising $SU(2)$ to represent the configuration space of the spacecraft, and the exact mapping to the computationally light quaternion representation, the motion planning methods utilised in this thesis use the matrix

Lie group $SU(2)$ to represent the kinematics of a rotating rigid body. This enables a solution to be more easily derived on $SU(2)$, then mapped exactly to $\mathbb{H}$ for practical implementation.

2.3 Kinematic Representation Using Matrix Lie Groups

As discussed in Section 2.2, the position and orientation of many practical engineering control problems can be expressed as nonholonomic systems on matrix Lie groups. This enables the conserved quantities of the system to be utilised to simplify the process of deriving optimal controls.

In this section, the general form of the kinematics on matrix Lie groups in terms of the basis of the Lie algebra are first stated. Next, the specific examples of the planar wheeled robot and the rigid body spacecraft are discussed, showing how their configuration space can equivalently be expressed using matrix Lie groups.

2.3.1 General Kinematic Representation

From [13, 17, 28], the kinematics of driftless nonholonomic systems can be generally expressed as

$$\frac{dg(t)}{dt} = g(t)\sum_{i=1}^{n} u_i(t)X_i \tag{2.22}$$

where for the 3D-Lie groups considered in this thesis, $i = 1, ..., n$ and $n \leq 3$. The curve $g(t) \in G$ describes the motions of the system in the configuration manifold G, while $X_1, ..., X_n$ are the arbitrary vector fields in the tangent space TG at $g(t)$, denoted $T_{g(t)}G$. The tangent space TG at the identity, I, is denoted T_IG. When the kinematics of systems are under consideration, the control functions, $u_1, ..., u_n$, are generally the translational or rotational velocities of the system. It follows that $X_1, ..., X_n \in T_{g(t)}G$ are the controlled vector fields on the manifold G. Note that Equation (2.22) can be modified for systems with drift by setting one of the controls $u_1, ..., u_n$ to be constant apriori.

When G is a matrix Lie group and X_i are left invariant vector fields, the vector fields

can be expressed in terms of the basis elements $A_1, ...A_n \in T_I G$ of the Lie algebra $\mathfrak{g}$ to give $X_1 = g(t)A_1, ..., X_n = g(t)A_n$ with $A_n \in T_{g(t)}G$. This results in the simplified form of the kinematics:

$$\frac{dg(t)}{dt} = g(t) \sum_{i=1}^{n} u_i(t) A_i \tag{2.23}$$

With the general kinematic representation using matrix Lie groups described, this mathematical framework is now linked explicitly to the real world applications, in the case of the planar wheeled robot and the freely rotating rigid spacecraft. This is achieved by showing the equivalence between conventional kinematic representations and the matrix Lie group approach. These kinematic representations on matrix Lie groups will be utilised in subsequent chapters when deriving optimal controls for the simple wheeled robot and rigid spacecraft using the mechanisms of geometric control theory.

2.3.2 Wheeled Robot

The simple planar wheeled robot is chosen as the first example. This system will be utilised in a kinematic motion planner, derived using the mechanisms of geometric control theory, in Chapter 3. For now, the basic model of the system is stated together with the matrix Lie group representation of the robot configuration space.

The wheeled robot model under consideration is shown in Figure 2.1. The distance

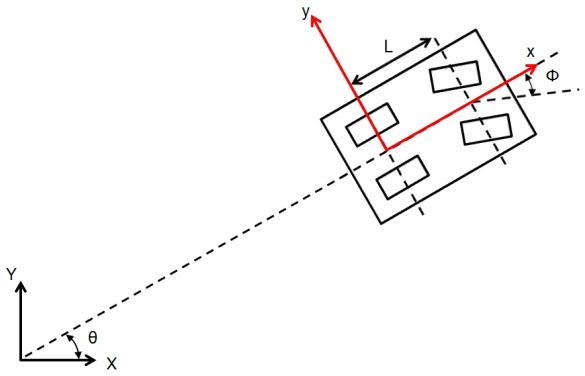

Figure 2.1: Wheeled robot model. Body axis is placed at centre of rear axle with x-axis lying along centre line of robot.

between the front and rear axles is given by L. The angle between the body fixed $x-y$ frame and the inertial $X-Y$ frame is denoted by θ. A sliding constraint is imposed by the assumption that in a small time interval dt the wheeled robot moves in approximately the direction that the rear wheels are pointing [14]. This condition can be written as the Pfaffian constraint

$$-\dot{X}\sin\theta + \dot{Y}\cos\theta = 0 \tag{2.24}$$

As in Choset [42] focus is placed on the position and orientation of the wheeled robot. Therefore it is possible to eliminate the steering angle ϕ from the representation of the configuration and treat it as part of the control. The control system is then described by

$$\begin{aligned} \dot{X} &= u_1\cos\theta \\ \dot{Y} &= u_1\sin\theta \\ \dot{\theta} &= u_3; \end{aligned} \tag{2.25}$$

where u_1 and u_3 are the controls in translation and rotation respectively.
The configuration space of the wheeled robot in Figure 2.1 can equivalently be described by a curve $g(t) \in SE(2)$ and expressed in matrix form using Equation (2.12) where the rotation matrix $Q(t)$ is given by

$$Q(t) = \begin{pmatrix} \cos\theta & -\sin\theta \\ \sin\theta & \cos\theta \end{pmatrix} \tag{2.26}$$

and $\bar{\gamma} = [X \quad Y]^T \in \mathbb{R}^2$. From the general definition of the kinematics (2.23), it follows that the kinematics of the simple wheeled robot can be expressed as a left invariant control system on SE(2) as

$$\frac{dg(t)}{dt} = g(t)(u_1A_1 + u_3A_3) \tag{2.27}$$

where $A_1, ..., A_3 \in \mathfrak{se}(2)$ are the basis elements of the Lie algebra $\mathfrak{se}(2)$ (2.13) which satisfy the relations in Table 2.1.

Note that the lateral direction, represented by the basis A_2, is not directly controlled ($u_2 = 0$) due to the sliding constraint expressed in (2.24). However the Lie bracket enables motions to be generated in the A_2 direction despite not having a control directly associated with it.

By differentiating (2.12) and substituting into (2.27) the control system defined in (2.25) is obtained. Note also that the driftless system in (2.27) can be augmented to include systems with drift by setting one of the controls u_i to a constant a priori without loss of generality. This case is considered in Chapter 3, Section 3.1.2.

2.3.3 Rotating Rigid Body

Following the example of the simple wheeled robot the kinematics of a rotating rigid body, which will form the basis of the two practically applied attitude motion planning methods for spacecraft introduced in Chapters 4 and 5, are stated. As with the planar wheeled robot case, it will be shown that the conventional kinematic representations can be equivalently expressed on matrix Lie groups. Although in reality a spacecraft will be subjected to disturbance torques, the motions are derived with the assumption that the spacecraft is a rigid body operating under ideal conditions. The validity of this assumption will then be tested in simulation in later chapters when the spacecraft is operating in a more realistic environment.

The rigid body under consideration is shown in Figure 2.2. A body fixed reference frame (BRF) with basis $\hat{i}, \hat{j}, \hat{k}$ is rigidly attached to the centre of mass of the body, and the kinematics specified with respect to an inertial frame with basis vectors $\hat{I}, \hat{J}, \hat{K}$.

Quaternions and SU(2)

In Section 2.2.4 it was stated that the quaternions are the most widely used attitude parameterisation as they are computationally efficient for on-board implementation and because they do not suffer from the singularities inherent in the Euler angles parameterisations [32, 58]. A brief definition of the quaternions will now be given, followed by the quaternion kinematic differential equations.

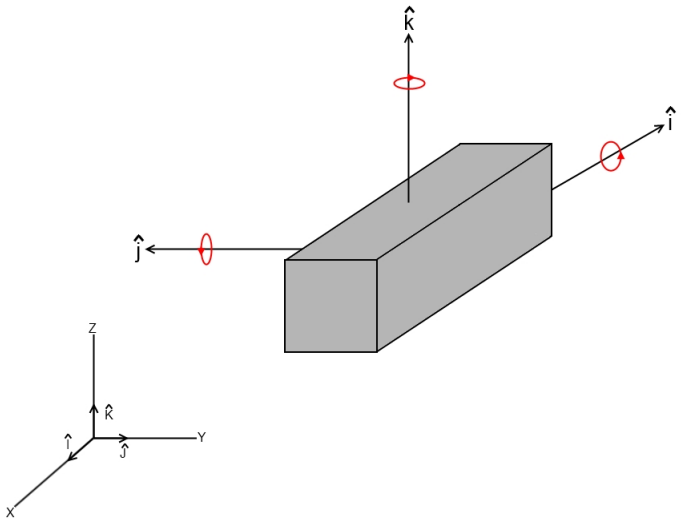

Figure 2.2: Rotating rigid body.

Consider the rigid body system shown in Figure 2.2. Euler's theorem states that the rigid body can be rotated from one attitude to any other attitude by an angle θ about an axis, known as the eigenaxis, that is fixed to the body and stationary with respect to the body and inertial frames. Denoting an eigenaxis vector by $\bar{e} = [e_1, e_2, e_3]^T$ the quaternions $\bar{q} = [q_0 \quad q_1 \quad q_2 \quad q_3]^T$ are defined as [32, 58]:

$$\begin{aligned} q_0 &= \cos(\theta/2) \\ q_1 &= e_1 \sin(\theta/2) \\ q_2 &= e_2 \sin(\theta/2) \\ q_3 &= e_3 \sin(\theta/2) \end{aligned} \tag{2.28}$$

It follows that the attitude kinematics of the rotating rigid body can be parameterised using quaternions as [32, 58]

$$\frac{d\bar{q}}{dt} = \frac{1}{2}\Omega\bar{q} \tag{2.29}$$

where the skew symmetric matrix Ω is given by

$$\Omega = \begin{pmatrix} 0 & -\omega_1 & -\omega_2 & -\omega_3 \\ \omega_1 & 0 & \omega_3 & -\omega_2 \\ \omega_2 & -\omega_3 & 0 & \omega_1 \\ \omega_3 & \omega_2 & -\omega_1 & 0 \end{pmatrix} \tag{2.30}$$

with $\bar{\omega} = [\omega_1 \quad \omega_2 \quad \omega_3]^T$ the angular velocities of the body frame with respect to the inertial frame, and $\bar{q}$ the quaternions of the body frame with respect to the inertial frame. Note that if the angular velocities of the body frame with respect to the orbital frame, $\bar{\omega}_{bo}$, are used then Equation (2.29) gives the time evolution of the quaternions of the body frame with respect to an orbital frame, $\bar{q}_{bo}$. Both cases are used in subsequent chapters. Furthermore the quaternions must satisfy the constraint $q_0^2 + q_1^2 + q_2^2 + q_3^2 = 1$ [63].

From Section 2.2.2, the configuration space of a rigid body can equivalently be expressed on the Special Unitary group $SU(2)$ as

$$\frac{dR(t)}{dt} = R(t)(\omega_1 A_1 + \omega_2 A_2 + \omega_3 A_3) \tag{2.31}$$

where $R(t) \in SU(2)$ is given by Equation (2.15) and represents the orientation of the spacecraft and A_1, A_2, A_3 form a basis for the Lie algebra $\mathfrak{su}(2)$ of the Lie group $SU(2)$ (2.16). Differentiating (2.15), substituting into (2.31) and utilising the isomorphism (2.20) yields the quaternion differential equations (2.29).

Rotation Matrices and SO(3)

The kinematics of a rigid body can also be expressed as the time derivation of the direction cosine matrix, $S(t) \in SO(3)$, commonly used in spacecraft attitude control [58]:

$$\frac{dS(t)}{dt} = S(t)\Omega \tag{2.32}$$

where $S(t) \in SO(3)$ is a 3×3 direction cosine matrix and Ω a skew symmetric matrix of the spacecraft angular velocities, given by

$$\Omega = \begin{pmatrix} 0 & \omega_3 & -\omega_2 \\ -\omega_3 & 0 & \omega_1 \\ \omega_2 & -\omega_1 & 0 \end{pmatrix} \tag{2.33}$$

This yields nine differential equations which must be numerically integrated. Equation (2.32) is equivalent to the kinematics on the Special Orthogonal group $SO(3)$, yielded by substituting the basis of $\mathfrak{so}(3)$ (2.18) into (2.31).

In Section 2.2.4, it was stated that the attitude of the spacecraft can be represented uniquely and globally on $SO(3)$. Despite this the quaternion representation is favoured for on-board implementation due to less computation being required to integrate the four quaternion equations as opposed to the nine equations in (2.32).

2.4 Optimal Kinematic Motion Planning

As stated in Section 1.2, not only is there a need to find a control which drives the system between specified configurations in a set time, but there is also the need to optimise the control with respect to a particular cost function. Therefore in this thesis an optimal control problem is formulated, with the total energy of the system chosen as a cost function. Spindler [8] utilised this cost to minimise the rotational speed of a spacecraft, to enable sensors to update more efficiently. However, the main benefit of utilising this form of cost function is that it enables analytical solutions to be derived. Assessing the practicality of this cost function in real applications is an aim of this thesis. An application of the Maximum Principle of optimal control then yields the optimal kinematic controls, generally the system velocities, required to carry out the manoeuvre.

Firstly, it is necessary to determine if the systems under consideration are controllable and hence if the optimal control problem is well posed. A system is controllable if there exists an admissible control which can drive the system between two specified states

on a manifold in a set time [13]. For left invariant systems on matrix Lie groups, the controllability of the system can be determined by use of the Lie bracket. If the Lie algebra can be formed through Lie bracketing of the controlled vector fields $A_i, ..., A_n$ then the system is controllable. For example for the system in Equation (2.27), if the system is controllable then A_1 and A_3 must generate $\mathfrak{g}$. From Table 2.1, $[A_3, A_1] = A_2$ and therefore the optimal control problem is well posed. It follows that the rigid body systems in Equations (2.31) and (2.32) are also controllable, as A_1, A_2 and A_3 generate $\mathfrak{g}$.

Subject to the kinematic nonholonomic constraint given by (2.23) and given that the system is controllable, the problem is then to find a trajectory $g(t) \in G$ from an initial position and orientation $g(0) \in G$ to a final position and orientation $g(T) \in G$, where T is some fixed final time, that minimises the functional

$$J = \frac{1}{2} \int_0^T \sum_{i=1}^{n} c_i u_i^2 dt \tag{2.34}$$

where $i = 1, ..., n$ with $n \leq 3$ and c_i are constant weights. In addition it enables the problem to be formulated in the context of geometric optimal control and this enables questions to be asked of the integrability of the system, and in some cases solve the system in closed form. Furthermore, obtaining a closed form solution essentially reduces the motion planning to a problem of optimising the available parameters to match the prescribed boundary conditions.

2.5 Hamiltonian Systems and the Maximum Principle of Optimal Control

The application of the coordinate free Maximum Principle to left-invariant optimal control problems is well known, see Jurdjevic [17] and Sussman [64]. If a Hamiltonian is left-invariant the cotangent bundle T^*G can be realised as the direct product $G \times \mathfrak{g}^*$ where $\mathfrak{g}^*$ is the dual of the Lie algebra $\mathfrak{g}$ of G as stated in Section 2.1. Therefore, the

original Hamiltonian defined on T^*G can be expressed as a reduced Hamiltonian on the dual of the Lie algebra $\mathfrak{g}^*$ as $T^*G/G \cong \mathfrak{g}^*$. Essentially this means that the symmetry of the problem enables the Hamiltonian to be defined independently of configuration co-ordinates on the dual of the Lie algebra. This means that the Hamiltonian is highly simplified, and makes the process of solving for the optimal controls simpler.

In this section the application of the co-ordinate free Maximum Principle to left-invariant systems on matrix Lie groups is described. Firstly, it is shown how the kinematics and the cost function are combined to yield the time-dependent Hamiltonian. Following this, the Maximum Principle is stated. The consequence that solutions obtained via application of this principle yield optimal extremal curves is highlighted. Finally the method of utilising the Poisson bracket to obtain the optimal kinematic controls is described.

2.5.1 The Maximum Principle

The Maximum Principle [41], developed by Pontryagin as an extension of a theory by Weierstrass, gives necessary conditions for optimality for a Hamiltonian system when the Hamiltonian is minimised over the set of permissable controls. When the base manifold is a matrix Lie group, as in this thesis, the controlled Hamiltonian on the cotangent bundle T^*G can be expressed as a reduced Hamiltonian on the dual of the Lie algebra $\mathfrak{g}^*$. The resultant Hamiltonian is co-ordinate free. As the systems studied in this thesis are left-invariant (2.22), this enables a simplified form of the Maximum Principle to be used.

Assume that a control function $u(t) = (u_1(t), ..., u_n(t))$ generates an integral curve $g(t)$ in the interval $[0, T]$, with $(g(t), u(t))$ called a trajectory of (2.22). Additionally, the total cost $\int_0^T f_0(g(t), u(t))dt$ in the interval $[0, T]$ is a smooth function f_0 from $G \times \mathbb{R}^n \to \mathbb{R}$. The initial and terminal sub manifolds S_0 and S_1 are constant elements of G, and in the simplest case consist of single elements $g(0)$ and $g(T)$. Then a trajectory $(\bar{g}(t), \bar{u}(t))$ is optimal relative to the boundary conditions if $\bar{g}(0) \in S_0$ and $\bar{g}(T) \in S_1$

and

$$\int_0^T f_0(\bar{g}(t), \bar{u}(t))dt \leq \int_0^T f_0(g(t), u(t))dt \tag{2.35}$$

for any trajectory $(g(t), u(t)$ in $[0, T]$ such that $g(0) \in S_0$ and $g(T) \in S_1$.

A Hamiltonian function H on the cotangent bundle T^*G of any manifold G, is associated a Hamiltonian vector field $\overrightarrow{H}$ via

$$dH_\zeta(v) = \omega_\zeta(\overrightarrow{H}(\zeta), v) \tag{2.36}$$

where ω_ζ is the canonical symplectic two form. This relation is valid for each point $\zeta \in T^*G$ and each tangent vector $v \in T_\zeta(T^*G)$. Furthermore, a vector field X_i on manifold G produces a linear Hamiltonian function H_{X_i} on the cotangent bundle T^*G defined by:

$$H_{X_i}(\zeta) = \zeta(X_i(g(t))) \quad \forall \quad \zeta \in T^*_{g(t)}G \tag{2.37}$$

The non-autonomous vector fields $X_i(g(t), t)$ define time-varying functions. Then, the control functions $u(t)$ define a time-varying vector field on G which, together with the kinematics (2.22) and cost functional (2.34), define a time-dependent Hamiltonian H_{ρ_0}:

$$H_{\rho_0}(\zeta, u(t)) = \sum_{i=1}^{n} u_i(t) H_i(\zeta) - \rho_0 f_0(\eta(\zeta), u(t)) \tag{2.38}$$

where ρ_0 is a parameter equal to 1 or 0, and where η is the canonical projection from the cotangent bundle T^*G onto the base manifold G. It then follows that the integral curves of the Hamiltonian vector field $\overrightarrow{H}_{\rho_0}(\zeta, u(t))$ of (2.38), denoted ζ, are absolutely continuous curves which satisfy

$$\frac{d\zeta}{dt}(t) = \overrightarrow{H}_{\rho_0}(\zeta, u(t)) \tag{2.39}$$

for almost all t in the interval $[0, T]$. Using the canonical projection from T^*G onto the base manifold G, the projection $(\eta(\zeta), u(t))$ is a trajectory of (2.22) for each trajectory $(\zeta, u(t))$ of (2.39).

With these preliminaries stated, the geometric Maximum Principle from [65] can be

introduced. If $(\bar{g}(t), \bar{u}(t))$ is an optimal trajectory relative to the cost function (2.34) and the boundary conditions are S_0, S_1 in terminal time, T, then $(\bar{g}(t), \bar{u}(t))$ is the projection of the trajectory $(\zeta(t), u(t))$ of (2.39) on the interval $[0, T]$ such that:

1. If $\rho_0 = 0$ then $\zeta \neq 0$ for any $t \in [0, T]$.

2. the time dependent Hamiltonian $H_{\rho_0}(\zeta(t), \bar{u}(t))$ satisfies the maximality condition:

$$H_{\rho_0}(\zeta(t), \bar{u}(t)) \geq H_{\rho_0}(\zeta(t), u(t)) \tag{2.40}$$

   for any $u(t)$ and almost all t in $[0, T]$.

3. $\zeta(t)$ satisfies the transversality conditions $\zeta(0)(v) = 0$ for all tangent vectors $v \in S_0$ at $\bar{g}(0)$ and $\zeta(T)(v) = 0$ for all tangent vectors $v \in S_1$ at $\bar{g}(T)$.

The most important consequence of the Maximum Principle in relation to this thesis is that the trajectories $(\zeta(t), \bar{u}(t))$ that satisfy conditions 1 and 2 of the Maximum Principle are known as extremal curves. It then follows that every optimal trajectory is the projection of an extremal curve, a fact which will be used in the proceeding sections to solve for the optimal controls $\bar{u}(t)$. The extremals are called normal if $\rho_0 = 1$, and abnormal if $\rho_0 = 0$. Jurdjevic [17] showed that abnormal extremals are a subset of regular extremals. Therefore in this thesis the case when $\rho_0 = 1$ is considered.
With the necessary conditions for optimality stated, the general form of the Hamiltonian for the constraint (2.23) with respect to minimising the cost function (2.34) will now be introduced.

2.5.2 Hamiltonian Formalism

Recall that for left invariant vector fields, the vector fields can be expressed in terms of the basis $A_1, ...A_n \in T_I G$ of the Lie algebra $\mathfrak{g}$ to give $X_1 = g(t)A_1, ..., X_n = g(t)A_n$ with $A_n \in T_{g(t)}G$. Therefore the appropriate Hamiltonian for the constraint (2.23)

with respect to minimising the cost function (2.34) is derived from (2.38):

$$H(p,u,g) = \sum_{i=1}^{n} u_i p(g(t)A_i) - \rho_0 \frac{1}{2} \sum_{i=1}^{n} c_i u_i^2 \tag{2.41}$$

where as before $n \leq 3$, $p \in T^*G$ and $\rho_0 = 1$ for regular extremals. As stated the Hamiltonian (2.41) defined on T^*G is expressed as a reduced Hamiltonian on the dual of the Lie algebra $\mathfrak{g}^*$. It follows that $p(g(t)A_i) = \hat{p}(A_i)$ for any $p = (g(t), \hat{p})$ and any $A_i \in \mathfrak{g}$. Defining the extremal (linear) functions explicitly as $\lambda_i = \hat{p}(A_i)$, where $\hat{p} \in \mathfrak{g}^*$, the Hamiltonian (2.41) can be expressed on $\mathfrak{g}^*$ as

$$H = \sum_{i=1}^{n} u_i \lambda_i - \frac{1}{2} \sum_{i=1}^{n} c_i u_i^2 \tag{2.42}$$

With the general form of the Hamiltonian formulation defined, it will now be shown how the optimal Hamiltonian is utilised together with the Poisson bracket to derive the extremal curves necessary to produce the optimal controls.

2.5.3 Derivation of Optimal Hamiltonian

The control Hamiltonian (2.42) is a concave function of the control functions, u_i, if $\frac{\partial^2 H}{\partial {u_i}^2} < 0$. It then follows from the Maximum Principle that by calculating $\frac{\partial H}{\partial u_i} = 0$ the optimal kinematic control inputs are

$$u_i^* = \frac{1}{c_i} \lambda_i, \tag{2.43}$$

where $i = 1, ..., n$ and λ_i are the extremal curves. Substituting (2.43) back into (2.42) gives the optimal form of the appropriate left-invariant quadratic Hamiltonian:

$$H^* = \frac{1}{2} (\sum_{i=1}^{n} \frac{\lambda_i^2}{c_i}) \tag{2.44}$$

As left-invariant systems are being considered, each vector field on G defines a G invariant Hamiltonian function H on the dual of the Lie algebra $\mathfrak{g}^*$ which is co-ordinate

free. The corresponding Hamiltonian vector fields $\overrightarrow{H}^*(\cdot)$ are then calculated by

$$\overrightarrow{H^*}(\cdot) = \{\cdot, H^*\} \tag{2.45}$$

where $\{\cdot,\cdot\}$ denotes the Poisson bracket. The cotangent bundle T^*G is a Poisson manifold, with $\{m,h\}(\zeta) = \omega_\zeta(\overrightarrow{m}(\zeta), \overrightarrow{h}(\zeta))$ for all functions m and h. It then follows that M is an integral motion for H^* if and only if $\{M, H^*\} = 0$ and vice versa. These integrals of motion can then be used to solve explicitly for the optimal controls.
For each quadratic Hamiltonian (2.44), the corresponding vector fields are calculated using the Poisson bracket (2.11). Letting l denote an element in the dual of the Lie algebra $l \in \mathfrak{g}^*$, the Hamiltonian vector fields are given by

$$\frac{dl}{dt} = \{l, H^*\} \tag{2.46}$$

For semisimple Lie groups such as $SU(2)$ and $SO(3)$, each element in the dual of the Lie algebra can be identified with an element in the Lie algebra via the non-degenerate trace form [17]. Thus, the expression (2.46) can be written in Lax pair form [17, 57] as

$$\dot{L} = [L, \nabla H^*] \tag{2.47}$$

where $L \in \mathfrak{g}$ and ∇H^* is the gradient of the optimal Hamiltonian (2.44). This can then be used to solve explicitly for the optimal controls on semisimple Lie groups. For non-semisimple groups, such as $SE(2)$, (2.43) is substituted into (2.22) to yield

$$\frac{dg(t)}{dt} = g(t)\nabla H^* \tag{2.48}$$

where ∇H is the gradient of the Hamiltonian and $g(t) \in G$ are the corresponding paths. Finally, with the optimal paths derived it is necessary to solve for $g(t) \in G$ such that the boundary conditions $g(0) \in G$ and $g(T) \in G$ in some final time T are matched. In this thesis this is tackled using a parametric optimisation, which will be discussed in subsequent chapters.

Integrability

Note that integrals of motion are utilised in the derivation of the optimal controls. Equations (2.46) and (2.48) are integrable with the three integrals of motion: (i) the Hamiltonian H; (ii) the Casimir function M and ; (iii) the integral of motion φ_3 corresponding to a right-invariant vector field. The Casimir function is a constant of motion for a Hamiltonian system, and is defined as a function $M \in \Gamma(P)$ satisfying $\{M, H\} = 0$. For the 3D-Lie groups considered in this thesis two integrals of motion are necessary to reduce the system to a one-degree-of-freedom (1dof) system. This 1dof ordinary differential equation can then be solved analytically in certain cases and utilised in a motion planning algorithm, as will be shown in the proceeding chapters. In addition integrability is an intrinsic property of the system as it implies that all motions will be regular.

2.6 Chapter Summary

In this section the pre-existing geometric tools necessary to derive optimal analytical controls for left-invariant systems on 3D-matrix Lie groups have been formalised. The theory of Lie groups and Lie algebras was briefly introduced, before the matrix Lie groups considered in this thesis were described in detail. Following this, the matrix Lie group description of the configuration space of two simple systems was linked to the conventionally used approaches. Finally, the Maximum Principle of optimal control was stated, and the procedure for solving the extremals to yield the optimal form of the controls was described. These controls can then be applied in motion planning algorithms, as shown in subsequent chapters, in order to assess their use in real world systems.

The geometric approach enables complex systems to be reduced and solved analytically. However, there are a number of drawbacks with this approach. Firstly, the boundary conditions are not included in the cost function, and so the free parameters of the analytical equations must be optimised to match the boundary conditions. Secondly,

while the use of a quadratic cost ensures that motions will be smooth and regular, this may not be the most practical cost function for the system. Finally, the curves do not take into account the dynamics of the system, only the kinematics, so further investigation is required to determine if these curves are feasible for practical motion planning implementation.

In Chapter 3 the kinematic motion planning techniques stated in this chapter will be applied to derive optimal controls for a simple planar wheeled robot. These optimal paths will then be implemented in a kinematic motion planning algorithm, with a simple obstacle avoidance framework. Following this, in Chapter 4, the theory presented in this chapter will be applied to derive novel motion tracks for a rigid spacecraft in a disturbance free environment. The practicality of the derived tracks will then be assessed in simulation in the presence of disturbances. This will enable the potential problems with the geometric approach, namely the assumption of an ideal environment and the quadratic cost function, to be assessed via comparison with other methods. Finally, in Chapter 5 the practicality of a motion planning method, derived using the framework of geometric control theory, for a spacecraft constrained to spin around one axis will be tested via extensive numerical simulation to again assess the strengths and weaknesses of the geometric method.

Chapter 3

Motion Planning for Simple Wheeled Robots

In the previous chapter the use of matrix Lie groups and their accompanying algebras to represent the kinematics of rigid body systems, together with a general framework for solving related optimal kinematic control problems via Pontragyin's Maximum Principle, was introduced. In this chapter, this framework will be applied to derive motion primitives which form the basis of a kinematic motion planning method for a simple nonholonomic wheeled robot. The task of computing a suitable trajectory from a given initial condition to a desired final point is fundamental in robotics. However, as stated in Chapter 1, for some robotic systems such as wheeled robots, motion planning is challenging due to their inherent nonholonomic constraints.

The problem of motion planning for simple wheeled robots has been widely studied. In early work on the subject Dubins [3] derived a method for generating trajectories for a car like robot, termed Dubins' car [14], which is constrained to move forwards at unit speed. In this method the paths are constructed from straight line segments and arcs of constant curvature, and are referred to as Dubins' curves [14]. Dubins' curves are the shortest length curves in Euclidean space $\mathbb{R}^2$ which connect two arbitrary points [66] and whose curvature is uniformly bounded for all points along the curve. It was shown that Dubins' car is capable of arriving at any state (assuming there are no obstacles in

the configuration space) using a combination of no more than three motion primitives - left turn, right turn or straight ahead. Reeds and Shepp [4] extended the work of Dubins by defining the shortest paths for a car capable additionally of reversing at unit speed. Dubins' curves have been used extensively in motion planning for a range of systems, including unmanned air vehicles [7] and underwater vehicles [67].

Scheuer and Fraichard [68] developed a motion planning method to overcome an inherent limitation of Dubins' curves - that the wheeled robots are required to stop to reorientate at each section of the path. This method, derived from Dubins' curves, generates continuous curvature curves which do not require the robot to stop and reorientate, and was extended to include obstacle avoidance [69, 70]. However, while Dubin's curves are the shortest length curves in space for a robot constrained to move at unit speed, real systems are unlikely to be constrained in this manner and so Dubin's curves may not be optimal for robots which are able to move at arbitrary speed. Moreover, choosing a constant curvature curve which satisfies the orientation constraint at the endpoint can be difficult [71] and heuristics are often employed [72]. Thus more efficient solutions which include orientation constraints in the boundary conditions have been sought.

Murray and Sastry [20] showed that the periodicity of the derived trigonometric control functions enabled both the position and orientation constraints for a simple nonholonomic wheeled robot to be satisfied. However, the method is not optimal with respect to any specified cost and no obstacle avoidance framework is proposed. Meanwhile Brockett [73] showed that for a particular nonholonomic system the optimal controls were elliptic functions. These elliptic functions generalise the sine and cosine functions, and so give rise to a wider class of possible motion primitives.

In this chapter a simple analytical motion planning method is derived via the framework of geometric control theory that seeks to define a general class of optimal motion primitives for the nonholonomic wheeled robot in two cases (i) the most general case, where translational and rotational speeds are arbitrary, first derived in [54], and (ii) where the robot is constrained to move forwards at unit speed but with arbitrary rotational speed. Application of the framework of geometric control theory described in

Chapter 2 yields the optimal controls for each case with respect to a cost function that minimises control effort. The resulting curves in the arbitrary speed and unit speed cases are analogous to the definition of sub-Riemannian and elastic curves on $SE(2)$ respectively. A method of parametrically optimising the analytical equations describing the motion to match prescribed boundary conditions and produce low control effort reference tracks is described, and an extension to obstacle avoidance is detailed. This parametric optimisation and obstacle avoidance framework, derived for the simple kinematic wheeled robot motion planner, forms the basis of the spacecraft attitude motion planners in subsequent chapters.

Original Contributions

The original contributions in this chapter are outlined as follows:

- Special cases of the equations for the wheeled robot capable of translating and rotating at arbitrary speed are derived by considering the properties of the elliptic functions. The geometric intersection of the integrals is studied to graphically show integrability. Reachable sets are exactly defined for the general case and the specific cases.

- The optimal angular velocity for the wheeled robot constrained to move forward at unit speed is solved in terms of an elliptic function, and a truncated expression derived for the evolution of the real component of the position of the robot. Time-limited reachable sets are considered.

- A kinematic motion planning algorithm is constructed, based on the analytical expressions for the arbitrary and unit speed cases, which enables position and orientation constraints to be specified and produces reference motions via parametric optimisation.

- A simple obstacle avoidance method for static circular obstacles, which probes the reachable sets to find alternative trajectories to the target position, is derived and implemented for the arbitrary speed case.

This chapter is structured as follows. In Section 3.1, the framework of geometric control theory described in Chapter 2 is applied to derive the optimal controls for the simple nonholonomic wheeled robot in the arbitrary speed and unit speed cases. Following this, in Section 3.2, the reachable sets of the motion planners are considered, before the simple parametric optimisation and obstacle avoidance frameworks are described in Section 3.3. This framework forms the basis of the more complicated spacecraft attitude motion planners in later chapters. Examples of kinematic motion planning are then given for each case in Section 3.4, together with a discussion of the limitations of the planner. Finally, the results of the chapter are summarised in Section 3.5.

3.1 Analytic Derivation of Reference Motions for Wheeled Robot

In this section the optimal Hamiltonians, with respect to minimising control effort, are derived for the arbitrary speed and unit speed cases using the theory of geometric control on matrix Lie groups outlined in the previous chapter. Application of the Maximum Principle yields the optimal Hamiltonians in each case, which are then solved explicitly to give the optimal controls.

3.1.1 Arbitrary Translational and Rotational Speed

The case of a simple wheeled robot which is capable of moving at arbitrary rotational and translational speed is considered in this section. Initial work on this case was carried out by Biggs [54]. In this thesis this work is extended to consider the properties of the elliptic functions, which define a general class of curve, and to derive the exact reachable sets. Additionally, the equations are utilised in a kinematic motion planning algorithm with a simple obstacle avoidance framework, which will be extended to the spacecraft attitude motion planning problem in subsequent chapters.

It is assumed that the wheeled robot can move backward or forwards at a velocity v_r, and can rotate at an angular velocity $\omega_r = \dot{\theta}$, as shown in Figure 3.1.

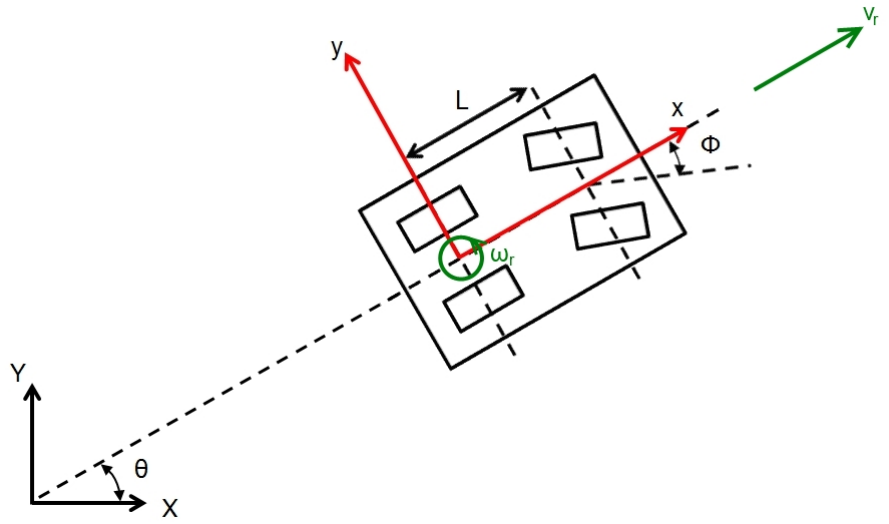

Figure 3.1: Wheeled robot model for the case where robot can move at arbitrary translational v_r and rotational ω_r velocity. Body axis is placed at centre of rear axle with x-axis lying along centre line of robot.

As this is a kinematic motion planning method, it is assumed that both of these velocities can be directly controlled. However, in practice control torques must be applied to achieve the desired speeds, and the impact of this assumption should be assessed via practical implementation.

In order to apply the mechanisms stated in Chapter 2 to this problem and so solve for the optimal form of these controls, the kinematics must be expressed on the matrix Lie group $SE(2)$. First, note that the sliding constraint (2.24) can be expressed as

$$\frac{d\bar{\gamma}}{dt} = Q(t) \begin{bmatrix} v_r \\ 0 \end{bmatrix} \tag{3.1}$$

where $\bar{\gamma} = [X \quad Y]^T$ and $Q(t) \in SO(2)$ and is given by Equation (2.26). Differentiating equation (2.12) yields

$$\frac{dg(t)}{dt} = \begin{pmatrix} -\sin(\theta)\dot{\theta} & -\cos(\theta)\dot{\theta} & \dot{X} \\ \cos(\theta)\dot{\theta} & -\sin(\theta)\dot{\theta} & \dot{Y} \\ 0 & 0 & 0 \end{pmatrix} \tag{3.2}$$

while taking the inverse of (2.12) gives

$$g(t)^{-1} = \begin{pmatrix} \cos(\theta) & \sin(\theta) & -\cos(\theta)X - \sin(\theta)Y \\ -\sin(\theta) & -\cos(\theta) & \sin(\theta)X - \cos(\theta)Y \\ 0 & 0 & 1 \end{pmatrix} \tag{3.3}$$

Combining (3.2) and (3.3), and taking into the account the constraint (3.1) yields the left-invariant differential equation which describes the nonholonomic kinematic constraint:

$$g(t)^{-1}\frac{dg(t)}{dt} = \begin{pmatrix} 0 & -\omega_r & v_r \\ \omega_r & 0 & 0 \\ 0 & 0 & 0 \end{pmatrix} \tag{3.4}$$

It follows from the definition of the Lie algebra on $SE(2)$ that Equation (3.4) can be expressed in the form

$$g(t)^{-1}\frac{dg(t)}{dt} = v_r A_1 + \omega_r A_3 \tag{3.5}$$

where the basis of the Lie algebra are given by (2.13). Relative to the general form of the kinematics (2.23) $u_1 = v_r, u_2 = 0$ and $u_3 = \omega_r$. Again note that while the direction A_2 is not directly controlled, the Lie bracket enables motions to be generated in this direction.

Considering the general form of the cost function (2.34), a quadratic cost function is defined as:

$$J = \frac{1}{2}\int_0^1 {v_r}^2 + c{\omega_r}^2 dt \tag{3.6}$$

where c is a constant weight. The time t is scaled such that in real time τ with final fixed time T is $t = \tau/T$. In relation to the general form (2.34) $c_1 = 1, c_2 = 0$ and $c_3 = c$. This cost function minimises steering effort and forward velocity. Therefore the motions generated with respect to this cost function will bring the wheeled robot to the target in a set time using minimum control effort. As the cost function is multi-objective, the degree of minimisation of the forward speed is weighted against that of the rotational speed using the parameter c. If no weighting is required, the parameter

c can be set equal to unity or included as a free parameter in the resulting parameter optimisation. However, if minimisation of steering effort should be given priority over minimisation of forward velocity, or vice versa, then the weight c can be pre-selected accordingly.

Together, the kinematic constraints (3.5) and the cost (3.6) are analogous to a sub-Riemannian curve on SE(2) [74]. That is, while in this case the motion planning problem is constrained to a fixed time T, a curve would be constrained by a fixed length.

From (2.42), the appropriate Hamiltonian considering the constraint (3.5) that minimises the cost function (3.6) is

$$H = v_r\lambda_1 + \omega_r\lambda_3 - \frac{1}{2}({v_r}^2 + c{\omega_r}^2) \tag{3.7}$$

It follows from the statement of Pontryagin's Maximum Principle in Section 2.5.1, that if

$$\frac{\partial H}{\partial v_r} = 0, \frac{\partial H}{\partial \omega_r} = 0, \frac{\partial^2 H}{\partial {v_r}^2} < 0, \frac{\partial^2 H}{\partial {\omega_r}^2} < 0, \tag{3.8}$$

then the functions v_r and ω_r are optimal. These conditions are satisfied if

$$v_r = \lambda_1, \quad \omega_r = \tfrac{\lambda_3}{c} \tag{3.9}$$

Substituting these values into (3.7) yields the optimal Hamiltonian H^* for the wheeled robot capable of rotating and translating at arbitrary speed:

$$H^* = \frac{1}{2}\left(\lambda_1^2 + \frac{\lambda_3^2}{c}\right) \tag{3.10}$$

The corresponding Hamiltonian vector fields which implicitly define the extremal solutions are given by the Poisson bracket $\frac{d\lambda_i}{dt} = \{\lambda_i, H^*\}$ where $i = 1, ..., 3$. For example $\dot{\lambda}_1 = \frac{\partial H^*}{\partial \lambda_1}\{\lambda_1, \lambda_1\} + \frac{\partial H^*}{\partial \lambda_2}\{\lambda_1, \lambda_2\} + \frac{\partial H^*}{\partial \lambda_3}\{\lambda_1, \lambda_3\}$ with the Poisson bracket relations given

by (2.11). This yields the differential equations:

$$\begin{aligned}\dot{\lambda}_1 &= \tfrac{\lambda_2\lambda_3}{c} \\ \dot{\lambda}_2 &= -\tfrac{\lambda_1\lambda_3}{c} \\ \dot{\lambda}_3 &= -\lambda_1\lambda_2\end{aligned} \tag{3.11}$$

In addition observe that the Casimir function

$$M = \lambda_1^2 + \lambda_2^2 \tag{3.12}$$

is constant along the Hamiltonian flow i.e. $\{M, H^*\} = 0$.

The integrability of the system can now be confirmed geometrically by plotting the intersection of the integrals of the system, the Hamiltonian (3.10) and the Casimir function (3.12), as shown in Figure 3.2.

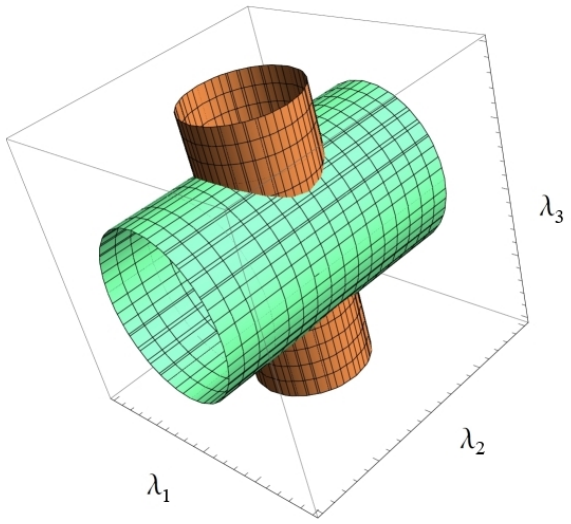

Figure 3.2: Plot of intersection between the Hamiltonian function (green) and Casimir (orange) in arbitrary speed case. In this case $m = M/2H^* < 1$.

It is known that the intersection of two quadratic surfaces define elliptic curves which in turn are parameterised by elliptic functions, see Husemoller [75]. Therefore the extremal curves can be solved via elliptic functions as shown in the following Lemma:

Lemma 1. *The optimal velocity v_r in the surge direction and angular velocity ω_r that*

minimise the cost function (3.6) subject to the kinematic constraint (3.5) are Jacobi elliptic functions $\mathrm{sn}(\cdot,\cdot), \mathrm{dn}(\cdot,\cdot)$ *of the form*

$$\begin{aligned} v_r &= \sqrt{M}\,\mathrm{sn}\,\Phi \\ \omega_r &= \sqrt{\tfrac{2H^*}{c}}\,\mathrm{dn}\,\Phi \end{aligned} \tag{3.13}$$

where H^* *and* M *are constants defined by (3.10) and (3.12) respectively and* c *is the constant weight in the cost function (3.6). The corresponding path is given by*

$$\begin{aligned} X &= -\sqrt{\tfrac{2H^*c}{M}}\,\mathrm{dn}\,\Phi + \sqrt{\tfrac{2H^*c}{M}} \\ Y &= \tfrac{2H^*t}{\sqrt{M}} - \sqrt{2H^*c}\,\mathrm{E}(\mathrm{am}\,\Phi, \tfrac{M}{2H^*}) \end{aligned} \tag{3.14}$$

where $\mathrm{E}(\cdot,\cdot)$ *is the elliptic integral of the second kind and* $\mathrm{am}(\cdot)$ *is the Jacobi amplitude. The rotation of the body along the path is*

$$R(t) = \begin{pmatrix} \mathrm{cn}\,\Phi & -\mathrm{sn}\,\Phi \\ \mathrm{sn}\,\Phi & \mathrm{cn}\,\Phi \end{pmatrix} \tag{3.15}$$

with $\Phi = \left(\sqrt{\tfrac{2H^*}{c}}t, \tfrac{M}{2H^*}\right)$, *and*

$$\theta = \mathrm{am}(\Phi). \tag{3.16}$$

Proof.

The conserved quantity (3.12) can be parameterised by the Jacobi elliptic functions

$$\lambda_1 = r\,\mathrm{sn}\,(\alpha t, m)\,, \quad \lambda_2 = r\,\mathrm{cn}\,(\alpha t, m) \tag{3.17}$$

Substituting (3.17) into (3.12) and using the relation $\mathrm{sn}^2 + \mathrm{cn}^2 = 1$ [76, 77] yields $r = \sqrt{M}$. Equation (3.10) can then be parameterised by defining:

$$\lambda_3 = a\,\mathrm{dn}\,(\alpha t, m) \tag{3.18}$$

Substituting (3.17) and (3.18) into (3.10) it follows from the relation $m\,\mathrm{sn}^2 + \mathrm{dn}^2 = 1$

that $a = \sqrt{2H^*c}$ and $m = M/2H^*$. Thus

$$\begin{aligned}
\lambda_1 &= r\,\mathrm{sn}\left(\alpha t, \tfrac{M}{2H^*}\right) \\
\lambda_2 &= r\,\mathrm{cn}\left(\alpha t, \tfrac{M}{2H^*}\right) \\
\lambda_3 &= \sqrt{2H^*c}\,\mathrm{dn}\left(\alpha t, \tfrac{M}{2H^*}\right)
\end{aligned} \tag{3.19}$$

Finally to obtain α substitute (3.19) into (3.11), giving $\alpha = \sqrt{2H^*/c}$ and enabling the complete expressions for the extremal functions to be written as

$$\begin{aligned}
\lambda_1 &= \sqrt{M}\,\mathrm{sn}\left(\sqrt{\tfrac{2H^*}{c}}t, \tfrac{M}{2H^*}\right) \\
\lambda_2 &= \sqrt{M}\,\mathrm{cn}\left(\sqrt{\tfrac{2H^*}{c}}t, \tfrac{M}{2H^*}\right) \\
\lambda_3 &= \sqrt{2H^*c}\,\mathrm{dn}\left(\sqrt{\tfrac{2H^*}{c}}t, \tfrac{M}{2H^*}\right)
\end{aligned} \tag{3.20}$$

The relationship between the optimal velocities and the extremals (3.9) then yields (3.13). Note that only the positive roots of the terms in Equation (3.20) are considered. The solution for the negative half of the geometric intersection between the Hamiltonian and Casimir function in Figure 3.2 is found in a similar manner by considering the negative roots of the terms in Equation (3.20). As $\omega_r = \dot{\theta}$ it follows from (3.13) that

$$\theta = \mathrm{am}(\Phi) + C_1 \tag{3.21}$$

where C_1 is a constant of integration. For simplicity $C_1 = 0$ such that the rotation matrix $R(t)$ emanates from the origin. This yields (3.16). Substituting (3.15) and (3.13) into equation (3.1) results in the differential equations

$$\frac{d\gamma}{dt} = \begin{bmatrix} \sqrt{M}\,\mathrm{sn}\,\Phi\,\mathrm{cn}\,\Phi \\ \sqrt{M}\,\mathrm{sn}^2\,\Phi \end{bmatrix} \tag{3.22}$$

These can be integrated analytically to give the expressions for the evolution of the robot's path (3.14). □

Remark 1. *It is interesting to note the change in behaviour of the elliptic functions as the parameter $m = M/2H^*$ changes. For $0 < m < 1$ the optimal controls are described by (3.13), and the Casimir and Hamiltonian intersect as in Figure 3.2.*
As $m = M/2H^* \to 0$ in (3.13), the velocity in translation tends to a sinusoid and the velocity in rotation tends to a constant, viz

$$\begin{aligned} v_r &= \sqrt{M}\sin(\sqrt{\tfrac{2H^*}{c}}t) \\ \omega_r &= \sqrt{\tfrac{2H^*}{c}} \end{aligned} \tag{3.23}$$

Note also that the elliptic functions in the expression (3.14) tend to sine and cosine, resulting in

$$\begin{aligned} X &= -\tfrac{1}{4}\sqrt{\tfrac{Mc}{2H^*}}\cos(2\sqrt{\tfrac{2H^*}{c}}t) + \tfrac{1}{4}\sqrt{\tfrac{Mc}{2H^*}} \\ Y &= -\tfrac{1}{8}\sqrt{M}(4t - \sqrt{\tfrac{2c}{H^*}}\sin(2\sqrt{\tfrac{2H^*}{c}}t)) \\ \theta &= \sqrt{\tfrac{2H^*}{c}}t \end{aligned} \tag{3.24}$$

As sine and cosine are special cases of the elliptic functions described above, this suggests that it may be possible to derive a more general form of the control using sinusoids described by Murray and Sastry [20].
As $m = M/2H^* \to 1$, the equations (3.13) tend to the hyperbolic functions

$$\begin{aligned} v_r &= \sqrt{M}\tanh(\sqrt{\tfrac{2H^*}{c}}t) \\ \omega_r &= \sqrt{\tfrac{2H^*}{c}}\,\mathrm{sech}(\sqrt{\tfrac{2H^*}{c}}t) \end{aligned} \tag{3.25}$$

Furthermore the elliptic functions in the expression (3.14) tend to hyperbolic functions, giving the following expressions for the evolution of the translational and rotational displacements of the wheeled robot:

$$\begin{aligned} X &= -\sqrt{\tfrac{Mc}{2H^*}}\,\mathrm{sech}(\sqrt{\tfrac{2H^*}{c}}t) + \sqrt{\tfrac{Mc}{2H^*}} \\ Y &= \sqrt{M}(t - \sqrt{\tfrac{c}{2H^*}}\tanh(\sqrt{\tfrac{2H^*}{c}}t)) \\ \theta &= 2\arctan(\tanh\sqrt{\tfrac{H^*}{2c}}t) \end{aligned} \tag{3.26}$$

This case is shown in Figure 3.3a).

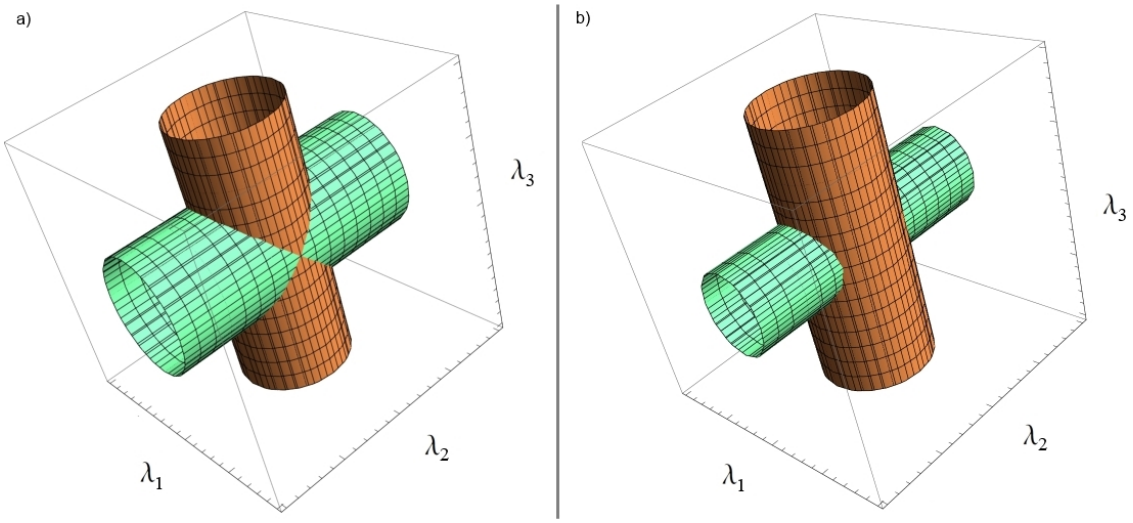

Figure 3.3: Plot of intersection between the Hamiltonian function (green) and Casimir (orange) in arbitrary speed case defining the extremal curves for a) $m = M/2H^* = 1$ and b) $m = M/2H^* > 1$.

Finally when $m = M/2H^* > 1$, the equations (3.13) are transformed using the Jacobi real transformations[76, 77]

$$\begin{aligned} \mathrm{sn}(u, m) &= \sqrt{\mu}\,\mathrm{sn}(v, \mu) \\ \mathrm{cn}(u, m) &= \mathrm{dn}(v, \mu) \\ \mathrm{dn}(u, m) &= \mathrm{cn}(v, \mu) \end{aligned} \tag{3.27}$$

where $\mu = 1/m$ and $v = u\sqrt{m}$. Applying these transformations to (3.13) results in equations of the form

$$\begin{aligned} v_r &= \sqrt{2H^*}\,\mathrm{sn}\left(\sqrt{\tfrac{M}{c}}t, \tfrac{2H^*}{M}\right) \\ \omega_r &= \sqrt{\tfrac{2H^*}{c}}\,\mathrm{cn}\left(\sqrt{\tfrac{M}{c}}t, \tfrac{2H^*}{M}\right) \end{aligned} \tag{3.28}$$

The elliptic functions for the rotational and translational position of the wheeled robot

are also transformed via (3.27), yielding:

$$\begin{aligned} X &= -\sqrt{\tfrac{2H^*c}{M}}\,\mathrm{cn}(\sqrt{\tfrac{M}{c}}t, \tfrac{2H^*}{M}) + \sqrt{\tfrac{2H^*c}{M}} \\ Y &= \sqrt{M}t - \sqrt{c}\,\mathrm{E}(\mathrm{am}(\sqrt{\tfrac{M}{c}}t, \tfrac{2H^*}{M}), \tfrac{2H^*}{M}) \\ \theta &= \sqrt{\tfrac{2H^*}{M}}\,\mathrm{am}(\sqrt{\tfrac{M}{c}}t, \tfrac{2H^*}{M}) \end{aligned} \tag{3.29}$$

This case is shown in Figure 3.3b). The behaviour of the elliptic functions can be further explained by analogy with the simple pendulum [78]. Plotting the curves in Figures 3.2 and 3.3 in 2D Figure 3.4 is obtained.

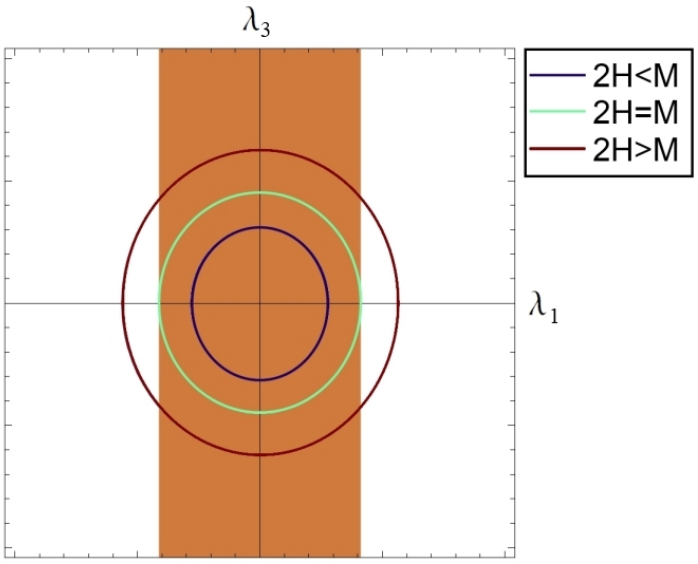

Figure 3.4: 2D plot of intersection between the Hamiltonian function and Casimir (orange) in arbitrary speed case for different values of m.

The case where $m = M/2H^* > 1$ can be thought of as corresponding to oscillatory solutions in the phase plane of the pendulum where it is swinging back and forth, while $m = 1$ defines a heteroclinic connection and $m < 1$ the case where the pendulum has high energy.

Note that while the general solution takes the form of a Jacobi elliptic function, these functions are not widely used in practice. Therefore if the Jacobi elliptic function cannot be utilised, the simplified trigonometric and hyperbolic equations for the optimal rotational and translational velocities of the robot may alternatively be used.

3.1.2 Unit Speed

In the previous section, the optimal controls for a wheeled robot capable of moving at arbitrary translational and rotational speeds were derived, and the properties of the resultant elliptic functions studied. In this section a wheeled robot constrained to move forwards at unit speed is considered. While this is similar to the case studied by Dubins [3], the key difference is that Dubins constrained the robot to move along arcs of constant curvature whereas in this thesis the wheeled robot is capable of turning at arbitrary rotational speed.

As stated above, the wheeled robot is constrained to move forward at fixed unit speed ($v_r = 1$) as shown in Figure 3.5.

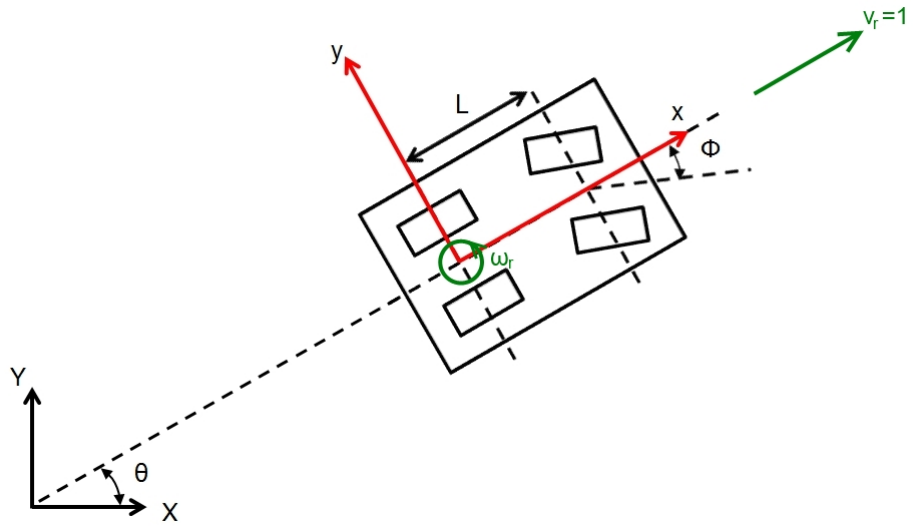

Figure 3.5: Wheeled robot model for the case where robot moves at unit speed $v_r = 1$ and arbitrary rotational ω_r velocity. Body axis is placed at centre of rear axle with x-axis lying along centre line of robot.

This corresponds to the case where the system has drift. Considering the general case in Equation (3.1), the velocity constraint can be expressed as

$$\frac{d\bar{\gamma}}{dt} = Q(t) \begin{bmatrix} 1 \\ 0 \end{bmatrix} \tag{3.30}$$

Furthermore, the robot can rotate at an angular velocity $\omega_r = \dot{\theta}$ which is again assumed to be controllable. Setting $v_r = 1$ in (3.4), the nonholonomic kinematic constraint for the unit speed case can be expressed as the left-invariant differential equation:

$$g(t)^{-1}\frac{dg(t)}{dt} = \begin{pmatrix} 0 & -\omega_r & 1 \\ \omega_r & 0 & 0 \\ 0 & 0 & 0 \end{pmatrix} \tag{3.31}$$

Equation (3.31) can then be written in terms of the basis of the Lie algebra of $SE(2)$ as

$$g(t)^{-1}\frac{dg(t)}{dt} = A_1 + \omega_r A_3 \tag{3.32}$$

where relative to the general form of the kinematics (2.23) $u_1 = 1, u_2 = 0$ and $u_3 = \omega_r$. The basis of the Lie algebra are given by (2.13). As the forward speed v_r is not controlled, the cost function is expressed as

$$J = \frac{1}{2}\int_0^1 {\omega_r}^2 dt \tag{3.33}$$

The time t is again scaled such that in real time τ with final fixed time T is $t = \tau/T$. Together, the kinematic constraint (3.32) and the cost function (3.33) are analogous to the definition of an elastic curve on SE(2), where ω_r is analogous to curvature. Jurdjevic [79] reduced the extremals of this problem to quadratures. However, this thesis extends this by explicitly solving the optimal steering control in terms of an elliptic function. The Hamiltonian function corresponding to the constraint (3.32) that minimises the cost function (3.33) is

$$H = \lambda_1 + \omega_r\lambda_3 - \frac{1}{2}({\omega_r}^2) \tag{3.34}$$

From the discussion of Pontryagin's Maximum Principle in Section 2.5, if the following conditions are satisfied

$$\frac{\partial H}{\partial \omega_r} = 0, \frac{\partial^2 H}{\partial {\omega_r}^2} < 0 \tag{3.35}$$

then the function ω_r is optimal. These conditions are satisfied when

$$\omega_r = \lambda_3 \tag{3.36}$$

Substituting these values into (3.34) yields the optimal Hamiltonian H^*:

$$H^* = \frac{1}{2}(\lambda_3^2) + \lambda_1 \tag{3.37}$$

The corresponding Hamiltonian vector fields which implicitly define the extremal solutions are given by the Poisson bracket $\frac{d\lambda_i}{dt} = \{\lambda_i, H^*\}$. This yields the differential equations:

$$\begin{aligned} \dot{\lambda}_1 &= \lambda_2\lambda_3, \\ \dot{\lambda}_2 &= -\lambda_1\lambda_3, \\ \dot{\lambda}_3 &= -\lambda_2 \end{aligned} \tag{3.38}$$

In addition the Casimir function (3.12) is again constant along the Hamiltonian flow. Note that setting $\lambda_1, \lambda_2 = 0$ in (3.38) yields $\dot{\lambda}_3 = 0$ and $\lambda_3 = \sqrt{2H^*}$. Therefore this corresponds to the curves of constant curvature commonly used in motion planning with $\omega_r = \sqrt{2H^*}$ and $\theta = \sqrt{2H^*}t$. In addition, setting $\lambda_1, \lambda_2, \lambda_3 = 0$ yields straight line segments. Therefore (3.38) can be manipulated to obtain the motion primitives which comprise Dubins' curves.

As for the arbitrary speed case, the integrability of the unit speed system can be confirmed geometrically by plotting the intersection of the integrals of the system, the Hamiltonian (3.37) and the Casimir function (3.12). This is shown in Figure 3.6. The two quadratic surfaces intersect and define elliptic curves which can again be parameterised by elliptic functions [75]. Therefore the system is integrable, and the extremal curves can be solved analytically via the use of Jacobi elliptic functions and Taylor expansions as stated in the following Lemma:

Lemma 2. *The optimal angular velocity ω_r that minimises the cost function (3.33)*

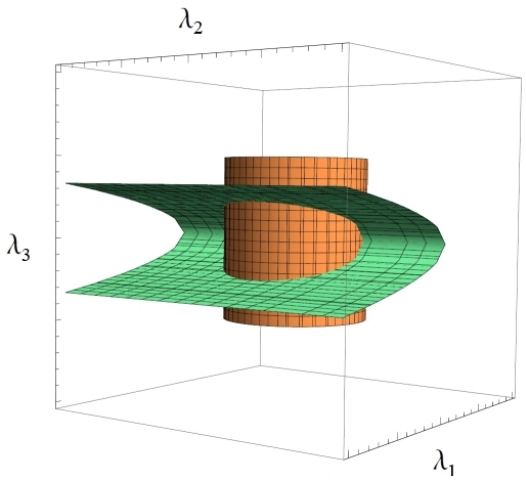

Figure 3.6: Plot of the Hamiltonian function (green) and Casimir (orange) in unit speed case.

subject to the kinematic constraint (3.32) is a Jacobi elliptic function of the form

$$\omega_r = \sqrt{s_1}\,\mathrm{sn}(\sqrt{\alpha s_2}t + K, \frac{s_1}{s_2}) \tag{3.39}$$

where the constant K is defined by

$$K = \mathrm{sn}^{-1}(\frac{\lambda_3(0)}{\sqrt{s_1}}, \frac{s_1}{s_2}) \tag{3.40}$$

with

$$\begin{aligned} s_1 &= \tfrac{-\beta+\sqrt{\beta^2-4\alpha\chi}}{2\alpha} \\ s_2 &= \tfrac{-\beta-\sqrt{\beta^2-4\alpha\chi}}{2\alpha} \end{aligned} \tag{3.41}$$

and

$$\begin{aligned} \alpha &= -\tfrac{1}{4} \\ \beta &= H^* \\ \chi &= M - H^{*2} \end{aligned} \tag{3.42}$$

Proof. By combining the conserved quantities (3.37) and (3.12) it follows that:

$$\lambda_2^2 = M - (H^* - \frac{1}{2}\lambda_3^2)^2 \tag{3.43}$$

Then, squaring the expression for $\dot{\lambda}_3$ in (3.38) and combining with (3.43) gives:

$$\dot{\lambda}_3^2 = -\frac{1}{4}\lambda_3^4 + H^*\lambda_3^2 + (M - H^{*2}) \tag{3.44}$$

This expression can be written in the form

$$\dot{\lambda}_3^2 = \alpha(s_1 - \lambda_3^2)(s_2 - \lambda_3^2) \tag{3.45}$$

and then rewritten as the integral

$$\int_0^t dt = \int_{\lambda_3(0)}^{\lambda_3(t)} \frac{1}{\sqrt{\alpha(s_1 - \lambda_3^2)(s_2 - \lambda_3^2)}} d\lambda_3 \tag{3.46}$$

In order to simplify the integration, the substitution

$$\lambda_3 = \sqrt{s_1}\,\mathrm{sn}(u, m) \tag{3.47}$$

is introduced where $m = \frac{s_1}{s_2}$. Differentiating (3.47) with respect to u gives:

$$d\lambda_3 = \sqrt{s_1}\,\mathrm{cn}(u, m)\,\mathrm{dn}(u, m)du \tag{3.48}$$

Substituting (3.47) and (3.48) into (3.46) leads to an equation of the form:

$$\int_0^t dt = \int_{u_1}^{u_2} \frac{\sqrt{s_1}\,\mathrm{cn}(u, m)\,\mathrm{dn}(u, m)}{\sqrt{\alpha}\sqrt{s_1 s_2 - s_1^2\,\mathrm{sn}^2(u, m) - s_1 s_2\,\mathrm{sn}^2(u, m) + s_1^2\,\mathrm{sn}^4(u, m)}} du \tag{3.49}$$

where

$$\begin{aligned} u_1 &= \mathrm{sn}^{-1}(\tfrac{\lambda_3(0)}{\sqrt{s_1}}, m) \\ u_2 &= \mathrm{sn}^{-1}(\tfrac{\lambda_3(t)}{\sqrt{s_1}}, m) \end{aligned} \tag{3.50}$$

With some manipulation Equation (3.49) reduces to

$$\int_0^t dt = \int_{u_1}^{u_2} \frac{1}{\sqrt{\alpha s_2}} du \tag{3.51}$$

Integrating and rearranging leads to an equation for $\lambda_3(t)$:

$$\lambda_3(t) = \sqrt{s_1}\,\mathrm{sn}(\sqrt{\alpha s_2}t + K, m) \tag{3.52}$$

where the constant K is given in (3.40). Remembering that $\omega_r = \lambda_3(t)$ yields the expression for the rotational angular velocity (3.39).□ The orientation of the wheeled robot is given by $\theta = \int \omega_r dt$, therefore

$$\theta = -2i\log(-\sqrt{m}\,\mathrm{cn}(K + \frac{1}{2}\sqrt{-s_2}t, m) + \mathrm{dn}(K + \frac{1}{2}\sqrt{-s_2}t, m)) + C_1 \tag{3.53}$$

where i is the imaginary unit and

$$C_1 = 2i\log(-\sqrt{m}\,\mathrm{cn}(K, m) + \mathrm{dn}(K, m)) \tag{3.54}$$

Substituting (3.53) into Equation (3.30) yields

$$\frac{d\gamma}{dt} = \begin{bmatrix} \cos(\theta) \\ \sin(\theta) \end{bmatrix} \tag{3.55}$$

These expressions cannot be integrated analytically for X and Y. Additionally, the derived expressions (3.39, 3.53 and 3.55) have a complex component, regardless of the choice of parameters. Therefore these complete expressions derived using the geometric control theory framework are not suitable for practical motion planning. However, by Taylor expanding (3.55) in t about $t = 0\,\mathrm{s}$ and integrating, approximate analytical expressions for the real parts of X and Y can be found. Figures 3.7 and 3.8 show a comparison between the solution of the numerical integration of the real component of Equation (3.55) and the solution obtained by Taylor expansion in t around $t = 0\,\mathrm{s}$ followed by analytical integration.

As a result of the Taylor expansion these expressions will only be convergent for t in $[0, 1)$s, requiring the references to be scaled to the desired time. Additionally, the series expansion is most accurate in the parameter range $H^*, M, \lambda_3(0) \in [-1.5, 1.5]$. Beyond

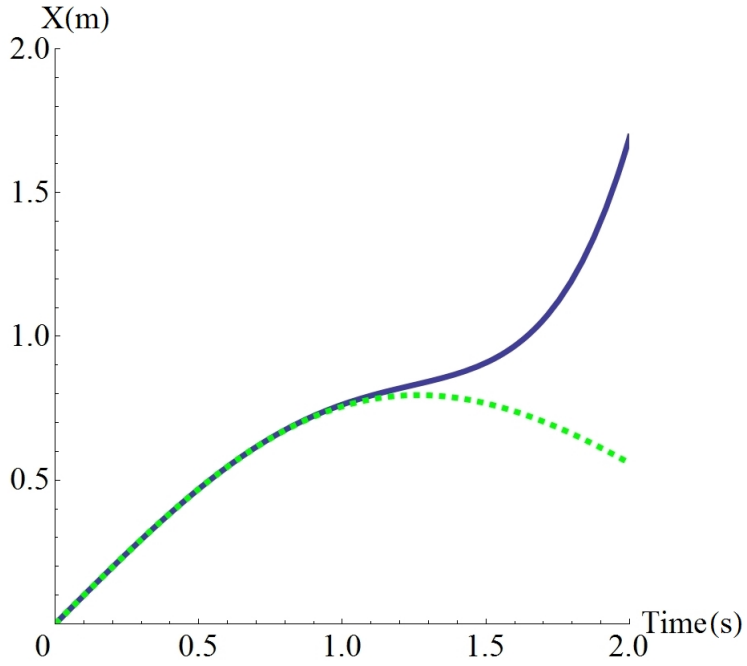

Figure 3.7: Comparison between 5th order Taylor expansion of real component of X position (blue) and numerical solution (green dashed) for $T = 2\,\mathrm{s}$, $H^* = 3.7 \times 10^{-16}, M = 0.75, \lambda_3(0) = 1.13$.

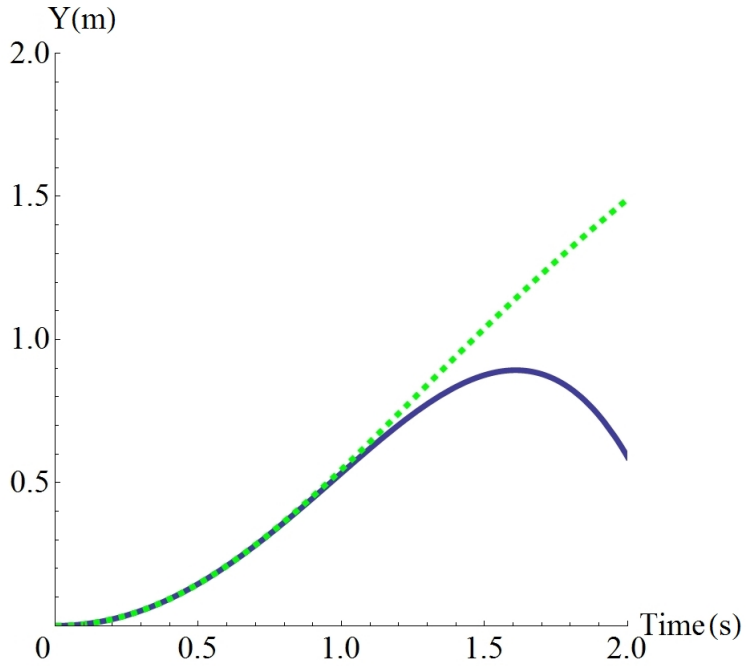

Figure 3.8: Comparison between 5th order Taylor expansion of real component of Y position (blue) and numerical solution (green dashed) for $T = 2\,\mathrm{s}$, $H^* = 3.7 \times 10^{-16}, M = 0.75, \lambda_3(0) = 1.13$.

these values, the error between the expansion and the numerical solution increases. Therefore the parameters are constrained to $H^*, M, \lambda_3(0) \in [-1.5, 1.5]$ for the unit speed case in the proceeding sections. Note that a 5th order Taylor expansion was utilised as the 4th order expansion was not convergent for t in $[0, 1)$s, and higher order expansions greatly increased computation time while providing little increase in accuracy.

Weierstrass Solution

As the equations derived in Section 3.1.2 contain imaginary parts and are therefore not suitable for practical motion planning in their complete form, an alternative solution to the extremals was sought.

Squaring the expression for $\dot{\lambda}_1$ in (3.38), and rearranging the conserved quantities (3.12) and (3.37) to give expressions for λ_2^2 and λ_3^2 respectively it follows that

$$\dot{\lambda}_1^2 = \lambda_2^2 \lambda_3^2 \tag{3.56}$$

where

$$\begin{aligned} \lambda_2^2 &= M - \lambda_1^2 \\ \lambda_3^2 &= 2(H^* - \lambda_1) \end{aligned} \tag{3.57}$$

Expanding Equation (3.56) results in an expression of the form:

$$\dot{\lambda}_1^2 = 2\lambda_1^3 - 2H^*\lambda_1^2 - 2M\lambda_1 + 2H^*M \tag{3.58}$$

Equation (3.58) can then be solved using a Weierstrass elliptic function, $\wp(z; g_2, g_3)$ [77]. The canonical equation for the Weierstrass $\wp$-function satisfies

$$\dot{\wp}^2 = 4\wp^3 - g_2\wp - g_3 \tag{3.59}$$

where g_2 and g_3 are elliptic invariants to be determined. In order to solve for λ_1 in terms of a Weierstrass function, let

$$\lambda_1 = c_1 \wp + c_2 \tag{3.60}$$

where c_1 and c_2 are constants to be determined. Differentiating (3.60) and squaring yields

$$\dot{\lambda}_1^2 = c_1^2 \dot{\wp}^2 \tag{3.61}$$

Substituting (3.60) and (3.61) into (3.58) and grouping terms results in the equation:

$$\begin{aligned} \dot{\wp}^2 = \wp^3(2c_1) + \wp^2(6c_2 - 2H^*) + \wp(\frac{6c_2^2 - 4H^* c_2 - 2M}{c_1}) \\ +(\frac{2MH^* - 2Mc_2 - 2H^* c_2^2 + 2c_2^3}{c_1^2}) \end{aligned} \tag{3.62}$$

Comparing coefficients of $\wp$ in (3.62) with those in (3.59) yields expressions for the constants:

$$\begin{aligned} c_1 &= 2 \\ c_2 &= \tfrac{H^*}{3} \\ g_2 &= M + \tfrac{H^*}{3} \\ g_3 &= \tfrac{H^{*3} - 9MH^*}{27} \end{aligned} \tag{3.63}$$

It follows from (3.60) and (3.63) that the extremal λ_1 can be written in Weierstrass form as

$$\lambda_1 = 2\wp(z; g_2, g_3) + \frac{H^*}{3} \tag{3.64}$$

Finally from the expression for λ_3^2 in (3.57) the solution for λ_3 can be written as

$$\lambda_3 = \sqrt{2(H^* - (2\wp(z; g_2, g_3) + \frac{H^*}{3}))} \tag{3.65}$$

Thus as $\omega_r = \lambda_3$ the solution for the optimal angular velocity of the unit speed wheeled robot has been derived. However, the expression (3.65) cannot be analytically integrated for θ, and so the Jacobi elliptic function solution, despite the imaginary component, remains the most useful in practice.

3.2 Reachable Sets of Motion Planners

In this thesis reachable sets are defined as the states in the wheeled robot's configuration space which are achievable via a single trajectory from the starting point at the origin. The robot's environment is assumed to be obstacle free when defining reachable sets.

3.2.1 Arbitrary Translational and Rotational Speed

Since the magnitudes of the forward and rotational speeds are unconstrained, the reachable sets in the $X-Y$ plane which can be reached via a single manoeuvre are limited only by the parameter space and the physical constraints of the robot (e.g. turning radius). All other $X-Y$ positions are reachable in time t in the interval $(0,\infty)$. Rearranging (3.16) leads to an expression for the orientation θ_f which is reached after some final time T:

$$T = \frac{\mathrm{F}(\theta_f, m)}{\alpha} \tag{3.66}$$

where $\mathrm{F}(\cdot,\cdot)$ is an elliptic integral of the first kind [77], with $m = M/2H^*$ and $\alpha = \sqrt{\frac{2H^*}{c}}$ as in Section 3.1.1. Therefore for some final orientation θ_f and some values of the free parameters H^*, M and c, the time required to reach this orientation is given by Equation (3.66). In addition, the final position $\bar{\gamma}_f = [X_f \quad Y_f]^T$ can be found from (3.14) at $t = T$. Then for $\theta_f \in [0, 2\pi]$ and $H^*, M, c \in (0,\infty]$ the complete reachable sets for the arbitrary speed case are defined.

For the special cases of the Jacobi elliptic functions it follows that by using the same approach as above that

$$T = \theta_f \sqrt{\frac{c}{2H^*}} \tag{3.67}$$

for the case where $m \to 0$. For the case where $m \to 1$ it follows by solving for T that

$$T = \sqrt{\frac{2c}{H^*}} \operatorname{arctanh}(\tan(\frac{\theta_f}{2})) \tag{3.68}$$

Finally, for the case where $m > 1$

$$T = \sqrt{\frac{c}{M}}\,\mathrm{F}(\theta_f \sqrt{\frac{M}{2H^*}}, \frac{2H^*}{M}) \tag{3.69}$$

Thus the reachable sets for the general case and special cases of the arbitrary speed wheeled robot have been specified completely.

3.2.2 Unit Speed

In Section 3.1.2, it was found that the expressions derived for the unit speed case have imaginary parts, and so are not suitable for practical motion planning. Additionally, the expression for θ (3.53) in the unit speed case cannot be solved explicitly for t and so the reachable sets are difficult to analytically define. Therefore in this case it is only possible to numerically evaluate the time-limited reachable sets for the real part of the curves. By constraining the free parameters $H^*, M, \lambda_3(0) \in [0, 1]$, the manoeuvre time to $T = 1\,\mathrm{s}$ and running random Monte Carlo simulations within these bounds the time-limited reachable sets for the real part of the curves can be evaluated. The results are shown in Figure 3.9.

Under these assumptions, the reachable sets for the wheeled robot constrained to move at unit speed but with arbitrary rotational velocity are similar to the time-limited reachable sets for Dubins' car, which is constrained to move at unit speed on arcs of fixed curvature [14]. This is to be expected as the paths which mark the upper and lower bounds of the graph are those in which the steering angle and hence curvature are at the maximum allowable value, and so the bounds are similar to those of Dubins' car.

Note that due to the Taylor expansion used to approximate the real part of the solution in (3.55), the curves in Figure 3.9 are of slightly different lengths and are not optimal, leading to the intersection of paths.

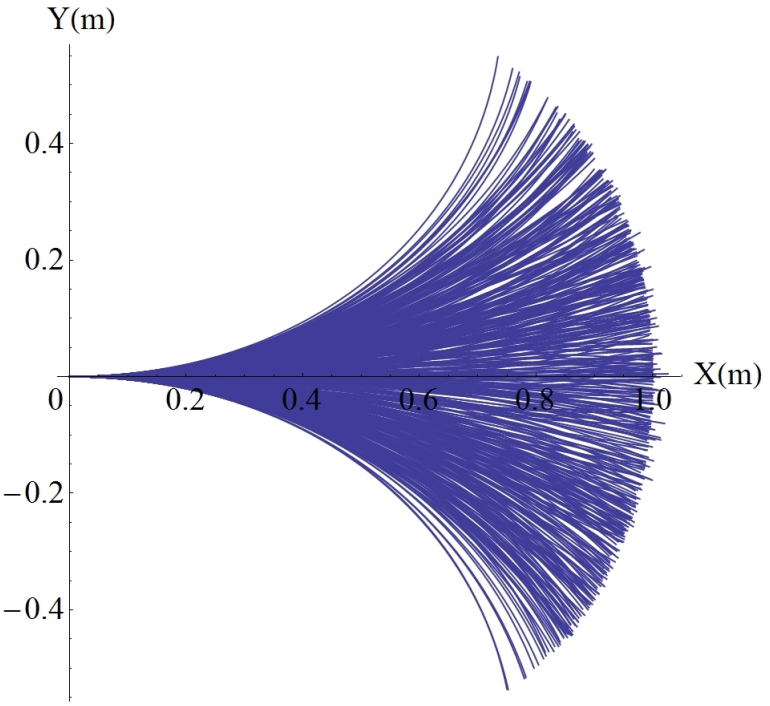

Figure 3.9: Time limited subset of reachable sets determined numerically for $T = 1\,\mathrm{s}$, $H^*, M, \lambda_3(0) \in [0, 1]$. 1000 trajectories plotted.

3.3 Motion Planning and Obstacle Avoidance for a Wheeled Robot

In this section a method of matching prescribed boundary conditions on the final position and orientation is introduced. This is achieved by parametrically optimising the free parameters of the equations derived in Section 3.1. This is necessary to overcome the fact that the boundary conditions are not included in the cost function, which is an inherent limitation of the geometric method. Furthermore, it is shown how the parametric optimisation can be adapted to create a simple obstacle avoidance algorithm for static obstacles in a known environment. This section establishes a parametric optimisation and obstacle avoidance framework for the simple wheeled robot, which will be extended to more complex systems in later chapters.

3.3.1 Parametric Optimisation

As the analytical expressions for the angular and translational displacements of the wheeled robot are functions of several free parameters, a parametric optimisation can be utilised in order to drive the robot to the desired target (provided the target is within the reachable sets of the planner.) However, as noted by LaValle [14], no natural performance metric exists on $SE(2)$ as the rotational and translational components do not have matching units. Therefore difficulties can occur when targeting both final position ($[X_f \quad Y_f]^T$) and orientation (θ_f) using the standard Euclidean metric:

$$L_2 = (X - X_f)^2 + (Y - Y_f)^2 + (\theta - \theta_f)^2 \tag{3.70}$$

where L_2 denotes the Euclidean metric [14] and the subscript f denotes the desired value of the parameter at the end of the manoeuvre. However, by using the complex representation of the angular displacement $\theta = a + ib$, where $a = cos(\theta)$ and $b = sin(\theta)$, greater accuracy can be achieved [14]. Therefore a cost function of the form

$$\min_{H^*,M,\Upsilon} \{(X - X_f)^2 + (Y - Y_f)^2 + (a - a_f)^2 + (b - b_f)^2\} \tag{3.71}$$

was used where H^*, M and Υ are the free parameters to be optimised. H^* is the optimal Hamiltonian, M the Casimir function and $\Upsilon = c$ is a weight in the arbitrary speed case and $\Upsilon = \lambda_3(0)$ is the initial angular velocity in the unit speed case. A parametric optimisation can then be carried out to minimise the error between the current and target position in $SE(2)$ by changing the values of the free parameters. Formally, this involves finding the curve $g(t) \in SE(2)$ that matches the boundary conditions $g(0) \in SE(2)$ and $g(T) \in SE(2)$ in some final time T.

The optimal values of the free parameters obtained as a result of the parametric optimisation are then input into the analytical expressions for the angular and translational displacements of the wheeled robot to give position and orientation reference tracks for the robot's path. This is demonstrated in Section 3.4.

A stochastic functional minimisation method was used for the parametric optimisation

as it proved the most effective at minimising the final error in comparison to the other available solvers such as genetic algorithm and direct search "simplex" methods [35]. This method was chosen in order to assess the form of the motion primitives. A deeper investigation would be required to determine if these solution methods were suitable for onboard implementation.

3.3.2 Obstacle Avoidance Algorithm

While the definition of the reachable sets in Section 3.2 and the parametric optimisation approach described in Section 3.3.1 assumed that the robot is operating in free space, in reality the configuration space may contain obstacles. In this case the set of all curves which match the boundary conditions on X and Y can be probed to determine if a suitable single curve exists which avoids the obstacle.

In the simplest case, where the obstacle is considered to be a point, the curves must not violate the condition

$$\sqrt{(X - X_o)^2 + (Y - Y_o)^2} = \chi \tag{3.72}$$

where $\bar{\gamma}_o = [X_o \quad Y_o]^T$ is the position of the obstacle and $\chi \neq 0$ for obstacle avoidance. However, real world obstacles have thickness, so the states which the wheeled robot cannot inhabit create a forbidden "zone" in the configuration space. Therefore in practice a range of states must be avoided during the manoeuvre. In this preliminary work, the obstacle is considered to be stationary and represented by a circle of radius χ_o in the $X-Y$ configuration space. The condition for obstacle avoidance is then given by (3.72) where $\chi > \chi_o$. Given the proposed method outlined in Section 3.3.1 for the analytical expressions defined in Sections 3.1.1 and 3.1.2, the parametric optimisation will return the optimal values of the free parameters H^*, M^*, Υ^* which satisfy the target position. As in Section 3.3.1, $\Upsilon = c$ is a weight in the arbitrary speed case and $\Upsilon = \lambda_3(0)$ is the initial angular velocity in the unit speed case. In the case that this manoeuvre violates $\chi > \chi_o \forall t$, a simple algorithm can be devised to overcome this.

Defining the forbidden region as a circle in the plane on $SE(2)$ with radius χ_o and centre $[X_o \quad Y_o]^T$, provided $\chi > \chi_o \forall t$ the trajectory will avoid the forbidden region. If $\chi < \chi_o$ for H^*, M^*, Υ^* for any t in the interval $(0, T)$ then the parameters p_1, p_2, p_3 are further optimised such that $p_1^2 > \eta, p_2^2 > \eta, , p_3^2 > \eta$, where $\eta > 0$ is a small parameter. This leads to a new set of free parameters $H^{**} = H^* + p_1, M^{**} = M^* + p_2, \Upsilon^{**} = \Upsilon^* + p_3$ being obtained, with the objective function

$$\min_{p_1, p_2, p_3} \{(X - X_f)^2 + (Y - Y_f)^2\} \tag{3.73}$$

such that $\chi > \chi_o \forall t$. Note that η can be tuned until $\chi > \chi_o \forall t$ is satisfied. This simple obstacle avoidance algorithm will be demonstrated in Section 3.4, and the framework revisited to plan constrained slews for spacecraft in Chapters 4 and 5.

3.4 Examples of Kinematic Motion Planning for a Wheeled Robot

In this section, the motion planning method described in Section 3.3 is used to plan motions for the arbitrary and unit speed wheeled robots. The behaviour of the curves produced by the motion planners is investigated, and the suggested obstacle avoidance method is tested.

3.4.1 Motion Planning and Obstacle Avoidance for Arbitrary Translational and Rotational Speed

In the absence of obstacles, any motion which meets the prescribed boundary conditions is sufficient. Figure 3.10 shows position and velocity curves for the wheeled robot, generated using the equations derived in Section 3.1.1, from the origin to the randomly selected points $[X_f, Y_f, \theta_f] = [0.18, 2.5, \frac{\pi}{2}]$, $[0.4, 2, \frac{\pi}{2}]$ and $[1, 3, \frac{\pi}{3}]$ in a manoeuvre time of $T = 1\,\text{s}$.

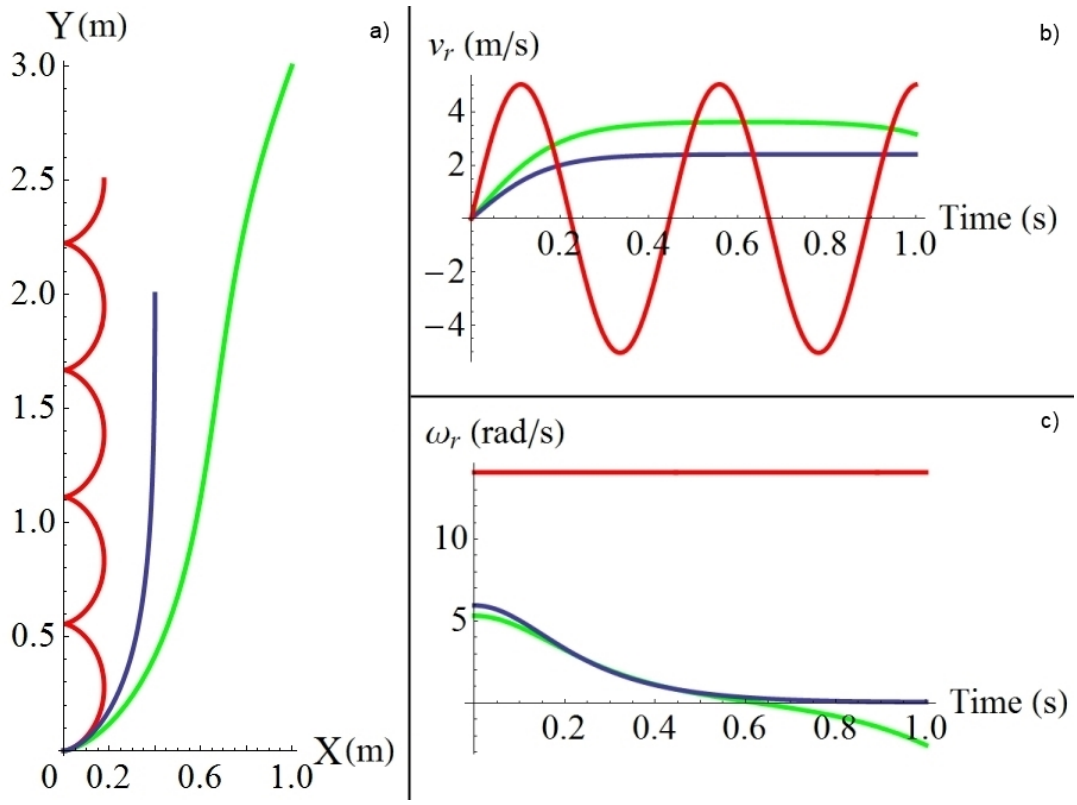

Figure 3.10: a) Smooth paths b) translational velocities and c) rotational velocities of wheeled robot for manoeuvres to $[X_f, Y_f, \theta_f] = [0.18, 2.5, \frac{\pi}{2}]$ (red), $[0.4, 2, \frac{\pi}{2}]$ (blue), $[1, 3, \frac{\pi}{3}]$ (green).

The values of the free parameters which produced these curves were $[H^*, M, c] = [37056.3, 25.3, 374.4]$, $[2.89, 5.78, 0.16]$ and $[6.55, 13.3, 0.46]$ respectively. The paths are smooth, and it is clear that the elliptic functions lead to a variety of different curves being produced as the free parameters are varied. Additionally, the ability of the car to move forwards and backwards at arbitrary speed is shown in the case of the manoeuvre to $[X_f, Y_f, \theta_f] = [0.18, 2.5, \frac{\pi}{2}]$, where the angular velocity is constant and the translational velocity is periodic. The behaviour of the different types of curve will now be studied in more detail.

In Section 3.1.1, the optimal equations for the robot constrained to move at arbitrary rotational and translational speed were found to have special cases comprising simple trigonometric and hyperbolic functions. These functions are more familiar and widely used in standard computational software in comparison to the Jacobi elliptic functions,

and so they may be easier to implement in practice. Examples of motion planning using the trigonometric (3.23, 3.24) and hyperbolic (3.25, 3.26) particular cases are shown in Figure 3.11.

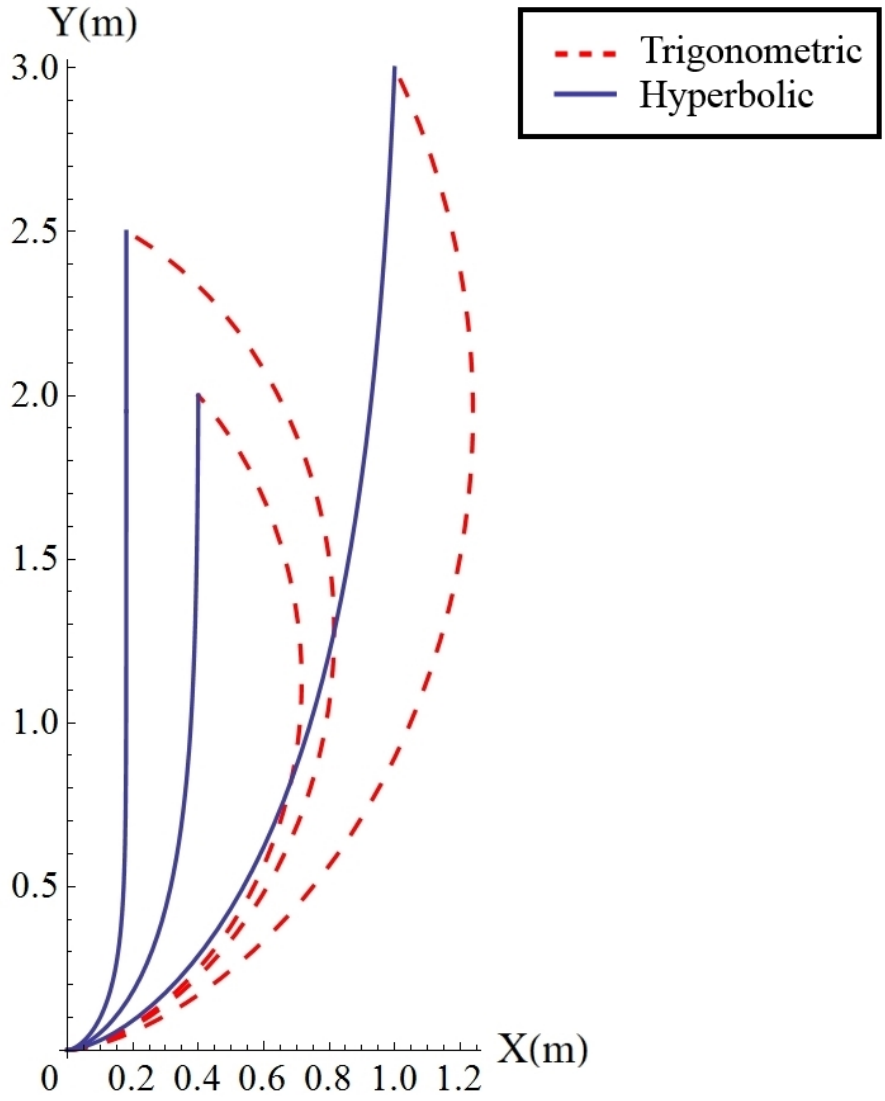

Figure 3.11: Smooth paths of wheeled robot for manoeuvres to (from left to right) $[X_f \quad Y_f]^T = [0.18 \quad 2.5]^T$, $[0.4 \quad 2]^T$ and $[1 \quad 3]^T$m - using trigonometric (red dashed) and hyperbolic (blue) special cases of elliptic functions.

With examples of the kinematic motion planner in free space given, the obstacle avoidance framework of Section 3.3.2 will now be tested. In the case that the configuration space contains an obstacle, the reachable sets of the planner must be probed to de-

termine if a suitable curve exists which avoids the obstacle. Figure 3.12 shows the existence of a subset of the curves produced by the kinematic motion planner which match a target position of $[X_f \quad Y_f]^T = [1 \quad 3]^T$m in a time of $T = 1$ s.

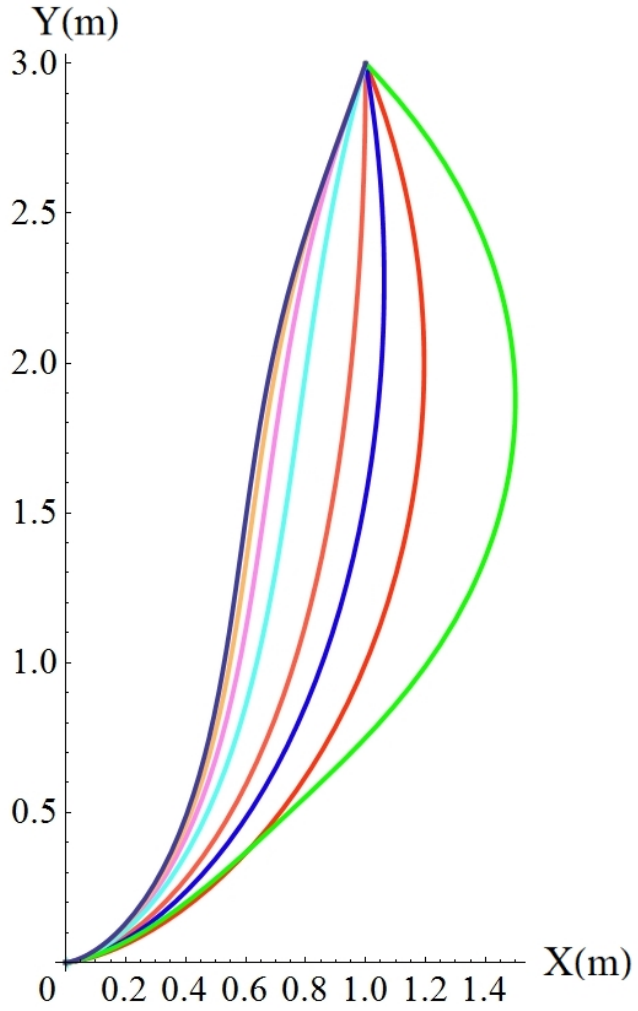

Figure 3.12: Illustration of a subset of curves which match $[X_f \quad Y_f]^T = [1 \quad 3]^T$m boundary conditions.

It is obvious that there are multiple curves which satisfy the position constraint, and therefore it may be possible to utilise this subset of curves in an obstacle avoidance algorithm.

For example for a manoeuvre from the origin to $[X_f \quad Y_f]^T = [1 \quad 3]^T$m with a static obstacle centred at $[X_o \quad Y_o]^T = [0.66 \quad 1.52]^T$m and with radius $\chi_f = 0.3$ m, the following approach could be employed. First, generate a manoeuvre using the motion

planning method described in Section 3.3.1 above. Then, check to see if the condition $\chi > \chi_o \forall t$ is violated at any time step. For instance, for the $T = 1\,\mathrm{s}$ repointing manoeuvre to $[1, 3, \frac{\Pi}{3}]$ shown in Figure 3.10 the wheeled robot collides with the obstacle at $t = 0.56\,\mathrm{s}$. Figure 3.13 illustrates this.

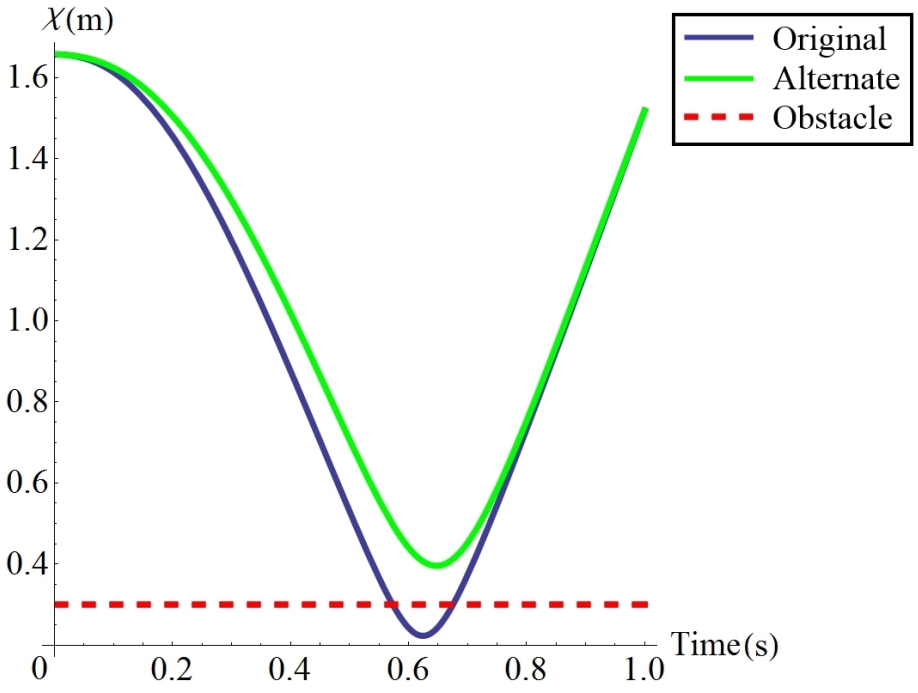

Figure 3.13: Error between current position and centre of forbidden zone of radius χ_o for original path (blue) and path generated using obstacle avoidance algorithm (green). Dashed red line marks radius of obstacle.

Now, a new trajectory can be generated by introducing the parameters p_i (where $i = 1, ..., 3$) to produce a new set of free parameters which drive the wheeled robot to the target via (3.73). This process is repeated, tuning the value of the parameter η until an appropriate solution is found which does not violate the constraint and still meets the desired final position to high precision. One such solution for a constrained manoeuvre from the origin to $[X_f \quad Y_f]^T = [1 \quad 3]^T\,\mathrm{m}$ is shown in Figures 3.13 and 3.14.

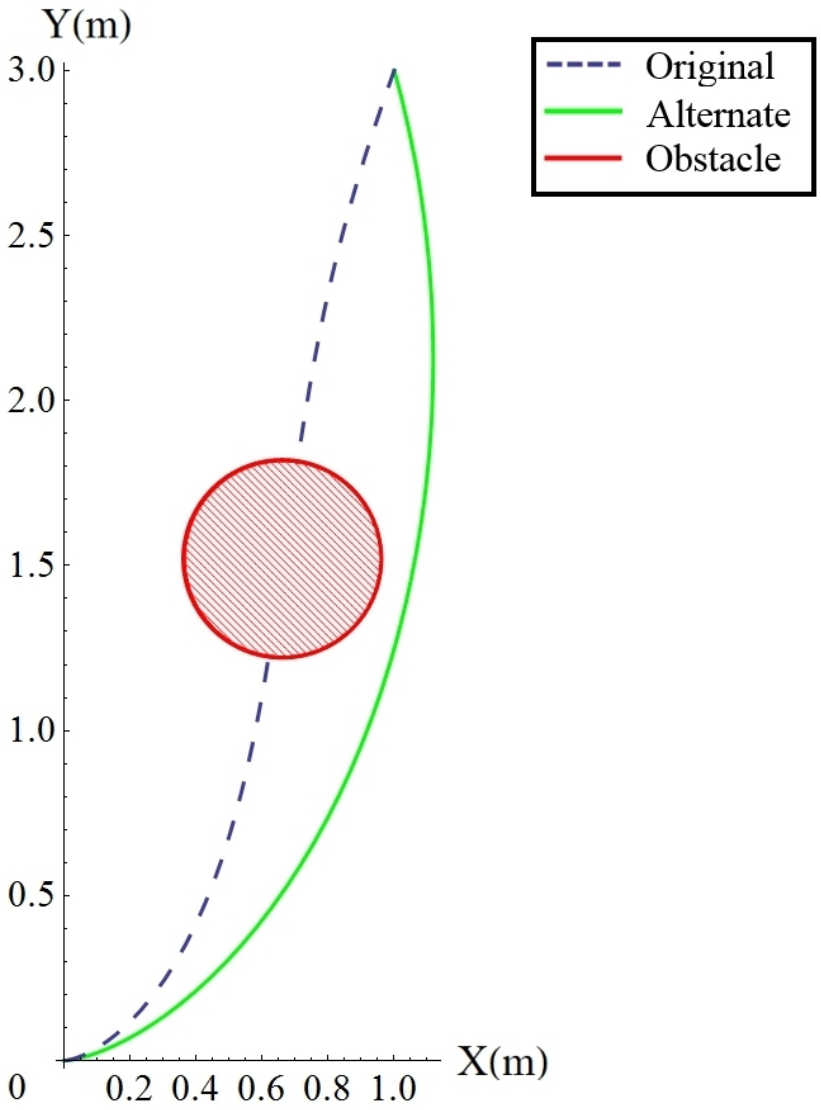

Figure 3.14: Alternative smooth trajectory for manoeuvre to $[X_f \quad Y_f]^T = [1 \quad 3]^T$m (green). Also shown is the original path (blue dashed line) intersecting with the obstacle (red circle).

It is evident that for the new path the constraint $\chi > \chi_o \forall t$ is respected and so the wheeled robot does not collide with the specified obstacle. Therefore the optimal controls derived using geometric control theory have been implemented in a kinematic motion planner which has been shown to be capable of obstacle avoidance. However, further work is required to assess the effectiveness of the obstacle avoidance algorithm in comparison to other methods such as artificial potential functions.

Note that while the obstacle avoidance algorithm was implemented for static obstacles

in a known environment, the analytical curves can be generated swiftly and efficiently and so an extension to dynamic obstacles in uncertain environments may be feasible in future. However, the method of generating the obstacle avoidance curves relies on heuristics at present and so a more automated algorithm would be necessary for the extension to uncertain environments.

3.4.2 Motion Planning for Unit Speed Case

With the arbitrary speed case shown to produce a wide range of curves and to be adaptable to simple obstacle avoidance, in this subsection the planning of motions for the wheeled robot constrained to move at unit speed is demonstrated. Note again that the solution for the unit speed case is complex and only the real part is used for motion planning. Therefore the full optimal solution derived in Section 3.1.2 is not utilised for motion planning, and so it is important to determine if there is any benefit to using the real part of the solution.

Due to the Taylor expansion, and the necessary constraints on the parameter space to $H^*, M, \lambda_3(0) \in [-1.5, 1.5]$ to ensure the accuracy of this expansion, the curves generated by the unit speed motion planner do not exhibit the same variety as that of the arbitrary speed motion planner. This is illustrated in Figure 3.15.

The constraints on the parameter space, in addition to limiting the range of curves available, also limit the reachable sets of the planner. Therefore the obstacle avoidance framework detailed in Section 3.3.2 is in practice not applicable to the unit speed method in it's current form.

As a result of the unit speed case not being capable of obstacle avoidance, and due to the constraints on the reachable sets of the planner due to the Taylor expansion, the unit speed case would appear to be of limited use in practical motion planning.

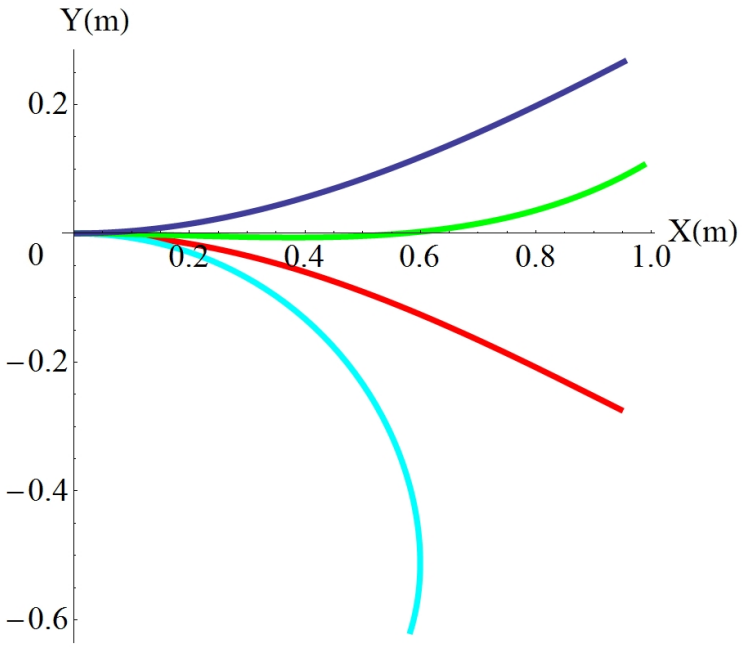

Figure 3.15: Smooth paths of unit speed wheeled robot for manoeuvres to $[X_f, Y_f, \theta_f] = [0.58, -0.62, -1.76]$, $[0.95, 0.27, 0.42]$, $[0.95, -0.27, -0.42]$ and $[0.98, 0.105, 0.42]$ for $H^*, M, \lambda_3(0) \in [-1.5, 1.5]$.

3.4.3 Limitations of Kinematic Motion Planning Method for a Wheeled Robot

The main limitation of the obstacle avoidance method detailed above is that while alternative trajectories can be generated to a specified position in the $X - Y$ plane, it is not always possible to generate an alternative curve which does not collide with the obstacle and which satisfies both a position ($[X_f \quad Y_f]^T$) and an orientation (θ_f) constraint. For example in Figure 3.14 the position constraint $[X_f \quad Y_f]^T = [1 \quad 3]^T$m is respected, but the final orientation differs from that of the original curve.

In the case where an alternative curve has been generated in the presence of an obstacle and a desired final orientation is not achievable via a single curve, or indeed if a desired final state cannot be reached due to sliding and turning constraints, a more complex motion planning algorithm is required. For example while a single curve generated via the motion planner described in this chapter may not be sufficient in all cases, a combination of curves generated by the motion planner and straight line segments may

enable the desired final state to be reached. The motion planning methodology can then be summarised in the following stages:

1. Use the motion planning method described in Section 3.3.1 to minimise the error between the actual and desired final state (X_f, Y_f, θ_f) by changing the values of the free parameters in the analytical expressions derived in Sections 3.1.1 and 3.1.2. If the accuracy of the solution is sufficiently high, and it does not intersect with any obstacles in the configuration space, the trajectory is suitable.

2. In the case where the trajectory intersects with a static, known obstacle, and where final orientation is not of paramount importance, further optimise the parameters p_i as described above to generate an alternative trajectory which does not collide with the obstacle and which sufficiently satisfies the desired final position constraint $[X_f \quad Y_f]^T$.

3. If no single suitable trajectory is found use a combination of curves, generated by motion planner, and straight lines to achieve the desired final state.

The difficulty in piecing together motions lies in ensuring that the transition between segments is smooth (as in the work of Scheuer and Fraichard [68]) and that there are no infeasible increases in translational and rotational speeds between sections. Several methods for achieving this have been proposed [80, 81, 82, 83]. These methods consider the free configuration space of the robot, and then query the reachable sets to create feasible paths for the robot by concatenation of different motion primitives. However, as the aim was simply to derive general classes of motion primitive rather than construct a complete motion planner, this process is outwith the scope of this thesis.

3.5 Chapter Summary

In this chapter a motion planning method for simple wheeled robots with a sliding constraint was derived using optimal control theory for systems defined on Lie groups. Two cases were considered: (i) the case where translational and rotational speeds are

arbitrary and; (ii) the case where the robot is constrained to move forwards at unit speed.

In the arbitrary speed case the optimal controls take the form of elliptic functions. This class of function degenerates to simple trigonometric and hyperbolic functions under certain conditions, and so a wide range of curve types are available for motion planning. In the unit speed case the rotational velocity was described in terms of elliptic functions and the expression for the position reduced to quadratures. A truncated approximation for the real component of the optimal expressions was then used to describe the position analytically. However, in order to ensure that the expansion was accurate it was necessary to limit the parameter space to $H^*, M, \lambda_3(0) \in [-1.5, 1.5]$.

Reachable sets were defined exactly and analytically in the arbitrary speed case by expressing the final manoeuvre time as an elliptic integral of the first kind, and were illustrated numerically in the unit speed case where the time-limited reachable sets resembled those of Dubins' car over short time spans. It was shown that the analytical expressions for position and orientation can be exploited to efficiently generate smooth and feasible paths for the wheeled robots via parametric optimisation. Finally, an algorithm for introducing obstacle avoidance into the parametric optimisation procedure was presented for static obstacles in a known environment. In this procedure a further parametric optimisation probes the reachable sets to find a curve which avoids the static obstacle while satisfying a position constraint. While an example was given for the arbitrary speed case, obstacle avoidance was not feasible for the unit speed case due to the Taylor expansion limiting the reachable sets of the planner. Therefore the unit speed case would not appear to be useful for practical motion planning.

While in this chapter only the kinematics of the wheeled robot were considered, in the following chapter the complexity of the motion planning problem is increased by considering the kinematics together with the dynamics and environment of an autonomous rigid spacecraft performing attitude reorientation manoeuvres. This will enable an assessment to be made of the feasibility and practicality of utilising a kinematic motion planner, derived using geometric control, in a non-ideal environment and in the presence of hardware constraints.

Chapter 4

Spacecraft Attitude Motion Planning and Control

In the previous chapter two kinematic motion planning methods were presented for a wheeled robot subject to kinematic nonholonomic constraints. In this chapter, a motion planning method is derived with respect to a dynamic nonholonomic constraint, the conservation of angular momentum, and then utilised to plan attitude manoeuvres for a small spacecraft. Small spacecraft, such as UKube-1, are limited both in the size of their actuators and in their on-board computational capacity. As a result a low torque, computationally efficient means of repointing these nano-spacecraft is required.

As in Chapter 3 the framework of a kinematic system on a matrix Lie group is used, and the integrals of motion of the system are exploited to analytically solve the problem. However, in contrast to the purely kinematic motion planning of Chapter 3, external disturbances and hardware constraints are considered, enabling the validity of using analytically defined natural motions to plan manoeuvres in a more complex, non-ideal environment to be assessed. Thus in this chapter an analytical motion planning algorithm for axisymmetric and asymmetric rigid spacecraft, based around the natural motion of a free rigid body, is derived in the framework of geometric mechanics detailed in Chapter 2 and applied to the reorientation of nano-spacecraft in order to assess its effectiveness and the feasibility of future on-board implementation. While the attitude

control of a rigid body has been widely studied, on-board attitude motion planning has received considerably less attention and a motivation of this work is to determine the effectiveness of motion planning methods in comparison to widely used conventional control.

Initial attitude control approaches focussed on a series of discrete single axis slews. However, these methods were costly in terms of time and fuel and so new methods were sought. Open loop controls [84, 85] were proposed as simple, low-cost solutions for spacecraft, but these methods are highly sensitive to uncertainties and disturbances. Despite this, open loop controls may be suitable for spacecraft attitude control in low disturbance environments with coarse pointing requirements [86]. Meanwhile, Sidi [58] proposed augmenting single-axis open loop "bang-off-bang" controls with linear feedback near the origin, thus maintaining relatively low control effort while improving stability. Shortest angular path eigenaxis slews have been proposed as simple, near time-optimal solutions [87, 88, 89], but they are in general not fuel-optimal. Other time-efficient retargeting methods have been proposed by Wie [90] and Verbin [91], which additionally consider actuator and pointing constraints.

Nonlinear optimal control methods that use the calculus of variations and dynamic programming have also been applied to the spacecraft attitude control problem. However, while these methods, such as those that require the numerical solution of the Hamilton-Jacobi-Bellman (HJB) equation, give globally optimal and theoretically superior solutions they are difficult to implement on-board a spacecraft as they are computationally intensive [92]. As a result, simple proportional-derivative (PD) controllers such as the quaternion feedback controllers [93, 94] continue to dominate the practical control of spacecraft due to the ease of gain tuning and low implementation risk. Recent inverse optimal control methods negate the need to solve the HJB equation by finding a control Lyapunov function which is itself a solution of the HJB, and designing the control around this [95]. This approach has been combined with the minimisation of control norms to form low energy attitude manoeuvres [96, 97].

Other guidance methods include the tracking of references generated by computationally efficient artificial potential functions (APFs) to reorientate spacecraft [51]. Mengali

[43] extended this work by utilising artificial potential functions in the manoeuvring of spacecraft with sensitive optical equipment, such as star trackers, which must reach the target attitude while avoiding luminous objects such as the Sun and Earth's Moon. However, as previously stated, APFs can demand excessive control effort [52, 53].

This work is motivated by the need to find a compromise between the computational simplicity of proportional-derivative control and the optimality of non-linear controllers. In free space and choosing appropriate initial conditions, the spacecraft will naturally drift towards a certain orientation in a set period of time. Therefore these "natural motions" are an intuitive basis around which to design spacecraft attitude manoeuvres. In this chapter the dynamics of a rigid body are exploited to derive analytical expressions for the time evolution of the attitude of the spacecraft in quaternion form. Despite suffering from the problem of ambiguity, due to the two-to-one mapping between the unit quaternions and $SO(3)$ detailed in Section 2.3.3, quaternions are singularity free and computationally efficient, and so are the most widely used form of attitude representation on-board spacecraft [32]. Boundary conditions on the attitude of the spacecraft are matched through parametric optimisation of the initial spacecraft angular velocities, building on the framework introduced in Chapter 3, and the resulting references are tracked using a simple proportional-derivative controller. The effectiveness of the motion planning method is assessed via comparison with the conventionally used quaternion feedback control, and it is shown that the references require low accumulated torque to track. In addition, in a similar manner to the kinematic wheeled robot motion planner of the previous chapter, the set of curves which match the boundary conditions on the final pointing direction can be probed to create a simple obstacle avoidance algorithm.

Original Contributions

The original contributions in this chapter are outlined as follows:

- While the classical global solution is on the attitude dynamics, in this thesis the kinematics for both axisymmetric and asymmetric spacecraft are derived analyt-

ically for global motion planning implementation in convenient quaternion form. This is accomplished using the machinery of geometric control theory which was detailed in Chapter 2 and used to construct a simple kinematic motion planner in Chapter 3. The classical solutions, to the authors' knowledge, can only be found expressed locally in terms of Euler angles [98, 99, 100].

- The analytical equations are implemented in a simple motion planning algorithm to produce easily trackable reference motions for a spacecraft, and it is shown that the motion planning algorithm is additionally capable of providing constrained slews.

- The strengths and weaknesses of the proposed method are evaluated through extensive numerical simulations in which environmental disturbances and actuator constraints are taken into account. It is shown that the natural motions provide substantial savings in accumulated torque over a conventional quaternion feedback benchmark. An obstacle avoidance manoeuvre is demonstrated.

The chapter is structured as follows. In Section 4.1, the spacecraft model is introduced, together with the realistic environmental model which will be utilised to test the robustness of the motion tracking. In Section 4.2, the general motion planning framework is first described, before the specific cases of the axisymmetric and asymmetric spacecraft are derived. The practical implementation of the motion planning method is discussed in Section 4.3, including the extension to obstacle avoidance. Simulation results are presented in Section 4.4 where the novel natural motion planning method is compared to conventional quaternion feedback control. The suitability of the method for on-board implementation is discussed in Section 4.5. Finally, the chapter concludes with Section 4.6 and a summary of results.

4.1 Spacecraft Attitude and Orbit Models

While in reality spacecraft have flexible modes, in this thesis the assumption is made that the spacecraft can be treated as a rigid body. This assumption is feasible for small

Cubesat spacecraft as they contain few moving parts and generally do not carry liquid propellant. The general equations describing the attitude control problem are then that of a rigid body with external torques describing the effect of the disturbances.

4.1.1 Reference Frame Definitions

The spacecraft under consideration is in orbit around the Earth. The centre of the Earth is chosen as the origin of a Geocentric Equatorial co-ordinate system with basis vectors $\hat{I}, \hat{J}, \hat{K}$. As in [101], the X-axis lies in the equatorial plane towards the vernal equinox direction, the Z-axis points in the direction of the North pole and the Y-axis lies in the equatorial plane and completes the orthonormal reference frame. The co-ordinate system is shown in Figure 4.1.

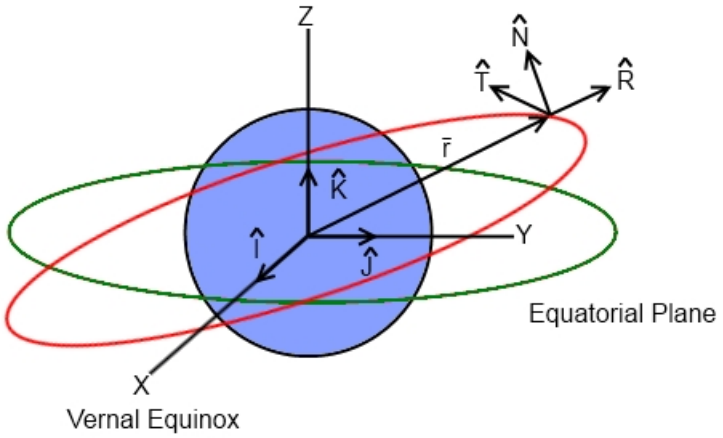

Figure 4.1: Geocentric Equatorial and RTN co-ordinate systems.

Also shown in Figure 1 is the Radial-Transverse-Normal (RTN) reference frame used to describe the orbit of the spacecraft. In this reference frame $\hat{R}$ is parallel with the radial vector, $\hat{N}$ is parallel with the orbit normal and $\hat{T}$ completes the orthonormal frame. A body fixed reference frame (BRF) with basis $\hat{i}, \hat{j}, \hat{k}$ is rigidly attached to the centre of mass of the spacecraft, as shown in Figure 4.2.

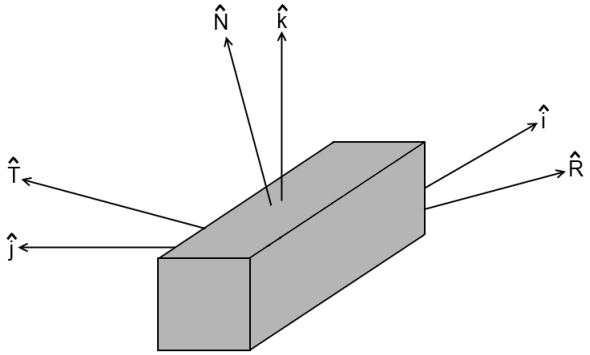

Figure 4.2: Body and RTN co-ordinate systems.

4.1.2 Kinematic Model

The attitude kinematics of the spacecraft can be parameterised using quaternions (2.29) and equivalently on the matrix Lie group $SU(2)$ (2.31), as stated in Section 2.3.3 of Chapter 2. In this chapter the quaternions are inertially referenced, with the inertial quaternions simply denoted $\bar{q} = [q_0 \quad q_1 \quad q_2 \quad q_3]^T$.

4.1.3 Dynamic Model

Euler's rotational equations of motion for a rigid spacecraft are defined as:

$$J \cdot \dot{\bar{\omega}} + \bar{\omega} \times J \cdot \bar{\omega} = \bar{N}_e + \bar{N}_w \tag{4.1}$$

where J denotes the moment of inertia matrix of the spacecraft, $\bar{\omega}$ and $\dot{\bar{\omega}}$ the angular velocity and angular acceleration vectors of the spacecraft body frame with respect to the inertial frame, $\bar{N}_e = [N_{1e} \quad N_{2e} \quad N_{3e}]^T$ the external torques and $\bar{N}_w = [N_{1w} \quad N_{2w} \quad N_{3w}]^T$ the reaction wheel torques. Assuming that the body frame originates from the spacecraft centre of mass and is coincident with the principal axes of

the spacecraft, Euler's equations reduce to

$$\begin{aligned}
\dot{\omega}_1 &= \frac{N_{1e}+N_{1w}+(J_2-J_3)\omega_2\omega_3}{J_1} \\
\dot{\omega}_2 &= \frac{N_{2e}+N_{2w}+(J_3-J_1)\omega_3\omega_1}{J_2} \\
\dot{\omega}_3 &= \frac{N_{3e}+N_{3w}+(J_1-J_2)\omega_1\omega_2}{J_3}
\end{aligned} \tag{4.2}$$

where J_1, J_2 and J_3 are the principal moments of inertia of the spacecraft.

4.1.4 Spacecraft Model

Two spacecraft based on the UKube-1 are primarily considered; one of which is axisymmetric and the other slightly asymmetric. The properties of these spacecraft are listed in Table 4.1.

Table 4.1: Physical properties of spacecraft

Principal inertias of axisymmetric spacecraft A	$J_1 = 0.0109\,\text{kgm}^2$
	$J_2 = J_3 = J_s = 0.05\,\text{kgm}^2$
Principal inertias of asymmetric spacecraft B	$J_1 = 0.0109\,\text{kgm}^2$
	$J_2 = 0.0504\,\text{kgm}^2$
	$J_3 = 0.0506\,\text{kgm}^2$
Drag coefficient	$C_d = 3$
Reflectivity	$\kappa = 0.6$
Residual dipole in $\hat{k}$ body axis	$M_{3res} = 10 \times 10^{-3}\,\text{Am}^2$
CoP/CoM offset	$\| \bar{r}_{m/p} \| = 0.02\,\text{m}$

It is assumed that the spacecraft is equipped with simple reaction wheels. The wheel data is based on the Sinclair Interplanetary picosatellite reaction wheels [102], and the wheel properties are shown in Table 4.2.

Table 4.2: Sinclair Interplanetary reaction wheel data

Wheel inertias	$J_w = 1.499 \times 10^{-5}\,\mathrm{kgm}^2$
Maximum wheel torque	$1 \times 10^{-3}\,\mathrm{Nm}$
Rate limit	$1 \times 10^{-2}\,\mathrm{Nm/s}$
Nominal wheel momentum	$7 \times 10^{-3}\,\mathrm{Nms@4460\,rpm}$

The wheels apply a control torque given by

$$\bar{N}_w = -\dot{\bar{h}}_w - \bar{\omega} \times \bar{h}_w \tag{4.3}$$

This simplified model can be easily integrated to yield the wheel angular momenta $\bar{h}_w = [h_{1w} \quad h_{2w} \quad h_{3w}]^T$ and wheel velocities $\bar{\omega}_w = [\omega_{1w} \quad \omega_{2w} \quad \omega_{3w}]^T$.

4.1.5 Orbit Model

A Cartesian orbit model was implemented in which the two-body problem equations [101] were numerically integrated to give the position and velocity at each time-step:

$$\ddot{\bar{r}} = -\frac{\mu}{(\mid\mid \bar{r} \mid\mid)^3}\hat{r} + \bar{a}_{ext} \tag{4.4}$$

The symbol $\bar{r}$ denotes the orbit radius vector and $\mid\mid \bar{r} \mid\mid$ the magnitude of the orbit radius vector, $\mu = 3.986\,01 \times 10^{14}\,\mathrm{m^3 s^{-2}}$ is the gravitational parameter, in this case of the Earth, and $\bar{a}_{ext}$ the accelerations caused by external environmental forces. These environmental effects will be discussed in the proceeding section.

4.1.6 Environmental Model

As a spacecraft orbits the Earth it is subjected to a number of environmental disturbances. Therefore in order to test the robustness of the motion planning method it is necessary to model these environmental disturbances, and assess the effect they have on the tracking of the motions which are derived for a free rigid body. The attitude

disturbances caused by the gravity gradients, residual magnetic dipoles, air drag and solar radiation pressure were modelled, together with the orbital perturbations due to air drag, solar radiation pressure and the Earth's oblateness.

Gravity Gradient Torque

The gravity gradient torque arises from the fact that the spacecraft is not a point mass, and so the gravitational field is not uniform over the spacecraft. Therefore each point on the spacecraft experiences a different gravitational attraction depending on its distance from the earth. The gravity gradient torque acting on the spacecraft is given by [32]

$$\bar{N}_{gg} = \frac{3\mu}{(\mid\mid \bar{r} \mid\mid)^5}\bar{r} \times J \cdot \bar{r} \tag{4.5}$$

where $\bar{N}_{gg}$ is the gravity gradient torque.

Magnetic Dipole Torque

The onboard electronics of the spacecraft generate a magnetic disturbance torque as a result of the Lorentz force. This disturbance torque is given by

$$\bar{N}_{md} = \bar{M}_{res} \times \bar{B} \tag{4.6}$$

where $\bar{N}_{md} = [N_{1md} \quad N_{2md} \quad N_{3md}]^T$ is the magnetic disturbance torque vector, $\bar{M}_{res} = [M_{1res} \quad M_{2res} \quad M_{3res}]^T$ is the residual dipole due to the spacecraft electronics and $\bar{B} = [B_1 \quad B_2 \quad B_3]^T$ is the Earth's magnetic field in the body reference frame.
The Earth's magnetic field was modelled as a simple dipole [103]:

$$\bar{B}_{grf} = -\frac{\mu_m}{\mid\mid \bar{r} \mid\mid^3}\begin{bmatrix} 3\sin\lambda_m \cos\lambda_m \cos\eta_m \\ 3\sin\lambda_m \cos\lambda_m \sin\eta_m \\ 3\sin^2\lambda_m - 1 \end{bmatrix} \tag{4.7}$$

where $\bar{B}_{grf} = [B_{1grf} \quad B_{2grf} \quad B_{3grf}]^T$ is the magnetic field vector in the geomagnetic reference frame, $\mu_m = 7.96 \times 10^{15}$ Wbm represents the Earth's magnetic dipole strength, λ_m is the latitude with respect to the geomagnetic equatorial plane and η_m is the longitude along the magnetic equator. The magnetic field in the body frame $\bar{B}$ can then be found by rotating from the geomagnetic reference frame to the body frame. The value of $\bar{M}_{res}$ detailed in Table 4.1 was based on a NASA guideline for estimation of magnetic disturbance torques for a small spacecraft [104]. In this document, a constant magnetic moment per unit mass is given for various types of spacecraft, leading to the calculation of the value above. However, it should be noted that in reality the magnetic dipole of the spacecraft will be time varying as components are switched on and off.

Air Drag Torque and Force

The air drag torque acting on a spacecraft is difficult to model accurately as a result of the chaotic nature of the Earth's atmosphere. In this thesis a simple approximation of the air drag torque is adopted, with the air density at a specific altitude assumed constant and the atmosphere assumed to rotate at the same speed as the Earth. Then, the air drag torque can be calculated by considering the forces acting on each face of the spacecraft. The offset between the centre of mass and centre of gravity was assumed to be $\| \bar{r}_{m/p} \| = 0.2\,\text{m}$ where $\bar{r}_{m/p}$ is the vector from the centre of mass to the centre of pressure. The air drag torque acting on the spacecraft can then be calculated from the expression [105]

$$\bar{N}_{ad} = \frac{1}{2}\rho v^2 C_D A_s (\hat{n} \cdot \hat{v}) \bar{r}_{m/p} \times (\hat{v}) \tag{4.8}$$

where $\bar{N}_{ad} = [N_{1ad} \quad N_{2ad} \quad N_{3ad}]^T$ is the air drag torque, ρ the atmospheric density, v the velocity of the air hitting the spacecraft in the body reference frame, C_D the drag coefficient, A_s the area of the spacecraft face(s) and $\hat{n}$ the unit vector of the spacecraft face in the body reference frame.

Solar Radiation Pressure Torque and Force

The solar radiation pressure torque is calculated in a similar manner to the air drag torque. The radial vector from the Sun to the spacecraft in the inertial frame, $\bar{r}_{sun}$, is calculated and this vector is used in the expression [105] below to calculate the solar radiation pressure torque:

$$\bar{N}_{SRP} = \frac{S_0 A_s (1+\kappa)}{c_l} (\hat{n} \cdot \hat{r}_{sun(b)}) \bar{r}_{m/p} \times (\hat{r}_{sun(b)}) \tag{4.9}$$

where $\bar{N}_{SRP} = [N_{1SRP} \quad N_{2SRP} \quad N_{3SRP}]^T$ is the solar radiation torque, S_0 is the solar constant ($1367\,\mathrm{W/m^2}$), κ the reflectance factor (0.6), c_l the speed of light in a vacuum and $\hat{r}_{sun(b)}$ the unit vector from the Sun to the spacecraft in the body reference frame.

Earth Oblateness

The Earth oblateness effects, which arise due to the non-spherical shape of the Earth, were modelled by considering the perturbing accelerations acting on the spacecraft's orbit in Cartesian co-ordinates. For more detail on these accelerations, see [106] pp. 553.

4.2 Analytic Derivation of the Natural Motion References

In this section analytical equations for the torque-free attitude motion of axisymmetric and asymmetric spacecraft are derived using Lax pair integration in global quaternion form. The general framework used to derive the equations is the same as that utilised in Chapter 3 in the kinematic motion planning for a simple wheeled robot. Once again the kinematics of the system are expressed on a matrix Lie group, in this case the Special Unitary group $SU(2)$, and the conserved quantities of the system are utilised to solve the Hamiltonian vector fields to yield the analytical optimal controls. The specific cases of the axisymmetric and asymmetric spacecraft are considered. The analytical equations will form the basis of the natural motion planning algorithm for spacecraft

attitude manoeuvres.

4.2.1 General Framework

In order to explicitly show the link between the optimal kinematic motion planning of Chapter 3 and the dynamic motion planning problem of this chapter, the rigid body equations of motion are derived in the context of an optimal control problem on a matrix Lie group. In this case the integrand of the cost function is the Lagrangian and the Lie group is the Special Unitary group $SU(2)$. This problem is analogous to the principle of least action in mechanics and the resulting extremal curves are shown to be the components of angular momentum. The Hamiltonian vector fields describing the necessary conditions are then the Euler equations. In this framework the Hamiltonian and Casimir functions are identified as in Chapter 3 and exploited in a similar fashion to integrate and solve the problem analytically.

The kinematics of the rigid body are described using the matrix Lie group $SU(2)$ (2.31), and a cost function of the form

$$J = \frac{1}{2}\int_0^1 J_1{\omega_1}^2 + J_2{\omega_2}^2 + J_3{\omega_3}^2 dt \tag{4.10}$$

is utilised. Relative to the general form of the cost function (2.34), the weights $c_i = J_i$ where J_i are the principal inertias of the rigid body and the controls $u_i = \omega_i$ with $i = 1, ..., 3$. As with the wheeled robot, torques will in reality be required to produce the desired angular velocities. The impact of this assumption will be assessed in simulation. The Hamiltonian function can be derived using the procedure detailed in Section 2.5.2:

$$H = \omega_1\lambda_1 + \omega_2\lambda_2 + \omega_3\lambda_3 - \frac{1}{2}(J_1{\omega_1}^2 + J_2{\omega_2}^2 + J_3{\omega_3}^2) \tag{4.11}$$

The cost function (4.10) minimises the rotational kinetic energy of the rigid body, and so tracking manoeuvres generated with respect to this cost should require low control effort. The validity of this cost function will also be tested in simulation in later sections. From the Maximum Principle of optimal control detailed in Section 2.5, if the following

conditions are satisfied

$$\frac{\partial H}{\partial \omega_i} = 0, \frac{\partial^2 H}{\partial {\omega_i}^2} < 0 \tag{4.12}$$

where again $i = 1, ..., 3$, then the controls ω_i are optimal. This yields:

$$\omega_i = \frac{\lambda_i}{J_i} \tag{4.13}$$

Substituting (4.13) into (4.11) leads to the optimal Hamiltonian H^* relative to the kinematics (2.31) and cost function (4.10):

$$H^* = \frac{1}{2}(\frac{\lambda_1^2}{J_1} + \frac{\lambda_2^2}{J_2} + \frac{\lambda_3^2}{J_3}) \tag{4.14}$$

Additionally, the Casimir function

$$M^2 = \lambda_1^2 + \lambda_2^2 + \lambda_3^2 \tag{4.15}$$

is constant along the Hamiltonian flow $\{M^2, H^*\} = 0$. The corresponding Hamiltonian vector fields which implicitly define the extremal solutions are given by the Poisson bracket $\frac{d\lambda_i}{dt} = \{\lambda_i, H^*\}$ where $i = 1, ..., 3$. The Poisson bracket relations are given by (2.11) relative to the commutative table for the Lie algebra of $SU(2)$, Table 2.2. This yields the differential equations:

$$\begin{aligned} \dot{\lambda}_1 &= \lambda_2\lambda_3(\tfrac{1}{J_3} - \tfrac{1}{J_2}) \\ \dot{\lambda}_2 &= \lambda_1\lambda_3(\tfrac{1}{J_1} - \tfrac{1}{J_3}) \\ \dot{\lambda}_3 &= \lambda_1\lambda_2(\tfrac{1}{J_2} - \tfrac{1}{J_1}) \end{aligned} \tag{4.16}$$

Equations (4.16) define the general extremal differentials for the specific case where $c_i = J_i$. Note that by substituting $\lambda_i = \omega_i J_i$ from (4.13) into (4.16), the equations become the Euler equations defining the natural motion of a rigid body in the absence of perturbations. Additionally, substituting $\lambda_i = \omega_i J_i$ into the optimal Hamiltonian

(4.14) and Casimir (4.15) results in expressions of the form:

$$\begin{aligned} H^* &= \tfrac{1}{2}\left(J_1\omega_1^2 + J_2\omega_2^2 + J_3\omega_3^2\right) \\ M^2 &= (J_1\omega_1)^2 + (J_2\omega_2)^2 + (J_3\omega_3)^2 \end{aligned} \tag{4.17}$$

Therefore in the specific case where the weights are equal to the principal inertias of the rigid body, the Hamiltonian corresponds to the total rotational kinetic energy of the body, and the Casimir function corresponds to the magnitude of the angular momentum. In the following sections these conserved quantities will be utilised to show that the optimal angular velocities are the free angular velocities of the rigid body, and to derive the time evolution of the attitude of the spacecraft in quaternion form.

Firstly, in order to derive the global solution in terms of quaternions, the local solution in terms of euler angles is utilised.

Lemma 3. *The euler angles representing the local orientation of the spacecraft can be written as functions of the angular velocities [98, 99, 100]:*

$$\begin{aligned} \varphi_1 &= \int \tfrac{M(2H - J_1{\omega_1}^2)}{M^2 - (J_1\omega_1)^2} dt \\ \varphi_2 &= \arccos(\tfrac{J_1\omega_1}{M}) \\ \varphi_3 &= \arctan(\tfrac{J_2\omega_2}{J_3\omega_3}) \end{aligned} \tag{4.18}$$

where $0 \leq \varphi_2 \leq \pi$ *and* $-\pi/2 < \varphi_3 < \pi/2$.

Proof. The Euler equations (4.2), in the case when $\bar{N}_e = \bar{N}_w = [0 \quad 0 \quad 0]^T$, can be written in Lax pair form on the semisimple Lie group $SU(2)$ as [57, 107]:

$$\frac{dL(t)}{dt} = [L(t), \omega] \tag{4.19}$$

where

$$\begin{aligned} L(t) &= J_1\omega_1 A_1 + J_2\omega_2 A_2 + J_3\omega_3 A_3 \\ \omega &= \omega_1 A_1 + \omega_2 A_2 + \omega_3 A_3 \end{aligned} \tag{4.20}$$

It is well known that the Lax pair equation and the kinematic equations are connected through the relation

$$L(t) = R(t)^{-1} L(0) R(t) \tag{4.21}$$

It is this relation that is used to solve for the corresponding rotations. Here $L(0)$ is the matrix $L(t)$ at $t = 0$ and is therefore a matrix with constant entries. Writing the dynamics and kinematics in the language of classical mechanics and making use of Lax pair integration provides a natural and elegant means of deriving analytically the expressions for the time evolution of the quaternions. Equivalently, it is possible to write

$$R(t)L(t)R(t)^{-1} = L(0) \tag{4.22}$$

where $R(t)L(t)R(t)^{-1}$ describes the conjugacy class of $L(t)$. Thus for simplicity and to obtain more explicit solutions it suffices to integrate the particular solution

$$R(t)L(t)R(t)^{-1} = MA_1 \tag{4.23}$$

where M is the conserved Casimir function from (4.17). Rearranging yields:

$$L(t) = MR(t)^{-1} A_1 R(t) \tag{4.24}$$

As $\exp(-\varphi_1 A_1) A_1 \exp(\varphi_1 A_1) = A_1$, $\exp(\varphi_1 A_1)$ is known as the stabilizer of A_1 [17]. It is therefore convenient to introduce the coordinate form

$$R(t) = \exp(\varphi_1 A_1) \exp(\varphi_2 A_2) \exp(\varphi_3 A_1) \tag{4.25}$$

Substituting (4.25) into (4.24) yields:

$$L(t) = \frac{iM}{2} \begin{pmatrix} \cos\varphi_2 & e^{-i\varphi_3}\sin\varphi_2 \\ e^{i\varphi_3}\sin\varphi_2 & -\cos\varphi_2 \end{pmatrix} \tag{4.26}$$

Equating (4.26) with $L(t)$ in (4.20) results in the following system of equations:

$$\begin{aligned} J_1\omega_1 &= M\cos\varphi_2 \\ J_2\omega_2 + iJ_3\omega_3 &= Me^{-i\varphi_3}\sin\varphi_2 \\ -J_2\omega_2 + iJ_3\omega_3 &= Me^{i\varphi_3}\sin\varphi_2 \end{aligned} \tag{4.27}$$

which can be immediately solved to provide the expression for φ_2 in (4.18). Now, adding the bottom two equations in (4.27) yields:

$$2iJ_3\omega_3 = M\sin\varphi_2(e^{-i\varphi_3} + e^{i\varphi_3}) \tag{4.28}$$

Subtracting the bottom two equations in (4.27) gives:

$$2J_2\omega_2 = -M\sin\varphi_2(-e^{-i\varphi_3} + e^{i\varphi_3}) \tag{4.29}$$

Equations (4.28) and (4.29) can be simplified by making use of the identities

$$\begin{aligned} \cos(\theta) &= \tfrac{e^{i\theta}+e^{-i\theta}}{2} \\ \sin(\theta) &= \tfrac{e^{i\theta}-e^{-i\theta}}{2i} \end{aligned} \tag{4.30}$$

which results in the following:

$$\begin{aligned} iJ_3\omega_3 &= M\sin(\varphi_2)\cos(\varphi_3) \\ \tfrac{J_2\omega_2}{i} &= -M\sin(\varphi_2)\sin(\varphi_3) \end{aligned} \tag{4.31}$$

Dividing these two equations gives:

$$\tan(\varphi_3) = \frac{J_2\omega_2}{J_3\omega_3} \tag{4.32}$$

Solving provides the expression for φ_3 in (4.18). To obtain an expression for φ_1, rearrange (2.31) to yield:

$$R(t)^{-1}\frac{dR(t)}{dt} = \omega_1 A_1 + \omega_2 A_2 + \omega_3 A_3 \tag{4.33}$$

Then, substituting the expressions for φ_2 and φ_3 into (4.25), and subsequently into (4.33), with some computation it follows that

$$\dot{\varphi}_1 = \frac{M\omega_1(M^2 - (J_1\omega_1)^2) - MJ_2J_3(\omega_3\dot{\omega}_2 - \omega_2\dot{\omega}_3)}{J_1\omega_1(M^2 - (J_1\omega_1)^2)} \tag{4.34}$$

Using the expressions for $\dot{\omega}_2$ and $\dot{\omega}_3$ in (4.2) for the free body (i.e. $\bar{N}_e = \bar{N}_w = 0$), the constants (4.17) and simplifying results in the expression for φ_1 in (4.18)$\square$.

Note that the expressions for the Euler angles (4.18) can also be expressed more generally in terms of the extremals as [109]

$$\begin{aligned}
\varphi_1 &= \int M\left(\frac{\frac{\partial H^*}{\partial \lambda_2}\lambda_2 + \frac{\partial H^*}{\partial \lambda_3}\lambda_3}{\lambda_2^2 + \lambda_3^2}\right)dt \\
\varphi_2 &= \arccos\left(\frac{\lambda_1}{M}\right) \\
\varphi_3 &= \arctan\left(\frac{\lambda_2}{\lambda_3}\right)
\end{aligned} \tag{4.35}$$

These more general expressions will be utilised in Chapter 5 in the derivation of the optimal analytical controls for a spinning spacecraft.

Substituting (4.18) into (4.25) and pulling the solution back to the identity via

$$R(t) = R_{int}R(0)^{-1}R(t) \tag{4.36}$$

provides the solution on the Special Unitary group $SU(2)$. In this expression R_{int} is the initial orientation and $R(0)^{-1}$ is the inverse of $R(t)$ at $t = 0$. Finally, using the isomorphism (2.20) and comparing the real and imaginary parts yields the globally defined analytical quaternion equations for the free motion of a rigid body.

The equations above will now be used to derive the globally defined analytic equations

for the free motion of the spacecraft in the axisymmetric and asymmetric cases.

4.2.2 Axisymmetric Spacecraft

In this subsection the equations for the free motion of an axisymmetric spacecraft, derived using the procedure in Section 4.2.1, are stated.

Lemma 4. *The time evolution of the quaternions* ($\bar{q} = [q_0 \quad q_1 \quad q_2 \quad q_3]^T$) *related to the free motion of an axisymmetric body can be written in the form:*

$$\begin{aligned}
q_0 &= \cos(x(t))\cos(\tfrac{\varphi_1}{2}) - y(t)\sin(x(t))\sin(\tfrac{\varphi_1}{2}) \\
q_1 &= \sin(x(t))\cos(\tfrac{\varphi_1}{2}) + y(t)\cos(x(t))\sin(\tfrac{\varphi_1}{2}) \\
q_2 &= \mathrm{sgn}(\omega_3(0))\sqrt{1-y(t)^2}\sin(\tfrac{\varphi_1}{2})\sin(z(t)) \\
q_3 &= \mathrm{sgn}(\omega_3(0))\sqrt{1-y(t)^2}\sin(\tfrac{\varphi_1}{2})\cos(z(t))
\end{aligned} \tag{4.37}$$

where

$$\begin{aligned}
x(t) &= \tfrac{c(J_s-J_1)}{2J_s}t \\
y(t) &= \tfrac{J_1 c}{M} \\
z(t) &= x(t) + \tan^{-1}(\tfrac{\omega_2(0)}{\omega_3(0)}) \\
\varphi_1 &= (M(2H - J_1c^2)/(M^2 - (J_1c)^2)t
\end{aligned} \tag{4.38}$$

subject to the given boundary conditions $\bar{q}(0) = [1 \quad 0 \quad 0 \quad 0]^T$ *and* $\bar{q}(T)$.

Proof. For an axisymmetric spacecraft with $J_2 = J_3 = J_s$, the general extremal differ-

ential equations (4.16) reduce to

$$\begin{aligned}\dot{\lambda}_1 &= 0 \\ \dot{\lambda}_2 &= \lambda_1\lambda_3(\tfrac{1}{J_1} - \tfrac{1}{J_s}) \\ \dot{\lambda}_3 &= \lambda_1\lambda_2(\tfrac{1}{J_s} - \tfrac{1}{J_1})\end{aligned} \tag{4.39}$$

Therefore λ_1 is constant. The Hamiltonian function (4.14) can then be rearranged to give:

$$(2H^* - \frac{\lambda_1^2}{J_1})J_s = \lambda_2^2 + \lambda_3^2 \tag{4.40}$$

Equation (4.40) can be solved using the polar co-ordinates

$$\lambda_2 = r\sin(\theta), \quad \lambda_3 = r\cos(\theta) \tag{4.41}$$

where $\theta = (At+B)$. From the left hand side of (4.40), it follows that $r = \sqrt{(2H^* - \frac{\lambda_1^2}{J_1})J_s}$. In order to solve for θ, divide the expressions in (4.41) to yield:

$$\frac{\lambda_2}{\lambda_3} = \tan(\theta) \tag{4.42}$$

Differentiating 4.42 gives:

$$\frac{\dot{\lambda}_2\lambda_3 - \dot{\lambda}_3\lambda_2}{\lambda_3^2} = \sec^2(\theta)\dot{\theta} \tag{4.43}$$

Substituting the expressions (4.41) and (4.39) into (4.43) and simplifying results in an expression for $\dot{\theta}$:

$$\dot{\theta} = \lambda_1(\frac{1}{J_1} - \frac{1}{J_s}) \tag{4.44}$$

Differentiating (4.44) yields:

$$\theta = \lambda_1(\frac{1}{J_1} - \frac{1}{J_s})t + B \tag{4.45}$$

where $A = \lambda_1(\frac{1}{J_1} - \frac{1}{J_s})$. In order to solve for B, set $t = 0$ in (4.41) and rearrange to give:

$$\sin(B) = \frac{\lambda_2(0)}{r}, \quad \cos(B) = \frac{\lambda_3(0)}{r} \tag{4.46}$$

where $B = \theta(0)$ and $\theta(0), \lambda_2(0)$ and $\lambda_3(0)$ are the values of θ, λ_2 and λ_3 at $t = 0$. It follows from simple trigonometry that $B = \arctan(\frac{\lambda_2(0)}{\lambda_3(0)})$. The complete expressions for λ_2 and λ_3 can now be written as

$$\begin{aligned} \lambda_2 &= \sqrt{(2H^* - \tfrac{\lambda_1^2}{J_1})J_s}\sin(\lambda_1(\tfrac{1}{J_1} - \tfrac{1}{J_s})t + \arctan(\tfrac{\lambda_2(0)}{\lambda_3(0)})) \\ \lambda_3 &= \sqrt{(2H^* - \tfrac{\lambda_1^2}{J_1})J_s}\cos(\lambda_1(\tfrac{1}{J_1} - \tfrac{1}{J_s})t + \arctan(\tfrac{\lambda_2(0)}{\lambda_3(0)})) \end{aligned} \tag{4.47}$$

It follows via (4.13) that the optimal analytical expressions for the angular velocities of an axisymmetric spacecraft, where $J_2 = J_3 = J_s$, are given by:

$$\begin{aligned} \omega_1 &= c \\ \omega_2 &= \operatorname{sgn}[\omega_3(0)]\sigma_1 \sin(\sigma_2 t + \tan^{-1}\left(\tfrac{\omega_2(0)}{\omega_3(0)}\right)) \\ \omega_3 &= \operatorname{sgn}[\omega_3(0)]\sigma_1 \cos(\sigma_2 t + \tan^{-1}\left(\tfrac{\omega_2(0)}{\omega_3(0)}\right)) \end{aligned} \tag{4.48}$$

where c is a constant angular velocity and where

$$\begin{aligned} \sigma_1^2 &= \tfrac{2H - J_1 c^2}{J_s} \\ \sigma_2 &= c\tfrac{J_s - J_1}{J_s} \end{aligned} \tag{4.49}$$

The expressions in (4.48) are the well-known equations for the free motion of an axisymmetric rigid body [32]. Substituting these expressions into (4.18) and then into (4.25), and pulling the solution back to the identity via (4.36) yields the solution on $SU(2)$. Using the isomorphism (2.20) gives the expressions for the evolution of the quaternions in the axisymmetric case □ See [108].

Remark 2. *The sign function* $\operatorname{sgn}(\omega_3(0))$ *in (4.37) and (4.48) is added to ensure that the initial first derivatives of these equations match the initial first derivatives of their numerical counterparts. That is, to ensure that the first derivatives of (4.37) and (4.48) at time* $t = 0$ *match the first derivatives of (2.29) and (4.1), with zero external torques, at* $t = 0$.

4.2.3 Asymmetric Spacecraft

In this subsection the equations for the free motion of an asymmetric spacecraft, derived using the procedure in Section 4.2.1, are stated.

Lemma 5. *The time evolution of the quaternions* ($\bar{q} = [q_0 \quad q_1 \quad q_2 \quad q_3]^T$) *related to the free motion of an asymmetric body can be written in the form:*

$$\begin{aligned}
q_0 &= \mathcal{F}_1 \left(\cos(\tfrac{\varphi_1}{2})\, \mathcal{F}_3 - \sin(\tfrac{\varphi_1}{2})\, \mathcal{F}_4\right) \\
q_1 &= \mathcal{F}_1 \left(\sin(\tfrac{\varphi_1}{2})\, \mathcal{F}_3 + \cos(\tfrac{\varphi_1}{2})\, \mathcal{F}_4\right) \\
q_2 &= \mathcal{F}_2 \left(\cos(\tfrac{\varphi_1}{2})\, \mathcal{F}_3 + \sin(\tfrac{\varphi_1}{2})\, \mathcal{F}_4\right) \\
q_3 &= \mathcal{F}_2 \left(\sin(\tfrac{\varphi_1}{2})\, \mathcal{F}_3 - \cos(\tfrac{\varphi_1}{2})\, \mathcal{F}_4\right)
\end{aligned} \tag{4.50}$$

where

$$\varphi_1 = \tfrac{M}{J_1} t + \kappa \Pi(n; \vartheta | \, m) + D,$$

$$\begin{aligned}
\mathcal{F}_1 &= \mathcal{S}_1 \sqrt{\tfrac{1+x(t)}{2}}, \\
\mathcal{F}_2 &= \mathcal{S}_2 \sqrt{\tfrac{1-x(t)}{2}}, \\
\mathcal{F}_3 &= \mathcal{S}_3 \tfrac{1}{\sqrt{1+y^\star(t)^2}}, \\
\mathcal{F}_4 &= \mathcal{S}_4 \tfrac{y^\star(t)}{\sqrt{1+y^\star(t)^2}},
\end{aligned} \tag{4.51}$$

$$\mathcal{S}_i = \pm 1, \ \textit{for } i = 1, 2, 3, 4,$$

$$y^\star(t) = \tfrac{y(t)}{1+\sqrt{1+y(t)^2}},$$

$$x(t) = \tfrac{J_1 \omega_1}{M},$$

$$y(t) = \tfrac{J_2 \omega_2}{J_3 \omega_3}.$$

where $\Pi(n;\vartheta|\,m)$ *is the incomplete elliptic integral of the third kind with*

$$\begin{aligned} n &= s_1/M^2 \\ f(t) &= \pm\sqrt{s_2\alpha}\; t + C_{11} \\ m &= s_1/s_2 \\ \vartheta &= \mathrm{am}(f(t), m) \\ \kappa &= \pm\left(2HJ_1 - M^2\right) / \left(MJ_1\sqrt{s_2\alpha}\right) \end{aligned} \tag{4.52}$$

when $\mid s_1/s_2 \mid \leq 1$. *When* $\mid s_1/s_2 \mid > 1$ *the Jacobi real transform is applied [77], giving:*

$$\begin{aligned} n &= s_2/M^2 \\ f(t) &= \pm\sqrt{s_1\alpha}\; t + \sqrt{\tfrac{s_1}{s_2}}C_{11} \\ m &= s_2/s_1 \\ \vartheta &= \mathrm{am}(f(t), m) \\ \kappa &= \pm\left(2HJ_1 - M^2\right) / \left(MJ_1\sqrt{s_1\alpha}\right) \end{aligned} \tag{4.53}$$

where D *is a constant of integration and* $\omega_1, \omega_2, \omega_3$ *are the free rigid body angular velocities.*

The analytical expressions for the quaternions are subject to the given boundary conditions $\bar{q}(0) = [1 \quad 0 \quad 0 \quad 0]^T$ *and* $\bar{q}(T)$.

Proof. For an asymmetric spacecraft with principal inertias J_1, J_2 and J_3, the general extremal differential equations are given by (4.16). In this section the derivation is given for λ_1. The derivations for λ_2 and λ_3 follow a similar procedure, and the general case will subsequently be detailed.

Squaring the expression for $\dot{\lambda}_1$ in (4.16) yields:

$$\dot{\lambda}_1^2 = \lambda_2^2\lambda_3^2(\frac{1}{J_3} - \frac{1}{J_2})^2 \tag{4.54}$$

Rearranging the expressions for the Hamiltonian (4.14) and Casimir (4.15) results in

the following equations:

$$\begin{aligned}\lambda_2^2 &= \frac{J_2(2J_3H^*-M^2+\lambda_1^2-\frac{J_3\lambda_1^2}{J_1})}{J_3-J_2}\\ \lambda_3^2 &= \frac{J_3(2J_2H^*-M^2+\lambda_1^2-\frac{J_2\lambda_1^2}{J_1})}{J_2-J_3}\end{aligned} \tag{4.55}$$

Substituting (4.55) into (4.54) and simplifying yields:

$$\dot{\lambda}_1^2 = \alpha\lambda_1^4 + \beta\lambda_1^2 + \chi \tag{4.56}$$

where

$$\begin{aligned}\alpha &= -\frac{(J_1-J_2)(J_1-J_3)}{J_1^2J_2J_3}\\ \beta &= \frac{4J_2J_3H^*-2J_1(J_2+J_3)H^*+2J_1M^2-(J_2+J_3)M^2}{J_1J_2J_3}\\ \chi &= -\frac{\left(2J_2H^*-M^2\right)\left(2J_3H^*-M^2\right)}{J_2J_3}\end{aligned} \tag{4.57}$$

Equation (4.57) can be rewritten as

$$\dot{\lambda}_1^2 = \alpha(s_1-\lambda_1^2)(s_2-\lambda_1^2) \tag{4.58}$$

where

$$s_1 = \frac{-\beta+\sqrt{\beta^2-4\alpha\chi}}{2\alpha} \quad s_2 = \frac{-\beta-\sqrt{\beta^2-4\alpha\chi}}{2\alpha} \tag{4.59}$$

Rearranging (4.58) results in the integral

$$\int_0^t dt = \int_{\lambda_1(0)}^{\lambda_1(t)} \frac{d\lambda_1}{\sqrt{\alpha(s_1-\lambda_1^2)(s_2-\lambda_1^2)}} \tag{4.60}$$

In a similar manner to the unit speed wheeled robot case, a change in variable is introduced via the expression

$$\lambda_1 = \sqrt{s_1}\,\mathrm{sn}(u,m) \tag{4.61}$$

where $m = \frac{s_1}{s_2}$. Differentiating (4.61) with respect to u gives:

$$d\lambda_1 = \sqrt{s_1}\,\mathrm{cn}(u,m)\,\mathrm{dn}(u,m)du \tag{4.62}$$

Then, substituting (4.61) and (4.62) into (4.60) yields:

$$\int_0^t dt = \int_{u_1}^{u_2} \frac{\sqrt{s_1}\,\mathrm{cn}(u,m)\,\mathrm{dn}(u,m)}{\sqrt{\alpha}\sqrt{s_1 s_2 - s_1^2\,\mathrm{sn}^2(u,m) - s_1 s_2\,\mathrm{sn}^2(u,m) + s_1^2\,\mathrm{sn}^4(u,m)}} du \tag{4.63}$$

where

$$\begin{aligned} u_1 &= \mathrm{sn}^{-1}(\tfrac{\lambda_1(0)}{\sqrt{s_1}}, m) \\ u_2 &= \mathrm{sn}^{-1}(\tfrac{\lambda_1(t)}{\sqrt{s_1}}, m) \end{aligned} \tag{4.64}$$

With some manipulation equation (4.63) reduces to

$$\int_0^t dt = \int_{u_1}^{u_2} \frac{1}{\sqrt{\alpha s_2}} du \tag{4.65}$$

Integrating and rearranging leads to an equation for λ_1:

$$\lambda_1 = \sqrt{s_1}\,\mathrm{sn}(\sqrt{\alpha s_2}t + C_1, m) \tag{4.66}$$

where the constant of integration C_1 is given by:

$$C_1 = \mathrm{sn}^{-1}\left(\frac{J_1\omega_1(0)}{\sqrt{s_1}}, \frac{s_1}{s_2}\right) \tag{4.67}$$

It then follows from (4.13), where $\omega_1 = \lambda_1/J_1$, that the free rigid body angular velocities ω_i can be generally expressed in the analytic form:

$$\omega_i = \frac{\sqrt{s_i}}{J_i}\,\mathrm{sn}\left(\pm\sqrt{\alpha s_j}t + C_i, \frac{s_i}{s_j}\right) \tag{4.68}$$

when

$$|\ \frac{s_i}{s_j}\ | \leq 1$$

or

$$\omega_i = \frac{\sqrt{s_j}}{J_i}\,\mathrm{sn}\left(\pm\sqrt{\alpha s_i}t + \sqrt{\frac{s_i}{s_j}}C_i, \frac{s_j}{s_i}\right) \tag{4.69}$$

otherwise by application of the Jacobi real transformation. The constants C_i are defined

by

$$C_i = \mathrm{sn}^{-1}\left(\frac{J_i\omega_i(0)}{\sqrt{s_i}}, \frac{s_i}{s_j}\right) \tag{4.70}$$

with

$$s_i = \frac{-\beta + \sqrt{\beta^2 - 4\alpha\chi}}{2\alpha} \quad s_j = \frac{-\beta - \sqrt{\beta^2 - 4\alpha\chi}}{2\alpha} \tag{4.71}$$

and

$$\begin{aligned} \alpha &= -\tfrac{(J_i - J_j)(J_i - J_k)}{J_i^2 J_j J_k} \\ \beta &= \tfrac{4J_jJ_kH - 2J_i(J_j+J_k)H + 2J_iM^2 - (J_j+J_k)M^2}{J_iJ_jJ_k} \\ \chi &= -\tfrac{\left(2J_jH - M^2\right)\left(2J_kH - M^2\right)}{J_jJ_k} \end{aligned} \tag{4.72}$$

where the indexes do not represent a sum; i, j and k follow a "cyclic permutation", which means they appear in a consecutive recursion (e.g. i=1, j=2, k=3 or i=2, j=3, k=1 etc. ...) See [109]. These expressions (4.68) are the equations for the free motion of an asymmetric body [109, 110]. Substituting these expressions into (4.18) and then into (4.25), and pulling the solution back to the identity via (4.36) yields the solution on $SU(2)$. Using the isomorphism (2.20) gives the expressions for the evolution of the quaternions in the asymmetric case. See [111].

Remark 3. *The sign $\pm$ in (4.68) is dependent on the initial conditions. For implementation the sign has to be chosen so that the sign of the first derivative of (4.68) at the initial time $t = 0$:*

$$\dot{\omega}_i(0) = \pm\sqrt{\alpha s_j}\frac{\sqrt{s_i}}{J_i}\,\mathrm{cn}\left(C_i, \frac{s_i}{s_j}\right)\mathrm{dn}\left(C_i, \frac{s_i}{s_j}\right) \tag{4.73}$$

is matched to the sign of the Euler equations (4.2), with zero external torques, at $t = 0$.

Remark 4. *The $\mathcal{S}_i$ functions are sign functions. To implement the equations it is enough to consider only $\mathcal{S}_1$ or $\mathcal{S}_2$ and $\mathcal{S}_3$ or $\mathcal{S}_4$ respectively. The sign functions can be set by comparison with the known initial first derivative of the quaternions (2.29).*

4.3 Practical Implementation of the Motion Planning Method

With the analytical equations for the free motion of an axisymmetric and an asymmetric rigid body derived in quaternion form, a method to utilise these solutions in a motion planning algorithm is now described. This requires the specification of an appropriate cost function and the implementation of some means of optimising the free parameters of the analytical solutions to match the set boundary conditions, as in Chapter 3. Following this, the extension of the method to include any arbitrary initial condition is described before the obstacle avoidance method detailed in Chapter 3 is adapted and applied to the natural motion planning method to yield simple constrained manoeuvres.

4.3.1 Parametric Optimisation

In order to utilise the analytical expressions for the angular velocities and the globally defined quaternions for motion planning, the equations were entered into a computational software programme. A cost function of the form

$$\min_{\bar{\omega}(0)}\{||\ (\bar{q} - \bar{q}(T))\ ||\} \tag{4.74}$$

was constructed, where $\bar{\omega}(0)$ are the initial angular velocities, $\bar{q}$ is the current quaternion value, $\bar{q}(T)$ is the target quaternion at time $t = T$ and T is the manoeuvre time. This cost function minimises the norm of the error between the current quaternion and the target quaternion by changing the initial angular velocities. It follows that a parametric optimisation can be carried out to find the values of the initial angular velocities $\bar{\omega}(0)$ required to bring the spacecraft to the target $\bar{q}(T)$ in a fixed time.

A stochastic functional minimisation method was used for the parametric optimisation as it proved the most effective at minimising the final pointing error in comparison to the other available solvers such as genetic algorithm and direct search "simplex" methods. This method was chosen in order to assess the suitability of using the nat-

ural motions of the rigid body as the basis for designing attitude motions. A deeper investigation would be required to identify the most suitable method of determining the required initial angular velocities if the references were to be generated on-board a nano-spacecraft. However, this is outwith the scope of this thesis.

The optimal values of the initial angular velocities, $\bar{\omega}^*(0)$, resulting from the optimisation can then be input into the analytical equations for the angular velocities and quaternions to generate the reference tracks for a natural motion manoeuvre.

4.3.2 Specifying Initial Conditions

The analytical quaternions stated in Section 4.2 are valid only for manoeuvres starting from $\bar{q}(0) = [1 \quad 0 \quad 0 \quad 0]^T$. In order to generate manoeuvres from any arbitrary initial condition, the following procedure is implemented at the motion planning stage.

Denote the fixed initial quaternions of the analytical expressions as $\bar{q}_{mpi} = [1 \quad 0 \quad 0 \quad 0]^T$. Then, rewriting (2.15) as

$$R(t) = \begin{pmatrix} q_0 + iq_1 & q_2 + iq_3 \\ -q_2 + iq_3 & q_0 - iq_1 \end{pmatrix} \tag{4.75}$$

the actual initial quaternions, $\bar{q}_{ai}$, and the actual final quaternions, $\bar{q}_{af}$, are substituted into (4.75) to generate two rotation matrices R_{m2a} and R_{af} on $SU(2)$. These rotation matrices can be manipulated to yield the following rotation matrix on $SU(2)$:

$$R_{mpf} = R_{m2a}^{-1} R_{af} \tag{4.76}$$

Using the isomorphism (2.20) for R_{mpf} yields the final motion planner quaternions $\bar{q}_{mpf}$. These boundary conditions are then input into the parametric optimisation as described in Section 4.3.1 to generate a manoeuvre from $\bar{q}_{mpi}$ to $\bar{q}_{mpf}$. The quaternion reference tracks resulting from the optimisation are substituted into (4.75) to yield the rotation matrix R_{mpq} and then rotated back to the actual desired quaternion reference

tracks via

$$R_{aq} = R_{m2a} R_{mpq} \tag{4.77}$$

The isomorphism (2.20) is used to map R_{aq} to the desired quaternion reference tracks from $\bar{q}_{ai}$ to $\bar{q}_{af}$.

4.3.3 Extension to Constrained Repointing

Often a spacecraft is required to perform a constrained slew: that is, to repoint while avoiding or tracking certain objects. For example camera lenses can be damaged if they are pointed directly at a bright object such as the Sun or the Earth's Moon, while in contrast for power generation purposes it may be necessary to maintain a certain minimum angle between a solar array and the Sun throughout a manoeuvre. To achieve such constrained slews, the obstacle avoidance method detailed in Section 3.3.2 is adapted to the rigid body spacecraft of this chapter. Therefore by probing the set of the natural motions which satisfy the boundary conditions on the final orientation of the spacecraft, $\bar{q}(T)$, the parametric optimisation method of Section 4.3.1 is extended to achieve such constrained slews.

Assuming that a camera is mounted along the spacecraft body x-axis, a bright object such as the Sun creates a "cone" which the x-axis unit vector must not intercept during a repointing manoeuvre. This constraint can be formalised as [43]

$$\delta_p \triangleq \arccos(\hat{n}_p \cdot \hat{n}_c) > \delta_c \tag{4.78}$$

That is, the angle δ_p between the unit vectors of the spacecraft body x-axis, $\hat{n}_p$, and the centreline of the cone, $\hat{n}_c$, must be greater than the half-angle of the cone δ_c throughout the manoeuvre.

Given the proposed method outlined above in Section 4.3.1, without a constraint on the pointing direction the parametric optimisation will return the optimal initial angular velocities ${\omega_1}^*(0), {\omega_2}^*(0), {\omega_3}^*(0)$. In the case that this returns a motion that intersects a forbidden region ($\delta_p \leq \delta_c$ for any $t \in [0, T]$) the parameters p_1, p_2, p_3 are introduced

as increments to the angular velocities ${\omega_1}^*(0), {\omega_2}^*(0), {\omega_3}^*(0)$, where $-\epsilon < p_1, p_2, p_3 < \epsilon$ and ϵ is a parameter which can be tuned. Then the objective function

$$\min_{p_1,p_2,p_3} \{|| \left(\bar{q} - \bar{q}(T)\right) ||\} \tag{4.79}$$

is optimised to find an alternative natural motion manoeuvre from $\bar{q}$ to $\bar{q}(T)$. The parameter ϵ is then incremented iteratively to obtain a solution such that $\delta_p > \delta_c \forall t$. This leads to a new set of initial angular velocities ${\omega_1}^{**}(0) = {\omega_1}^*(0) + p_1, {\omega_2}^{**}(0) = {\omega_2}^*(0) + p_2, {\omega_3}^{**}(0) = {\omega_3}^*(0) + p_3$ being obtained, which bring the spacecraft from $\bar{q}$ to $\bar{q}(T)$ with $\delta_p > \delta_c \forall t$. These angular velocities can then be input into the analytical expressions for the angular velocities and quaternions to generate reference tracks for the constrained natural motion manoeuvre.

4.4 Natural Motion Planning Simulations

The natural motion planning method described above was tested in simulation to assess the strengths and limitations of the method. As proportional-derivative (PD) controllers are the most commonly used means of carrying out repointing manoeuvres due to their simplicity and ease of gain tuning, a PD controller [93, 96] was chosen as a benchmark:

$$\bar{u} = \ -K_\omega \bar{\omega}_e - K_q \bar{q}_e \tag{4.80}$$

In this expression $\bar{u}$ is the desired control signal and $K_\omega = k_\omega J$ and $K_q = k_q J$ are constant gain matrices. The gains are multiplied by the inertia matrix so that the gains are proportionally higher on the axes with higher moments of inertia, simplifying the gain tuning process such that only two parameters need to be tuned. The angular

velocity error is given by $\bar{\omega}_e = \bar{\omega} - \bar{\omega}_d$, and the quaternion error by

$$\bar{q}_e = \begin{bmatrix} q_{0d} & q_{1d} & q_{2d} & q_{3d} \\ -q_{1d} & q_{0d} & q_{3d} & -q_{2d} \\ -q_{2d} & -q_{3d} & q_{0d} & q_{1d} \\ -q_{3d} & q_{2d} & -q_{1d} & q_{0d} \end{bmatrix} \bar{q} \tag{4.81}$$

where $\bar{\omega}_d$ and $\bar{q}_d$ are the desired angular velocities and quaternions at time t. Only the vector part of the error quaternion $\bar{q}_e$ (i.e. q_{1e}, q_{2e}, q_{3e}) is used in tracking. Note that a gyroscopic term is often added to the proportional-derivative controller of Equation (4.80). However, for axisymmetric and slightly asymmetric spacecraft, and long, slow manoeuvres, this term has negligible effect and so is omitted here [88, 97]. Given the control signal (4.80), the reaction wheels supply a torque $\bar{N}_w = \underset{N_{w(max)}}{sat}\{\bar{u}\}$, where $N_{w(max)}$ is the maximum available torque in each axis.

As the natural motion references are not inherently rest-to-rest, the manoeuvre is planned such that the references bring the spacecraft to the target in time $(T - \tau)$, where τ is a small period of time. At time $(T - \tau)$ until the end of the manoeuvre at time T, a stabilising control is applied to bring the spacecraft to rest at the target. The manoeuvre can be summarised as:

$$\begin{aligned} For \quad t = [0, T-\tau) \quad \bar{\omega}_d &= \bar{\omega}_{ref} \\ \bar{q}_d &= \bar{q}_{ref} \\ For \quad t = [T-\tau, T] \quad \bar{\omega}_d &= 0 \\ \bar{q}_d &= \bar{q}(T) \end{aligned} \tag{4.82}$$

where the subscript "ref" refers to the natural motion reference tracks generated using parametric optimisation, and τ is the length of time the stabilising control is applied. In the following simulations, a value of $\tau = 20\,\mathrm{s}$ is utilised as this was found to be the shortest time required to bring the spacecraft to rest at the target attitude. When quaternion feedback is being considered, $\bar{q}_d$ does not vary and is the final desired attitude i.e. $\bar{q}_d = \bar{q}(T) \forall t$. Equation (4.80) then describes a conventional quaternion

feedback controller.

The performance of the natural motion tracking is assessed in comparison to the benchmark quaternion feedback controller in terms of the accumulated torque [96] of the reaction wheels. That is, the integral of the norm of the control torque vector, given the symbol I_N. The accumulated torque is used as an indication of the control effort required to carry out the manoeuvre, with lower control effort especially important for small spacecraft due to their limited power and actuation.

For the quaternion feedback and natural motion manoeuvres the gains were adjusted until the final pointing and velocity constraints were satisfied, to 4 decimal places, with the lowest accumulated torque. In the case of the natural motions the gains were tuned using an iterative process. The gains for quaternion feedback were initially tuned using an iterative process and then, to ensure the fairest comparison between the natural motions and quaternion feedback, the quaternion feedback gains were further tuned by using a genetic algorithm method. A cost function consisting of the angular velocity and quaternion errors at time T and the total accumulated torque of the manoeuvre was constructed. The optimisation process was repeated until the gains which yielded the lowest accumulated torque while matching the desired boundary conditions were found.

A 600 km altitude circular orbit beginning at the vernal equinox position is utilised in all simulations unless it is stated otherwise.

4.4.1 Axisymmetric Case: Example Manoeuvres

The performance of the axisymmetric natural motions was assessed via comparison with a quaternion feedback benchmark for a spacecraft with principal inertias $J_1 = 0.0109\,\text{kgm}^2$ and $J_2 = J_3 = 0.05\,\text{kgm}^2$. A manoeuvre was carried out from $\bar{q}(0) = [1 \quad 0 \quad 0 \quad 0]^T$ to $\bar{q}(T) = [0.5 \quad 0.5 \quad 0.5 \quad 0.5]^T$ in a time of $T = 120\,\text{s}$. The gains used in the simulation were $k_\omega = 0.2095$ and $k_q = 0.0222$ for quaternion feedback, and $k_\omega = 1.81$ and $k_q = 0.83$ for the natural motions. The results are shown in Figures 4.3,

4.4 and 4.5 for quaternion feedback and Figures 4.6, 4.7 and 4.8 for the natural motion tracking.

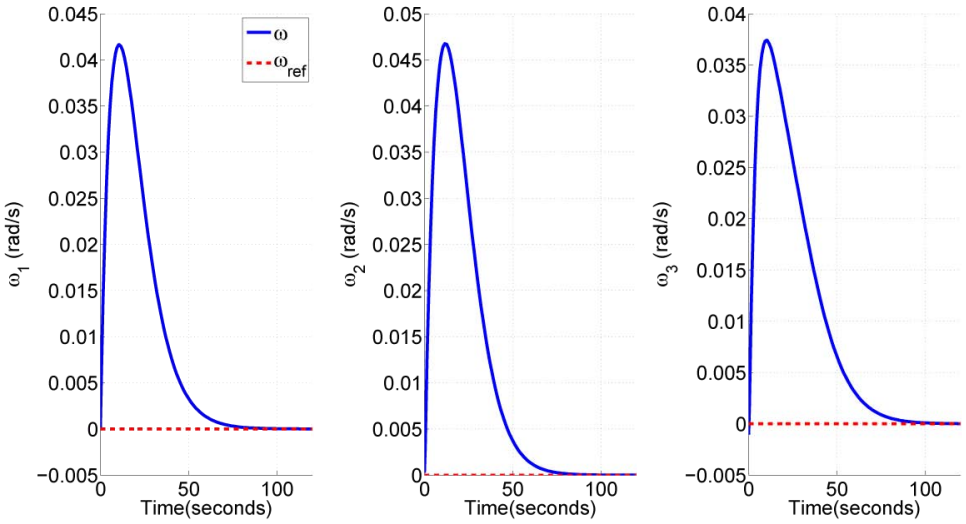

Figure 4.3: Angular velocities during quaternion feedback manoeuvre for axisymmetric spacecraft for Manoeuvre NM-A.

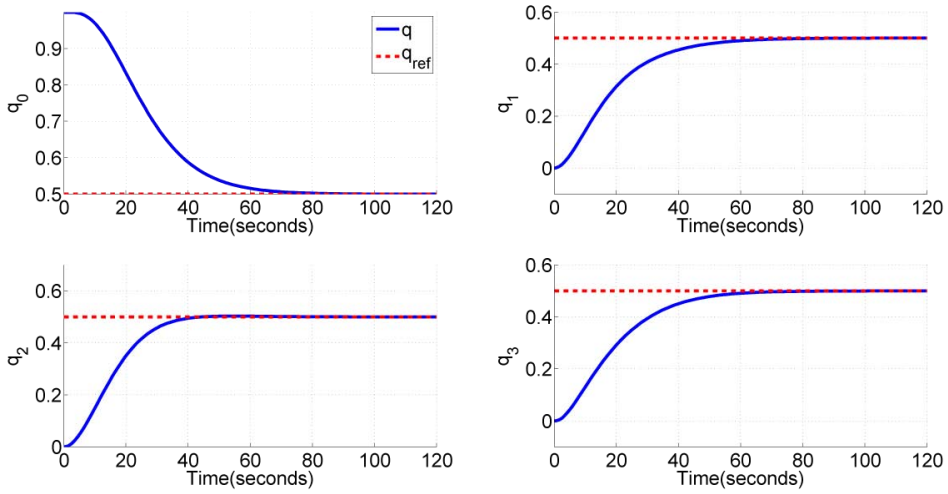

Figure 4.4: Quaternions during quaternion feedback for axisymmetric spacecraft for Manoeuvre NM-A.

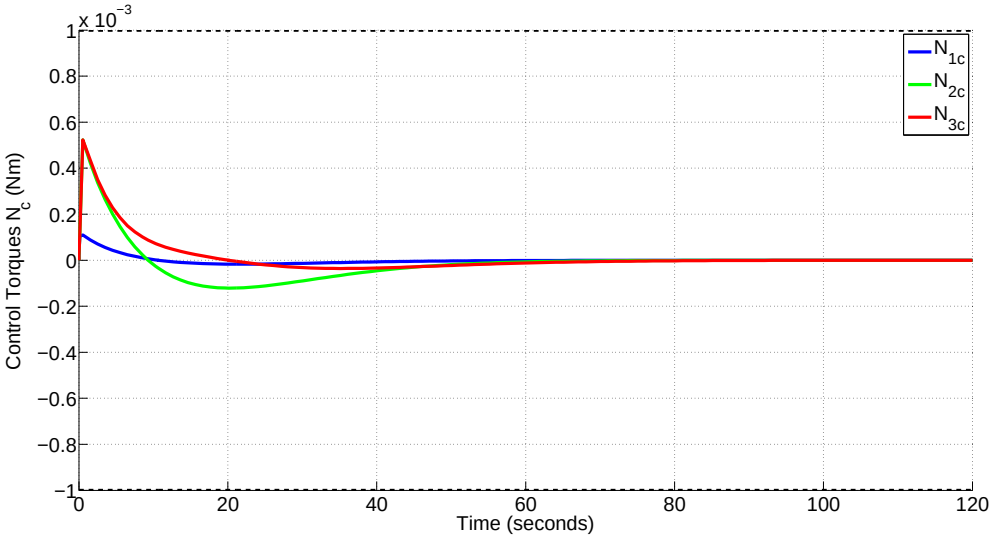

Figure 4.5: Control torques during quaternion feedback manoeuvre for axisymmetric spacecraft for Manoeuvre NM-A.

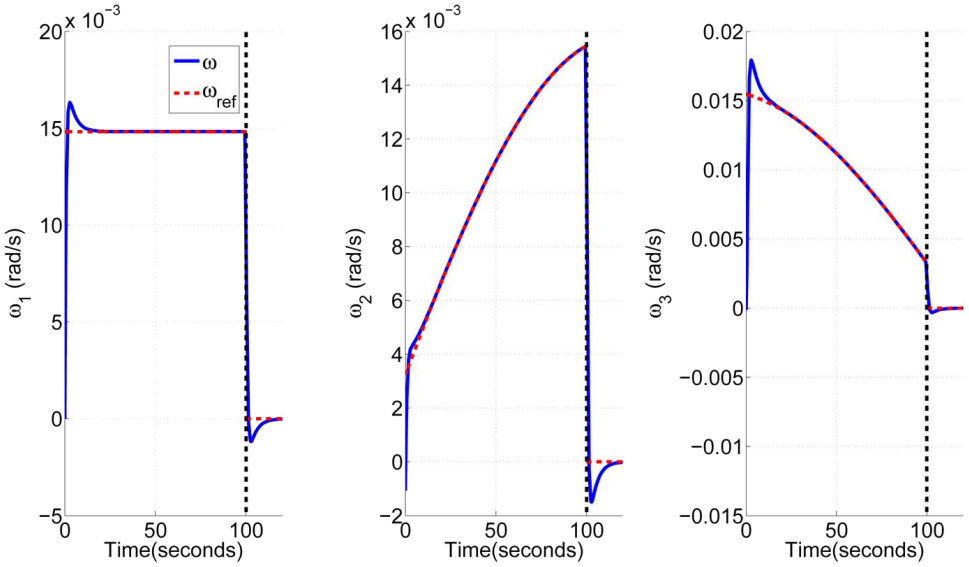

Figure 4.6: Angular velocities during natural motion manoeuvre for axisymmetric spacecraft for Manoeuvre NM-A.

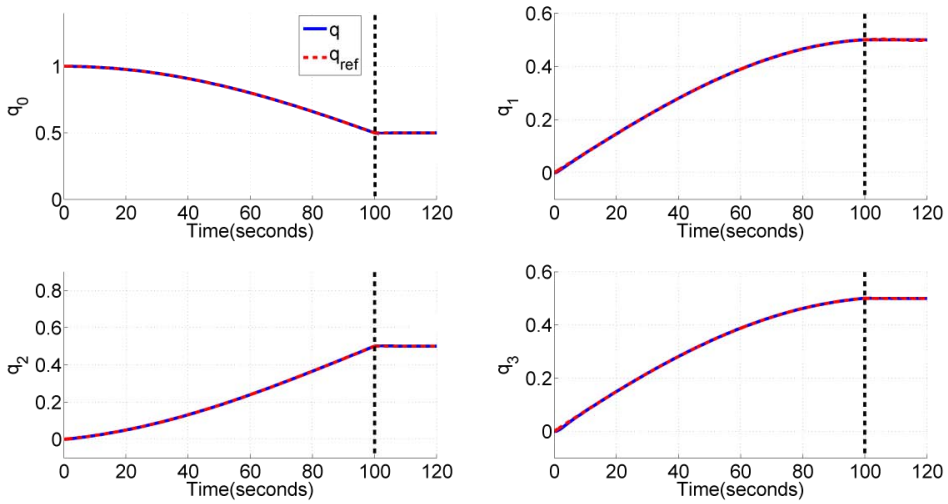

Figure 4.7: Quaternions during natural motion manoeuvre for axisymmetric spacecraft for Manoeuvre NM-A.

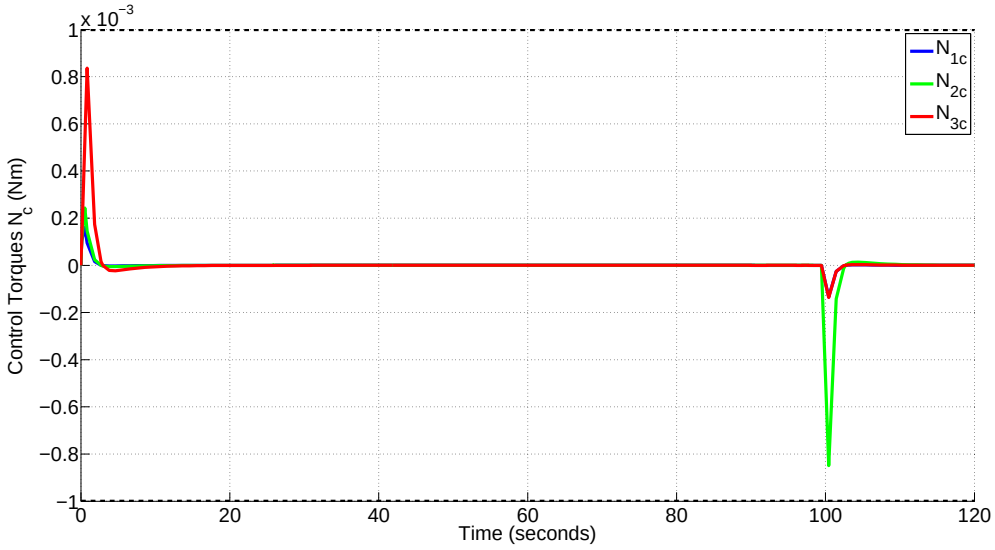

Figure 4.8: Control torques during natural motion manoeuvre for axisymmetric spacecraft for Manoeuvre NM-A.

It is clear that the natural motion tracking approach is essentially "bang-off-bang" in nature. Initial torques bring the spacecraft angular velocities to those required to perform a natural motion. This is then followed by a "coasting phase" of zero or near zero

torque (a small torque is often applied to compensate for disturbances) as the spacecraft moves toward the target attitude. When the target attitude is achieved at time $(T-\tau)$, the angular velocity references are then switched to stabilise the spacecraft at the target. This results in a final torquing phase to bring the spacecraft to rest at the target, the start of which is indicated by a dotted vertical line in the figures. In contrast note that the quaternion feedback controller, which tracks a constant rather than time varying reference, results in the quaternions following broadly sigmoidal paths during the manoeuvre.

Tables 4.3 and 4.4 summarise the results of this and several other manoeuvres. The superscripts "$Q.F.$" and "$N.M(Axi)$" refer to quaternion feedback and the axisymmetric natural motion manoeuvres respectively.

Table 4.3: Labelling of attitude manoeuvres for axisymmetric nanospacecraft

Manoeuvre	Initial quaternion	Final quaternion
NM-A	$\bar{q}(0) = [1 \quad 0 \quad 0 \quad 0]^T$	$\bar{q}(T) = [0.5 \quad 0.5 \quad 0.5 \quad 0.5]^T$
NM-B	$\bar{q}(0) = [-0.124 \quad 0.705 \quad 0.698 \quad 0.039]^T$	$\bar{q}(T) = [-0.768 \quad 0.557 \quad -0.0815 \quad -0.307]^T$
NM-C	$\bar{q}(0) = [-0.563 \quad 0.018 \quad 0.446 \quad 0.695]^T$	$\bar{q}(T) = [-0.596 \quad 0.65 \quad 0.371 \quad 0.29]^T$
NM-D	$\bar{q}(0) = [-0.202 \quad -0.811 \quad -0.151 \quad 0.528]^T$	$\bar{q}(T) = [-0.059 \quad -0.349 \quad -0.767 \quad -0.535]^T$
NM-E	$\bar{q}(0) = [0.588 \quad 0.749 \quad 0.098 \quad -0.289]^T$	$\bar{q}(T) = [0.484 \quad 0.522 \quad -0.561 \quad -0.423]^T$

Table 4.4: Comparison between quaternion feedback and natural motions for axisymmetric spacecraft. $T = 120\,\mathrm{s}$.

Manoeuvre	${I_N}^{Q.F.}$ (Nms)	${I_N}^{N.M(Axi)}$ (Nms)
NM-A	0.0068	0.0025
NM-B	0.0103	0.0014
NM-C	0.0086	0.0013
NM-D	0.0146	0.003
NM-E	0.0046	0.0018

The natural motion tracking offers significant savings in accumulated torque over the more computationally efficient quaternion feedback for a range of manoeuvres. However, the peak torques of the natural motion method are generally slightly higher than those for quaternion feedback. This is a limitation of the natural motion method, as

the maximum torques cannot be specified in the quadratic cost function used to derive the analytical references.

4.4.2 Asymmetric Case: Example Manoeuvres

The motion planner for asymmetric spacecraft was then tested in simulation for a spacecraft with principal inertias $J_1 = 0.0109\,\text{kgm}^2$, $J_2 = 0.0504\,\text{kgm}^2$ and $J_3 = 0.0506\,\text{kgm}^2$. A manoeuvre from $\bar{q}(0) = [0.208 \quad 0.622 \quad 0.431 \quad 0.620]^T$ to $\bar{q}(T) = [1 \quad 0 \quad 0 \quad 0]^T$ in a time of $T = 120\,\text{s}$ is illustrated. The gains used were $k_\omega = 0.194$ and $k_q = 0.01972$ for quaternion feedback, and $k_\omega = 1.8$ and $k_q = 0.86$ for the natural motions. The results are shown in Figures 4.9, 4.10 and 4.11 for quaternion feedback and Figures 4.12, 4.13 and 4.14 for the natural motion tracking.

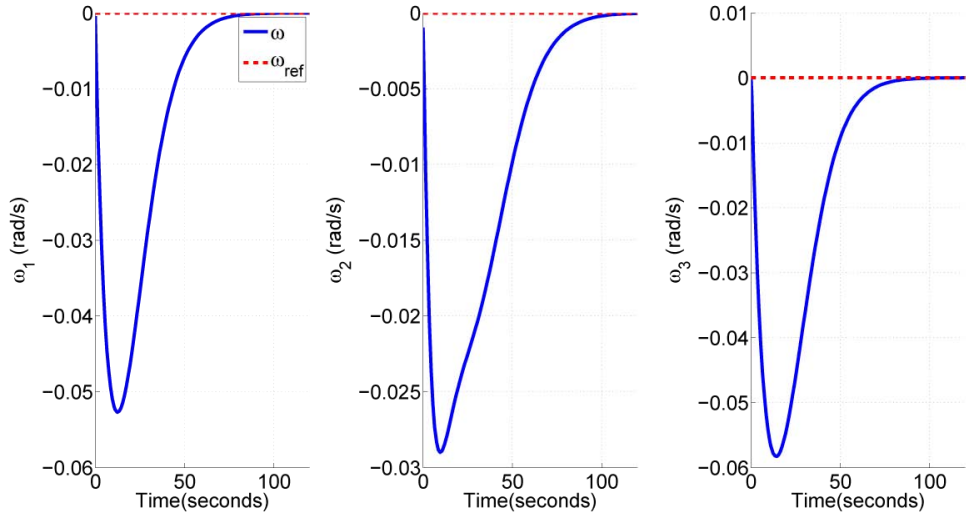

Figure 4.9: Angular velocities during quaternion feedback manoeuvre for asymmetric spacecraft for Manoeuvre NM-F.

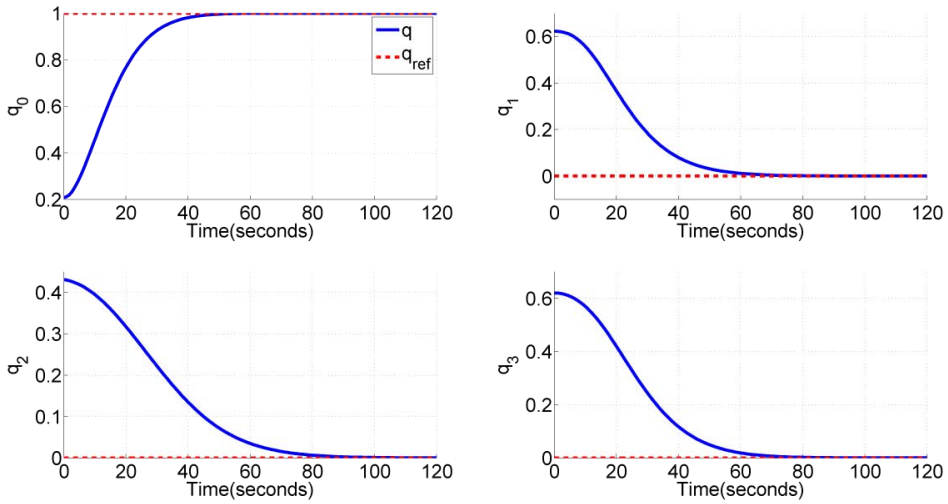

Figure 4.10: Quaternions during quaternion feedback manoeuvre for asymmetric spacecraft for Manoeuvre NM-F.

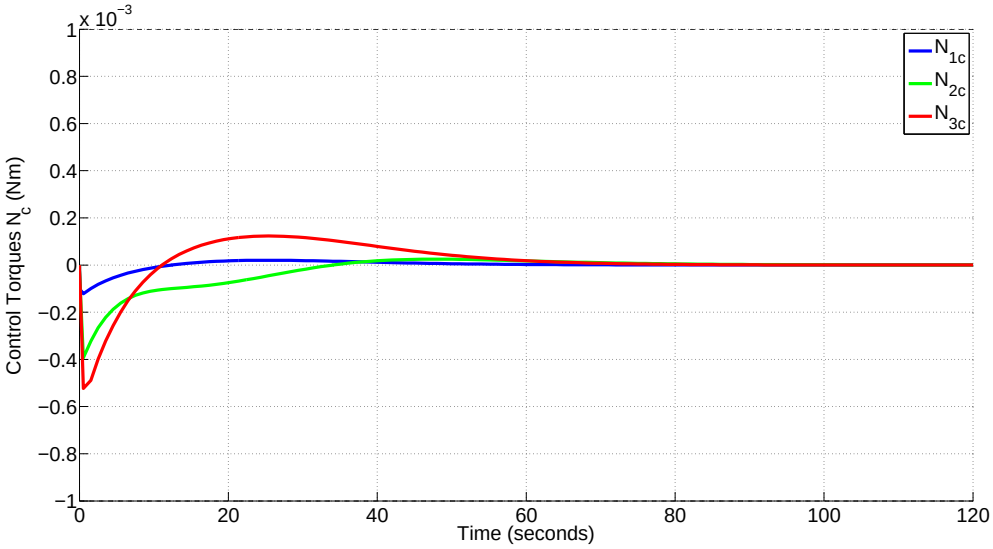

Figure 4.11: Control torques during quaternion feedback manoeuvre for asymmetric spacecraft for Manoeuvre NM-F.

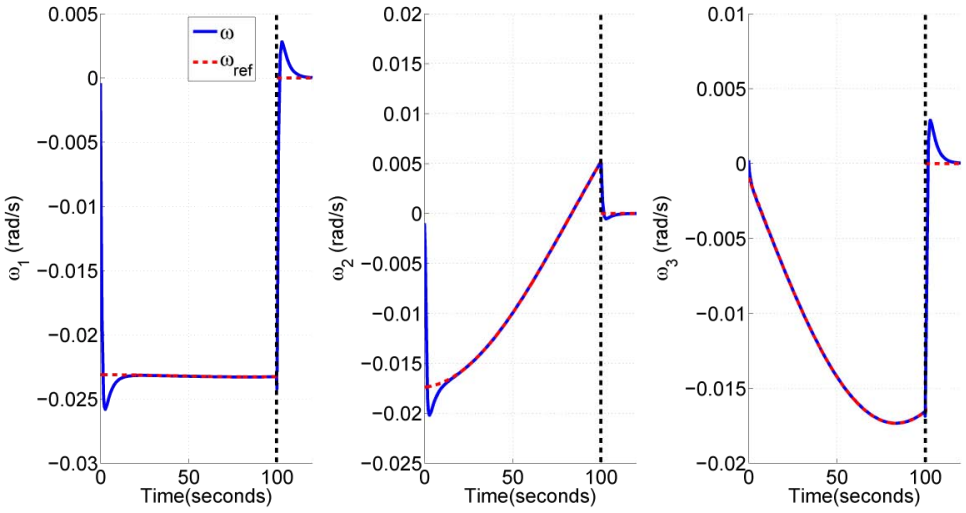

Figure 4.12: Angular velocities during natural motion manoeuvre for asymmetric spacecraft for Manoeuvre NM-F.

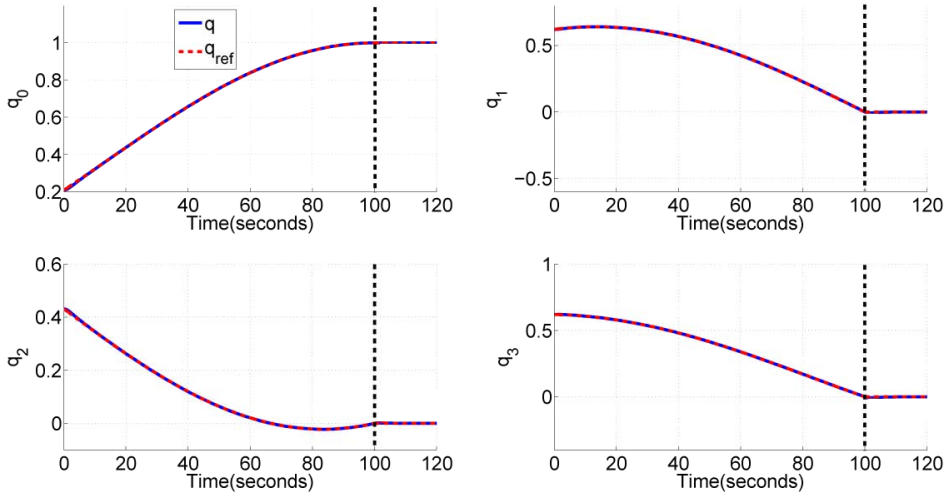

Figure 4.13: Quaternions during natural motion manoeuvre for asymmetric spacecraft for Manoeuvre NM-F.

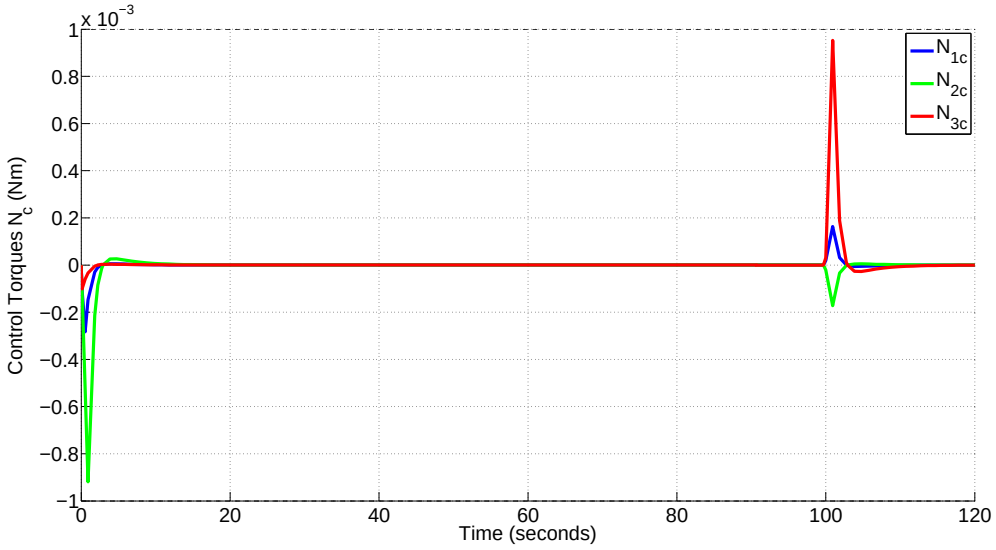

Figure 4.14: Control torques during natural motion manoeuvre for asymmetric spacecraft for Manoeuvre NM-F.

Tables 4.5 and 4.6 summarises the results of this and several other manoeuvres. The superscript "$N.M(Asy)$" refers to the asymmetric natural motion manoeuvre.

Table 4.5: Labelling of attitude manoeuvres for asymmetric nanospacecraft

Manoeuvre	Initial quaternion	Final quaternion
NM-F	$\bar{q}(0) = [0.208 \quad 0.622 \quad 0.431 \quad 0.620]^T$	$\bar{q}(T) = [1 \quad 0 \quad 0 \quad 0]^T$
NM-G	$\bar{q}(0) = [0.049 \quad -0.77 \quad -0.547 \quad 0.32]^T$	$\bar{q}(T) = [0.64 \quad -0.68 \quad -0.34 \quad -0.13]^T$
NM-H	$\bar{q}(0) = [-0.12 \quad 0.76 \quad -0.63 \quad 0.068]^T$	$\bar{q}(T) = [0.44 \quad -0.15 \quad -0.83 \quad 0.32]^T$
NM-I	$\bar{q}(0) = [-0.32 \quad 0.92 \quad -0.18 \quad -0.096]^T$	$\bar{q}(T) = [0.39 \quad 0.62 \quad -0.62 \quad 0.27]^T$
NM-J	$\bar{q}(0) = [0.45 \quad 0.26 \quad -0.38 \quad 0.76]^T$	$\bar{q}(T) = [-0.65 \quad -0.4 \quad -0.43 \quad -0.49]^T$

Table 4.6: Comparison between quaternion feedback and natural motions for slightly asymmetric spacecraft. $T = 120\,\text{s}$.

Manoeuvre	${I_N}^{Q.F.}$ (Nms)	${I_N}^{N.M(Asy)}$ (Nms)
NM-F	0.008	0.0024
NM-G	0.0083	0.0016
NM-H	0.0076	0.0033
NM-I	0.0115	0.0022
NM-J	0.0119	0.0043

It is clear that the natural motion tracking in the asymmetric case once again offers significant savings in accumulated torque over quaternion feedback alone.

4.4.3 Effect of Inertia

While ideally the asymmetric motion planner would be used to plan motions for asymmetric spacecraft, the elliptic functions present in this motion planner result in increased computation times in comparison with the axisymmetric motion planner. This will be discussed in detail in Section 4.5. However, as most Cubesat spacecraft are only slightly asymmetric, it may be possible to use the axisymmetric motion planner in these cases. In this section an assessment is made to determine whether the axisymmetric motion planning method can still offer savings in accumulated torque even as the inertias vary from those of the axisymmetric spacecraft. This also serves as a study of how sensitive the method is to the inertia fluctuations which could arise during a mission (e.g. due to the deployment of solar panels or the jettison of a payload).

The references generated in Section 4.4.1 for the $T = 120\,\text{s}$ manoeuvre NM-A for the axisymmetric spacecraft were applied to several asymmetric spacecraft with inertias ranging from $\pm 0 - 100\%$ difference over the inertias of the axisymmetric spacecraft. In order to determine the effect of the inertia error on the axisymmetric natural motions, references were also generated for each spacecraft configuration using the asymmetric motion planner, and a quaternion feedback benchmark again included for comparison. The results are shown in Table 4.7.

Table 4.7: Effect of varying spacecraft inertia on tracking of axisymmetric references for Manoeuvre NM-A in $T = 120\,\text{s}$.

Principal Inertias (kgm^2)	${I_N}^{N.M(Axi)}$ (Nms)	${I_N}^{N.M(Asy)}$ (Nms)	${I_N}^{Q.F.}$ (Nms)
$J_1 = 0.0109, J_2 = 0.0504, J_3 = 0.0506$	0.0023	0.0022	0.0069
$J_1 = 0.0164, J_2 = 0.075, J_3 = 0.025$	0.0033	0.0018	0.0106
$J_1 = 0.0218, J_2 = 0.1, J_3 = 0.05$	0.0047	0.003	0.0123

It is obvious that the accumulated torque required to track the axisymmetric references increases as the inertia uncertainty increases. This is to be expected as for an asymmetric spacecraft the axisymmetric references do not represent a natural motion, and so torque extra control effort is required to track the references. However, for a slightly asymmetric spacecraft the axisymmetric references require only slightly more torque to track. Therefore in these cases the less computationally intensive axisymmetric motion planner would be the more practical choice. It should also be noted that the natural motion references for the axisymmetric spacecraft outperform quaternion feedback in terms of accumulated torque, even in the presence of considerable inertia error.

4.4.4 Effect of Manoeuvre Time

In this section the effect of manoeuvre time on the natural motion method is investigated. For a manoeuvre from $\bar{q}(0) = [1 \quad 0 \quad 0 \quad 0]^T$ to $\bar{q}(T) = [0.5 \quad 0.5 \quad 0.5 \quad 0.5]^T$, the time is varied from the shortest time quaternion feedback slew which could be performed without momentum saturation of the reaction wheels, 50 s, up to a manoeuvre time of 420 s. The results are shown in Table 4.8.

Table 4.8: Comparison between quaternion feedback and natural motions with varying manoeuvre time for axisymmetric spacecraft manoeuvre for Manoeuvre NM-A.

T (s)	${I_N}^{Q.F.}$ (Nms)	${I_N}^{N.M(Axi)}$ (Nms)	% Saving
50	0.0148	0.0083	44
120	0.0068	0.0022	68
220	0.0061	0.0011	82
420	0.0043	0.00057	87

The % saving is defined as $({I_N}^{Q.F.} - {I_N}^{N.M(Axi)})/{I_N}^{Q.F.} \times 100$. It can be seen that the natural motion method is still advantageous throughout, though the savings in accumulated torque are greater for greater time periods. For shorter time periods the stabilising control discussed in Section 4.4 takes up a greater proportion of the total manoeuvre time. In other words, as manoeuvre time decreases the length of time

which the natural motion references are tracked decreases and the manoeuvres become increasingly similar to conventional quaternion feedback manoeuvres. This accounts for the decrease in % saving for shorter time periods.

4.4.5 Effect of Orbital Altitude, Position and Inclination

Next, the effect of the spacecraft's orbit on the natural motion method was investigated. Disturbance torques such as air drag, solar radiation pressure and gravity gradient are dependent on orbit altitude, while the residual dipole torques are more significant at the poles due to the increased magnetic field strength. As the natural motion method is based around the motion of a rigid body in a disturbance free environment, the method may not be suitable for manoeuvres in a high disturbance environment and so it is important to test the method in these cases.

For an axisymmetric spacecraft on a 300 km altitude orbit beginning at the vernal equinox, a manoeuvre from $\bar{q}(0) = [1 \quad 0 \quad 0 \quad 0]^T$ to $\bar{q}(T) = [0.5 \quad 0.5 \quad 0.5 \quad 0.5]^T$ results in accumulated torques of $I_N = 0.0024\,\text{Nms}$ for the natural motions. This is slightly higher than the $I_N = 0.0022\,\text{Nms}$ obtained for the manoeuvre at 600 km. Therefore in this case the natural motion method is not significantly influenced by the increased air drag and gravity gradient disturbance torques. Testing at a 900 km altitude yielded the same results as for a 600 km altitude, suggesting that the decrease in air drag and gravity gradient torques and the increase in solar radiation pressure torques at higher altitudes has little effect on the manoeuvres. Additionally, beginning the manoeuvre at the poles on a 600 km altitude orbit rather than at the vernal equinox results in a small increase in accumulated torque due to the increased residual dipole disturbance torque, with $I_N = 0.0023\,\text{Nms}$ for the natural motions.

These results show that the variation in disturbance torques caused by varying the orbital parameters has little effect on the accumulated torque of the natural motion method. Therefore it may be possible to effectively switch the control off during the "coasting phase": that is, the section of the manoeuvre between the two main torquing phases. For altitudes less than 600 km this proves infeasible as the increased air drag

torque results in a significant drift from the reference tracks if no control is applied. However, for the 600 km altitude manoeuvre beginning at the vernal equinox described above the control torques during the "coasting phase" can be switched off once the norm of the error between the actual and desired values of angular velocities is less than 1×10^{-4} rad/s, and back on when the error is greater than this value, with no impact on the accumulated torque required or the accuracy of the manoeuvre. In contrast for the manoeuvre near the poles - a slightly higher disturbance environment - applying the same method of switching the control off when $|| \bar{\omega}_e || < 1 \times 10^{-4}$ rad/s, the accuracy of the manoeuvre suffers slightly when the control is switched off during the coasting phase, with a final attitude of $\bar{q}(T) = [0.4999 \quad 0.5001 \quad 0.5001 \quad 0.4998]^T$ achieved. This is as a result of the increased magnetic dipole torque, which means that the drift from the reference tracks is too great to compensate for when the control is switched back on. However, this strategy may still be feasible if a high pointing accuracy is not required.

Therefore, as expected, the natural motions require slightly more accumulated torque to track in lower Earth orbits due to the increased disturbance torques. In contrast in low disturbance environments the control can be switched off during the "coasting phase", resulting in potential savings in computation and power. In these cases the 3-axes natural attitude motions are roughly analogous to the single-axis "bang-off-bang" controls augmented by linear feedback proposed by Sidi [58], in that the control is only switched on near the boundaries of the motion to first achieve the desired angular velocities and then to stabilise the spacecraft at the target attitude.

4.4.6 Constrained Repointing

In this section the method of probing the set of natural motions which satisfy the boundary conditions on the target attitude to generate a constrained repointing manoeuvre is demonstrated.

Consider a 120 s manoeuvre from an initial quaternion $\bar{q}(0) = [1 \quad 0 \quad 0 \quad 0]^T$ to final quaternion $\bar{q}(T) = [-0.45 \quad -0.23 \quad 0.57 \quad 0.65]^T$ for the axisymmetric space-

craft from Section 4.4.1. A star tracker is mounted in the direction of the body x-axis unit vector, $[1 \quad 0 \quad 0]^T$. The centre of the forbidden cone is specified as $n_c = [-0.495 \quad 0.81 \quad 0.317]^T$ and the cone half angle as $\delta_c = 58°$. This corresponds to the Moon cone as defined by Mengali [43]. An initial optimisation to minimise the cost function (4.74) yields a solution which violates this constraint, as shown in Figure 4.15.

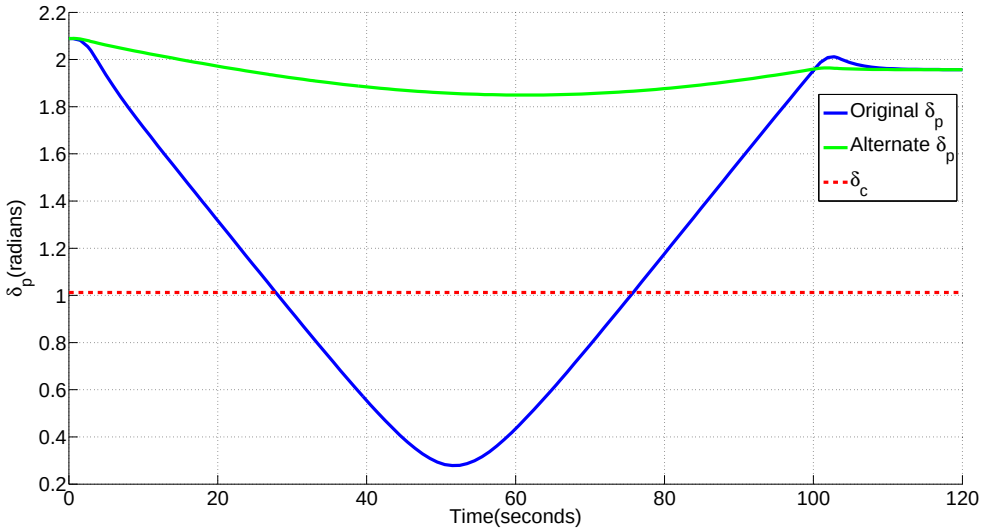

Figure 4.15: Angle between body x-axis and cone centreline unit vectors for manoeuvre from $\bar{q}(0) = [1 \quad 0 \quad 0 \quad 0]^T$ to $\bar{q}(T) = [-0.449 \quad -0.23 \quad 0.566 \quad 0.65]^T$. Original and alternate manoeuvres are shown.

Now, incrementing the angular velocities ${\omega_1}^*(0), {\omega_2}^*(0)$ and ${\omega_3}^*(0)$ by p_1, p_2 and p_3 respectively and performing a further parametric optimisation to minimise the cost function (4.79) leads to an alternate manoeuvre which does not violate the constraint, as shown in Figure 4.15. It is evident that the constraint $\delta_p > \delta_c \forall t$ is respected by the new natural motion and the camera would not pass through the forbidden zone during the manoeuvre. Therefore the natural motion method has been adapted to generate a constrained slew.

4.5 Computational Suitability of the Motion Planning Algorithm

In order for a control or guidance method to be suitable for implementation on-board a nano-spacecraft, the method must be both low torque and computationally efficient. As the natural motion planning method has proven to require significantly less accumulated torque than a quaternion feedback benchmark for a wide range of manoeuvres, the suitability of the method for on-board implementation will now be discussed.

The references were generated in a computational software programme using a 2 GHz, dual-core PC. While this is considerably more powerful than the 30 MHz processor on-board UKube-1, the difference is less marked for other 3U Cubesats such as OPS-SAT which has an 800 MHz dual-core processor. Using a stochastic functional minimisation method to find the globally optimal solution, the axisymmetric references take, on average, 0.17 s to generate. The asymmetric references, however, take between 15 and 20 min to generate using the same software. This is due to the presence of the incomplete Jacobi elliptic integral of the third kind in the analytic expressions for the quaternions (4.50). While mathematically elegant, current computer software finds this Jacobi elliptic integral computationally heavy. As a result, the asymmetric references, despite offering significant fuel savings, are not necessarily any more efficient than using a pseudospectral optimisation method such as PSOpt [112] or a multiple shooting method to produce reference motions. Therefore the asymmetric motion planner is not presently suitable for on-board implementation.

In contrast the generation of the axisymmetric references requires significantly less computation and as shown in Section 4.4.3 these references can be applied to axisymmetric and near axisymmetric spacecraft. However, the method of finding the globally optimal angular velocities via a parametric optimisation means that the axisymmetric natural motions are less computationally efficient than quaternion feedback, where only the final quaternion is tracked. As noted previously, the references are essentially "bang-off-bang" in nature and so provide significant savings in control effort. Furthermore, in low disturbance environments the control can be switched off during the region of

low or zero torque named the "coasting phase", potentially providing savings in power and computation. As a consequence, the reduction in control effort offered by the axisymmetric natural motion method on small spacecraft has to be weighed against the computation required to initially generate the references. While quantifying this trade-off will be the subject of future research, the following section contains a discussion of the relative strengths and weaknesses of another guidance method in artificial potential functions (APFs).

4.5.1 Trade-off Between Computation and Control Effort

While the reliance on quaternion feedback and eigenaxis controllers for attitude manoeuvres makes the generation of time-dependent references for attitude control relatively rare, the use of artificial potential functions [51] has been proposed as a non-optimal guidance method. Artificial potential functions require less computation than the natural motion method as they do not require parametric optimisation; rather they make use of Lyapunov functions to assign an attractive potential to the target orientation, and generate the desired references using inverse methods [51]. Artificial potential functions also provide a simple and effective means of obstacle avoidance. However, in contrast to the natural motion method, the APF method is not inherently low torque and can demand excessive control effort if care is not taken to constrain slew rates and maximum applied torques [52, 53]. In addition, as the manoeuvres are not based around the natural motion of the free rigid body, the references must be tracked throughout and so the artificial potential function method cannot be utilised in a quasi-open loop manner to save on power and computation. Thus the artificial potential functions, in contrast to the natural motion method, require less computation at the expense of a likely increase in control effort. A thorough comparison with the natural motion planning method will be the subject of future work in order to assess this trade-off between computational intensity and control effort.

4.5.2 On-board Implementation

The analytical approach presented in this chapter offers the potential to reduce the torque requirement with respect to using quaternion feedback alone, at the expense of an increase in computation. However, although the motion planning problem is reduced to one of parametric optimisation, further work will be required to assess the most appropriate parametric optimisation method for on-board implementation. Therefore a brief discussion of steps which could be taken to make the natural motion method easier to implement on-board a nano-spacecraft is now undertaken.

As described above, the references were generated on a 2 GHz, dual-core computer using a global parametric optimisation method. However, it may not be feasible to implement a global parametric optimisation method on-board a nano-spacecraft with a processor in the 30 to 800 MHz range. In this case, it may be possible to implement a simple gradient based search method [35] instead. In these methods the search is proportional to the negative of the gradient of the cost function, with the aim of finding a local rather than a global minimum. These methods are computationally more efficient than the stochastic functional minimisation methods used in this chapter, at the expense of only finding a local minimum.

A comparison of a local gradient based method with a global stochastic functional minimisation method for 50 randomly generated manoeuvres found that the performance of the gradient based method was highly dependent on the given initial guess. For example when the solver was given an initial guess of $\bar{\omega}(0) = [0.1 \quad 0.1 \quad 0.1]^T \times 10^{-3}$rad/s, the gradient based method gave the same results as the more computationally intensive global method in approximately 60% of cases. In the remaining 40% of cases, manual tuning of the initial guess resulted in the solvers achieving the same results. Therefore while the gradient based method may require less computation, it is heavily reliant on heuristics in the form of a good initial guess in order to function effectively.

The natural motion references only require the optimal initial angular velocities as inputs. Therefore it may be possible to store the analytical equations for the natural motions on-board the spacecraft, but to perform the necessary parametric optimisation

at the ground station. This would eliminate the need to perform the parametric optimisation on-board the spacecraft and would only necessitate the uploading of the optimal initial angular velocity vector. A problem with this approach is that if manoeuvres could be generated on a powerful computer at a ground station, more computationally intensive methods such as PSOpt could be used instead to generate potentially torque optimal references. However, in these cases it would be necessary to upload the time history of the entire manoeuvre rather than just a simple vector, which would require significantly more bandwith.

It is clear that while planning attitude manoeuvres around the natural motions of a rigid body is beneficial in terms of control effort in comparison to a quaternion feedback benchmark, the reliance on global parametric optimisation methods at present means that more work is required to assess the performance of the method when faced with constraints on processing power, and to determine the most practical reference generation method for on-board implementation.

4.6 Chapter Summary

In this chapter analytical equations of motion for axisymmetric and asymmetric spacecraft were derived using the geometric control framework and utilised to produce natural attitude motions by parametric optimisation. It was shown that the natural motion planning method offers significant savings in accumulated torque over a quaternion feedback benchmark, and the manoeuvres are essentially "bang-off-bang" in nature. The axisymmetric method is robust to errors in inertia and to the effects of disturbances. Indeed, in low disturbance environments the control can be switched off during a "coasting phase" to save on computation, giving rise to quasi open-loop 3-axis "bang-off-bang" manoeuvres. The set of natural motions which match the final attitude can also be probed to produce constrained slews.

Despite the potential savings in accumulated torque, the generation of references in the asymmetric case does not offer an advantage over numerical optimisation for on-

board use due to the difficulty in evaluating the Jacobi elliptic integral, which makes the method computationally heavy. The axisymmetric references, however, require less computation to generate and may be applicable to axisymmetric and near axisymmetric spacecraft such as UKube-1 and OPS-SAT. Nevertheless, the natural motion method requires a parametric optimisation to generate the references, and so further work is required to determine the most suitable method of implementing the method on-board a resource limited nano-spacecraft.

While in this chapter the motions were derived with respect to a dynamic nonholonomic constraint - the conservation of angular momentum - in the proceeding chapter the complexity of the problem is further increased. A large solar sail spacecraft is considered which is subject to a kinematic nonholonomic constraint, where it is constrained to spin at a constant rate around one axis, in addition to the dynamic nonholonomic constraint, environmental effects and hardware constraints considered in this chapter. Analytical equations, derived using the framework of geometric control theory utilised in this and previous chapters, are implemented in a motion planning algorithm and tested in the face of perturbations due to the environment and hardware constraints. The method is additionally applied to the small spacecraft considered in this chapter, to provide a comparison between the motion planning methods.

Chapter 5

Motion Planning and Control of Spin Stabilised Spacecraft

In the previous chapter a natural attitude motion planning method for a rigid spacecraft, subject to a dynamic nonholonomic constraint due to the conservation of angular momentum, was presented and applied in simulation to the repointing of a small spacecraft. In this chapter, the practicality and effectiveness of a geometric motion planning method derived with respect to a kinematic nonholonomic constraint on the spin rate of the spacecraft is assessed via extensive simulation. The motion planning method is primarily applied to a spinning solar sail. While the attitude control of these spacecraft has been studied, motion planning for solar sails has received little attention prior to this study. Solar sails can potentially provide propellantless propulsion and thus enable a wide range of interplanetary missions. However, solar sails are large and flexible which means that their attitude control is non-trivial. As a result a low torque geometric repointing method is applied which limits the angular velocities of the spacecraft and hence limits excitation of the sail structure.

The equations which form the basis of the motion planning method outlined in this chapter were originally derived, using the framework of a kinematic system on the matrix Lie group $SU(2)$ and the integrals of motion of the system, in Biggs and Horri [29]. However, the method was not rigorously tested in simulation, with only basic tracking

of the references illustrated for a micro-spacecraft and no comparison made to other methods. Thus the practicality of the method has not been determined. Furthermore, derivation of the optimal motions in this chapter generalise that in Biggs and Horri and describe a larger class of optimal motions that can be used as a basis for a geometric motion planner. Following this, the analytical motion planning algorithm for a spacecraft constrained to spin at a fixed rate around one axis is used to plan attitude manoeuvres for a spinning solar sail. The effectiveness of the references is assessed, together with the feasibility of tracking the references using current solar sail actuators.

While solar sailing as a concept has existed since the early part of the 20th century, it is only recently that advances in materials research has enabled practical solar sails to be designed and built. Solar sailing has gathered considerable interest as it has the ability to provide continuous, low thrust propulsion without the need for propellant, enabling mission lifetimes to be extended and the creation of previously unattainable orbits. Examples of missions enabled by solar sailing include the GeoSail mission [113, 114], the Solar-Polar Orbiter [115] and the Interstellar Heliopause Mission [116]. However, in the literature on the orbital dynamics of solar sails the attitude control required is often simplified by the assumption that the sail can slew instantaneously or at a certain fixed deg/day rate [32, 33, 115]. Nevertheless, there are a number of challenges associated with solar sails which means that the attitude control required of these missions may be difficult to carry out in practice.

In order to maximise the thrust produced via solar radiation pressure, solar sails are required to have a low mass per unit area [33]. Therefore all solar sail designs generally involve a large area of thin reflective film being held in tension by a light supporting structure [33]. Consequently, solar sails are relatively flexible, with the sail membrane billowing and the sail structure flexing under the influence of solar radiation pressure and control torques. This results in a decrease in performance and controllability. Additionally solar sails have large moments of inertia (typically of the order 10^3 to $10^5\,\mathrm{kgm}^2$), which means that the control torques required to manoeuvre the spacecraft are higher and actuators will subsequently be larger [32], adding to the mass of the spacecraft. Any method of controlling the attitude of the solar sail must be able to

effectively overcome these limitations.

In order to combat the flexibility of the solar sail, reorientation manoeuvres must firstly be slow and smooth to reduce the oscillation of the sail film, with typical manoeuvre times ranging from hours to days [32, 33, 117]. Furthermore, the sail membrane may be stiffened by spinning around the sail normal which results in the membrane being kept taut by the centrifugal effect and a reduction in billowing. However, despite IKAROS, the first solar sail demonstration mission, being of spin type, little research to date has focussed on the practical attitude control of spin stabilised spacecraft. This is perhaps due to the increased control effort required to repoint the spin type solar sails, as the large angular momentum vector generated by the spinning solar sails must be overcome [31]. IKAROS firstly utilises the centrifugal effect during the deployment phase to achieve the desired geometric shape, before maintaining a spin rate of around 1 rpm during normal operations [31]. Mimasu [118] detailed a methodology utilised on IKAROS which alters the spin-rate of the solar sail using cold gas thrusters, enabling the drift of the solar sail attitude to be controlled and so aiding in orbit steering. Wie [32] presented a linearised dynamic model for a spin stabilised spacecraft with a centre of mass, centre of pressure offset, while making clear that further research with a higher fidelity model was necessary. Meanwhile, Gong [119] derived the coupled orbit and attitude stability criterion for a spin stabilised cone-shaped solar sail in a heliocentric orbit.

Nevertheless, despite the advantageous stiffening and resistance to disturbances offered by spin stabilisation, the increase in angular momentum means that control torques for a spin-type sail must be larger than those for a non-spinning sail of equivalent inertia in order to effect a change in attitude. This gyroscopic stiffness, in addition to the large disturbance torques due to solar radiation pressure and gravity gradient [32] which solar sails are subjected to, means that the choice of actuation for spin stabilised solar sails is further complicated. For a non-spinning solar sail in a geocentric orbit, Wie [32] found that maintaining a desired attitude in the face of disturbance torques resulted in momentum saturation of 2 kg reaction wheels. While this problem may be counteracted for non-spinning solar sails in Earth orbits using magnetorquers [32, 120], this

method has not been tested on a spinning solar sail. In heliocentric or interplanetary trajectories magnetorquers cannot be utilised, and another form of desaturation such as thrusters may be necessary if momentum exchange devices such as reaction wheels were to be used as actuators. The impulsive nature of thrusters means that they are less suited for application to solar sails as they may excite the structure of the solar sail, while their mounting location may cause bending of the sail spars [32]. Despite this, cold gas thrusters were the primary form of actuation on-board the first ever solar sail mission to Venus, IKAROS [121, 122], where they were used to control the spin rate of the sail.

Due to these issues with conventional actuation, alternative, propellantless methods for solar sail actuation have been proposed. These include sliding masses [117, 123], electrochromic devices [31] and control vanes [32, 33, 124], the primary form of actuation on-board the upcoming NASA Sunjammer mission [125]. These methods control the offset between the centre of mass and centre of pressure of the spacecraft. The SRP force then acts on the solar sail to produce continuous torques. However, these methods have primarily focussed on non-spin type solar sails; only electrochromic devices have been tested on the spin stabilised IKAROS where they were used to correct a 0.5° degree drift in the Sun angle. The increased control torques required by spinning sails, together with the fact that these methods do not provide full independent 3-axis control, means that they may not be suitable for spinning sails.

This work is motivated both by the need to test the practicality of references derived using geometric control and the need for further research into the attitude control of spin stabilised solar sails, via an extension of the motion planning method derived in [29]. The method is derived through the mechanisms of geometric control theory [17], resulting in globally defined, analytical expressions for the optimal angular velocities and the time evolution of the spinning spacecraft's attitude in quaternion form. These analytical expressions, which minimise both the body rates during the manoeuvre and the control effort required, can then be parametrically optimised, as in Chapters 3 and 4, to meet boundary conditions imposed on the final attitude. The references can then be tracked using a simple proportional-derivative (PD) controller. As stated in Chapter

4, the PD controller is the preferred method of attitude control onboard real spacecraft due to it's simplicity and reliability, and is favoured over more efficient but computationally intensive nonlinear optimisation methods [96, 97]. Therefore by utilising the PD controller alongside the analytical reference motions, a compromise is reached between reliability, optimality and ease of on-board implementation.

Original Contributions

The original contributions in this chapter are outlined as follows:

- The extremals in the general case of the quadratic cost function are derived and found to take the form of Weierstrass elliptic functions. The solution [29] is shown, via phase plane analysis, to be a particular solution of the general case.

- The analytical equations for time evolution of the attitude of a spinning spacecraft in quaternion form derived by Biggs and Horri are implemented in a motion planning algorithm for a spin stabilised solar sail to produce slow, smooth reference tracks via parametric optimisation. Additionally, the method of producing constrained slews for a spacecraft demonstrated in Chapter 4 is adapted to the geometric method of this chapter.

- The resulting reference motions are applied to the repointing of spin stabilised solar sails in heliocentric and geocentric orbits. The strengths and weaknesses of the motion planning method are evaluated in comparison to the tracking of pure spin reference motions, and the method found to produce smaller angular velocities and require lower accumulated torque to track than the pure spin references in the majority of cases. However, in certain cases the pure spin references are able to repoint the solar sail in less than 1250 sec without violating the maximum torque constraints, whereas the geometric spin repointing references cannot. Additionally, for two of the simulated manoeuvres, the pure spin references required lower accumulated torque.

- Based on the results of the simulations, an actuator study is carried out to assess

the feasibility of different actuators for use with the solar sail motion planning method.

- A comparison is made with the natural motion references of Chapter 4 for a small spacecraft.

The chapter is structured as follows. In Section 4.1, the solar sail models utilised in simulation are introduced, detailing the two solar sails under consideration. In Section 4.2, the particular case of the solutions derived by Biggs and Horri [29] is linked to the general solution derived in this thesis via a phase plane analysis. The practical implementation of the particular case of the motion planning method is discussed in Section 4.3, including the extension to constrained slews. Simulation results are presented in Section 4.4 where the geometric spin repointing reference motions are compared to pure spin reference motions tracked using a simple PD controller. An application of the method to the small spacecraft of Chapter 4 is carried out to provide a comparison between the geometric spin repointing and natural motion methods. Finally, the suitability of different actuation methods for tracking the references are considered in Section 5.6, together with a discussion of the feasibility of applying the motion planning method under consideration to the attitude manoeuvring of a spinning solar sail.

5.1 Solar Sail Attitude and Orbit Models

While the solar sail is a flexible structure, in the initial study in this thesis the simplifying assumption is made that the spacecraft can be treated as a rigid body. This assumption is feasible as the spinning sail structure will be stiffened via the centrifugal effect, and the body rates will be minimised to avoid excitation of the flexible structure. The general equations describing the attitude control problem are then that of a rigid body with external forces describing the effect of the actuators and perturbations.

5.1.1 Reference Frame Definitions

Solar sails in orbit around the Earth and the Sun are considered. The reference frames for a spacecraft in a geocentric orbit are defined in Chapter 4, Section 4.1.1. When a heliocentric orbit is considered, the centre of the Sun is chosen as the origin of a Heliocentric Ecliptic reference system [101] with basis vectors $\hat{I}, \hat{J}, \hat{K}$. The X and Y axes lie in the ecliptic plane towards the vernal equinox and winter solstice positions of the Earth respectively, with the Z-axis completing the orthonormal reference frame. This co-ordinate system is shown in Figure 5.1.

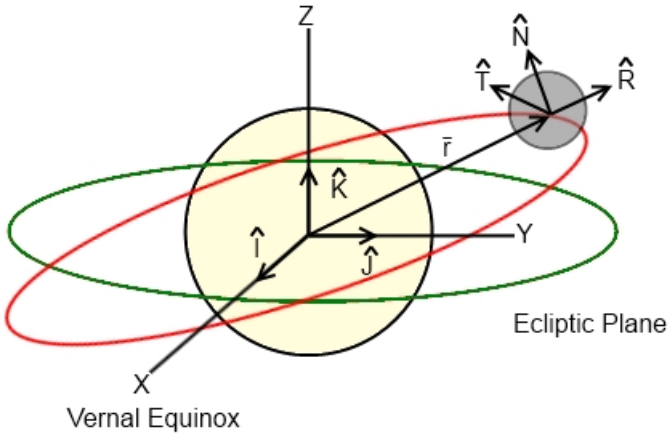

Figure 5.1: Heliocentric Ecliptic and RTN co-ordinate systems for Sun centred sail.

The RTN and BRF frames described in Chapter 4 are again used for the heliocentric sail.

5.1.2 Kinematic Model and Dynamic Models

The attitude kinematics of the spacecraft are parameterised using quaternions, as in Chapter 4. In the case of the solar sail attitude manoeuvres are generally performed in order to repoint the thrust vector of the sail. Therefore the attitude of the body frame of the spacecraft is more practically described with respect to the RTN orbit frame, rather than the inertial frame as in the previous chapter. To accomplish this,

the quaternion equations (2.29) are rewritten in terms of the angular velocity of the body frame with respect to the orbit frame, ω_{bo}, using the relation

$$\bar{\omega}_{bo} = \bar{\omega} - \bar{\omega}_{oi(b)} \tag{5.1}$$

where $\bar{\omega}$ is the absolute angular velocity of the spacecraft in the inertial frame and $\bar{\omega}_{oi(b)}$ is the angular velocity of the orbital frame with respect to the inertial frame, expressed in body frame components. This component can be computed via

$$\bar{\omega}_{oi(b)} = R_{ob}\bar{\omega}_{oi} \tag{5.2}$$

where R_{ob} is the quaternion rotation matrix from the orbit frame to the body frame in quaternion components with elements [32, 58]

$$R_{ob} = \begin{bmatrix} 1-2(q_{2bo}^2+q_{3bo}^2) & 2(q_{1bo}q_{2bo}+q_{3bo}q_{0bo}) & 2(q_{1bo}q_{3bo}-q_{2bo}q_{0bo}) \\ 2(q_{1bo}q_{2bo}-q_{3bo}q_{0bo}) & 1-2(q_{1bo}^2+q_{3bo}^2) & 2(q_{3bo}q_{2bo}+q_{1bo}q_{0bo}) \\ 2(q_{1bo}q_{3bo}+q_{2bo}q_{0bo}) & 2(q_{2bo}q_{3bo}-q_{1bo}q_{0bo}) & 1-2(q_{1bo}^2+q_{2bo}^2) \end{bmatrix} \tag{5.3}$$

where $\bar{q}_{bo} = [q_{0bo} \quad q_{1bo} \quad q_{2bo} \quad q_{3bo}]^T$ denote the quaternions of the body frame with respect to the orbital frame.

5.1.3 Solar Sail Models

In order to test the motion planning method for realistic solar sails, the parameters suggested by Wie for ATK's scalable sailcraft [32] were used as the basis of the 40 m square and 140 m disk solar sail models. Table 5.1 lists some of the properties of the solar sails under consideration.

As one of the aims of the chapter is to assess the feasibility of different actuation methods for a spinning solar sail, simple models of a number of actuators are included. As an initial study, it is assumed that the geocentric spacecraft is equipped with simple reaction wheels. The wheel data is based on the Honeywell Constellation Series HR12

Table 5.1: Properties of solar sails

Parameter	Sail A	Sail B
Sail shape	Square	Disk
Sail width (m)	40	140
Sail area (m^2)	1200	15394
Sail characteristic acceleration (m/s^2)	0.11×10^{-3}	5×10^{-4}
Principal Inertias (kgm^2)		
J_x	4340	188650
J_x	2171	94325
J_x	2171	94325
Total spacecraft (kg)	85	280.377
Sail mass (kg)	6	76.97
Centre of mass/centre of pressure offset (m)	$[0 \quad 0.0707 \quad 0.0707]^T$	$[0 \quad 0.2475 \quad 0.2475]^T$

reaction wheels [126], and the wheel properties are shown in Table 5.2. The wheels apply a control torque as in Equation (4.3).

Table 5.2: Honeywell HR12 reaction wheel data

Parameter	Sail A
Wheel inertias	$J_w = 0.075\,\mathrm{kgm}^2$
Maximum wheel torque	$0.1\,\mathrm{Nm}$
Rate limit	$1 \times 10^{-2}\,\mathrm{Nm/s}$
Nominal wheel momentum	$12\,\mathrm{Nms@6000\,rpm}$

In addition, it is assumed that the geocentric solar sail is equipped with magnetorquers with a peak magnetic dipole of $100\,\mathrm{Am}^2$ on each axis, and continuous actuators of to-be-determined size for desaturation. The magnetorquers apply a control torque given by

$$\bar{N}_{mtq} = \bar{M}_{mtq} \times \bar{B} \tag{5.4}$$

where $\bar{N}_{mtq}$ is the magnetorquer control torque, $\bar{M}_{mtq}$ the magnetorquer magnetic dipole and $\bar{B}$ the magnetic field vector in the body frame.

The heliocentric solar sail is assumed to have simple continuous actuators with a rate limit of $1\,\mathrm{Nm/s}$. The most feasible method of actuation for the implementation of the

motion planning method is an outcome of this study, as discussed in Section 5.6.

5.1.4 Environmental Model

In Section 4.1.6, the environmental disturbances caused by gravity gradients, residual magnetic dipoles, air drag and solar radiation pressure were detailed for a spacecraft in a geocentric orbit. For the geocentric solar sail, these disturbances were again modelled, together with the orbital perturbations due to air drag, solar radiation pressure and Earth oblateness, in order to test the robustness of the motion planning method in a non-ideal environment.

For the solar sail in a heliocentric orbit, assuming that the Sun is the source of all disturbance torques (i.e. that the planetary bodies exert negligible gravitational pull), the sail primarily experiences disturbances due to solar radiation pressure with a smaller disturbance due to gravity gradients. The gravity gradient torques are modelled as in Section 4.1.6, with $\mu = 1.327 \times 10^{20}\,\mathrm{m^3 s^{-2}}$ the gravitational parameter of the Sun for the heliocentric orbit. However, in this chapter an alternative solar radiation pressure model is utilised. The model (4.9) is suitable for calculating the solar radiation pressure acting on the cuboidal nano-spacecraft structure as it is a general representation which could be easily adapted to find the projected area of each spacecraft face. Meanwhile, the model used in this chapter was derived specifically for use in modelling solar sails, and is described below.

Solar Radiation Pressure Torque and Force

The sails under consideration are assumed to be perfectly reflecting. From [33] the acceleration due to solar radiation pressure, $\bar{a}_{SRP}$, for an ideal sail is given by

$$\bar{a}_{SRP} = F_0(\hat{r}_{sun} \cdot \hat{n}_{sail})^2 \hat{n}_{sail} \tag{5.5}$$

where $\bar{r}_{sun}$ is the radial vector from the Sun to the spacecraft, and $\hat{r}_{sun}$ the unit vector. The sail normal unit vector, $\hat{n}_{sail}$, corresponds to $[1 \quad 0 \quad 0]^T$ in the body frame, and

$$F_0 = (\frac{r_{au}}{|| \bar{r}_{sun} ||})^2 a_c \tag{5.6}$$

with r_{au} the mean distance from the Earth to the Sun (1 au) and a_c the sail characteristic acceleration. The characteristic acceleration of an ideal sail is expressed as

$$a_c = \frac{2P}{\sigma_s + \sigma_a} \tag{5.7}$$

where $P = 4.563 \times 10^{-6}\,\mathrm{N/m^2}$ is the nominal solar radiation pressure constant at 1 au from the Sun. The sail and attached mass assembly loadings are given as $\sigma_s = \frac{m_s}{A_r}$ and $\sigma_a = \frac{m_a}{A_r}$ respectively, where m_s and m_a are the masses of the sail and attached mass and A_r is the reflective area.

It follows that $\bar{F}_{SRP} = [F_{1SRP} \quad F_{2SRP} \quad F_{3SRP}]^T$, the force due to solar radiation pressure, is simply the mass of the entire spacecraft, $m_{s/c} = m_s + m_a$, times the acceleration due to solar radiation pressure in Equation 5.5. The torque due to solar radiation pressure, $\bar{N}_{SRP}$ is then calculated using the equation

$$\bar{N}_{SRP} = \bar{r}_{m/p} \times \bar{F}_{SRP} \tag{5.8}$$

where $\bar{r}_{m/p}$ is again the offset between the centre of mass and the centre of pressure.

5.2 Analytic Derivation of the Geometric Spin Repointing Reference Motions

In this section, the general framework utilised in Chapters 3 and 4 is applied to the case of the spacecraft constrained to spin at a constant rate around one axis. As in Chapter 4 the kinematics of the system are expressed on the matrix Lie group $SU(2)$, and the conserved quantities of the system utilised to solve the Hamiltonian vector fields and thus yield the analytical optimal controls. This framework is first applied to a general

form of quadratic cost, and an attempt made to solve for the most general form of the solution. Then, the particular case of the analytic reference motions which form the basis of the motion planning algorithm used in this chapter, as derived by Biggs and Horri [29], are linked to this general case. Additionally, the pure spin references considered for comparison purposes are detailed.

These analytical reference motions will then be tested in simulation to assess the performance of references derived using geometric control theory in motion planning for real engineering systems.

5.2.1 General Framework

The kinematics of the rigid body, constrained to rotate at a constant speed around one axis, are described using the matrix Lie group $SU(2)$ (2.31) in the case where $\omega_1 = v$:

$$\frac{dR(t)}{dt} = R(t)(vA_1 + \omega_2 A_2 + \omega_3 A_3) \tag{5.9}$$

Additionally, a cost function of the form

$$J = \frac{1}{2}\int_0^1 c\omega_2^2 + \omega_3^2 dt \tag{5.10}$$

is utilised. Relative to the general form of the cost function (2.34), the constant angular velocity v is not controllable and so it is omitted. Therefore $c_1 = 0, c_2 = c$ and $c_3 = 1$. Additionally, the controls $u_i = \omega_i$ with $i = 1, ..., 3$. This initial cost function is chosen as it (i) ensures smooth motions (ii) minimises the integral of angular velocities on the unconstrained axes which avoids the system accumulating more angular velocity than needed (iii) avoids dangerously fast slew rates which could excite the sail membrane and (iv) allows the construction of the optimal motions in closed form using the framework of geometric control theory.

The Hamiltonian function corresponding to the left-invariant kinematic constraint (5.9) that minimises the function (5.10) is derived, using the procedure detailed in Section

2.5.2, as

$$H(p,u) = v\lambda_1 + \omega_2\lambda_2 + \omega_3\lambda_3 - \frac{1}{2}(c\omega_2^2 + \omega_3^2) \tag{5.11}$$

From the Maximum Principle of optimal control detailed in Section 2.5, if the following conditions are satisfied:

$$\frac{\partial H}{\partial \omega_i} = 0, \quad \frac{\partial^2 H}{\partial {\omega_i}^2} < 0 \tag{5.12}$$

where again $i = 1, ..., 3$, then the controls ω_i are optimal. This yields:

$$\omega_2 = \frac{\lambda_2}{c}, \quad \omega_3 = \lambda_3 \tag{5.13}$$

Substituting (5.13) into (5.11) leads to the optimal Hamiltonian H^* relative to the kinematics (5.9) and cost function (5.10):

$$H^* = v\lambda_1 + \frac{1}{2}(\frac{\lambda_2^2}{c} + \lambda_3^2) \tag{5.14}$$

Additionally, the Casimir function (4.15) is again constant along the Hamiltonian flow. As in Chapter 4, the Hamiltonian vector fields which implicitly define the extremal solutions are given by the Poisson bracket. This yields the differential equations:

$$\begin{aligned} \dot{\lambda}_1 &= \lambda_2\lambda_3(1 - \tfrac{1}{c}) \\ \dot{\lambda}_2 &= \lambda_3(v - \lambda_1) \\ \dot{\lambda}_3 &= \lambda_2(\tfrac{\lambda_1}{c} - v) \end{aligned} \tag{5.15}$$

These equations (5.15) define the general extremal differentials for the rigid body constrained to spin at a constant rate v around one axis. In subsequent sections these extremal differentials will be used to show that the most general solution to the problem is not practical, while the particular case when $c = 1$ results in simple trigonometric functions.

In order to derive the global solution in terms of quaternions, the local solution in terms of the euler angles (4.35) derived in Section 4.2.1 is again utilised together with Lax pair integration to yield the solution on the semisimple 3D Lie group $SU(2)$. Following

this, the isomorphism from the Special Unitary group to the unit quaternions (2.20) is used to enable the solution to be expressed in convenient quaternion form.

5.2.2 General Case

Following the derivation of the general Hamiltonian functions and extremal differentials in Section 5.2.1, the most general solution to the extremals will be derived in this section.

Squaring $\dot{\lambda}_1$ in (5.15) results in an equation of the form:

$$\dot{\lambda}_1^2 = (\lambda_2\lambda_3)^2(\frac{1}{c^2} - \frac{2}{c} + 1) \tag{5.16}$$

Solving for ${\lambda_3}^2$ and then for ${\lambda_2}^2$ using (5.14) and the Casimir (4.15) yields:

$$\begin{aligned} {\lambda_3}^2 &= 2(H^* - v\lambda_1) - \tfrac{{\lambda_2}^2}{c} \\ {\lambda_2}^2 &= \tfrac{M^2 - {\lambda_1}^2 - 2(H^* - v\lambda_1)}{1 - \frac{1}{c}} \end{aligned} \tag{5.17}$$

Substituting these expressions into (5.16) results in an expression of the form:

$$\dot{\lambda}_1^2 = a_1{\lambda_1}^4 + a_2{\lambda_1}^3 + a_3{\lambda_1}^2 + a_4\lambda_1 + a_5 \tag{5.18}$$

where

$$\begin{aligned} a_1 &= -\tfrac{1}{c} \\ a_2 &= \tfrac{2(1+c)v}{c} \\ a_3 &= -\tfrac{2(H+cH-M^2+2cv^2)}{c} \\ a_4 &= 8Hv - \tfrac{2(1+c)M^2v}{c} \\ a_5 &= -\tfrac{(2H-M)(2cH-M^2)}{c} \end{aligned} \tag{5.19}$$

Solving for the roots e_i with $i = 1, ..., 4$ enables (5.18) to be expressed in the form:

$$\dot{\lambda}_1^2 = a_1(\lambda_1 - e_1)(\lambda_1 - e_2)(\lambda_1 - e_3)(\lambda_1 - e_4) \tag{5.20}$$

where

$$\begin{aligned} e_1 &= v - \sqrt{-2H + M^2 + v^2} \\ e_2 &= v + \sqrt{-2H + M^2 + v^2} \\ e_3 &= cv - \sqrt{-2cH + M^2 + (cv)^2} \\ e_4 &= cv + \sqrt{-2cH + M^2 + (cv)^2} \end{aligned} \tag{5.21}$$

This can then be solved to yield λ_1 in terms of a Weierstrass elliptic function.

Equation (5.20) can be expressed as a third order polynomial by using the transformations

$$\begin{aligned} \Lambda_1 &= \tfrac{1}{(\lambda_1 - e_1)} \\ \Lambda_2 &= \tfrac{\dot{\lambda}_1}{(\lambda_1 - e_1)} \end{aligned} \tag{5.22}$$

This yields an equation of the form:

$$\Lambda_2{}^2 = b_1 \Lambda_1{}^3 + b_2 \Lambda_1{}^2 + b_3 \Lambda_1 + a_1 \tag{5.23}$$

where

$$\begin{aligned} b_1 &= a_1(e_1 - e_2)(e_1 - e_3)(e_1 - e_4) \\ b_2 &= a_1(3e_1^2 + e_3 e_4 + e_2(e_3 + e_4) - 2e_1(e_2 + e_3 + e_4)) \\ b_3 &= a_1(3e_1 - e_2 - e_3 - e_4) \end{aligned} \tag{5.24}$$

Equation (5.23) can be solved using a Weierstrass elliptic function in a similar manner to the unit speed wheeled robot of Chapter 3. The canonical equation for the Weierstrass $\wp$-function is given by Equation (3.59). Then, let

$$\begin{aligned} \Lambda_1 &= c_1 \wp + c_2 \\ \Lambda_2 &= \dot{\wp} \end{aligned} \tag{5.25}$$

where c_1 and c_2 are constants to be determined. The cubic function (5.23) can then be written in the form (5.25). Substituting (5.25) into (5.23) and comparing coefficients

of $\wp$ with those in (3.59), it follows that:

$$\begin{aligned} c_1 &= (\tfrac{4}{b_1}) \\ c_2 &= -\tfrac{b_2}{3b_1} \\ g_2 &= \tfrac{b_2^2 - 3b_1^2}{12} \\ g_3 &= \tfrac{1}{432}(9b_1^2 b_2 - 2b_2^3 - 27a_1 b_1^3) \end{aligned} \tag{5.26}$$

Substituting (5.26) into (5.25) yields:

$$\Lambda_1 = (\frac{4}{b_1})^{1/3}\wp - \frac{b_2}{3b_1} \tag{5.27}$$

where $\wp(z; g_2; g_3)$ defines the Weierstrass elliptic function, with z a complex variable. Using the relations (5.22) results in an expression for λ_1:

$$\lambda_1 = \frac{1}{\Lambda_1} + e_1 \tag{5.28}$$

Expressions for λ_2 and λ_3 follow from (5.17).

Note that the Weierstrass elliptic function can be equivalently expressed as a Jacobi elliptic function. Defining the roots of the cubic Equation (3.59) as R_j where $j = 1...3$ it follows from [98] that:

$$\wp(z) = R_3 + \frac{R_1 - R_3}{\mathrm{sn}^2(z\sqrt{R1 - R3}, \sqrt{\frac{R2-R3}{R1-R3}})} \tag{5.29}$$

Performing this substitution enables a complete expression for λ_1 in terms of the Jacobi elliptic sn function to be written:

$$\lambda_1 = \frac{1}{\alpha(R_3 + \frac{R_1 - R_3}{\mathrm{sn}^2(t\sqrt{R1-R3}, \sqrt{\frac{R2-R3}{R1-R3}})}) + \beta} + e_1 \tag{5.30}$$

This form is easier to integrate than the Weierstrass function, which computing software finds difficult to handle.

From (4.35), it follows that $\dot{\varphi}_1$ can be expressed as:

$$\dot{\varphi}_1 = M(\frac{2(H^* - v\lambda_1)}{M^2 - \lambda_1^2}) \tag{5.31}$$

While this integral can be evaluated in the symbolic software tool, the presence of the Weierstrass or Jacobi elliptic functions mean that the general solution is long and complex and so it is not realistically viable for implementation in practical systems. Therefore the general solution is not used as the basis of a motion planner in this thesis. Despite the general solution being impractical for motion planning, as with the arbitrary speed wheeled robot case discussed in Chapter 3 there may exist a choice of parameter which results in a subset of more computationally efficient trigonometric or hyperbolic solutions being obtained. To this end, a phase plane analysis was carried out. Rewriting (5.18) to give an expression for $\dot{\lambda}_1$ in terms of λ_1, parametric plots were produced by varying the parameters c, H^*, M and v over a range of values for λ_1. It was discovered that by fixing the values of H^*, M and v and varying the parameter c, that a special case occurs at $c = 1$. This is illustrated in Figure 5.2.

At $c = 1$, the roots (5.21) of equation (5.18) reduce to form two repeated roots and $\dot{\lambda} = 0$ in (5.15). Thus it has been shown that the solution of Biggs [29] is a special case of the impractical general solution presented in this section. In the proceeding section the particular solution when $c = 1$ will be derived as in [29] before being utilised to plan attitude motions for a spinning spacecraft in order to determine if the solutions obtained using geometric control theory are of use in practical motion planning.

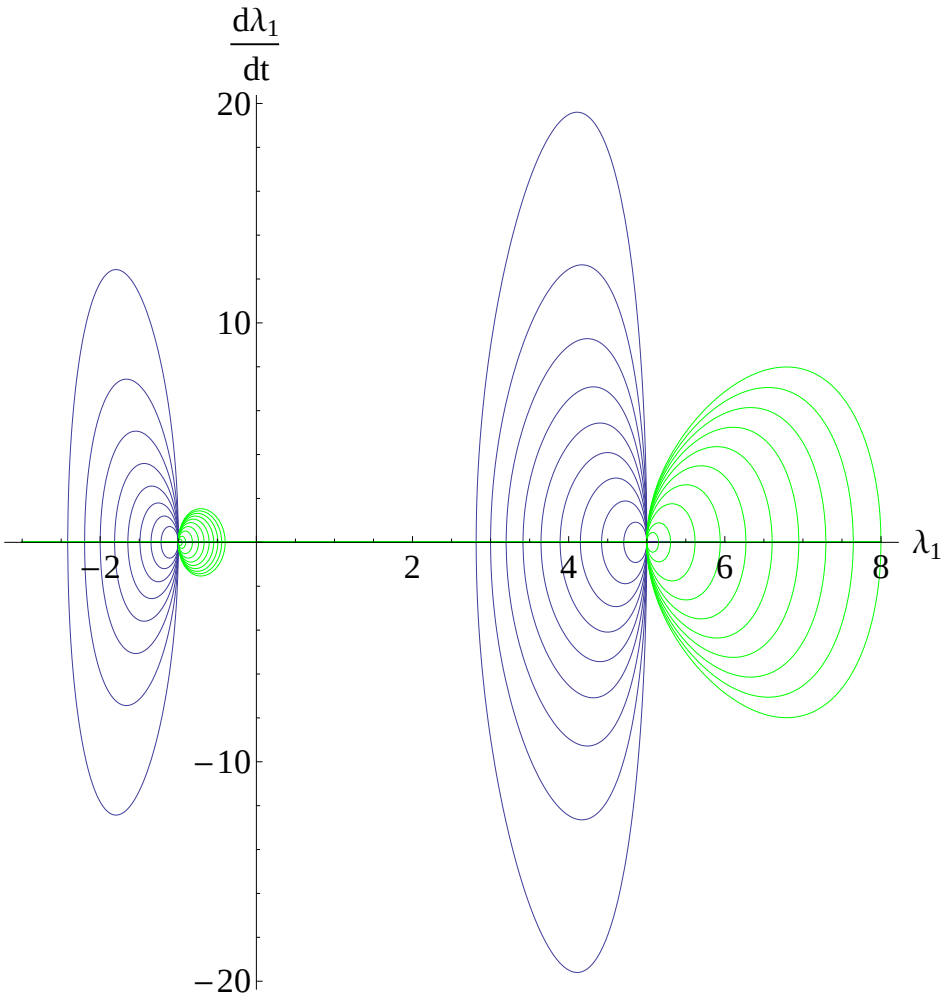

Figure 5.2: Phase plane plot for varying $0.1 \leq c \leq 1.9$, with $H^* = 1, M = 7$ and $v = 2$. Blue curves denote values of $0.1 \leq c < 1$ while green curves denote values of $1 < c \leq 1.9$

5.2.3 Particular Case: c=1

In this section the equations first derived in [29] for the particular case $c = 1$ are derived in full, before their use in the motion planning algorithm which forms the basis of this chapter.

Lemma 6. *The class of reference motions that minimise the cost function (5.10) subject*

to the kinematics (5.9) for the particular case when $c = 1$ are defined by

$$\begin{aligned} \omega_2 &= \zeta \sin((v+\psi)t + \beta) \\ \omega_3 &= \zeta \cos((v+\psi)t + \beta) \end{aligned} \tag{5.32}$$

$$\begin{aligned} q_0 &= \cos(\tfrac{1}{2}t(\psi+v))\cos(\tfrac{Mt}{2}) + \tfrac{\psi}{M}\sin(\tfrac{1}{2}t(\psi+v))\sin(\tfrac{Mt}{2}) \\ q_1 &= \sin(\tfrac{1}{2}t(\psi+v))\cos(\tfrac{Mt}{2}) - \tfrac{\psi}{M}\cos(\tfrac{1}{2}t(\psi+v))\sin(\tfrac{Mt}{2}) \\ q_2 &= \tfrac{\zeta}{M}\sin\left(\tfrac{\psi+v}{2}t + \beta\right)\sin\left(\tfrac{M}{2}t\right) \\ q_3 &= \tfrac{\zeta}{M}\cos\left(\tfrac{\psi+v}{2}t + \beta\right)\sin\left(\tfrac{M}{2}t\right) \end{aligned} \tag{5.33}$$

where $\omega_1 = v$, ω_2 and ω_3 are the optimal angular velocities and q_0, q_1, q_2, q_3 the corresponding quaternion components subject to the given boundary conditions $\bar{q}(0) = \bar{q}_i = [1 \quad 0 \quad 0 \quad 0]^T$ and $\bar{q}(T) = \bar{q}_f$ and where ζ, ψ, β are parameters available for optimisation, v is the given spinning angular velocity and $M = \sqrt{\psi^2 + \zeta^2}$ is equal to the root of the Casimir function (4.15).

Proof [29]. By setting $c = 1$ in the equations for the optimal form of the controls (5.13), it follows that $\omega_2 = \lambda_2$ and $\omega_3 = \lambda_3$. In a similar manner, the extremal differential equations (5.15) simplify to:

$$\begin{aligned} \dot{\lambda}_1 &= 0 \\ \dot{\lambda}_2 &= \lambda_3(v - \lambda_1) \\ \dot{\lambda}_3 &= -\lambda_2(v - \lambda_1) \end{aligned} \tag{5.34}$$

Denoting $\lambda_1 = -\psi$ as a constant, inspection of Equation (5.14) enables a constant reduced Hamiltonian $H_r = 2(H^* + \psi v)$ to be defined as in Chapter 4, Section 4.2.2:

$$H_r = 2(H^* + \psi v) = \lambda_2^2 + \lambda_3^2 \tag{5.35}$$

Following a similar process to that outlined in Section 4.2.2, the extremals can then be parameterised using polar co-ordinates and solved to yield the expressions for the optimal angular velocities (5.32).

The euler angles given in Equation (4.35) of Chapter 4 are also applicable to this particular case. Performing the necessary partial derivatives of the optimal Hamiltonian (5.14) in the expression for ϕ_1 it follows that:

$$\varphi_1 = \int M dt \tag{5.36}$$

Carrying out the integration and letting $\varphi(0) = \gamma$ results in $\varphi_1 = Mt + \gamma$. The quaternions are once again obtained by substituting the optimal angular velocities (5.32) into the expressions for the euler angles and then into (4.25). The solution is pulled back to the identity via (4.36) to yield the solution on $SU(2)$. Finally the isomorphism (2.20) is used to give the expressions for the time evolution of the quaternions of a rigid body constrained to spin at a constant rate v, for the particular case when $c = 1$.

This defines analytically a subset of admissible smooth motions expressed in terms of several free parameters v, ζ, ψ, β, which as in Chapter 4 will be used as the basis of a motion planning algorithm for a spacecraft simulated under realistic environmental conditions.

In order to assess the strengths and weaknesses of the method derived using geometric control theory, it must be compared to another method. To this end in the following section reference motions for a spacecraft in a state of pure spin are derived to provide a means of comparison.

5.2.4 Pure Spin Repointing

The previous subsection stated the analytical reference tracks for a rigid body constrained to spin at a constant rate v around one-axis, while minimising the body rates in the other two-axes. In this section, the time-evolution of the quaternions for a rigid body constrained to spin at constant rates around each axis are stated. This is achieved by using the Rodrigues expansion for an element of $SU(2)$, and then making use of the

isomorphism (2.20) to yield the quaternions as stated in the following lemma:

Lemma 7. *The quaternions for the case when the angular velocities ω_1, ω_2 and ω_3 of a rigid body are constant are defined by:*

$$q_0 = \cos(\Lambda t), \quad q_1 = \frac{\omega_1}{2\Lambda}\sin(\Lambda t), \quad q_2 = \frac{\omega_2}{2\Lambda}\sin(\Lambda t), \quad q_3 = \frac{\omega_3}{2\Lambda}\sin(\Lambda t) \tag{5.37}$$

where q_0, q_1, q_2, q_3 are quaternion components and where $\Lambda = \sqrt{\frac{1}{4}(\mid \omega_1 \mid^2 + \mid \omega_2 \mid^2 + \mid \omega_3 \mid^2)}$ is a constant.

Proof. For the case where ω_1, ω_2 and ω_3 are constant, the kinematics can be expressed as:

$$\frac{dR(t)}{dt} = R(t)V \tag{5.38}$$

where $V \in \mathfrak{su}(2)$ is given by

$$V = \begin{pmatrix} \alpha & \beta \\ -\bar{\beta} & \bar{\alpha} \end{pmatrix} \tag{5.39}$$

The Rodrigues formula [17] for the exponential of a matrix A is given by

$$exp(At) = \sum_{k=0}^{+\infty} \frac{t^k A^k}{k} \tag{5.40}$$

Denoting that $V^2 = -\Lambda^2 * I$ where I is the identity element in $SU(2)$, substituting into (5.40) and using the Taylor series expansions of sine and cosine, it follows that the closed form solutions of (5.38) are given by

$$R(t) = R(0)\begin{pmatrix} \cos(\Lambda t) + \frac{\alpha}{\Lambda}\sin(\Lambda t) & \frac{\beta}{\Lambda}\sin(\Lambda t) \\ \frac{-\bar{\beta}}{\Lambda}\sin(\Lambda t) & \cos(\Lambda t) + \frac{\bar{\alpha}}{\Lambda}\sin(\Lambda t) \end{pmatrix} \tag{5.41}$$

where $\alpha + \bar{\alpha} = 0$. Equation (5.41) together with the isomorphism (2.20) from $SU(2)$ to $\mathbb{H}$ yields the quaternions for constant angular velocities (5.37). Furthermore, comparing the RHS of (4.33) with that of (5.38) it is found that $\alpha = \frac{1}{2}i\omega_1$ and $\beta = \frac{1}{2}(\omega_2 + i\omega_3)$. Thus $\Lambda = \sqrt{\frac{1}{4}(\mid \omega_1 \mid^2 + \mid \omega_2 \mid^2 + \mid \omega_3 \mid^2)}$ $\square$

The quaternions (5.37) are utilised in the special case where $\omega_1 = v$ and $\omega_2 = \omega_3 = 0$ to

both stabilise the solutions (5.33) at the target quaternion $\bar{q}(T)$, and also to provide a benchmark against which to compare the proposed motion planning method as detailed in the following section.

5.3 Practical Implementation of the Motion Planning Method

With the analytical equations for the motion of a spinning rigid body stated in quaternion form, a method is now described to utilise these solutions in a motion planning algorithm. Firstly, an appropriate cost function is selected that meets the desired accuracy on the final pointing direction while minimising the required torque, before the parametric optimisation methods utilised in Chapters 3 and 4 are adapted and applied to yield reference tracks which match the set boundary conditions. Finally, the extension to simple obstacle avoidance is detailed.

5.3.1 Parametric Optimisation

As in Chapter 4, the analytical expressions for the angular velocities and the globally defined quaternions were entered into a computational software programme in order to construct a motion planner. A cost function of the form

$$F_1 = || \, (\bar{q} - \bar{q}(T)) \, || \tag{5.42}$$

is again used to minimise the norm of the error between the current quaternion and the target quaternion.

Additionally, as in Biggs [29], a second term is included in order to minimise the torque required during the manoeuvre. By substituting (5.32) and $\omega_1 = v$ into (4.1), the theoretical control torque input $\bar{N}_{tc} = [N_{1tc}, \quad N_{2tc}, \quad N_{3tc}]^T$ required to carry out the manoeuvre is obtained. A cost function of the form

$$F_2 = \int_0^T \left\langle \bar{\mathbf{N}}_{\mathbf{tc}}, \bar{\mathbf{N}}_{\mathbf{tc}} \right\rangle^2 dt \tag{5.43}$$

can then be constructed, which minimises the integral of the theoretical control torques. For motion planning implementation, this integral can be evaluated analytically and equates to finding the minimum of the analytic function [29]

$$F_2 = \frac{\zeta^2}{32\alpha}\begin{pmatrix} \zeta^2\left(4T\alpha + \sin\left(4\beta\right)\right) - \sin\left(4(T\alpha+\beta)\right) J_1^2\delta_1^2 \\ +8\left(2T\alpha - \sin\left(2\beta\right) + \sin\left(2(T\alpha+\beta)\right) J_2^2\left(\alpha - v\delta_2\right)^2 \\ +8\left(2T\alpha + \sin\left(2\beta\right) - \sin\left(2(T\alpha+\beta)\right) J_3^2\left(\alpha + v\delta_3\right)^2 \end{pmatrix} \tag{5.44}$$

where $\alpha = v + \psi$. Therefore, to obtain the optimal parameters for the reference motions (5.32, 5.33) which meet the required accuracy constraints while minimising the accumulated torque, the following multi-objective function is utilised:

$$\min_{\zeta,\psi,\beta}(F_1 + kF_2) \tag{5.45}$$

where ζ, ψ, β are the free parameters to be optimised, F_1 and F_2 are defined in (5.42) and (5.44) respectively and k is a weighting parameter which must be manually tuned. As the cost function is multi-objective, the tuning of this parameter is dependent on the relative weighting assigned to the final pointing accuracy and control effort of the manoeuvre. If minimising control effort is not required, then setting $k = 0$ negates the need for manual tuning. However, in this work it is desirable to plan high accuracy, low control effort manoeuvres as higher required torques would mean that the actuators would necessarily be larger, undesirably increasing the mass of the sail. Thus, given the moments of inertia J_1, J_2, and J_3, spinning angular velocity v and terminal time T a parametric optimisation can be carried out to find a reference motion which meets the desired final pointing accuracy to four decimal places while minimising the accumulated torque of the manoeuvre. Note that the terminal time T can also be included in the parametric optimisation as a free parameter, and thus if the manoeuvre time is unconstrained the motion planner can be used to determine the manoeuvre time which results in the lowest accumulated torque.

A genetic algorithm method was used for the parametric optimisation as it proved the most adept at finding the values of the free parameters which minimised the cost

function, in comparison to the other available solvers such as stochastic functional minimisation and direct search "simplex" methods. That is, the genetic algorithm method often found solutions to certain manoeuvres when the other solvers could not. This method was chosen in order to assess the suitability of using the reference motions to plan motions for a solar sail. Again, a deeper investigation would be required to identify the most suitable method of determining the required initial angular velocities if the references were to be generated on-board a spacecraft. However, this is outwith the scope of this thesis.

The optimal values of the free parameters, ζ^*, ψ^*, β^*, resulting from the optimisation can then be input into the analytical equations for the angular velocities and quaternions to generate the reference tracks for the repointing manoeuvre.

5.3.2 Extension To Constrained Repointing

The method of producing constrained slews detailed in Chapter 4 Section 4.3.3 for the natural motions is again applicable here. In contrast to the nano-spacecraft, a solar sail is more likely to have to maintain a certain minimum angle between the sail normal and the Sun throughout a manoeuvre for either power generation purposes or to maximise thrust. Therefore by probing the set of the curves which satisfy the boundary conditions on the final orientation of the spacecraft, $\bar{q}(T)$, constrained slews can be generated.

Recall that a bright object such as the Sun creates a "cone" in the configuration space. If the body x-axis unit vector must not deviate significantly from the Sun, then the unit vector must not lie outwith the cone during the manoeuvre, viz

$$\delta_p \triangleq \arccos(\hat{n}_p \cdot \hat{n}_c) \leq \delta_c \tag{5.46}$$

With these constraints defined, the method for finding curves which do not violate the appropriate constraint is briefly described in the context of the motion planner of this chapter.

Without a constraint on the pointing direction the parametric optimisation of Section 5.3.1 will return the optimal values of the free parameters ζ^*, ψ^*, β^*. In the case that

this returns a motion that violates the chosen constraint the parameters p_1, p_2, p_3 are added as increments to the parameters ζ^*, ψ^*, β^*, where $-\epsilon < p_1, p_2, p_3 < \epsilon$ and ϵ is a parameter which can be tuned. In this case the multi-objective function

$$\min_{p_1,p_2,p_3} (F_1 + kF_2) \tag{5.47}$$

is optimised to find an alternative geometric spin repointing manoeuvre from $\bar{q}$ to $\bar{q}(T)$. The parameter ϵ is incremented iteratively to obtain a solution that satisfies the chosen constraint, leading to a new set of parameters $\zeta^{**} = \zeta^* + p_1, \psi^{**} = \psi^* + p_2, \beta^{**} = \beta^* + p_3$ being obtained. Inputting these parameters into the analytical equations then generates reference tracks which bring the spacecraft from $\bar{q}$ to $\bar{q}(T)$ with $\delta_p \leq \delta_c \forall t$.

Note that the parameter k of the multi-objective cost-function (4.79) introduces an added heuristic into the process of finding a suitable curve which respects the orientation constraint. This process can be simplified by setting $k = 0$ at the possible expense of added control effort.

5.4 Solar Sail Motion Planning Simulations

The motion planning method described in Section 5.3 was tested in simulation to assess the strengths and limitations of the method. The PD controller described in Equation (4.80) of Chapter 4 was again chosen to track the references due to it's simplicity and ease of gain tuning. Once again the gyroscopic term was omitted from the controller as solar sail manoeuvres are generally long and slow.

As in Chapter 4, the manoeuvre is planned such that the references bring the spacecraft to the target in time $(T - \tau)$, where τ is a small period of time. However, whereas in Chapter 4 simple quaternion feedback references were used to stabilise the spacecraft, in this chapter at time $(T - \tau)$ until the end of the manoeuvre at time T, the pure spin references are tracked to bring the spacecraft to a state of pure spin at the target.

The geometric spin repointing manoeuvres can be summarised as:

$$\begin{aligned} For \quad t = [0, T-\tau) \quad \bar{\omega}_d &= \bar{\omega}_{ref} \\ \bar{q}_d &= \bar{q}_{ref} \end{aligned} \tag{5.48}$$
$$\begin{aligned} For \quad t = [T-\tau, T] \quad \bar{\omega}_d &= \bar{\omega}_{ps} \\ \bar{q}_d &= \bar{q}_{ps} \end{aligned}$$

where the subscripts "ref" and "ps" refer to the reference tracks generated using parametric optimisation and the pure spin references respectively, and τ is the length of time the stabilising control is applied.

The reference tracking in comparison to the pure spin benchmark references is assessed in terms of the accumulated torque I_N of the actuators, together with other factors such as momentum accumulation of the reaction wheels for the geocentric sail, and the peak angular velocities throughout the manoeuvre. The gains were adjusted iteratively until the final pointing and velocity constraints were satisfied, to 4 decimal places, with the lowest accumulated torque.

Note that solar sail attitude is often expressed in terms of cone and clock angles [32]. As the analytical references are expressed in quaternion form, a conversion from cone and clock to quaternions is necessary. This can be achieved using the simple quaternionic multiplication rules to rotate the initial quaternion in the body frame $\bar{q}_i$ first by an angle $-\delta$ and then by $-\alpha$, viz

$$\bar{q}_f = \begin{bmatrix} q_{0r} & -q_{1r} & -q_{2r} & -q_{3r} \\ q_{1r} & q_{0r} & q_{3r} & -q_{2r} \\ q_{2r} & -q_{3r} & q_{0r} & q_{1r} \\ q_{3r} & q_{2r} & -q_{1r} & q_{0r} \end{bmatrix} \bar{q}_i \tag{5.49}$$

where $\bar{q}_r = [q_{0r} \quad q_{1r} \quad q_{2r} \quad q_{3r}]^T$ are the quaternions specifying the rotation, $\bar{q}_i$ the quaternions before the rotation is applied and $\bar{q}_f$ the quaternions resulting from the rotation. For example for $\alpha = 30°$ and $\delta = 0°$, it follows from (5.49) that $\bar{q}_f =$

$[\cos(\frac{7\pi}{72}) \quad 0 \quad -\sin(\frac{7\pi}{72}) \quad 0]^T$. This conversion is utilised to generate realistic manoeuvres for the heliocentric solar sail in Section 5.4.2 from cone and clock angles given in the solar sail literature.

In Section 5.1.2, it was stated that in this chapter the references are tracked with respect to the orbital, rather than the inertial frame. This is due to solar sails generally performing attitude manoeuvres to repoint the thrust vector for orbital manoeuvres. In order to track the references, derived with respect to an inertial frame, in the rotating orbital frame, the orbital component of the angular velocity is added to the angular velocity reference tracks.

As the sail is axisymmetric, only the final attitude of the sail normal (the body x-axis) is of concern. Therefore when the sail is in a state of pure spin at the target there will be a plane of quaternions which match the desired pointing constraints, and targeting a static reference as in Chapter 4 is not feasible. Thus a target quaternion is specified which lies on this plane, and the first column of the quaternion matrix (5.3) is utilised to check that the spacecraft has reached the target attitude on $SO(3)$. Note that the quaternions from the body to the orbit frame are input into (5.3), and so the first column of the rotation matrix represents the co-ordinates of the body x-axis with respect to the orbit frame in $SO(3)$. The orbital quaternions in (5.3) are replaced with the inertial quaternions $\bar{q}$ if the references are being tracked with respect to the inertial frame.

In the following sections the motion planning algorithm for a spinning spacecraft is tested in simulation to assess the performance of the method, derived using geometric control theory, when applied to a spinning solar sail.

5.4.1 Geocentric Spinning Square Solar Sail

In this section the motion planning method is applied to the attitude control of the 40 m square solar sail, detailed in Table 5.1. The sail is in an 800 km altitude Earth centred circular orbit. It is assumed that the geocentric solar sail is equipped with reaction wheels as actuators, with the data given in Table 5.2.

The references were tracked with respect to the RTN orbital reference frame. A manoeuvre from $\bar{q}_{bo}(0) = [0.5 \quad 0.5 \quad 0.5 \quad 0.5]^T$ to $\bar{q}_{bo}(T) = [0.63 \quad 0.33 \quad 0.33 \quad -0.63]^T =$ in a time of $T = 3000\,\text{s}$ and with a spin rate of $v = 0.0209\,\text{rad/s}$ was simulated. The gains used in the simulation were $k_\omega = 2.1$ and $k_q = 0.036$ for pure spin repointing, and $k_\omega = 0.8$ and $k_q = 0.1$ for the spin stabilised motions. The results are shown in Figures 5.3 to 5.6 for pure-spin reference tracking and Figures 5.7 to 5.10 for the geometric spin repointing reference tracking. Note that the dashed horizontal lines in the control torque and wheel momentum graphs represent the torque and momentum saturation limits respectively, while the vertical dashed lines indicate the switch to the stabilising control.

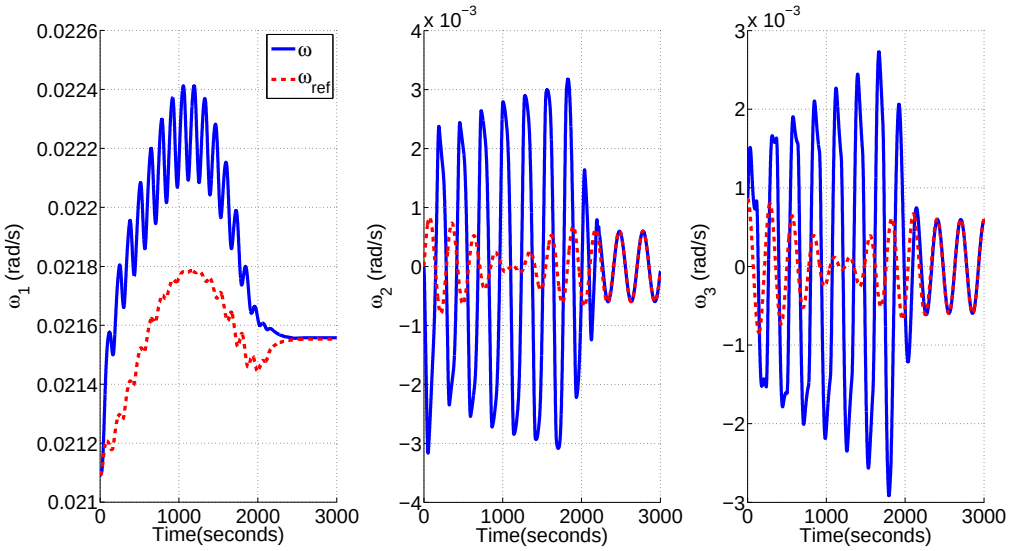

Figure 5.3: Inertially referenced angular velocities during pure spin manoeuvre for geocentric solar sail for Manoeuvre SR-B with a spin rate of $v = 0.0209\,\text{rad/s}$.

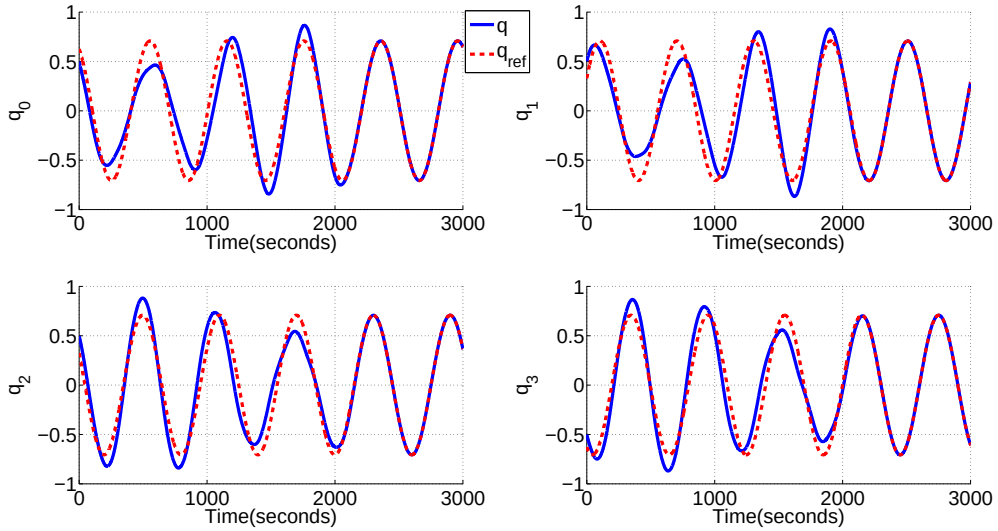

Figure 5.4: Orbit-referenced quaternions during pure spin manoeuvre for geocentric solar sail for Manoeuvre SR-B with a spin rate of $v = 0.0209\,\mathrm{rad/s}$.

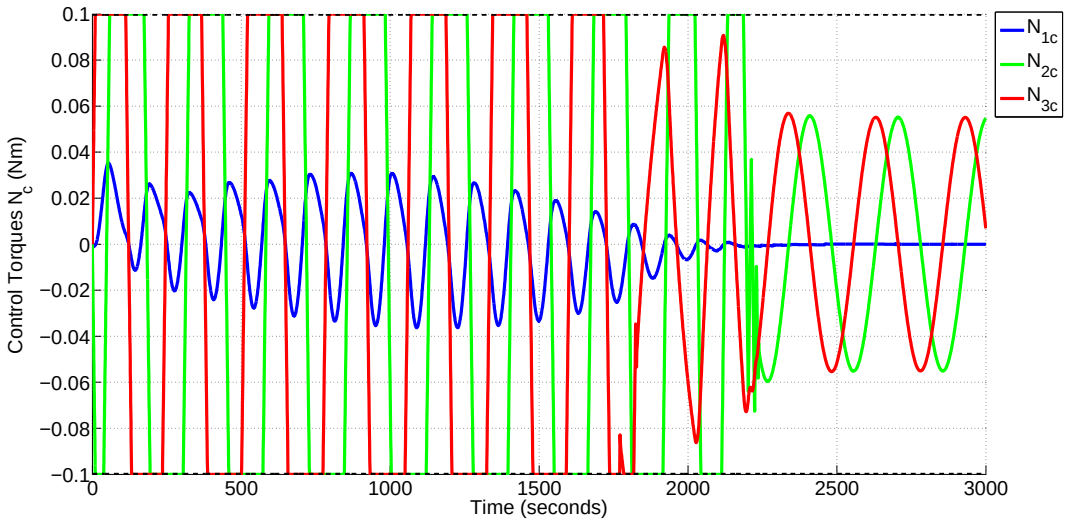

Figure 5.5: Control torques during pure spin manoeuvre for geocentric solar sail for Manoeuvre SR-B with a spin rate of $v = 0.0209\,\mathrm{rad/s}$.

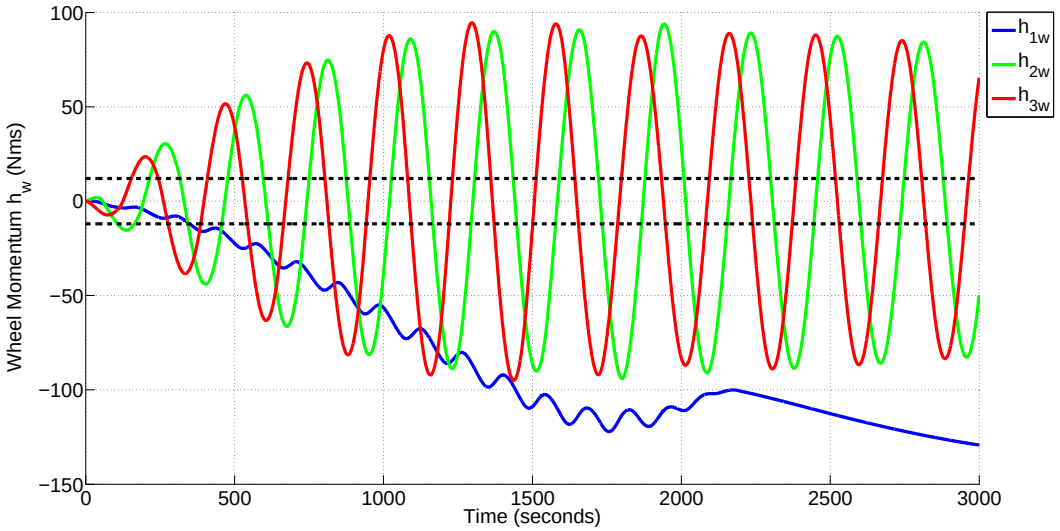

Figure 5.6: Wheel angular momentum during pure spin manoeuvre for geocentric solar sail for Manoeuvre SR-B with a spin rate of $v = 0.0209\,\text{rad/s}$.

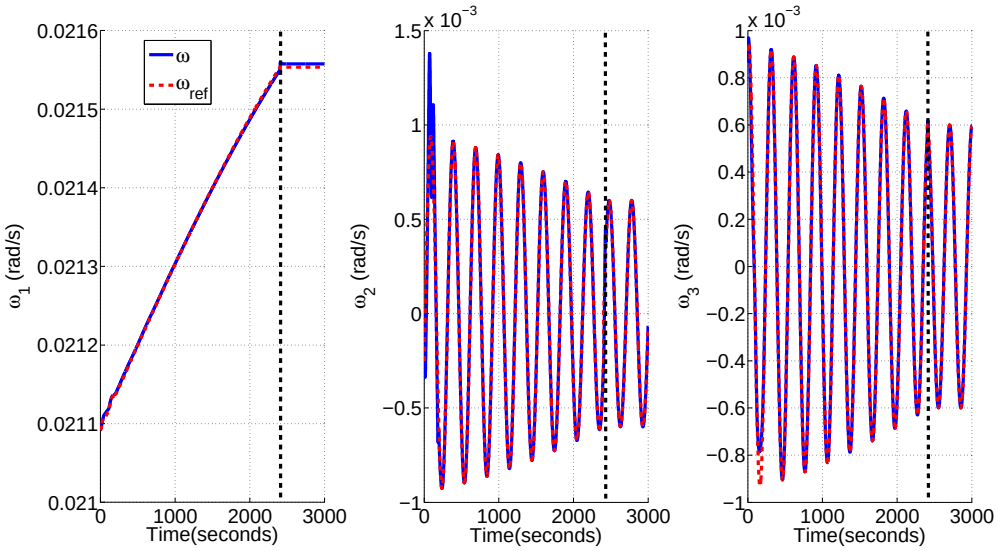

Figure 5.7: Inertially referenced angular velocities during spin repointing manoeuvre for geocentric solar sail for Manoeuvre SR-B with a spin rate of $v = 0.0209\,\text{rad/s}$.

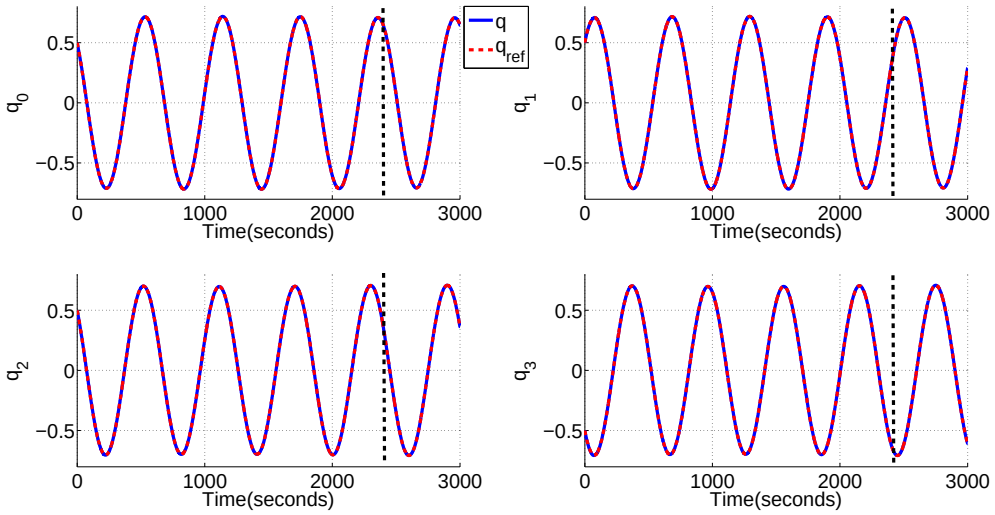

Figure 5.8: Orbit-referenced quaternions during spin repointing manoeuvre for geocentric solar sail for Manoeuvre SR-B with a spin rate of $v = 0.0209 rad/s$.

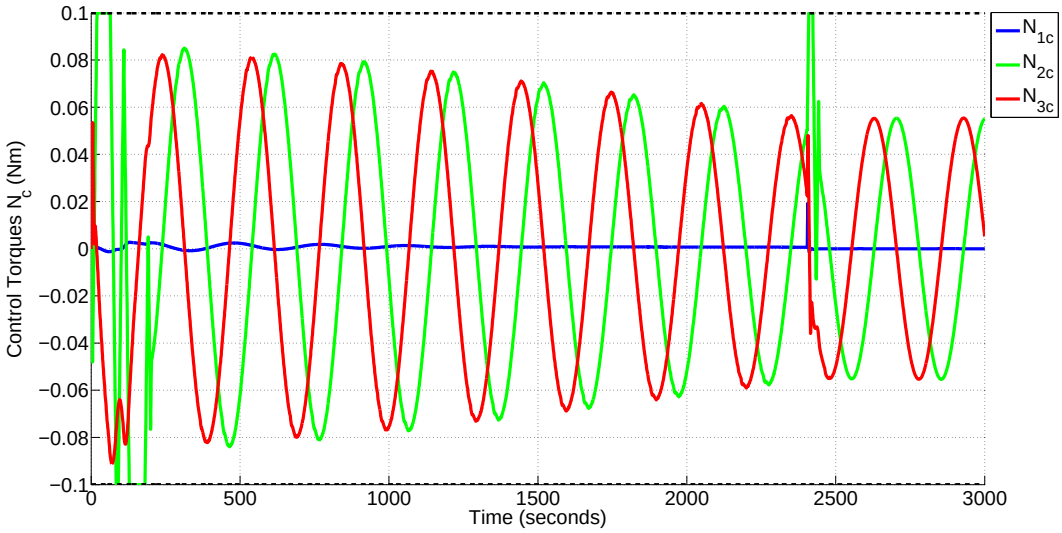

Figure 5.9: Control torques during spin repointing manoeuvre for geocentric solar sail for Manoeuvre SR-B with a spin rate of $v = 0.0209\,\mathrm{rad/s}$.

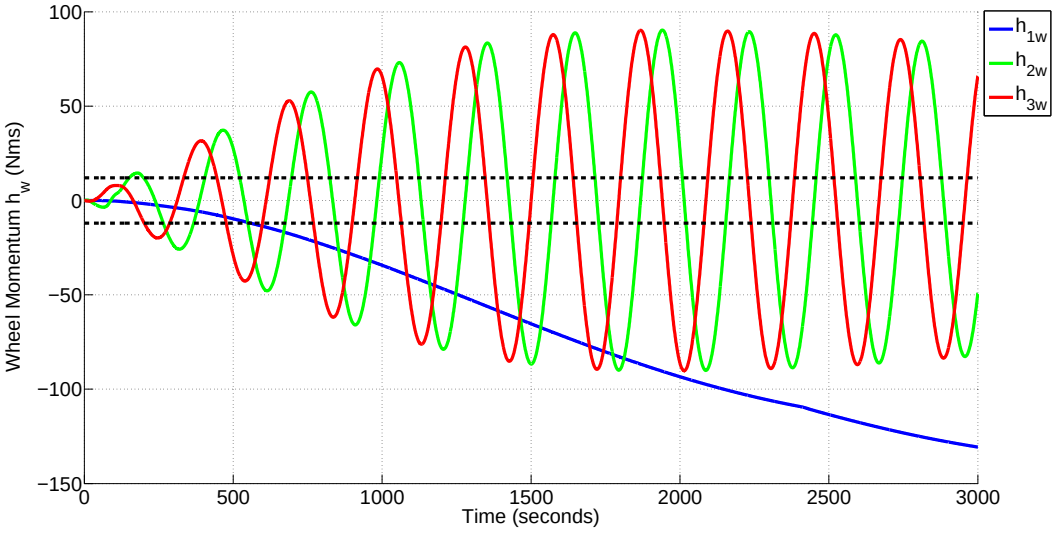

Figure 5.10: Wheel angular momentum during spin repointing manoeuvre for geocentric solar sail for Manoeuvre SR-B with a spin rate of $v = 0.0209\,\text{rad/s}$.

Tables 5.3 and 5.4 summarise the results of this and several other manoeuvres. The superscripts "*P.S.*" and "*S.R.*" refer to pure spin and geometric spin repointing motion planning manoeuvres respectively.

Table 5.3: Labelling of attitude manoeuvres for geocentric solar sail

Manoeuvre	Initial quaternion	Final quaternion
SR-A	$\bar{q}_{bo}(0) = [0.32 \quad -0.47 \quad -0.47 \quad -0.67]^T$	$\bar{q}_{bo}(T) = [0.71 \quad 0 \quad 0 \quad -0.71]^T$
SR-B	$\bar{q}_{bo}(0) = [0.5 \quad 0.5 \quad 0.5 \quad 0.5]^T$	$\bar{q}_{bo}(T) = [0.63 \quad 0.33 \quad 0.33 \quad -0.63]^T$
SR-C	$\bar{q}_{bo}(0) = [0.71 \quad 0 \quad 0 \quad -0.71]^T$	$\bar{q}_{bo}(T) = [0.5 \quad 0.5 \quad 0.5 \quad -0.5]^T$

Table 5.4: Comparison between pure spin references and geometric spin repointing references for geocentric solar sail

Manoeuvre	v (rad/s)	Time (s)	$I_N{}^{P.S.}$ (Nms)	$I_N{}^{S.R.}$ (Nms)
SR-A	0.0209	6100	254	349
	0.00785	2000	94	72
SR-B	0.0209	3000	330	211
	0.00785	1200	98.5	NA
SR-C	0.0209	2500	286.2	263
	0.00785	1250	128	NA

It was found that the gain tuning in the pure spin case was non-trivial, and as a result it was difficult to achieve the desired final pointing accuracy for long manoeuvres. As a result, the pure spin simulations were carried out first and the final manoeuvre time which was input into the geometric spin repointing motion planner was selected based on these results. The tuning of the gains for the geometric spin repointing was considerably easier, and the references can be easily generated to meet any required final manoeuvre time. However, the geometric spin repointing method was not able to perform all of the manoeuvres that the pure spin method could while respecting the final manoeuvre time and actuator constraints. For Manoeuvres SR-B and SR-C with $v = 0.007\,85\,\text{rad/s}$, the geometric spin repointing method required a peak torque of larger than 0.1 Nm to track the references, and hence these manoeuvres are marked "NA" in Table 5.4 as no suitable manoeuvre could be generated by the motion planner in these cases. Additionally, while the geometric spin repointing motion tracking offers savings in accumulated torque over the tracking of simple pure spin references in some cases, in others, such as Manoeuvre SR-A for $v = 0.0209\,\text{rad/s}$, the pure spin references required lower accumulated torque. This case is illustrated in Figures 5.11 to 5.14 for pure-spin reference tracking and Figures 5.15 to 5.18 for the geometric spin repointing reference tracking.

For the illustrated manoeuvres, it is clear that the spin repointing references have lower peak angular velocities and demand peak torques for a lower proportion of the total manoeuvre time. This was the case with all manoeuvres tested. However, in Manoeuvre SR-A with $v = 0.0209\,\text{rad/s}$, the pure spin method decays swiftly to a smaller periodic torque and thus results in lower accumulated torque overall. This is perhaps because tracking in the orbital frame requires the components of the orbital velocity to be added to the angular velocity reference tracks. As a result added control effort may be required to track the geometric spin repointing references with respect to the orbital frame.

Therefore in the case of the solar sail in a geocentric orbit, tracking of geometric spin repointing references with respect to the orbital frame offers no clear advantage over

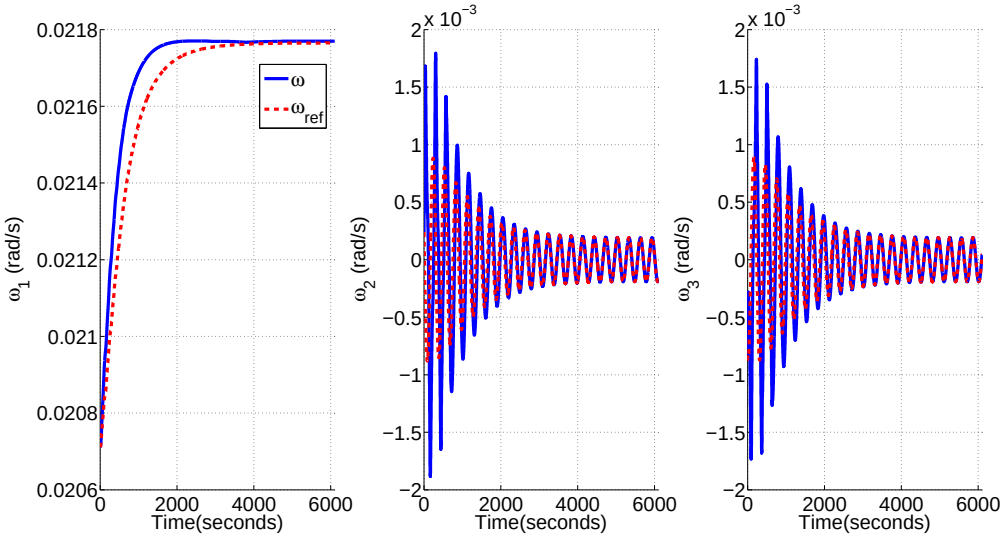

Figure 5.11: Inertially referenced angular velocities during pure spin manoeuvre for geocentric solar sail for Manoeuvre SR-A with a spin rate of $v = 0.0209\,\mathrm{rad/s}$.

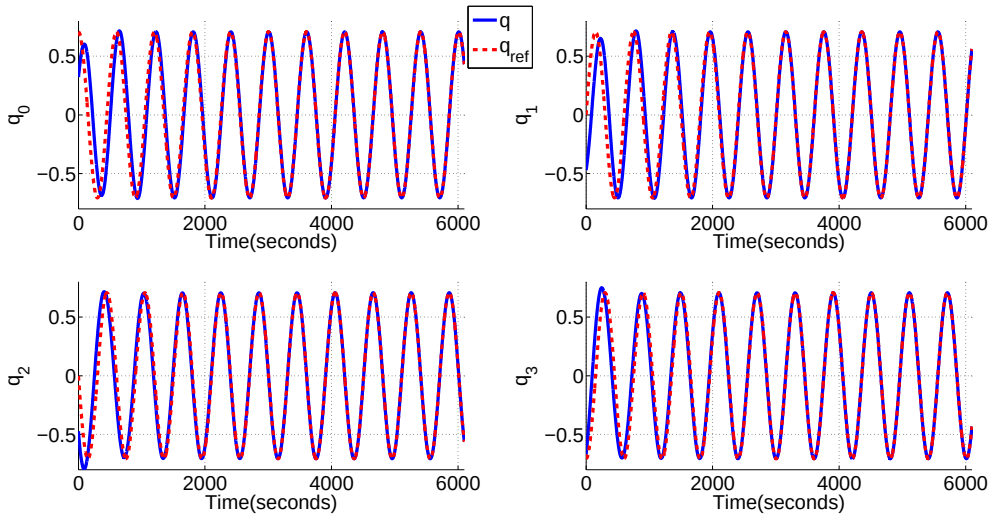

Figure 5.12: Orbit-referenced quaternions during pure spin manoeuvre for geocentric solar sail for Manoeuvre SR-A with a spin rate of $v = 0.0209\,\mathrm{rad/s}$.

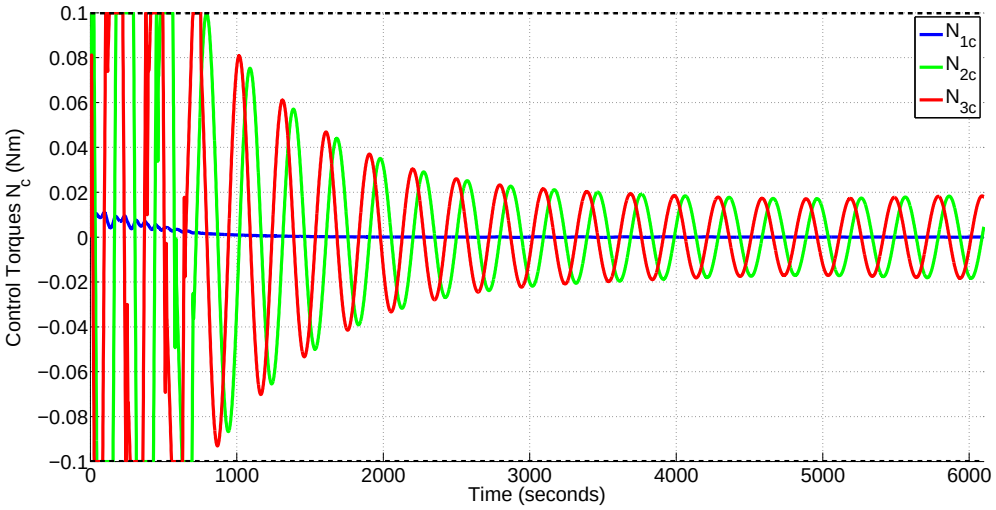

Figure 5.13: Control torques during pure spin manoeuvre for geocentric solar sail for Manoeuvre SR-A with a spin rate of $v = 0.0209\,\text{rad/s}$.

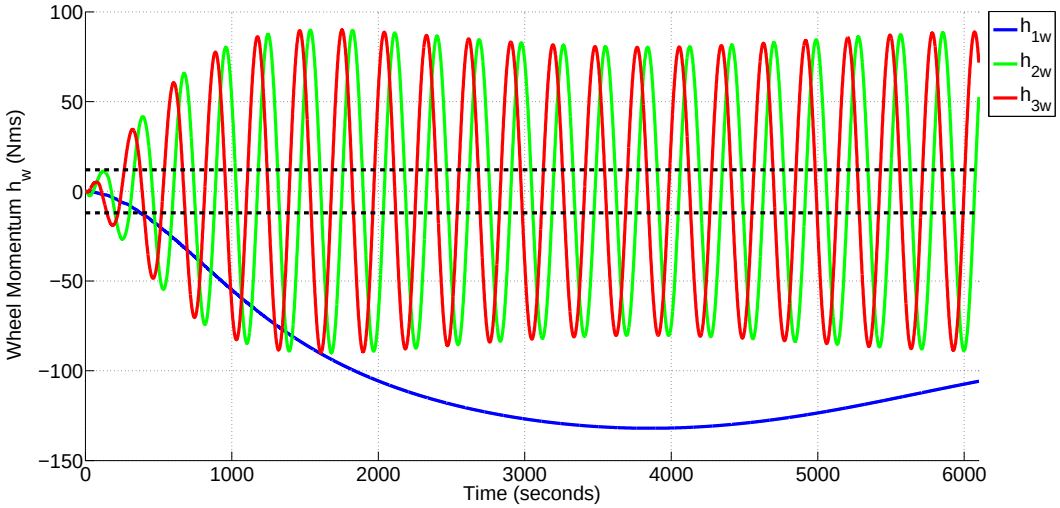

Figure 5.14: Wheel angular momentum during pure spin manoeuvre for geocentric solar sail for Manoeuvre SR-A with a spin rate of $v = 0.0209\,\text{rad/s}$.

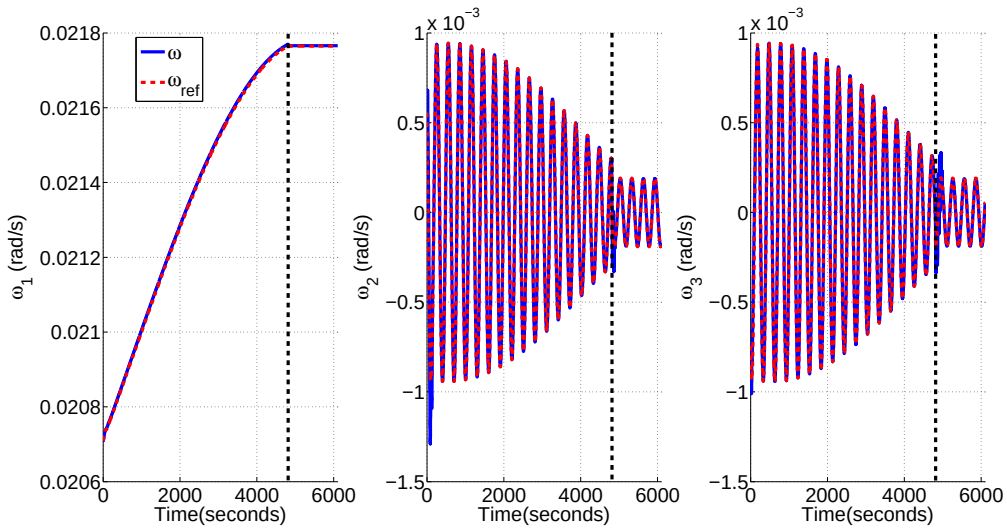

Figure 5.15: Inertially referenced angular velocities during spin repointing manoeuvre for geocentric solar sail for Manoeuvre SR-A with a spin rate of $v = 0.0209\,\mathrm{rad/s}$.

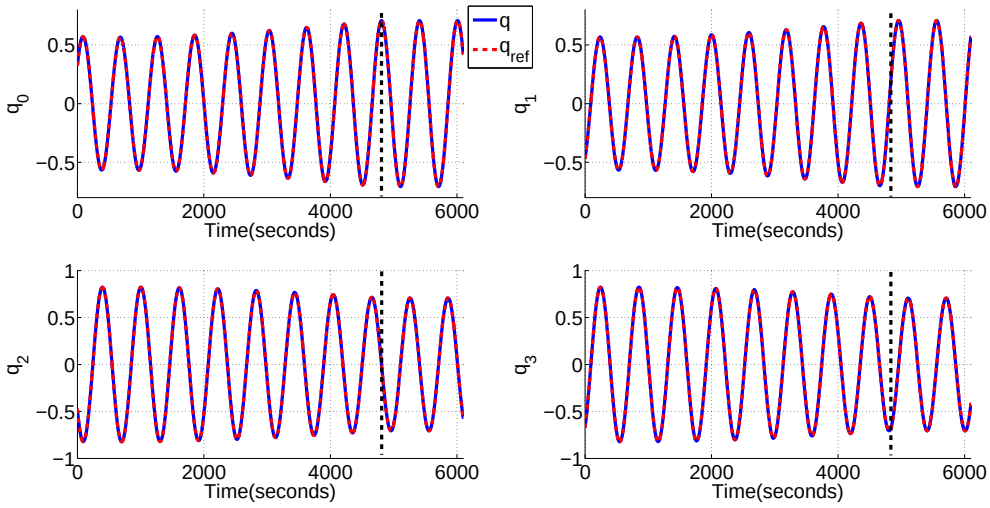

Figure 5.16: Orbit-referenced quaternions during spin repointing manoeuvre for geocentric solar sail for Manoeuvre SR-A with a spin rate of $v = 0.0209\,\mathrm{rad/s}$.

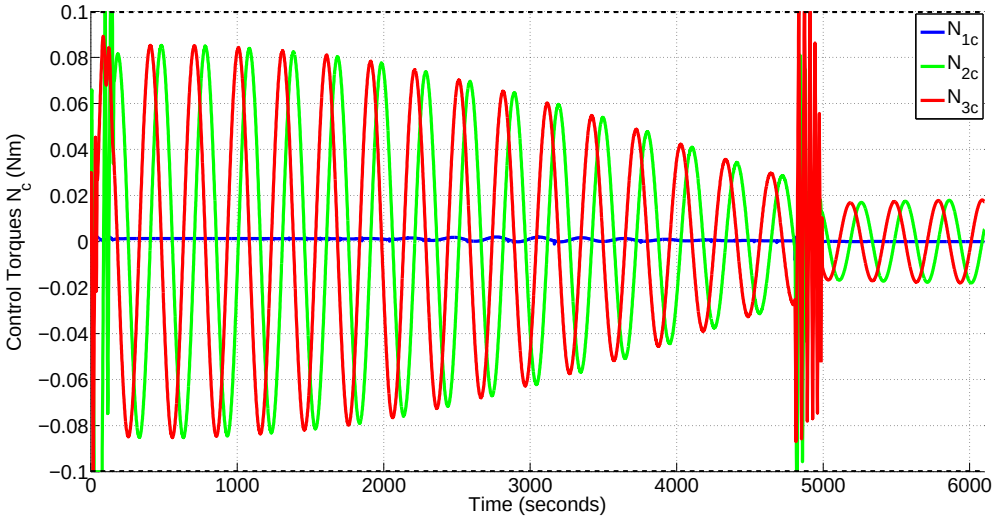

Figure 5.17: Control torques during spin repointing manoeuvre for geocentric solar sail for Manoeuvre SR-A with a spin rate of $v = 0.0209\,\text{rad/s}$.

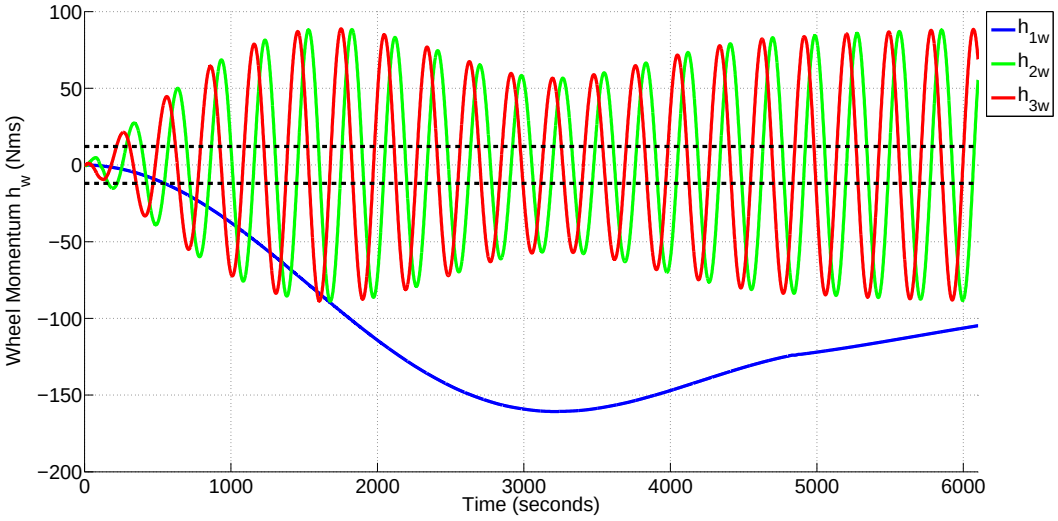

Figure 5.18: Wheel angular momentum during spin repointing manoeuvre for geocentric solar sail for Manoeuvre SR-A with a spin rate of $v = 0.0209\,\text{rad/s}$.

pure spin references. It should also be noted that both methods are infeasible with reaction wheels alone as actuators, as they quickly result in momentum saturation. Methods of tackling the momentum accumulation will be discussed in Section 5.6.

In this section a geocentric solar sail has been considered. However, Earth centred solar sails have primarily been considered as technology demonstration missions and the rapid attitude slews required to sustain an Earth orbit using solar sail propulsion alone has proven to be infeasible. Therefore in the following subsection a spacecraft in a heliocentric orbit is considered, where the continuous low-thrust propulsion can be more feasibly exploited.

5.4.2 Heliocentric Spinning Disk Solar Sail

In this subsection the reference motions are applied to the 70 m radius spinning disk sail, detailed in Table 5.1. The sail is assumed to be orbiting the Sun in a circular orbit at an altitude of 0.24 au. For the purposes of this study the sail is assumed to have minimal supporting structure, such as the "hoop" structure proposed by McInnes [33], to enable thrusters and other actuators under consideration to be mounted.

Figures 5.19 to 5.21 and 5.22 to 5.24 illustrate an 8000 s manoeuvre from $\bar{q}_{bo}(0) = [1 \quad 0 \quad 0 \quad 0]^T$ to $\bar{q}_{bo}(T) = [0.5 \quad 0.5 \quad 0.5 \quad 0.5]^T$, with a spin rate $v = 0.0209$ rad/s, for the pure spin and geometric spin repointing methods respectively.

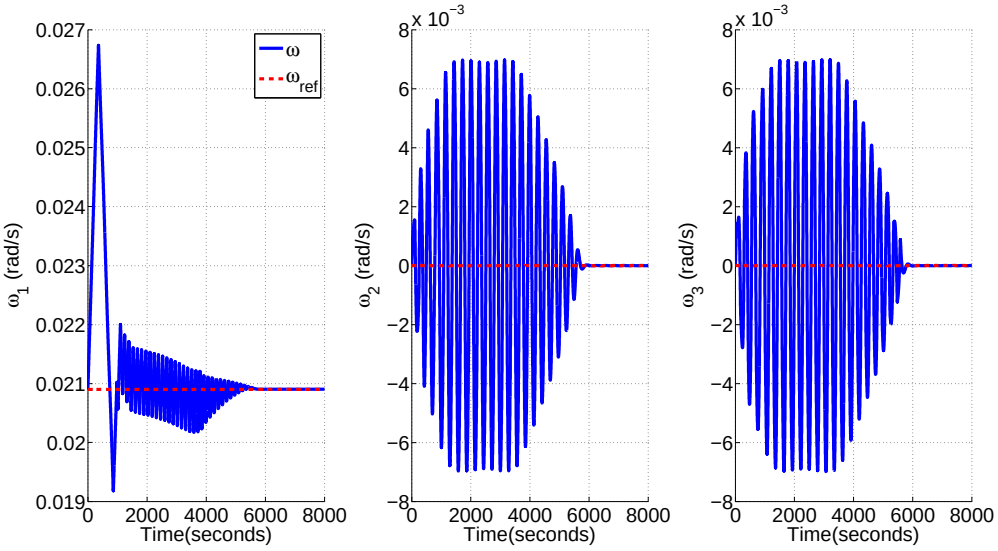

Figure 5.19: Inertially referenced angular velocities during pure spin manoeuvre for heliocentric solar sail for Manoeuvre SR-E with a spin rate of $v = 0.0209\,\mathrm{rad/s}$.

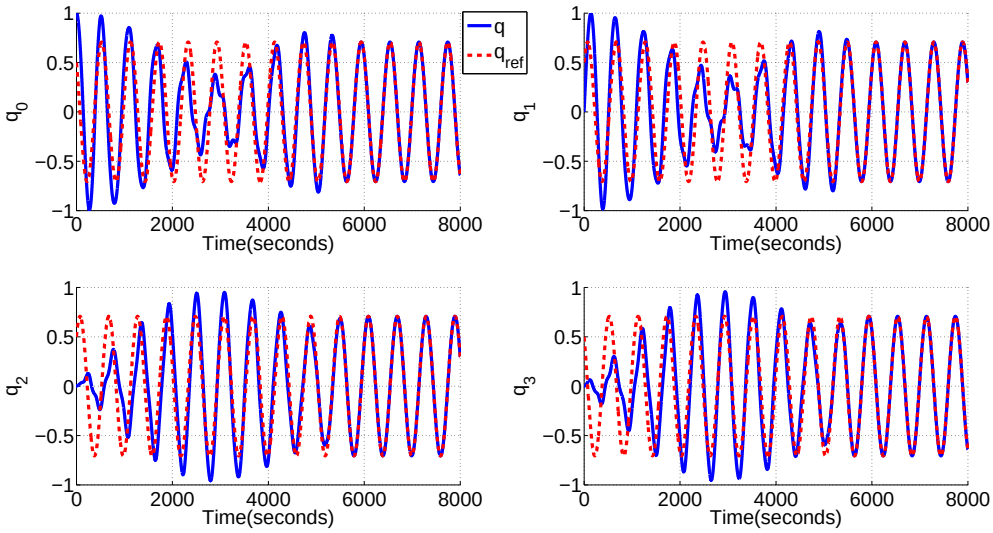

Figure 5.20: Orbit-referenced quaternions during pure spin manoeuvre for heliocentric solar sail for Manoeuvre SR-E with a spin rate of $v = 0.0209\,\mathrm{rad/s}$.

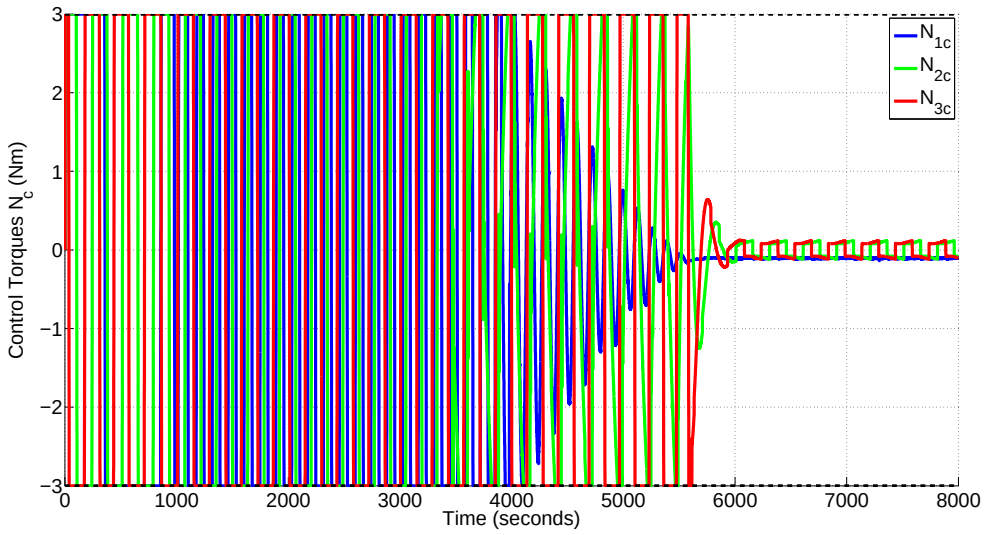

Figure 5.21: Control torques during pure spin manoeuvre for heliocentric solar sail for Manoeuvre SR-E with a spin rate of $v = 0.0209\,\mathrm{rad/s}$.

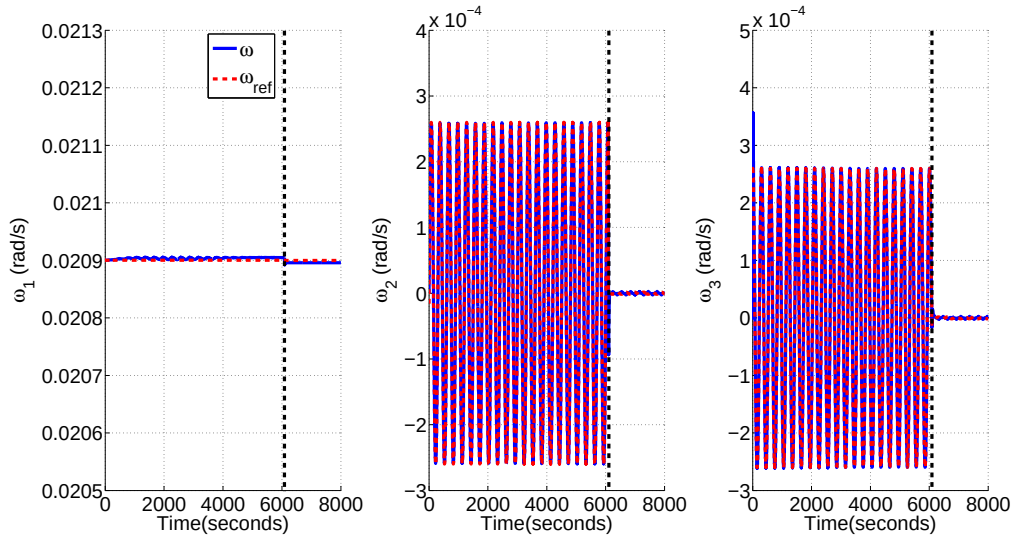

Figure 5.22: Inertially referenced angular velocities during spin repointing manoeuvre for heliocentric solar sail for Manoeuvre SR-E with a spin rate of $v = 0.0209\,\mathrm{rad/s}$.

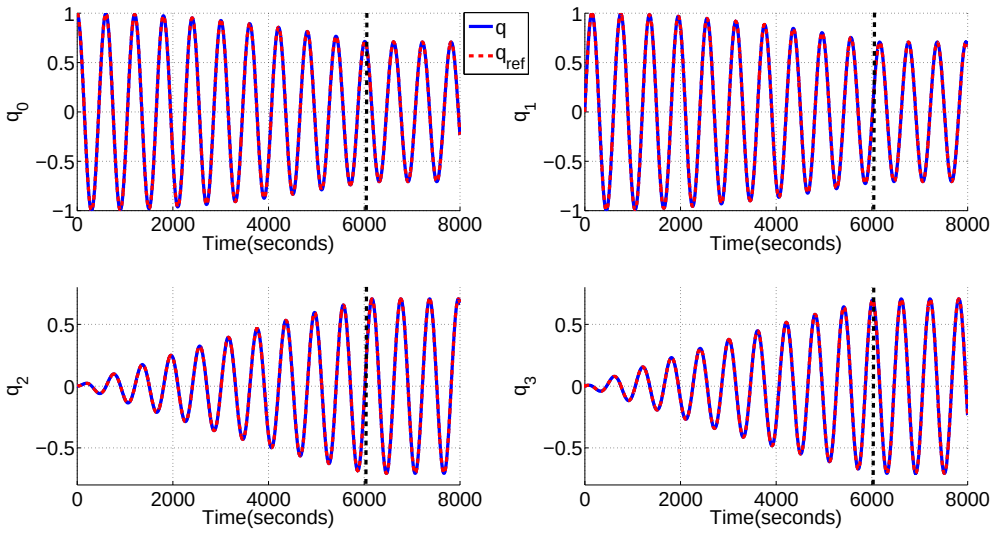

Figure 5.23: Orbit-referenced quaternions during spin repointing manoeuvre for heliocentric solar sail for Manoeuvre SR-E with a spin rate of $v = 0.0209\,\text{rad/s}$.

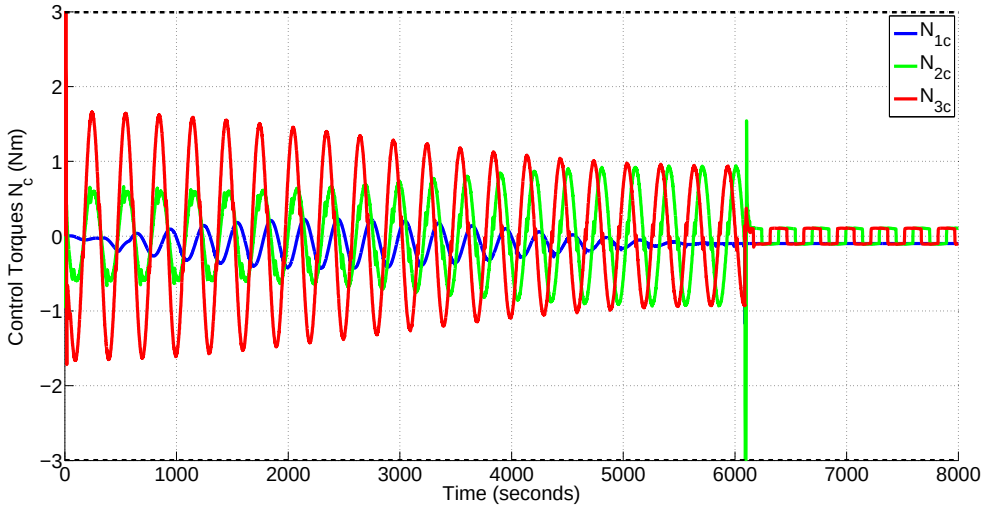

Figure 5.24: Control torques during spin repointing manoeuvre for heliocentric solar sail for Manoeuvre SR-E with a spin rate of $v = 0.0209\,\text{rad/s}$.

Tables 5.5 and 5.6 summarise the manoeuvres performed and their results.

Table 5.5: Labelling of attitude manoeuvres for heliocentric solar sail

Manoeuvre	Initial quaternion	Final quaternion
SR-D	$\bar{q}_{bo}(0) = [1 \quad 0 \quad 0 \quad 0]^T$	$\bar{q}_{bo}(T) = [0 \quad 1 \quad 0 \quad 0]^T$
SR-E	$\bar{q}_{bo}(0) = [1 \quad 0 \quad 0 \quad 0]^T$	$\bar{q}_{bo}(T) = [0.5 \quad 0.5 \quad 0.5 \quad 0.5]^T$
SR-F	$\bar{q}_{bo}(0) = [1 \quad 0 \quad 0 \quad 0]^T$	$\bar{q}_{bo}(T) = [\cos(\frac{7\pi}{72}) \quad 0 \quad -\sin(\frac{7\pi}{72}) \quad 0]^T$
SR-G	$\bar{q}_{bo}(0) = [\cos(\frac{7\pi}{72}) \quad 0 \quad -\sin(\frac{7\pi}{72}) \quad 0]^T$	$\bar{q}_{bo}(T) = [0 \quad -\cos(\frac{7\pi}{72}) \quad 0 \quad \sin(\frac{7\pi}{72})]^T$
SR-H	$\bar{q}_{bo}(0) = [-0.32 \quad -0.12 \quad -0.9 \quad 0.27]^T$	$\bar{q}_{bo}(T) = [0.46 \quad -0.74 \quad -0.03 \quad -0.5]^T$

Table 5.6: Comparison between pure spin references and geometric spin repointing references for heliocentric solar sail

Manoeuvre	v (rad/s)	Time (s)	${I_N}^{P.S.}$ (Nms)	${I_N}^{S.R.}$ (Nms)
SR-D	0.0209	4000	3×10^4	1.28×10^4
	0.00785	4500	1.23×10^4	4.8×10^3
SR-E	0.0209	8000	2.7×10^4	6.57×10^3
	0.00785	2500	5.4×10^3	2.72×10^3
SR-F	0.0209	2000	4.72×10^3	4.24×10^3
	0.00785	1000	1.55×10^3	NA
SR-G	0.0209	8000	3.81×10^4	6.8×10^3
	0.00785	4000	4.9×10^3	7.43×10^3
SR-H	0.0209	5000	2×10^4	1.05×10^4
	0.00785	4000	1.29×10^4	5.07×10^3

By inspection of Table 5.6, it is clear that the tracking of geometric spin repointing references offers savings in accumulated torque in the majority of manoeuvres, with lower peak angular velocities and fewer instances of torque saturation in all manoeuvres. However, once again in certain cases the motion planner for geometric spin repointing is not capable of producing a motion which is trackable for the given torque constraints, and for Manoeuvre SR-G for $v = 0.007\,85\,\text{rad/s}$ the pure spin references required lower overall accumulated torque to track.

Note that the geometric spin repointing reference tracking performed better in comparison to the pure spin references for the heliocentric sail than it did for the geocentric sail. This is again possibly due to the references being tracked with respect to the orbital frame rather than the inertial frame. For a heliocentric orbit at 0.24 au the orbital angular velocity term is of the order $10^{-6}\,\text{rad/s}$ in comparison to $10^{-3}\,\text{rad/s}$ in an 800 km altitude geocentric orbit. Therefore the orbital term has almost negligible

effect on the tracking of the references for the heliocentric sail, but significantly alters the angular velocity reference tracks for the geocentric sail. However, as solar sail attitude manoeuvres are primarily performed in order to reorientate the thrust vector for orbital manoeuvres, the performance of the geometric spin repointing method when tracking with respect to the orbital frame is of most relevance.

5.4.3 Constrained Repointing

In this section the set of motions which satisfy the boundary conditions on the target attitude are probed to generate a constrained repointing manoeuvre for the heliocentric solar sail. In contrast to the obstacle avoidance manoeuvre of Chapter 4, in this section the body x-axis unit vector is constrained to lie within the cone generated by the Sun. A 1200 s slew from $\bar{q}_{bo}(0) = [1 \quad 0 \quad 0 \quad 0]^T$ to $\bar{q}_{bo}(T) = [-0.49 \quad 0.67 \quad 0.51 \quad 0.22]^T$ for the heliocentric sail from Section 5.4.2 was considered, with the body x-axis unit vector given by $[1 \quad 0 \quad 0]^T$. The centre of the cone is specified as $n_c = [0.71 \quad 0.071 \quad 0.71]^T$ and the cone half angle as $\delta_c = 68°$. The initial optimisation to minimise the cost function (5.47) yields a solution which violates this constraint, as shown in Figure 5.25.

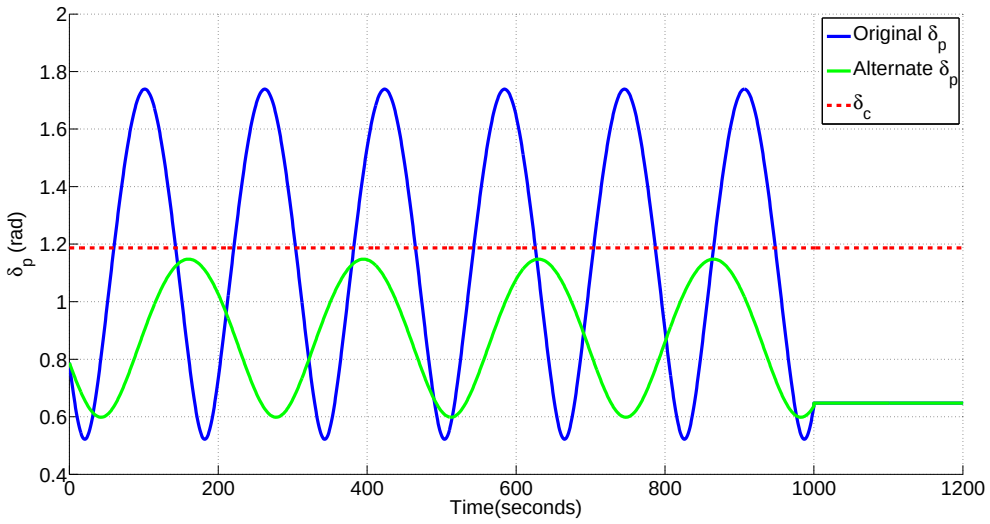

Figure 5.25: Angle between body x-axis and cone centreline unit vectors for manoeuvre from $\bar{q}_{bo}(0) = [1 \quad 0 \quad 0 \quad 0]^T$ to $\bar{q}_{bo}(T) = [-0.49 \quad 0.67 \quad 0.51 \quad 0.22]^T$. Original and alternate manoeuvres are shown.

Incrementing the free parameters by p_1, p_2 and p_3 respectively and performing a further parametric optimisation to minimise the cost function (5.47) leads to an alternate manoeuvre which does not violate the constraint. Therefore the geometric spin repointing method has been used to generate a constrained slew.

5.5 Application to a Nano-Spacecraft

In this section the geometric spin repointing references are applied to the nano-spacecraft of Chapter 4 and compared to the axisymmetric natural motion references and quaternion feedback, in addition to the pure spin references. The application to a spinning solar sail showed that in a high disturbance environment, the geometric spin repointing and pure spin references result in significant momentum accumulation. Additionally, the geometric spin repointing references did not always produce the lowest control effort manoeuvres. Thus the purpose of this section is two-fold - to assess the performance of the geometric spin repointing references when applied to a spacecraft in a low-disturbance environment and to compare the results with the natural motion method.

Initially the geometric spin repointing method was stabilised to a state of pure spin as in the solar sail simulations (5.48), and compared to the pure spin references. Thereafter, the simulations were repeated and the nano-spacecraft brought to rest at the target, as for the natural motion references (4.82). In order to enable a comparison to be made with the axisymmetric natural motion method, the manoeuvres of Section 4.4.1 were repeated using the geometric spin repointing method and the tracking completed with respect to the inertial frame.

5.5.1 Comparison to Pure Spin References

A manoeuvre from $\bar{q}(0) = [1 \quad 0 \quad 0 \quad 0]^T$ to $\bar{q}(T) = [0.5 \quad 0.5 \quad 0.5 \quad 0.5]^T$ in a time of $T = 120\,\text{s}$, with a spin rate of $v = 5.236 \times 10^{-3}\,\text{rad/s}$, was simulated. The gains used in the simulation were $k_\omega = 1.7$ and $k_q = 0.29$ for the pure spin references and $k_\omega = 1.7$

and $k_q = 0.83$ for the geometric spin repointing references. The results are shown in Figures 5.26 to 5.28 for the pure spin reference tracking, and Figures 5.29 to 5.31 for the geometric spin repointing.

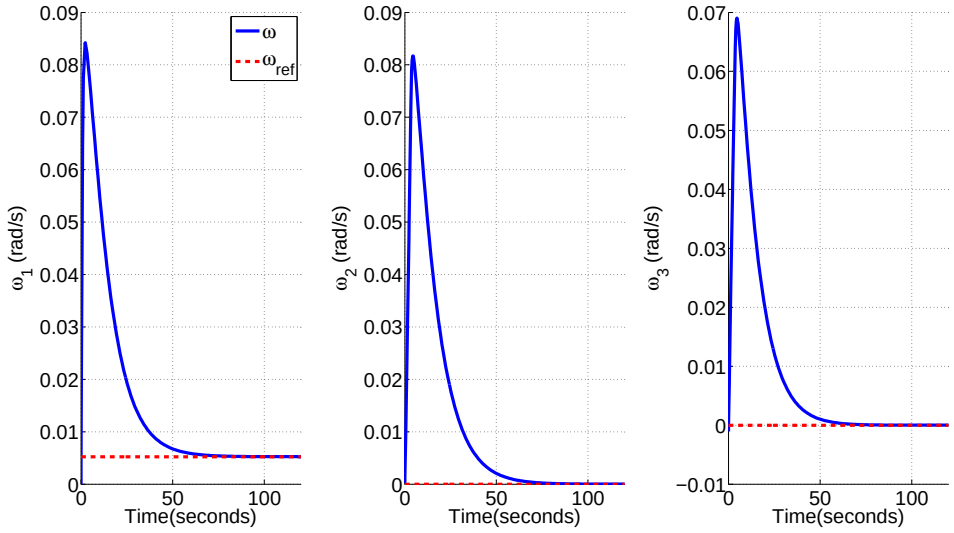

Figure 5.26: Angular velocities during pure spin manoeuvre for axisymmetric spacecraft for Manoeuvre NM-A with a spin rate of $v = 5.236 \times 10^{-3}$ rad/s.

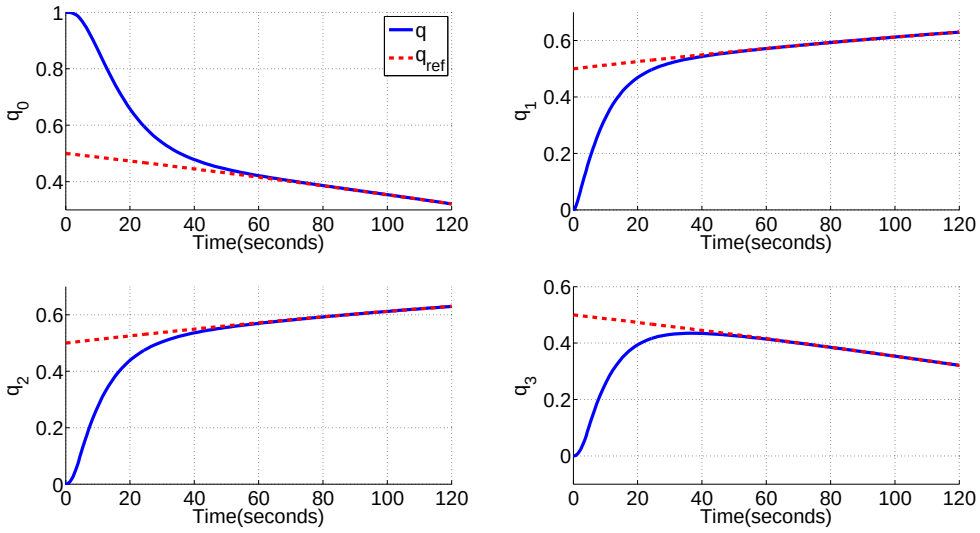

Figure 5.27: Quaternions during pure spin manoeuvre for axisymmetric spacecraft for Manoeuvre NM-A with a spin rate of $v = 5.236 \times 10^{-3}$ rad/s.

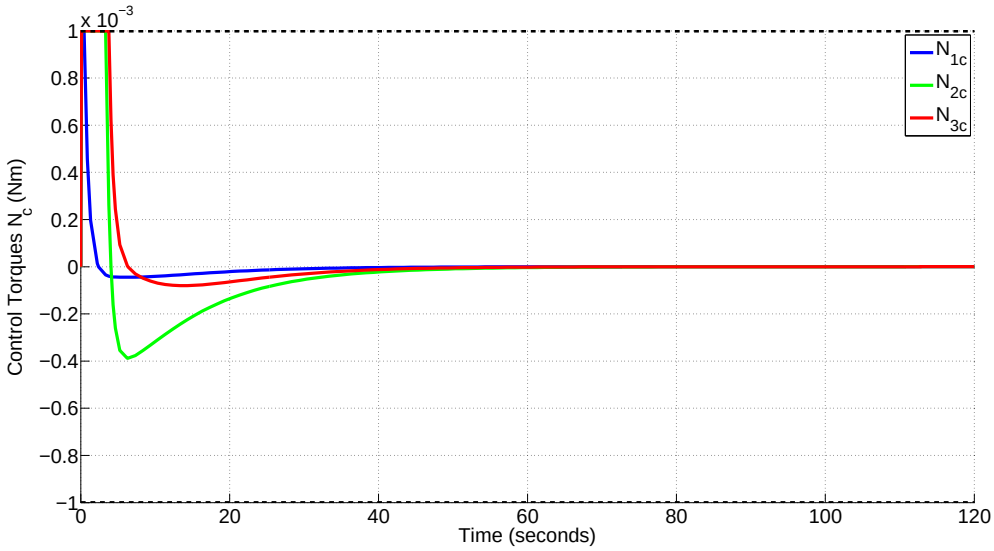

Figure 5.28: Control torques during pure spin manoeuvre for axisymmetric spacecraft for Manoeuvre NM-A with a spin rate of $v = 5.236 \times 10^{-3}$ rad/s.

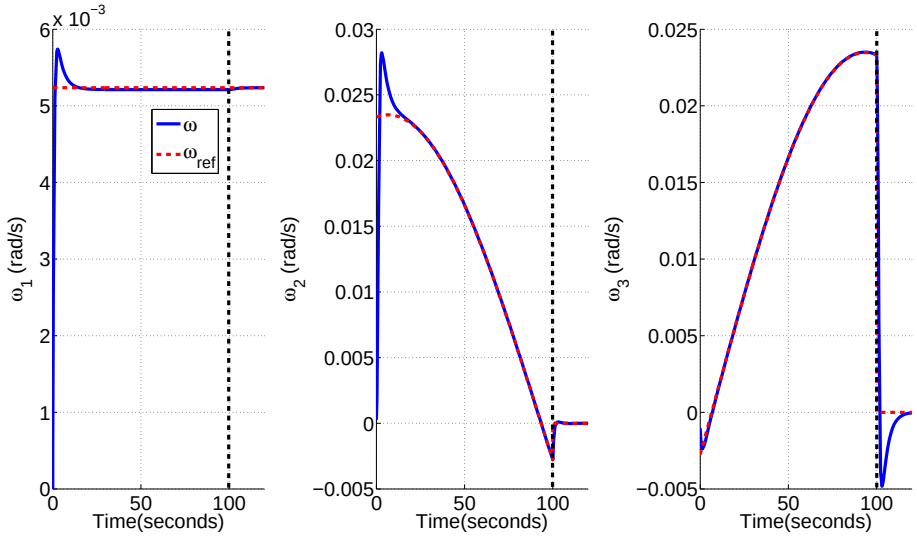

Figure 5.29: Angular velocities during spin repointing manoeuvre for axisymmetric spacecraft for Manoeuvre NM-A with a spin rate of $v = 5.236 \times 10^{-3}$ rad/s.

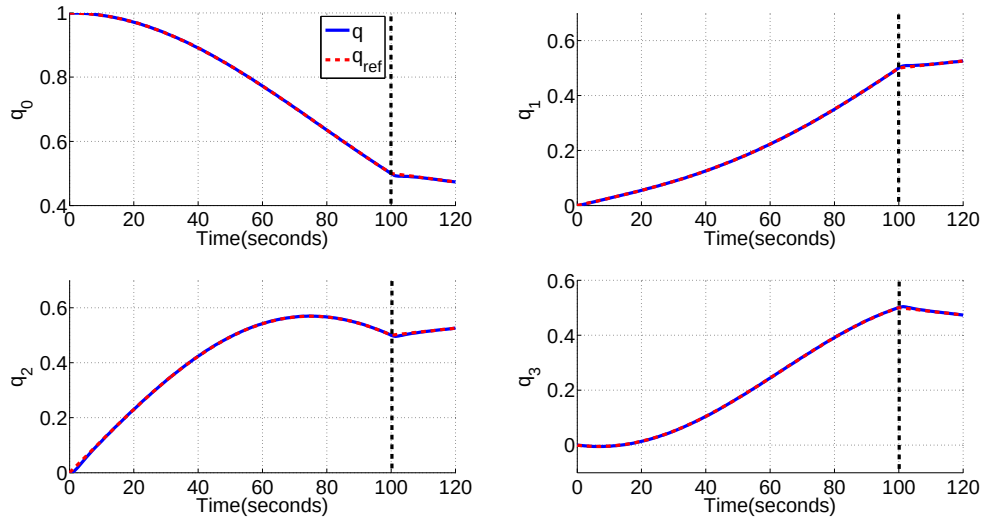

Figure 5.30: Quaternions during spin repointing manoeuvre for axisymmetric spacecraft for Manoeuvre NM-A with a spin rate of $v = 5.236 \times 10^{-3}$ rad/s.

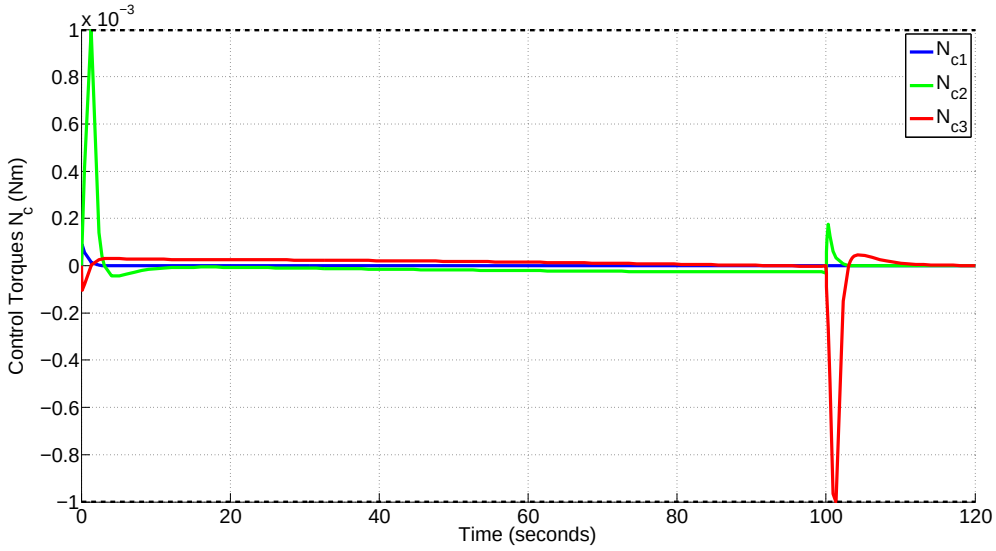

Figure 5.31: Control torques during spin repointing manoeuvre for axisymmetric spacecraft for Manoeuvre NM-A with a spin rate of $v = 5.236 \times 10^{-3}$ rad/s.

The results of this and several other manoeuvres are shown in Table 5.7.

Table 5.7: Spin repointing and pure spin reference tracking for axisymmetric spacecraft. $T = 120\,\text{s}$.

Manoeuvre	${I_N}^{P.S}$ (Nms)	${I_N}^{S.R}$ (Nms)
NM-A	0.0119	0.0057
NM-B	0.0111	0.0077
NM-C	0.0105	0.0062
NM-D	0.0159	0.0077
NM-E	0.0098	0.0024

It is clear that in comparison to the pure spin references, the geometric spin repointing references offer significant savings in accumulated torque for the nano-spacecraft spinning at $v = 5.236 \times 10^{-3}\,\text{rad/s}$. Additionally, the body rates are smaller during the geometric spin repointing manoeuvres.

These results again suggest that the geometric spin repointing method is more effective when tracking with respect to an inertial or near-inertial reference frame. Additionally, the nano-spacecraft is subjected to significantly smaller disturbance torques than a large solar sail, and thus the geometric method may be more suited to spacecraft in a low disturbance environment.

5.5.2 Comparison to Natural Motion References

The geometric spin repointing references were then compared with the natural motion references and quaternion feedback manoeuvres of Section 4.4.1. To this end, the spacecraft was brought to rest at the target as in the natural motion simulations, rather than to a state of pure spin. Figures 5.32 to 5.34 show the results of the rest-to-rest tracking of geometric spin repointing references for manoeuvre NM-C from Table 4.3, with $v = 5.236 \times 10^{-3}\,\text{rad/s}$.

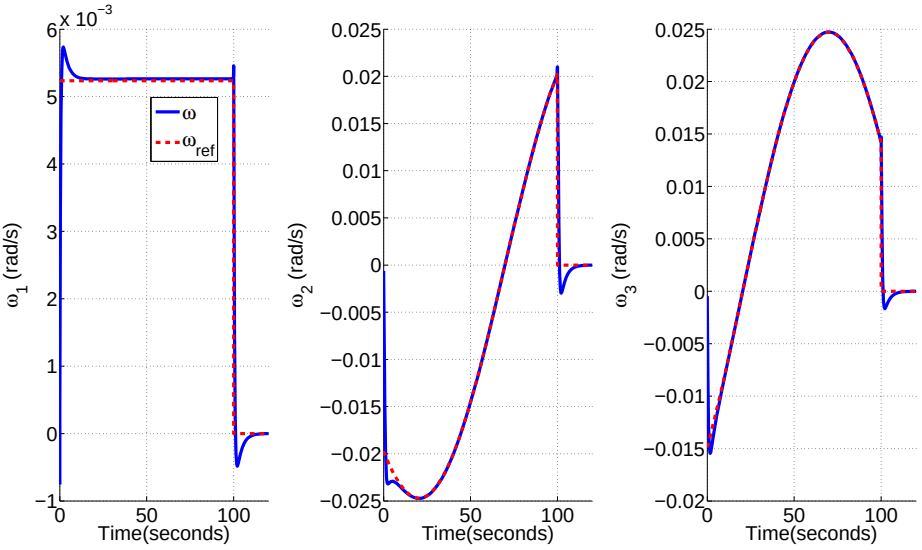

Figure 5.32: Angular velocities during rest-to-rest spin repointing manoeuvre for axisymmetric spacecraft for Manoeuvre NM-A with a spin rate of $v = 5.236 \times 10^{-3}\,\mathrm{rad/s}$.

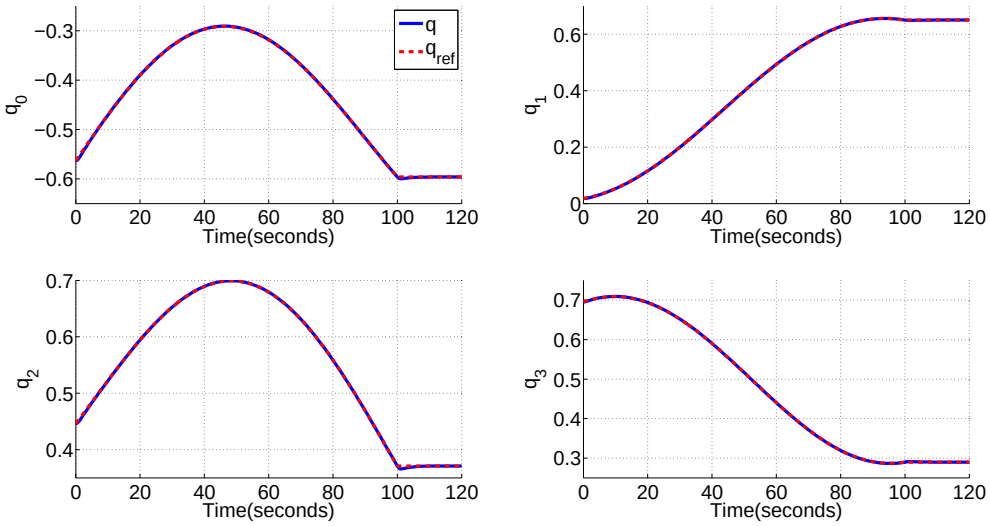

Figure 5.33: Quaternions during rest-to-rest spin repointing manoeuvre for axisymmetric spacecraft for Manoeuvre NM-A with a spin rate of $v = 5.236 \times 10^{-3}\,\mathrm{rad/s}$.

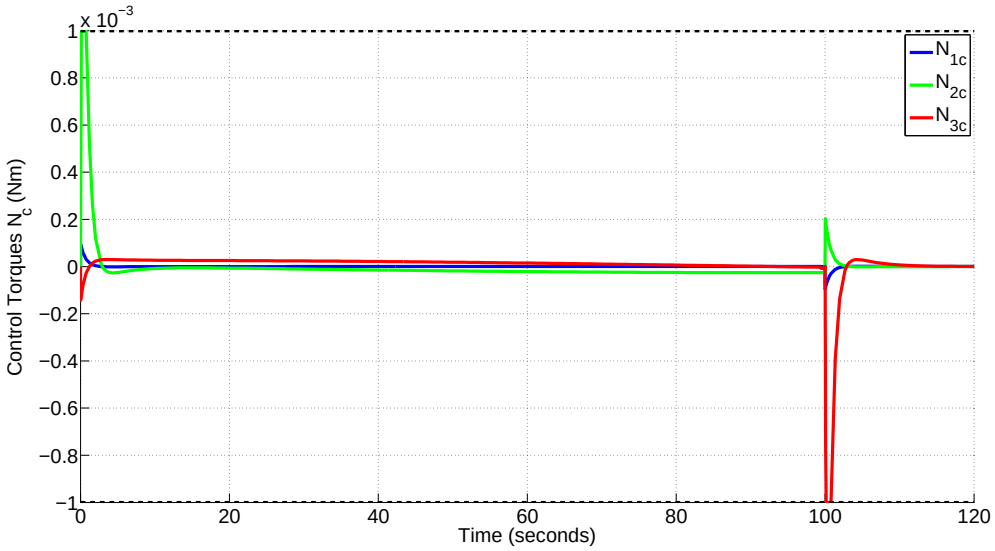

Figure 5.34: Control torques during rest-to-rest spin repointing manoeuvre for axisymmetric spacecraft for Manoeuvre NM-A with a spin rate of $v = 5.236 \times 10^{-3}$ rad/s.

The results of the geometric spin repointing manoeuvres are shown in Table 5.8.

Table 5.8: Quaternion feedback, natural motion reference tracking and geometric spin repointing reference tracking for axisymmetric spacecraft. $T = 120$ s.

Manoeuvre	${I_N}^{Q.F.}$ (Nms)	${I_N}^{N.M(Axi)}$ (Nms)	${I_N}^{S.R}$ (Nms)
NM-A	0.0068	0.0025	0.0057
NM-B	0.0103	0.0014	0.0077
NM-C	0.0086	0.0013	0.0062
NM-D	0.0146	0.003	0.0077
NM-E	0.0046	0.0018	0.0024

The geometric spin repointing references offer savings in accumulated torque over the quaternion feedback benchmark, but require more accumulated torque than the natural motions. Note also that in contrast to the natural motion references the geometric spin repointing references require a small torque throughout the manoeuvre to track the references. Therefore they cannot be utilised in a "bang-off-bang" manner.

It is interesting to note, however, that if the spin rate v is entered into the parametric optimisation of Section 5.3.1 as a free parameter, then the optimal spin rate is found

to be the natural motion spin rate, and the geometric spin repointing motion planner returns a natural motion. Therefore the axisymmetric natural motions are a subset of the geometric spin repointing motion planner, and offer the largest savings in accumulated torque. As a result, the geometric spin repointing manoeuvres which require larger accumulated torque than the pure spin benchmark may be those which are far from the natural motion for the manoeuvre.

5.6 Solar Sail Actuator Study

It is clear from the results of the simulations in Section 5.4, that the actuation of spinning solar sails is non-trivial as conventional actuators such as reaction wheels quickly saturate due to the solar radiation pressure disturbance torques caused by the centre of mass/centre of pressure offset. For the 40 m geocentric sail considered in this thesis, with no spin rate constraint, Wie showed that the reaction wheels could be desaturated using 100 Am^2 magnetorquers and the simple control law [32]

$$\bar{u}_{des} = -K_{desat}(\bar{h}_w - \bar{h}_{wd}) \tag{5.50}$$

where $\bar{u}_{des}$ is the desaturation control signal, K_{desat} is a scalar gain, $\bar{h}_w$ is the reaction wheel angular momentum vector from Equation (4.3) and $\bar{h}_{wd}$ is the desired wheel momentum vector. When using magnetorquers for desaturation, the requested dipole of the magnetorquer is then $\bar{M}_{mtq} = \underset{M_{max}}{sat}\{\bar{u}_{des}\}$, where M_{max} is the maximum requested dipole in each axis. The control torques are subsequently obtained from Equation (5.4). At the spin rates considered in this chapter, desaturation using magnetorquers is not feasible for the spin-type solar sails. This is illustrated in Figures 5.35 to 5.37 for Manoeuvre SR-C from Table 5.3, in 3600 s for a spin rate of $v = 0.007\,85$ rad/s.

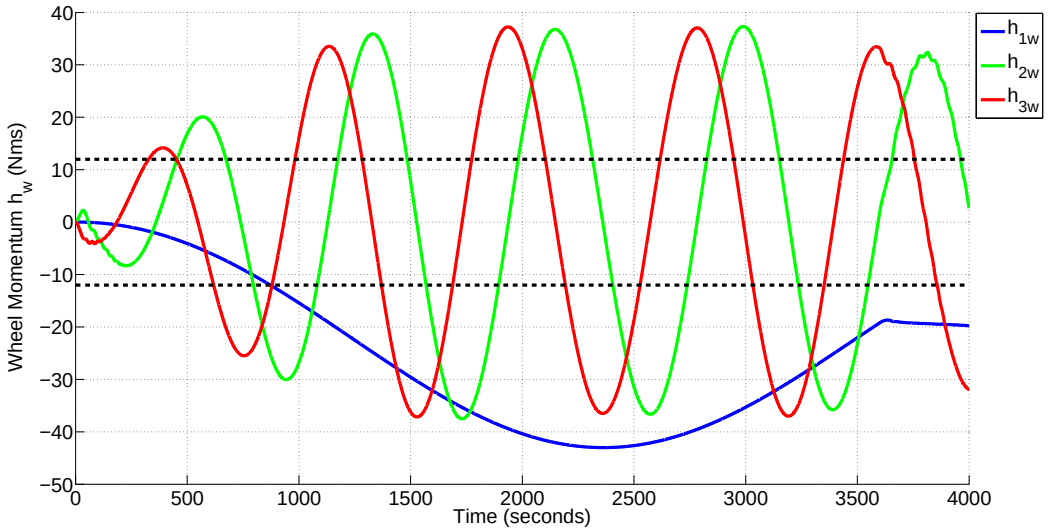

Figure 5.35: Angular momentum of reaction wheels without desaturation for Manoeuvre SR-C in 3600 s for $v = 0.007\,85$ rad/s.

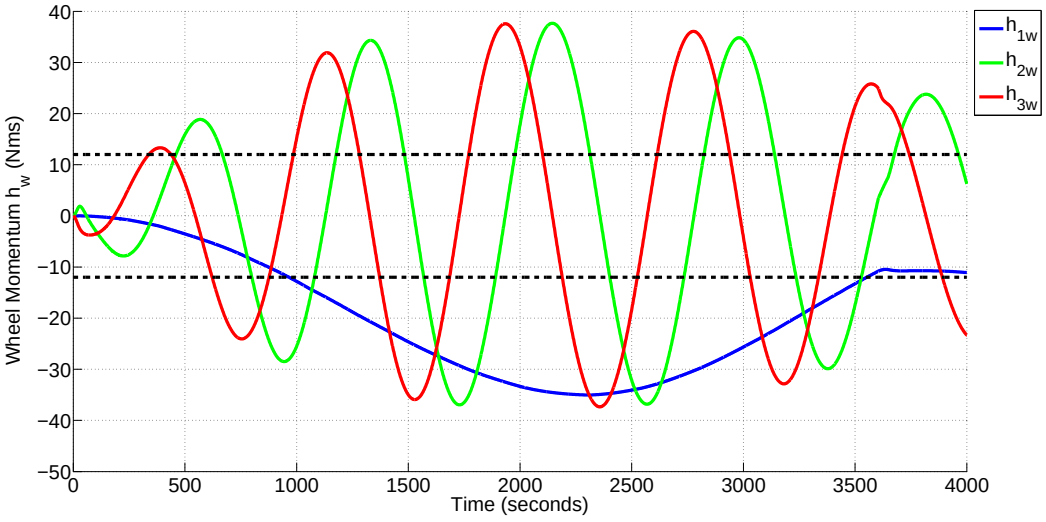

Figure 5.36: Angular momentum of reaction wheels using magnetorquers for desaturation for Manoeuvre SR-C in 3600 s for $v = 0.007\,85$ rad/s.

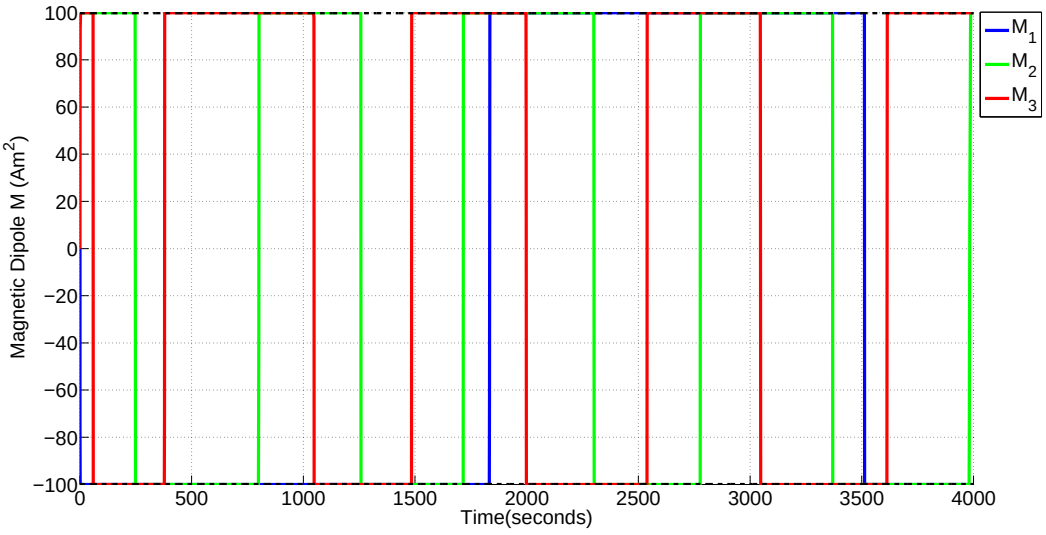

Figure 5.37: Requested dipole of magnetorquers during momentum unloading of reaction wheels for Manoeuvre SR-C in 3600 s for $v = 0.007\,85\,\text{rad/s}$.

While the magnetorquers decrease the momentum of the reaction wheels slightly they do not bring the wheel momenta to within acceptable limits, despite the $100\,\text{Am}^2$ magnetorquers supplying the maximum possible torque. Therefore it is clear that the $100\,\text{Am}^2$ magnetorquers suggested by Bong Wie are not suitable for momentum unloading of the reaction wheels when applied to a spinning sail. As a result, another form of desaturation, such as thrusters, would be required in the case of a spinning sail. Repeating the simulations with continuous actuators in place of the magnetorquers, an initial sizing of the thrusters necessary for momentum unloading of the geocentric solar sail reaction wheels can be carried out. The desaturation control torque vector is denoted $\bar{N}_{des} = [\bar{N}_{des} \quad \bar{N}_{des} \quad \bar{N}_{des}]^T$. For continuous actuators $\bar{N}_{des} = \underset{N_{des(max)}}{sat}\{\bar{u}_{des}\}$ where $N_{des(max)}$ is the maximum available desaturation control torque in each axis, the value of which is to be determined. The results are shown in Figures 5.38 and 5.39.

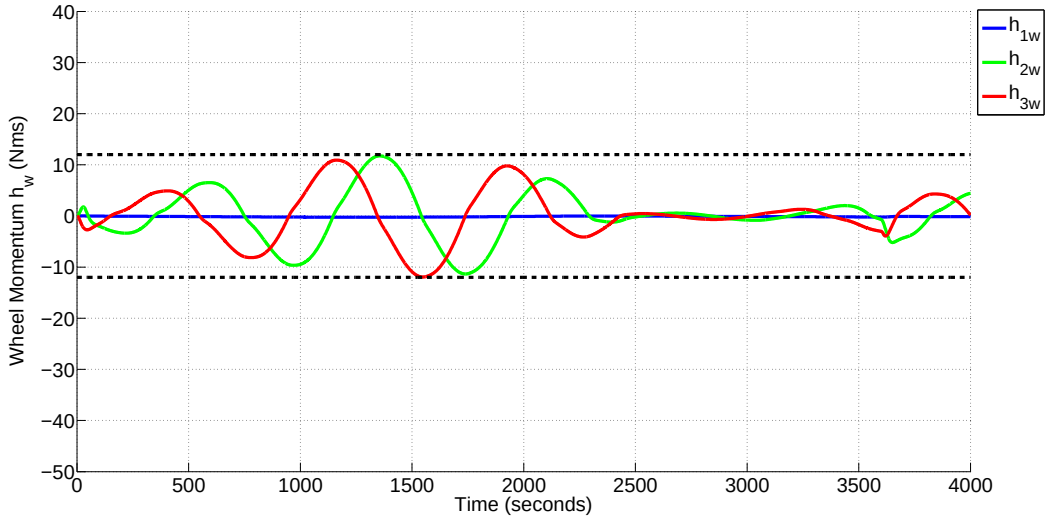

Figure 5.38: Momentum of reaction wheels using continuous actuators for desaturation for Manoeuvre SR-C in 3600 s for $v = 0.007\,85$ rad/s.

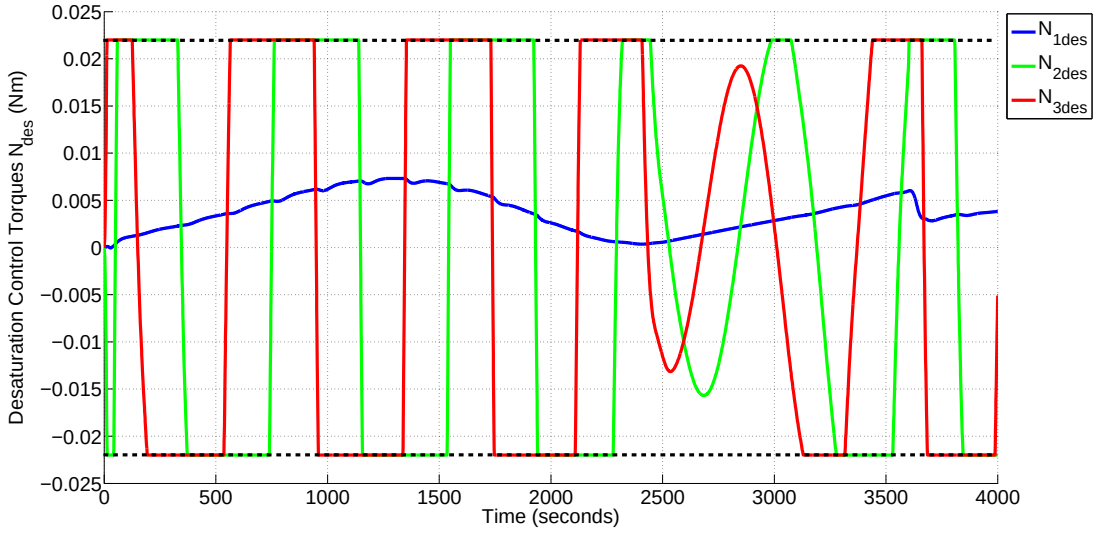

Figure 5.39: Desaturation control torques during momentum unloading of reaction wheels for Manoeuvre SR-C in 3600 s for $v = 0.007\,85$ rad/s.

Therefore for Manoeuvre SR-C, a maximum torque of 0.022 Nm is necessary to desaturate the reaction wheels using continuous actuators. Repeating the simulations in Table 5.3 using continuous actuators for desaturation, it was found that for the $v = 0.0209$ rad/s spin rate the reaction wheels cannot be desaturated using continu-

ous actuators. In these cases, the control torques required to desaturate the reaction wheels are of the same order as the control torques supplied by the reaction wheels, and reference tracking is not possible. For the $v = 0.007\,85\,\text{rad/s}$ spin rate, the continuous actuators must be capable of providing a thrust between $0.022 - 0.029\text{Nm}$ in order to keep the wheel momenta within the $\pm 12\,\text{Nms}$ limits. Therefore, if thrusters mounted at the tips of the 40 m square sail were used for desaturation, they would have a moment arm of 28.3 m and thus would need to be capable of producing a thrust of $1.025 \times 10^{-3}\,\text{N}$ in order to supply the required desaturation control torques. However, despite their inclusion on IKAROS and their ability to function either as primary or a secondary actuators, thrusters are impulsive and so can cause the sail film to oscillate undesirably, while the propellant can contaminate the sail film resulting in a loss of performance. Therefore it may not be feasible to implement thrusters for desaturation. For heliocentric spinning solar sails, in addition to swift momentum accumulation, conventional reaction wheels are not feasible due to the large required peak torques of between $3 - 7\text{Nm}$ for the 70 m radius sail. Reaction wheels currently in production are only capable of producing peak torques of up to 2 Nm [58]. However control moment gyros (CMGs), gimballed spinning wheels which produce control torques by changing the direction of the angular momentum vector, are capable of producing larger torques [32]. For example the four gimbal arrangement on-board the Pleiades High-Resolution imaging spacecraft could produce an average maximum torque of 20 Nm [32], while on manned spacecraft control moment gyros have produced torques of up to 200 Nm [58]. Nevertheless control moment gyros are generally heavier than reaction wheels for a given momentum storage, and thus have not been suggested as feasible actuators for a solar sail presumably due to the attendant increase in mass.

These difficulties with conventional actuators have resulted in several new methods of actuating solar sails being proposed. These alternative methods were described in the introduction to this chapter, and include control booms, sliding masses, reflectivity controlled devices (RCDs) and control vanes. These methods seek to control the offset between the centre of mass and centre of pressure of the sail. The action of the SRP force on the sail then generates continuous control torques, without the need for

propellant. The advantages and disadvantages of these methods, together with the conventional actuators, are summarised in Table 5.9.

Table 5.9: Advantages and disadvantages of different solar sail actuators.

Actuator	Advantages	Disadvantages
Reaction Wheels	Strong flight heritage, continuous independent 3-axis control torques	Momentum saturation, heavy, lower torque capability than CMGs
CMGs	3-axis control torques, large torques	Heavier than RWs, gimbal-lock
Thrusters	Strong flight heritage, independent 3-axis control torques, large torques	Impulsive, mission lifetime limited due to propellant consumption
Control Booms	Propellantless, continuous control torques	Weak flight heritage, boom poses engineering challenge, cross-coupling between torques, time-varying inertia
Sliding Masses	Propellantless, continuous control torques, less complex than booms	Weak flight heritage, actuation of masses required, cross-coupling between torques, time-varying inertia
RCDs	Propellantless, continuous control torques, few mechanical parts, some flight heritage	Small torques, only small reorientations demonstrated
Control Vanes	Propellantless, continuous control torques, relatively few mechanical parts	Weak flight heritage, actuation of vanes required, cross-coupling between torques

In the remainder of this section, the possibility of implementing sliding masses and control vanes as actuators on a spinning sail will be discussed, together with the feasibility of using these actuators to track the reference motions detailed in this chapter.

5.6.1 Sliding Masses

The sliding mass method for solar sail actuation changes the distance between the centre of mass and centre of pressure of the spacecraft by moving controllable masses to a specific point on the surface of the solar sail. Several configurations have been proposed, from a simple two-mass system which moves along the sail supporting structure [32], to a configuration where the entire payload is moved [123]. In this section, the feasibility of implementing the two-mass method is investigated.

Assuming that there is no offset in the $\hat{i}$ body axis i.e. $\bar{r}_{m/p} = [0 \quad r_{2m/p} \quad r_{3m/p}]^T$, the available torques $\bar{N}_{sm} = [N_{1sm} \quad N_{2sm} \quad N_{3sm}]^T$ due to an offset between the centre of mass and centre of pressure can be found from [32, 123]:

$$\bar{N}_{sm} = (r_{2m/p}F_{3SRP} - r_{3m/p}F_{2SRP})\hat{i} + (r_{3m/p}F_{1SRP})\hat{j} - (r_{2m/p}F_{1SRP})\hat{k} \tag{5.51}$$

From Equation (5.51), the torques in the $\hat{j}$ and $\hat{k}$ body axes directions are dependent solely on the F_{1SRP} component of the SRP force. For the axisymmetric solar sail, these directions require the largest control torques. Therefore it suffices to find the maximum value of F_{1SRP}. For the geocentric sail in an 800 km altitude orbit, the maximum value of $F_{1SRP} = 9.351 \times 10^{-3}$ N. Similarly for the heliocentric sail in a 0.24 au altitude orbit, the maximum value of $F_{1SRP} = 2.43$ N. From Section 5.4, the geocentric sail requires a maximum torque of 0.1 Nm and the heliocentric sail requires a maximum torque of 7 Nm. It follows from the maximum solar radiation pressure forces for the geocentric and heliocentric sails that the centre of mass/centre of pressure offsets needed to produce these torques are 10.7 m and 2.88 m respectively. Clearly, a much larger offset is required in the geocentric case as a result of the much weaker solar radiation pressure force at approximately 1 au in comparison to the heliocentric sail at 0.24 au. The distances and masses required to produce the necessary offset can then be calculated using the expression

$$\bar{r}_{m/p} = \frac{m_{sm}}{m_{s/c}}(0\hat{i} + y\hat{j} + z\hat{k}) \tag{5.52}$$

where m_{sm} is the mass of the translating mass(es), $m_{s/c}$ is the total mass of the spacecraft (including the translating masses) and y and z are the distances the mass(es) are required to move along the $\hat{j}$ and $\hat{k}$ body axes respectively. From Equation (5.52) it is clear that in order to produce the required offset, there is a trade-off between the mass of the translating masses and the distance moved. For the geocentric sail, assuming that the masses can move along the full length of the sail ($\pm$28 m [32]) then a single mass of 32.5 kg is required to produce an offset of 10.7 m in either the $\hat{j}$ or $\hat{k}$ body axes. This mass is approximately equal to one half of the mass of the spacecraft excluding the solar sail, and so would likely be infeasible for practical implementation for tracking of the geometric spin repointing method. Moving a mass of 32.5 kg to the extremities of the sail would cause a large variation in the inertia of the spacecraft, affecting the performance of the references. Additionally, the mechanical effort required to move a mass of that size would pose a considerable engineering challenge. In the case of the

heliocentric sail the masses involved are more feasible, with a mass of 11.54 kg required at a distance of ±70 m to produce the necessary 2.88 m offset. However, the sliding mass method would be difficult to implement on current spinning disk prototypes due to their lack of spars.

The maximum solar radiation disturbance torques acting on the solar sails were 6.64×10^{-4} Nm and 0.61 Nm for the geocentric and heliocentric sails respectively. If the sliding masses were needed simply to cancel out these disturbance torques, the masses and distances involved in the method would be greatly reduced. For example for the geocentric sail the disturbance torques could be cancelled out by a mass of 1 kg at a distance of 6 m, while the heliocentric disturbances could be negated by a mass of 5 kg at a distance of 14 m. This is considerably more feasible, and suggests that the sliding masses could be used as a secondary actuator on a spinning solar sail in order to limit the effect of the solar disturbance torques. This would decrease the rate of momentum accumulation for reaction wheels or control moment gyros, and the rate of propellant consumption for thrusters, making the implementation of these methods more feasible.

5.6.2 Control Vanes

Control vanes are pieces of reflective material mounted at the extremities of the solar sail structure, which can be articulated to produce control torques due to solar radiation pressure.

The control torque produced by a single control vane of area A_v, situated at a distance $\bar{l}_v$ from the centre of mass, is given by the expression [32]

$$\bar{N}_v = \bar{l}_v \times \eta P (\frac{r_{au}}{|| \bar{r}_{sun} ||})^2 A_v (\hat{r}_{sun} \cdot \hat{n}_v)^2 \hat{n}_v \tag{5.53}$$

where η is the overall thrust coefficient, assumed to be 2 for a perfectly reflecting sail, $P = 4.563 \times 10^{-6}$ N/m^2 is again the nominal solar radiation pressure constant at 1 au from the Sun and $\hat{n}_v$ the unit vector of the control vane normal. Assuming that the sail is equipped with a single control vane at a distance $\bar{l}_v = [0 \quad 0 \quad l_v]^T$ and that the Sun and vane normal unit vectors are coincident, the torque produced by the vane is

equal to $(2l_v P(\frac{r_{au}}{||\bar{r}_{sun}||})^2 A_v)\hat{j}$. Therefore from this the area of control vane necessary to produce the maximum torques required for the spinning solar sails studied in Section 5.4 can be calculated.

The moment arms l_v are assumed to be $l_v = 28.3\,\mathrm{m}$ for the geocentric sail, and $l_v = 70\,\mathrm{m}$ for the heliocentric sail. In reality these moment arms would be slightly larger as the control vane centre of pressure would lie beyond the edge of the solar sail. However, these can be taken as worst case scenario moment arms. This leads to $A_v = 391.35\,\mathrm{m}^2$ for the geocentric sail, and $A_v = 631.2\,\mathrm{m}^2$ for the heliocentric sail. In order to provide reasonable control authority, a four control vane configuration is generally used [32, 33]. Therefore for the geocentric spinning solar sail, the total control vane area necessary to produce the maximum required torque would be larger than the proposed total area of the solar sail given in Table 5.1. This is obviously infeasible and thus this study suggests that control vanes are not suitable as the primary actuation on-board a geocentric spinning solar sail. However, for the larger heliocentric sail the control vane area is 16.4% of the total solar sail area. While this is high in comparison to other studies into the use of control vanes, such as that carried out by Mettler [124] where the total control vane area was 4% of the sail area, the necessary control vane area for the heliocentric case is not likely to be prohibitively high. Nevertheless, the cross-coupling of the control torques means that control vanes are unlikely to be feasible for reference tracking for a heliocentric spinning solar sail, even if the maximum torques could be supplied.

Despite control vanes likely being unsuitable as primary actuators for motion tracking for a spinning solar sail, they may possibly be used as secondary actuators to alleviate the effect of the solar disturbance torques. The maximum solar radiation disturbance torques acting on the solar sails were $6.64 \times 10^{-4}\,\mathrm{Nm}$ and $0.61\,\mathrm{Nm}$ for the geocentric and heliocentric sails respectively. Thus, the vane areas required to counteract these torques are $A_v = 2.6\,\mathrm{m}^2$ for the geocentric sail, and $A_v = 55\,\mathrm{m}^2$ for the heliocentric sail. These vane areas are considerably more feasible, and therefore the control vanes may be of some use as secondary actuators onboard a spinning solar sail to counteract the disturbance torques and so decrease the load on the primary actuators.

5.6.3 Discussion of Most Suitable Actuation for Reference Tracking

The preliminary sizing of sliding masses and control vanes for the spinning solar sails considered in this chapter suggests that these methods cannot be implemented as primary actuators onboard a geocentric spinning sail. Additionally, while the study suggests that the necessary maximum torques could be feasibly produced for a heliocentric solar sail at 0.24 au, the cross-coupling between the control torques means independent 3-axis control is not possible with these actuators, which means that reference tracking may not be possible. Finally, the sliding masses or control vanes may not be able to move quickly enough to generate the required torques within an appropriate time-scale. However, while conventional actuators are capable of tracking the references, the disturbance torques due to the centre of mass/centre of pressure offset results in swift momentum accumulation for momentum exchange devices, and would likely result in thrusters exhausting their propellant supply more quickly and so limiting the mission lifetime. While further testing is necessary to determine the most feasible method to actuate the solar sails in order to track the references described in this chapter, the results suggest that the most feasible solution would be to supplement a momentum exchange device such as a control moment gyro with propellantless actuators such as sliding masses or control vanes. In this way the secondary actuation system could act to minimise the momentum saturation by limiting the effect of the disturbance torques, while the primary 3-axis attitude control method could provide the necessary control authority to reorientate the spinning spacecraft while maintaining centrifugal stiffening.

5.7 Chapter Summary

In this chapter a motion planning method for a spinning spacecraft subject to both dynamic and kinematic nonholonomic constraints was utilised to plan repointing manoeuvres for a spinning solar sail and nano-spacecraft. The solution of Biggs and Horri was shown to be a particular solution of the general case, which takes the form of a Weierstrass elliptic function. However, this function is not suitable for practical motion

planning, and so the particular case was the focus of a motion planner which produced reference motions via parametric optimisation. It was shown that the geometric spin repointing method resulted in low body rates throughout the manoeuvre, and offered savings over a pure spin benchmark in the majority of cases. However, in some cases the pure spin references could repoint the spinning sail in a shorter time period, while in other cases it required lower accumulated torque. In particular tracking of the geometric spin repointing references with respect to the orbital frame for the geocentric solar sail did not have any significant benefits over tracking of the pure spin references. This suggests that the geometric spin repointing references are more suited to tracking with respect to inertial or near inertial frames. The motion planning method was shown to be capable of producing constrained slews, with a manoeuvre which lay entirely within a 68° degree cone demonstrated. Additionally, the method was linked to the natural motion method of Chapter 4 and it was found that the axisymmetric natural motions are a particular case of the geometric spin repointing motions. Finally, an actuator study was carried out and sliding masses and control vanes sized for future study into the most feasible method to actuate a spinning solar sail.

Chapter 6

Conclusions

The previous chapters focussed on the practical implementation of motion planning methods which consist of analytical reference motions derived using geometric control theory. This chapter summarises the contributions of this thesis, and presents suggestions for future areas of research.

6.1 Research Outcomes

This thesis was motivated by the need to determine if motion planning methods based on geometric control theory were useful for application to real autonomous systems. To this end, motion planning methods were required which could take into account nonholonomic constraints, have an inherent optimality and be adaptable to obstacle avoidance. The Lie group setting of geometric control theory had previously been shown to be capable of deriving analytical optimal controls for nonholonomic systems. However, the primary limitation of the method was that it had not previously been practically applied, and thus the suitability of the controls derived using this mathematical framework when applied to real engineering systems had not been determined. The main aim of this thesis was to address these limitations by implementing the analytical equations derived using geometric control theory in rigid body motion planning in realistic environments.

This work has furthered this field in a number of ways. Firstly, new optimal controls were derived in the case of the unit speed wheeled robot, the axisymmetric and asymmetric small spacecraft and the nonholonomic spinning spacecraft. However, in the case of the unit speed wheeled robot and nonholonomic spinning spacecraft, these controls took the form of Jacobi and Weierstrass elliptic functions which were not suitable for practical implementation.

Despite these controls proving unsuitable for practical motion planning, study of the optimal controls for a robot capable of rotating and translating at arbitrary speed found that the Jacobi elliptic functions produce a wide range of motions and have particular cases including trigonometric and hyperbolic functions. The analytical solution enabled the reachable sets of the kinematic motion planner for the arbitrary speed robot to be exactly defined. Following this, a simple obstacle avoidance framework was derived for the nonholonomic wheeled robot for static circular obstacles in a known environment. The reachable sets of the arbitrary speed wheeled robot were probed by incrementing the optimal values of the free parameters output from an initial parametric optimisation. This produced a range of curves which satisfied the boundary conditions on the final position of the robot. A curve could then be chosen which avoided the specified obstacle, as shown in Figure 6.1. The parametric optimisation and obstacle avoidance framework derived for the simple wheeled robot formed the basis of the motion planning methods for the more complex natural motions and geometric spin repointing references.

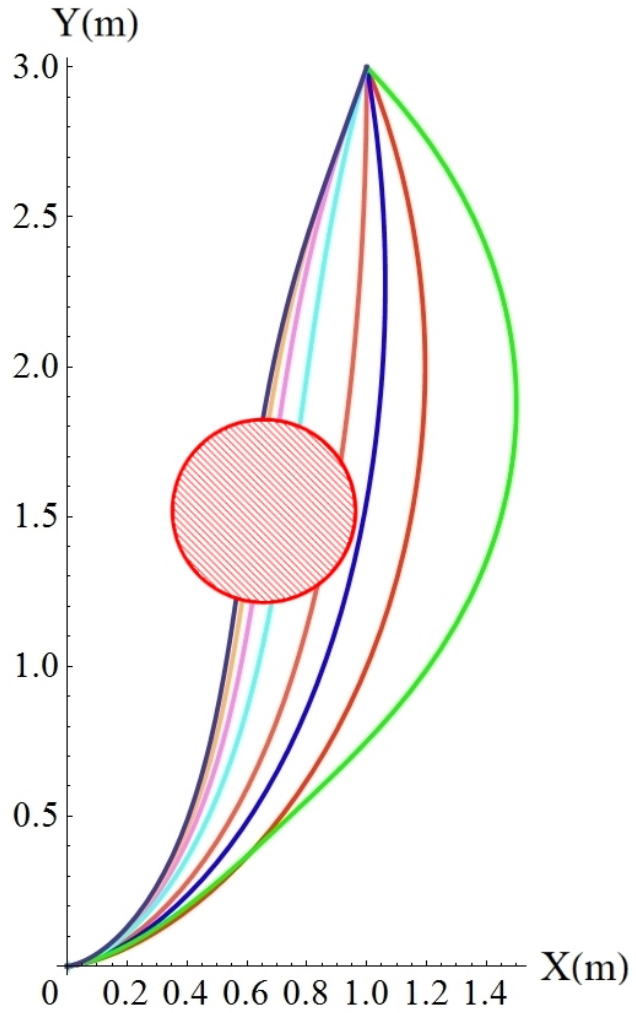

Figure 6.1: Alternative smooth trajectories to $[X_f \quad Y_f]^T = [1 \quad 3]$m. Several paths intersect the obstacle (shaded circle), while several avoid it.

The key contribution to knowledge of this thesis was that the natural motion and geometric spin repointing references, derived in the framework of geometric control theory, were rigorously tested in simulation. This was the first such rigorous testing of references generated via geometric control theory, and so provided a link with real engineering applications. The work included considering actuators limitations and non-ideal environments which are not part of the geometric control theory framework, and so had the potential to reduce the effectiveness of the methods. Both methods were compared to standard benchmark control methods to assess their effectiveness in re-

pointing rigid body spacecraft.

The natural motion method, novelly derived in this thesis, offered significant savings in accumulated torque over a quaternion feedback benchmark in all cases tested. These results are summarised in Table 6.1.

Table 6.1: Summary of main results of natural motion simulations for 120 s manoeuvres.

Manoeuvre	${I_N}^{Q.F.}$ (Nms)	${I_N}^{N.M}$ (Nms)	% Saving
Axisymmetric Spacecraft			
NM-A	0.0068	0.0025	63.2
NM-B	0.0103	0.0014	86.4
NM-C	0.0086	0.0013	84.9
NM-D	0.0146	0.003	79.5
NM-E	0.0046	0.0018	60.9
Asymmetric Spacecraft			
NM-F	0.008	0.0024	70
NM-G	0.0083	0.0016	80.7
NM-H	0.0076	0.0033	56.6
NM-I	0.0115	0.0022	80.9
NM-J	0.0119	0.0043	63.9

However, only the axisymmetric references have potential for practical use at this time, as the asymmetric references include an incomplete elliptic integral of the third kind which requires a prohibitively long time to compute. In contrast, the axisymmetric references were more computationally efficient and could be used in a quasi open-loop, "bang-off-bang" manner in low disturbance environments, to save on computation and control effort. In addition, a study into the effect of inertia variations on the performance of the axisymmetric references found that a saving in accumulated torque could be achieved over quaternion feedback control even when the axisymmetric natural motion references were applied to an asymmetric spacecraft. The method of probing the reachable sets to create constrained slews, first derived for the nonholonomic wheeled robot, was adapted and applied to enable constrained repointing manoeuvres to be generated with respect to forbidden cones in the configuration space. This was applied to the natural motion method to generate a manoeuvre which avoided the forbidden

cone generated by the Moon. Therefore the axisymmetric natural motion references, derived in the framework of geometric control theory, have shown some promise for use in practical motion planning.

The geometric spin repointing references, which had been derived prior to this work but had not been fully tested in simulation, were less successful when practically applied to a spinning solar sail. In this case the benchmark method of tracking pure spin references was more favourable in a small number of cases, where it was capable of repointing the solar sail in a shorter time and with lower accumulated torque. However, the geometric spin repointing method did offer savings in accumulated torque and lower body rates in a majority of cases simulated. Tracking for a heliocentric solar sail proved more successful than for a geocentric sail, suggesting that the geometric spin repointing method is less suitable for tracking references in the rotating orbital frame when the orbital component of the angular velocity is significant. These results are summarised in Table 6.2.

Table 6.2: Summary of main results of geometric spin repointing simulations. Tracking with respect to orbital frame.

Geocentric Sail					
Manoeuvre	v (rad/s)	Time (s)	${I_N}^{P.S.}$ (Nms)	${I_N}^{S.R.}$ (Nms)	% Saving
SR-A	0.0209	6100	254	349	-27.2
	0.00785	2000	94	72	23.4
SR-B	0.0209	3000	330	211	36.1
	0.00785	1200	98.5	NA	-100
SR-C	0.0209	2500	286.2	263	8.1
	0.00785	1250	128	NA	-100
Heliocentric Sail					
SR-D	0.0209	4000	3×10^4	1.28×10^4	57.3
	0.00785	4500	1.23×10^4	4.8×10^3	61
SR-E	0.0209	8000	2.7×10^4	6.57×10^3	75.7
	0.00785	2500	5.4×10^3	2.72×10^3	49.6
SR-F	0.0209	2000	4.72×10^3	4.24×10^3	10.2
	0.00785	1000	1.55×10^3	NA	-100
SR-G	0.0209	8000	3.81×10^4	6.8×10^3	82.2
	0.00785	4000	4.9×10^3	7.43×10^3	-34.1
SR-H	0.0209	5000	2×10^4	1.05×10^4	47.5
	0.00785	4000	1.29×10^4	5.07×10^3	60.7

The % saving is defined as $({I_N}^{P.S.} - {I_N}^{S.R})/{I_N}^{P.S.} \times 100$ for the cases when the geometric spin repointing method requires lower accumulated torque, and $({I_N}^{S.R.} - {I_N}^{P.S})/{I_N}^{S.R.} \times 100$ otherwise. The cases where the pure spin references require lower accumulated torque are marked as a negative saving.

Additionally, the geometric spin repointing motion planner was shown to be capable of producing constrained slews. A manoeuvre which lay entirely within a cone in the configuration space generated by the Sun was demonstrated. Tracking of the geometric spin repointing references for the nano-spacecraft of Chapter 4 found that the geometric spin repointing method offered savings in accumulated torque over the pure spin and quaternion feedback control benchmarks in all cases simulated. Comparison with the natural motion references found that the axisymmetric natural motion references are a subset of the geometric spin repointing references. Thus the geometric spin repointing references which require larger accumulated torque are likely to be far from the natural motion for the manoeuvre. Conversely, the lowest accumulated torque manoeuvres are achieved when the manoeuvre is close to the natural motion of the spacecraft.

6.2 Limitations and Future Work

Based on the outcomes of the thesis presented above, in this section some suggestions are made for extensions of the work in this thesis.

The kinematic motion planner for the simple wheeled robots described in Chapter 3 was utilised as a means of illustrating the mechanisms of geometric control theory, and formulating the parametric optimisation and obstacle avoidance frameworks for the proceeding chapters. As a result, the robot motion planner was not practically applied. Therefore future work could involve the implementation of a concatenation method to feasibly piece together the curves of the robotic motion planner to give a more complete motion planning algorithm. This would involve amending the motion planning method to have non-zero initial speeds, and developing an algorithm to choose the paths most suited to being pieced together. This would lead to the possibility of extending the simple obstacle avoidance algorithm to dynamic and unknown environments. If these

goals could be achieved, the motion planning algorithm could be implemented on-board a small wheeled robot and used to plan motions. This would enable the practicality of the cost function to be assessed, together with the feasibility of tracking the motions generated by the planner using real actuators.

In the natural motion motion planning method, detailed in Chapter 4, the spacecraft sensors and the internal dynamics of the actuators were not modelled. In reality the reaction wheels are subject to friction which affects their operating efficiency, while sensor readings are subject to noise and other errors. These factors could influence the effectiveness of the natural motion method. Additionally, the processor used to generate the references was much faster than that of a spacecraft and so the feasibility of implementing the natural motion planning method on-board a realistic spacecraft processor has not been determined. To address these issues, the method could be tested on an attitude control testbed, such as that which is currently under construction at the University of Strathclyde. This is shown in Figure 6.2.

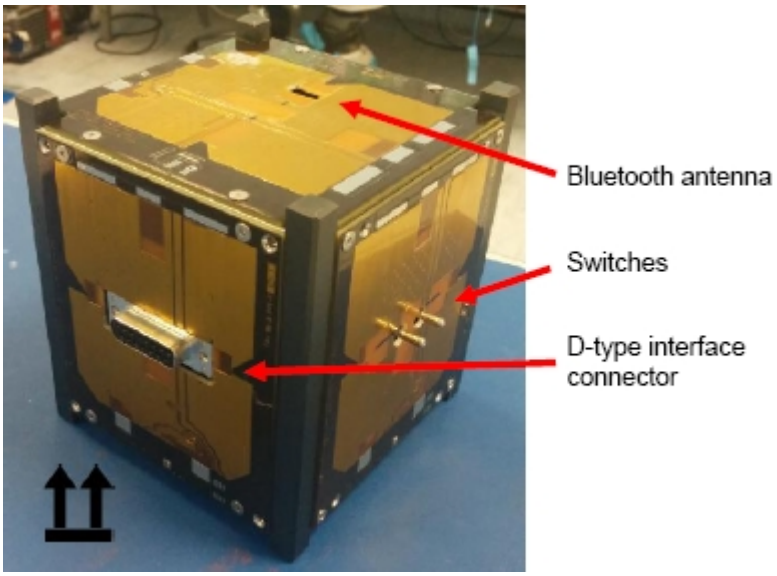

Figure 6.2: Exterior of Cubesat component of testbed (Image Credit: Clyde Space Ltd).

The testbed consists of a 1U-Cubesat spacecraft attached to an air bearing which enables the spacecraft to rotate freely within (to be determined) bounds, providing a close

approximation of the natural environment of the spacecraft. The natural motion planning method would be implemented on a 30 MHz processor, with an exact replica of the software flown on UKube-1, which would enable the performance of the method in the face of reduced computation, errors due to inaccurate sensing and actuator constraints to be assessed. Allied to this would be finding a means to improve the computational efficiency of the asymmetric method, as at present the savings in accumulated torque are greatly outweighed by the time taken to generate the references due to the presence of an incomplete elliptic integral of the third kind.

Additionally, as the quaternion feedback controller causes the quaternions to evolve in broadly sigmoidal curves, the possibility of generating and tracking sigmoidal, rather than constant, quaternion references between the initial and final attitudes could be investigated to determine if this results in a saving in control effort when compared to the natural motion method. Finally, in order to rank the natural motion method alongside other attitude control and guidance methods, the method could be compared to other non-optimal guidance methods such as the artificial potential function method or pseudospectral optimal control methods. The aim of these comparisons would be to determine whether the savings in accumulated torque offered by the natural motion method justify the increased computation required to generate the references. Additionally, the comparison to artificial potential functions and pseudospectral methods would enable more rigorous testing of the derived algorithm for generating constrained slews to be carried out. At present the method relies heavily on heuristics and as such is not suitable for fast generation of constrained attitude slew reference tracks.

The assumption that the solar sail is a rigid body which was made in Chapter 5 is commonly found in solar sail attitude control, but nevertheless requires further testing to determine the validity of making such as assumption. One such means may be to utilise the model recently developed by JAXA [127] for their spinning solar sail, and compare the results with the simple rigid body model utilised in this thesis. Furthermore, detailed actuator modelling is necessary to determine the most suitable method, if any exists, for implementing the motion planning method on a spinning solar sail. In a similar manner to the motion planning method utilised in Chapter 4, the compu-

tational efficiency of the method could be assessed via implementation on the attitude control testbed under development at the University of Strathclyde. A preliminary study into the feasibility of applying the natural motion and geometric spin repointing references to motion planning on the testbed found that current nano-spacecraft actuator technology using magnetic torquers was not sufficient to track references. Therefore the development of nano-spacecraft reaction wheels would enable the real benefits of the geometric motion planning planning methods studied in this thesis to be assessed on actual spacecraft hardware and software.

Bibliography

[1] Wilson, R. H. and Latombe, J.C., "Geometric Reasoning About Mechanical Assembly," *Artificial Intelligence Journal*, Vol. 71, No. 2, pp. 371-396, 1994.

[2] Latombe, J. C., "Robot Motion Planning," Boston, Kluwer, 1991.

[3] Dubins, L. E., "On Curves of Minimal Length With a Constraint on Average Curvature, and With Prescribed Initial and Terminal Positions and Tangents,' *American Journal of Mathematics*, Vol. 79, pp. 497-516, 1957.

[4] Reeds J. A. and Shepp, L. A., "Optimal Paths for a Car That Goes Both Forwards and Backwards," *Pacific Journal of Mathematics*, Vol. 145, No. 2, pp. 367-393, 1990.

[5] Duindam, V., Xu, J., Alterowitz, R., Sastry, S. and Goldberg, K., "3D Motion Planning Algorithms for Steerable Needles Using Inverse Kinematics," *The International Journal of Robotics Research*, Vol. 29, No. 7, pp. 789-800, 2010.

[6] Sturtevant, N. R., "Moving Path Planning Forward," In: *Motion in Games*, Lecture Notes in Computer Science, Kallmann, M. and Bekris, K. Eds., Vol. 7660, Springer-Verlag, 2012.

[7] Tsourdos, A., White, B. A. and Shanmugavel, M., "Cooperative Path Planning of Unmanned Aerial Vehicles," Wiley, 2011.

[8] Spindler, K., "Optimal Attitude Control of a Rigid Body," *Applied Mathematics and Optimisation*, Vol. 34, pp. 79-90, 1996.

[9] Lozano-Perez, T., "The Design of a Mechanical Assembly System," Report AI-TR-397, MIT Artificial Intelligence Laboratory, 1976.

[10] Lazanas A. and Latombe, J.C. "Motion Planning With Uncertainty: A Landmark Approach,' *Artificial Intelligence*, Vol. 76, No. 1, pp. 287-317, 1995.

[11] Martinez, S., Cortes, J. and Bullo, F., "Motion Planning and Control Problems for Underactuated Robots,' In: *Control Problems in Robotics*, Bicchi, A., Christensen, H. and Prattichizzo, D. Eds., Vol. 4, pp. 59-74, Springer-Verlag, 2003.

[12] Shammas, E. A., Choset, H. and Rizzi, A.A., "Geometric Motion Planning Analysis for Two Classes of Underactuated Mechanical Systems,' *The International Journal of Robotics Research*, Vol. 26, No. 10, pp. 1043-1073, 2007.

[13] Bloch, A. M., "Nonholonomic Mechanics and Control," Springer-Verlag, 2003.

[14] LaValle, S. M., "Planning Algorithms," Cambridge University Press, 2006.

[15] Laumond, J. P., "Robot Motion Planning and Control," Lecture Notes in Control and Information Sciences, Springer, 1998.

[16] Leonard N. and Krishnaprasad, P. S., "Motion Control of Drift Free, Left-Invariant Systems on Lie Groups," *IEEE Transactions on Automatic Control*, **40**, 1539-1554, (1995).

[17] Jurdjevic, V., "Geometric Control Theory", Advanced Studies in Mathematics, Cambridge University Press, Vol. 52, 1997.

[18] Selig, J. M., "Geometric Fundamentals of Robotics," Monographs in Computer Science, Springer, 2006.

[19] Murray, R., Li, Z. and Sastry, S., "A Mathematical Introduction to Robotic Manipulation," CRC Press, 1994.

[20] Murray R. and Sastry, S., "Steering Nonholonomic Systems Using Sinusoids," In: *Proceedings of 29th IEEE Conference on Decision and Control*, Honolulu, Hawaii, pp. 2097-2101, 1990.

[21] Brockett, R. W., "Control Theory and Singular Riemannian Geometry," In: *New Directions in Applied Mathematics*, Hilton, P. J. and Young, G. S. Eds., pp. 11-27, Springer-Verlag, 1982.

[22] Leonard, N. E. and Krishnaprasad, P. S., "Averaging for Attitude Control and Motion Planning,' In: *Proceedings of the 32nd Conference on Decision and Control*, Texas, USA, 1993.

[23] Ross, I. M., and Karpenko, M.,"A Review of Pseudospectral Optimal Control: From Theory to Flight," *Annual Reviews in Control*, Vol. 36, No.2, pp. 182-197, 2012.

[24] Bryson, A. E. and Ho, Y.C.,"Applied Optimal Control", Hemisphere Publishing Corp., New York, 1975.

[25] Laumond, J.P., Jacobs, P.E., Taix, M. and Murray, R.M., "A Motion Planner for Nonholonomic Mobile Robots," *IEEE Transactions on Robotics and Automation*, Vol. 10, No. 3, 1994.

[26] Brockett, R. W., "System Theory on Group Manifolds and Coset Spaces," *SIAM Journal on Control*, Vol 10, No. 2, pp. 265-284, 1972.

[27] Walsh, G., Montgomery, R., Sastry, S., "Optimal Path Planning on Matrix Lie Groups," In: *Proceedings of IEEE Conference on Decision and Control*, Florida, USA, 1994.

[28] Biggs, J. D. and Holderbaum, W., "Optimal Kinematic Control of an Autonomous Underwater Vehicle," *IEEE Transactions on Automatic Control*, Vol. 54, No. 7, pp. 1623-1626, 2009.

[29] Biggs, J. D. and Horri, N., "Optimal Geometric Motion Planning for Spin-Stabilized Spacecraft," *Systems and Control Letters*, Vol. 61, No. 4, pp. 609-616, 2012.

[30] Kim, B. K. and Shin, K. G., "Minimum-Time Path Planning for Robot Arms and Their Dynamics," *IEEE Transactions on Systems, Man, and Cybernetics*, Vol. SMC-15, No. 2, pp.213-223, 1985.

[31] Funase, R., Shirasawa, Y., Mimasu, Y., Mori, O., Tsuda, Y., Saiki, T. and Kawaguchi, J., "On-Orbit Verification of Fuel-Free Attitude Control System for Spinning Solar Sail Utilizing Solar Radiation Pressure," *Advances in Space Research*, Vol. 48, pp. 1740-1746, 2011.

[32] Wie, B., "Space Vehicle Dynamics and Control," AIAA Education Series, 2nd addition, 2008.

[33] McInnes, C. R., "Solar Sailing: Technology Dynamics and Mission Applications," Springer-Praxis, Chichester, 1999.

[34] Nelder, J. A. and Mead, R., "A Simplex Method for Function Minimisation," *Computer Journal*, Vol. 7, No. 4, pp. 308-313, 1965.

[35] Deb, K., "Optimization for Engineering Design: Algorithms and Examples," PHI Learning Private Limited, 2013.

[36] Gong, Q., Lewis, R. and Ross, M., "Pseudospectral Motion Planning for Autonomous Vehicles," *Journal of Guidance, Control, and Dynamics*, Vol. 32, No. 3, pp. 1039-1045, 2009.

[37] Gong, Q., Kang, W., Bedrossian, N. S., Fahroo, F., Sekhavat, P. and Bollino, K., "Pseudospectral Optimal Control for Military and Industrial Applications," In: *46th IEEE Conference on Decision and Control*, New Orleans, USA, pp. 4128-4142, 2007.

[38] Kuwata, Y., Karaman, S., Teo, J., Frazzoli, E., How, J. P. and Fiore, G., "Real-Time Motion Planning With Applications to Autonomous Urban Driving," *IEEE Transactions on Control Systems Technology*, Vol.17, No. 5, pp. 1105-1118, 2009.

[39] Urmson, C. and Simmons, R., "Approaches for Heuristically Biasing RRT Growth," In: *Proceedings 2003 IEEE/RSJ International Conference on Intelligent Robots and Systems*, Vol.2, pp.1178-1183, 2003.

[40] Geraerts, R. and Overmars, M. H., "Creating High-quality Paths for Motion Planning," *International Journal of Robotics Research*, Vol. 26, No. 8, pp. 845-863, 2007.

[41] Boltyanskii, V. G., Gamkrelidze, R. V. and Pontryagin, L.S., "Towards a Theory of Optimal Processes," *Reports Acad. Sci. USSR*, Vol. 110, No. 1, pp. 7-10, 1956.

[42] Choset, H., Lynch, K., Hutchinson, S., Kantor, G., Burgard, W., Kavraki, L. and Thrun, S., "Principles of Robot Motion - Theory, Algorithms, and Implementation," Boston, MIT press, 2005.

[43] Mengali, G. and Quarta, A.A., "Spacecraft Control with Constrained Fast Reorientation and Accurate Pointing", *The Aeronautical Journal*, Vol. 108, No.1080, pp. 85-91, 2004.

[44] Nilsson, N. J., "A Mobile Automaton: An Application of Artificial Intelligence Techniques," In: *1st International Conference on Artificial Intelligence*, pp. 509-520, 1969.

[45] Lozano-Perez, T. and Wesley, M. A., "An Algorithm for Planning Collision-Free Paths Among Polyhedral Obstacles," *Communications of the ACM*, Vol. 22, No. 10, pp. 560-570, 1979.

[46] Laumond, J.P., "Obstacle Growing in a Nonpolygonal World," *Information Processing Letters*, Vol. 25, No. 1, pp. 41-50, 1987.

[47] Schwartz, J. T. and Sharir, M., "On the 'Piano-Movers' Problem. I. The Case of a Two-dimensional Rigid Polygonal Body Moving Amidst Polygonal Barriers", *Communications on Pure and Applied Mathematics*, Vol. 36, No. 3, pp. 345-398, 1983.

[48] Schwartz, J. T. and Sharir, M., "On the 'Piano-movers' Problem. III. Coordinating the Motion of Several Independent Bodies: The Special Case of Circular Bodies Moving Amidst Polygonal Barriers," *The International Journal of Robotics Research*, Vol. 2, No. 3, pp. 46-75, 1983.

[49] Barraquand, J. and Latombe, J. C., "Robot Motion Planning: A Distributed Representation Approach," *The International Journal of Robotics Research*, Vol. 10, No. 6, pp. 628-649, 1991.

[50] Khatib, O., "Real-time Obstacle Avoidance for Manipulators and Mobile Robots," *The International Journal of Robotics Research*, Vol. 5, No. 1, pp. 90-98, 1986.

[51] McInnes, C. R., "Non-linear Control for Large Angle Attitude Slew Manoeuvres", In: *Proceedings Third International Conference on Spacecraft Guidance, Navigation and Control Systems*, Noordwijk, The Netherlands, 1997.

[52] Radice, G. and Ali, I., "Autonomous Attitude Control Using Potential Function Method Under Control Input Saturation", In: *Proceedings of the 59th International Astronautical Congress*, Glasgow, Scotland, 2008.

[53] Clark, C., McInnes, C.R. and Radice, G., "Space Activities in Glasgow; Advanced Microspacecraft From Scotland", In: *Proceedings of the 59th International Astronautical Congress*, Glasgow, Scotland, 2008.

[54] J. Biggs, 'Optimal Path Planning for Nonholonomic Robotics Systems via Parametric Optimisation,' In: *Proceedings of TAROS 2011*, Sheffield, UK, 2011.

[55] Klein F., "The Mathematical Theory of the Top", Chelsea Publishing Company, New York, Lectures delivered in Princeton in 1896.

[56] Wei, J. and Norman, E., "On Global Representations of the Solution of Linear Differential Equations as a Product of Exponentials," In: *Proceedings of the American Mathematical Society*, Vol. 15, pp. 327-334, 1964.

[57] Audin, M., "Spinning Tops: A Course on Integrable Systems," Cambridge Studies in Advanced Mathematics, Cambridge University Press, 1996.

[58] Sidi, M.J., "Space Dynamics and Control: A Practical Engineering Approach", Cambridge University Press, Vol. 7, 1997.

[59] Biggs, J. D., Maclean, C. D. and Caubet, A., "Heteroclinic Optimal Control Solutions for Attitude Motion Planning," In: *Australian Control Conference*, Perth, Australia, 2013.

[60] Hall, B. C., "Lie Groups, Lie Algebras, and Representations: An Elementary Introduction," Springer-Verlag, New York, 2003.

[61] Bhat, S.P. and Bernstein, D.S., "A Topological Obstruction to Continuous Global Stabilization of Rotational Motion and the Unwinding Phenomenon," *Systems and Control Letters*, Vol. 39, pp. 63-70, 2000.

[62] Chaturvedi, N., Sanyal, A. and McClamroch, N., "Rigid-Body Attitude Control," *IEEE Control Systems*, Vol.31, No. 3, pp. 30-51, 2011.

[63] Kuipers, J. B., "Quaternions and Rotation Sequences: A Primer with Applications to Orbits, Aerospace, and Virtual Reality," Princeton University Press, New Jersey, 1999.

[64] Sussmann, H. J., "An Introduction to the Coordinate-Free Maximum Principle," In: *Geometry of Feedback and Optimal Control*, Jakubczyk, B. and Respondek, W. Eds., pp. 463-557, Marcel Dekker, New York, 1997.

[65] Jurdjevic, V., "Maximum Principle in Optimal Control," In: *Mathematics of Complexity and Dynamical Systems* Meyers, R. A. Ed, pp 953-963, Springer New York, 2011.

[66] Jurdjevic, V. and Monroy-Perez, F., "Variational Problems on Lie Groups and Their Homogeneous Space: Elastic Curves, Tops, and Constrained Geodesic Problems," In: *Contemporary Trends in Nonlinear Geometric Control Theory and its Applications*, Anzaldo-Meneses, A., Bonnard, B., Gauthier, J. P. and Monroy-Perez, F. Eds., pp. 3-51, World Scientific, 2002.

[67] Mahmoudian, N. and Woolsey, C., "Underwater Glider Motion Control," In: *Proceedings of the 47th IEEE Conference on Decision and Control*, Cancun, Mexico, pp. 552-557, 2008.

[68] Scheuer, A. and Fraichard, Th., "Continuous Curvature Path Planning for Car-Like Vehicles," In: *Proceedings of the IEEE International Conference on Intelligent Robots and Systems*, Montbonnot-Saint-Martin, France, Vol. 2, pp. 997-1003, 1997.

[69] Scheuer, A. and Fraichard, Th., "Collision-Free and Continuous-Curvature Path Planning for Car-Like Robots," In: *Proceedings of International Conference on Robotics and Automation*, Albuquerque, New Mexico, pp. 867-873, 1997.

[70] Fraichard, Th. and Ahuactzin, J. M., "Smooth Path Planning for Cars," In: *Proceedings of International Conference on Robotics and Automation*, Seoul, South Korea, Vol. 4, pp. 3722-3727, 2001.

[71] Macharet, D. G., Neto, A. A., Neto, V. F. C. and Campos, M. F. M., "Nonholonomic Path Planning Optimization for Dubins' Vehicles," In: *IEEE International Conference on Robotics and Automation* , Shanghai, China, 2011.

[72] Savla, K., Frazzoli, E. and Bullo, F., "On the Point-to-Point and Traveling Salesperson Problems for Dubins' Vehicle," In: *Proceedings of the American Control Conference*, Portland, USA, pp. 786-791, 2005.

[73] Brockett, R. W. and Dai, L., "Non-Holonomic Kinematics and the Role of Elliptic Functions in Constructive Controllability," In: *Nonholonomic Motion Planning*, Robotics: Vision, Manipulation and Sensors, Zexiang, L. and Canny, J. Eds., pp. 1-21, Springer US, 1993.

[74] Jurdjevic, V., "Hamiltonian Point of View of Non-Euclidean Geometry and Elliptic Functions," *Systems and Control Letters*, Vol. 43, pp. 25-41, 2001.

[75] Husemoller, D., "Elliptic Curves," Springer, 2004.

[76] Olver, F. W. J., Lozier, D. W., Boisvert, R. F. and Clark, C. W., "NIST Handbook of Mathematical Functions," Cambridge University Press, 2010.

[77] Abramowitz, M. and Stegun, I. A., "Handbook of Mathematical Functions with Formulas, Graphs, and Mathematical Tables," Dover, 1972.

[78] Meyer, K. R., "Jacobi Elliptic Functions From a Dynamical Systems Point of View," *The American Mathematical Monthly*, Vol. 108, No. 8, pp. 729-737, 2001.

[79] Jurdjevic, V., "Non-Euclidean Elastica," *American Journal of Mathematics*, Vol. 117, No. 1, pp. 93-124, 1995.

[80] Mazer, E., Ahuactzin, J. M., Talbi, E. G. and Bessiere, P., "Robot Motion Planning With the Ariadne's Clew Algorithm," In: *Proceedings of the International Conference on Intelligent Autonomous Systems*, Pittsburgh, USA, 1993.

[81] Svetska, P. and Overmars, M. H., "Probabilistic Path Planning," Technical Report UU-CS-1995-22, Utrecht University, Utrecht, The Netherlands, 1995.

[82] Frazzoli, E., Dahleh, M. A. and Feron, E., "Maneuver-Based Motion Planning for Nonlinear Systems with Symmetries," *IEEE Transactions on Robotics.*, Vol. 21, No. 6, pp. 1077-1091, 2005.

[83] Pivtoraiko, M. and Kelly, A., "Generating Near Minimal Spanning Control Sets for Constrained Motion Planning in Discrete State Spaces,' In: *Proceedings of the IEEE/RSJ International Conference on Intelligent Robots and Systems*, IROS, pp. 3231 - 3237, 2005.

[84] Barba, P.M. and Aubrun, J.N., "Satellite Attitude Acquisition by Momentum Transfer," *AIAA Journal*, Vol. 14, pp. 1382-1386, 1976.

[85] Vadali, S.R. and Junkins, J.L., "Spacecraft Large Angle Rotational Maneuvers with Optimal Momentum Transfer," *Journal of Astronautical Sciences*, Vol. XXXI, No.2, pp. 217-235, 1983.

[86] Raus, R., Gao, Y., Wu, Y. and Watt, M., "Analysis of State-of-the-Art Single-Thruster Attitude Techniques for Spinning Penetrator," *Acta Astronautica*, Vol. 76, pp. 60-78, 2012.

[87] D'Amario, L.A. and Stubbs, G.S., "A New Single-Rotation-Axis Autopilot for Rapid Spacecraft Attitude Maneuvers," *Journal of Guidance and Control*, Vol. 2, No. 4, pp. 339-346, 1979.

[88] Wie, B., Weiss, H., and Arapostathis, A., "Quaternion Feedback Regulator for Spacecraft Eigenaxis Rotations," *Journal of Guidance, Control, and Dynamics*, Vol. 12, No. 3, pp. 375-380, 1989.

[89] Steyn, W.H., "Near-Minimum-Time Eigenaxis Rotation Maneuvers Using Reaction Wheels," *Journal of Guidance, Control, and Dynamics*, Vol. 18, No. 5, pp. 1184-1189, 1995.

[90] Wie, B., Bailey, D. and Heiberg, C., "Rapid Multitarget Acquisition and Pointing Control of Agile Spacecraft," *Journal of Guidance, Control, and Dynamics*, Vol. 25, No. 1, pp. 96-104, 2002.

[91] Verbin, D., Lappas, V.J. and Ben-Asher, J.Z., "Time-Efficient Angular Steering Laws for Rigid Satellites," *Journal of Guidance, Control, and Dynamics*, Vol. 34, No. 3, pp. 878-892, 2011.

[92] Lawton, J., Beard, R., and Mclain, T., "Successive Galerkin Approximation of Nonlinear Optimal Attitude Control," In: *Proceedings of the American Control Conference*, San Diego, USA, 1999.

[93] Wie, B., Barba, P.M., "Quaternion Feedback for Spacecraft Large Angle Maneuvers," *Journal of Guidance, Control, and Dynamics*, Vol. 8, No. 3, pp. 360-365, 1985.

[94] Vadali, S. R. and Junkins, J. L., "Optimal Open-Loop and Stable Feedback Control of Rigid Spacecraft Attitude Maneuvers," *Journal of the Astronautical Sciences*, Vol. 32, pp. 105-122, 1984.

[95] Krstić, M. and Tsiotras, P., "Inverse Optimal Stabilization of a Rigid Spacecraft," *IEEE Transactions on Automatic Control*, Vol. 44, No. 5, pp. 1042-1049, 1999.

[96] Horri, N. M., Palmer, P. and Roberts, M., "Energy Optimal Spacecraft Attitude Control Subject to Convergence Rate Constraints," *Control Engineering Practice*, Vol. 19, pp. 1297-1314, 2011.

[97] Horri, N. M., Palmer, P. and Roberts, M., "Gain-Scheduled Inverse Optimal Satellite Attitude Control," *IEEE Transactions on Aerospace and Electronic Systems*, Vol. 48, No. 3, pp. 2437-2457, 2012.

[98] Whittaker, E. T., "A Treatise on the Analytical Dynamics of Particles and Rigid Bodies," Cambridge Mathematical Library, Cambridge University Press, 1999.

[99] Bates, L. and Fassò, F., "The Conjugate Locus for the Euler Top I. The Axisymmetric Case," *International Mathematical Forum*, Vol. 2, No. 43, pp. 2109-2139, 2007.

[100] Fassò, F., "The Euler-Poinsot Top: A Non-Commutatively Integrable System Without Global Action-Angle Coordinates," *Zeitschrift für angewandte Mathematik und Physik ZAMP*, Vol. 47, No. 6, pp. 953-976, 1996.

[101] Bate, R.R., Mueller, D.D. and White, J., "Fundamentals of Astrodynamics," Dover Books, pp. 156-159, 1971.

[102] Sinclair Interplanetary, *Reaction Wheels*, [Online], Available from: `http://www.sinclairinterplanetary.com/reactionwheels`, [Accessed 19/11/13].

[103] Hughes, P.C., "Spacecraft Attitude Dynamics," Dover Books, 1986.

[104] Schalkowsky, S. and Harris, M., "Spacecraft Magnetic Torques," Report SP-8018, NASA, 1969.

[105] Larson, W.J and Wertz, J.R., "Space Mission Analysis and Design," Space Technology Series, 3rd Edition, 1999.

[106] Schaub, H and Junkins, J.L., "Analytical Mechanics of Space Systems," AIAA Education Series, 2nd Edition, 2009.

[107] Dubrovin B.A., Krichever I.M. and Novikov S.P., "Integrable Systems I," In: *Dynamical Systems IV, Encyclopaedia of Mathematical Sciences*, Arnol'd, V.I. and Novikov, S.P. Eds., pp. 173-280, Springer, 1990.

[108] Maclean, C., Pagnozzi, D. and Biggs, J.D., "Computationally Light Attitude Controls for Resource Limited Nano-spacecraft," In: *Proceedings of the 2011 International Astronautical Congress*, Cape Town, South Africa, 2011.

[109] Biggs, J. D., "Singularities of Optimal Attitude Motions," In: *18th IFAC Conference on Automatic Control in Aerospace*, Nara, Japan, 2010.

[110] Marsden, J. E. and Ratiu, T.S., "Introduction to Mechanics and Symmetry," Springer, 2nd Edition, 1999.

[111] Pagnozzi, D., Maclean, C. and Biggs, J.D., "A New Approach to the Solution of Free Rigid Body Motion for Attitude Maneuvers," In: *European Control Conference*, Zurich, Switzerland, 2013..

[112] Becerra, V.M., *PSOPT Project Home*, [Online], Available from: `http://www.psopt.org/`, [Accessed 01/09/13].

[113] Macdonald, M. and McInnes, C.R., "GeoSail; An Enhanced Magnetosphere Mission, Using a Small Low Cost Solar Sail," In: *Proceedings of the 51st International Astronautical Congress*, Rio de Janeiro, Brazil, 2000.

[114] Macdonald, M., Hughes, G.W., McInnes, C.R., Lyngvi, A., Falkner, P. and Atzei, A., "GeoSail: An Elegant Solar Sail Demonstration Mission," *Journal Spacecraft and Rockets*, Vol. 44, No. 4, pp. 784-796, 2007.

[115] Macdonald, M., Hughes, G.W., McInnes, C.R., Lyngvi, A., Falkner, P. and Atzei, A., "Solar Polar Orbiter: A Solar Sail Technology Reference Study," *Journal of Spacecraft and Rockets*, Vol. 43, No. 5, pp. 960-972, 2006.

[116] Macdonald, M., McInnes, C.R. and Hughes, G.W., "Technology Requirements of Exploration Beyond Neptune by Solar Sail Propulsion," *Journal of Spacecraft and Rockets*, Vol. 47, No. 3, pp. 472-483, 2010.

[117] Bolle, A., Circi, C., "Solar Sail Attitude Control Through In-Plane Moving Masses," *Journal of Aerospace Engineering*, Vol. 222, No. 1, pp. 81-94, 2008.

[118] Mimasu, Y., Yamaguchi, T., Matsumoto, M., Nakamiya, M., Funase, R. and Kawaguchi, J., "Spinning Solar Sail Orbit Steering via Spin Rate Control," *Advances in Space Research*, Vol. 48, pp. 1810-1821, 2011.

[119] Gong, S., Li, J. and Zhu, K., "Dynamical Analysis of a Spinning Solar Sail," *Advances in Space Research*, Vol. 48, pp. 1797-1809, 2011.

[120] Polites, M., Kalmanson, J. and Mangus, D., "Solar Sail Attitude Control Using Small Reaction Wheels and Magnetic Torquers," *Proceedings of the Institution Of Mechanical Engineers Part G - Journal Of Aerospace Engineering*, Vol. 222(G1), pp. 53-62, 2008.

[121] Kishino, Y., Tamura, M., Yamamoto, T. and Mori, O., "Development of Gas-Liquid Equilibrium Propulsion System for IKAROS RCS", In: *Proceedings of the 61st International Astronautical Congress*, Prague, Czech Republic, 2010.

[122] Tsuda, Y., Mori, O., Funase, R., Sawada, H., Yamamoto, T., Saiki, T., Endo, T. and Kawaguchi, J., "Flight Status of IKAROS Deep Space Solar Sail Demonstrator", *Acta Astronautica*, Vol. 69, No. 9-10, pp. 833-840, 2011.

[123] Steyn, W.H. and Lappas, V., "Cubesat Solar Sail 3-axis Stabilization Using Panel Translation and Magnetic Torquing", *Aerospace Science and Technology*, Vol. 15, pp. 476-485, 2011.

[124] Mettler, E., Acikmese, A.B. and Ploen, S.R., "Attitude Dynamics and Control of Solar Sails with Articulated Vanes", In: *AIAA Guidance, Navigation, and Control Conference and Exhibit*, San Francisco, USA, 2005.

[125] Barnes, N.C., Derbes, W.C., Player, C.J. and Diedrich, B.L., "Sunjammer: A Solar Sail Demonstration", In: *Advances in Solar Sailing Vol. 1*, Macdonald, M. Ed., pp. 115-127, Springer-Verlag, 2014.

[126] Honeywell, *Constellation Series Reaction Wheels*, [Online], Available from: `http://aerospace.honeywell.com/~/media/UWSAero/common/documents/myaerospacecatalog-documents/Constellation_Reaction_Wheels.pdf`, [Accessed 19/11/13].

[127] Tsuda, Y., Saiki, T., Funase, R., and Mimasu, Y., "Generalized Attitude Model for Spinning Solar Sail Spacecraft," *Journal of Guidance, Control and Dynamics*, Vol. 36, No. 4, pp. 967-974, 2013.